THE CATHOLIC UNIVERSITY OF AMERICA

The Search for Missing Resonances in $\gamma p \to K^+ \Lambda$ Using Circularly Polarized Photons on a Longitudinally Polarized Frozen Spin Target

A DISSERTATION

Submitted to the Faculty of the

Department of Physics

School of Arts and Sciences

Of The Catholic University of America

In Partial Fulfillment of the Requirements

For the Degree

Doctor of Philosophy

By

Liam Robert Casey

Washington, D.C.

2011

The Search for Missing Resonances in γp->K$^+\Lambda$ Using Circularly Polarized Photons on a Longitudinally Polarized Frozen Spin Target

Liam R. Casey, Ph.D.

Director: Franz Klein, Ph.D.

This works presents the first measurements of three double-polarization observables for the γp->K$^+\Lambda$ reaction on polarized target: E (beam-target asymmetry), $L_{x'}$ and $L_{z'}$ (target-recoil asymmetries). Each of these measurements required the longitudinal polarization of target protons. To that end, a longitudinally polarized frozen-spin butanol target was constructed for use in the Thomas Jefferson National Accelerator Facility's Hall B. The data presented in this analysis were taken during the g9a run period from November 2007 – February 2008 using the aforementioned target and a circularly polarized photon beam in the energy range of 0.5 – 2.4 GeV .

The motivation for this experiment was to extend the set of measured observables describing the reaction channel in order to aid in the search for missing baryon resonances. The complete set of polarization observables can be used to perform a model-independent partial wave analysis (PWA) of the reaction channel and extract resonant contributions to the cross section.

Consistency checks with previously measured polarization observables were also performed by extracting the Λ recoil polarization and the beam-recoil asymmetries $C_{x'}$ and $C_{z'}$. The recoil polarization P extracted from g9a data is in good agreement with previous data. On the other hand, some major discrepancies are found between the g9a results and previous data for the beam-recoil transfer $C_{x'}$ and $C_{z'}$.

The statistics generated for $K^+\Lambda$ were insufficient to adequately resolve between models, although better agreement with the Mart-Bennhold model, which includes a missing $D_{13}(1960)$ resonance, was evident in much of the data. Nonetheless, little evidence of resonant structure appears in the smoothly varying measurements of E; and the target-recoil transfer $L_{x'}$ and $L_{z'}$. are frequently consistent with a flat asymmetry or none at all. Identification of missing resonances from individual observable measurements is unlikely. Instead, these new measurements will serve to further constrain parameters for the full PWA of $\gamma p \rightarrow K^+\Lambda$.

This dissertation by Liam Casey fulfills the dissertation requirement for the doctoral degree in Physics approved by Franz Klein, Ph.D., as Director, and by Daniel Sober, Ph.D., and by Hall Crannell, Ph.D., as Readers.

_____
Franz Klein, Ph.D., Director

_____
Daniel Sober, Ph.D., Reader

_____
Hall Crannell, Ph.D., Reader

Contents

List of Figures

List of Tables

Acknowledgements

I first want to express my gratitude to my adviser, Professor Franz Klein, who helped me every step along the way from my first feeble attempts at data analysis to the final touches on my dissertation. Throughout this ordeal he was always ready to answer any questions I had whether they be rooted in basic physics or some technical issue.

I am also indebted to my two readers from the Nuclear Physics group, Professor Daniel Sober and Professor Hall Crannell. Dr. Sober recruited me into the group when I was still uncertain of my research path and offered many helpful comments on this dissertation. Dr. Crannell is an assiduous reader who not once, but twice went over my dissertation with me page by page to help me make the appropriate corrections.

The guidance and instruction of faculty were integral to the completion of this dissertation, but equally important to the success of a doctoral candidate is the support of the university community. I am grateful for the moral support that my fellow physics graduate students offered me during my time in the doctoral program. I especially wish to thank Natalie Walford, my comrade in the Nuclear group and a true, loyal friend. Without her constant encouragement, I would never have completed this work.

Aside from faculty and students there are other members of the community I would be remiss in neglecting to mention. My thanks, of course, to Gail Hershey, the assistant to the department chair, who was always available to talk during breaks in my writing and she would never forget to remind me that I needed to keep "writing and writing" when deadlines drew nigh. Dr. Jude, a former CUA student and guardian of the Hannan lights, is probably the only person who understands the title I just gave him, so good show. Lu, if you see this, I haven't forgotten surviving the "dark days of Newport News."

I would also like to recognize the FROST analysis group collectively. Analysis of the g9a dataset is a collaborative effort with input from many CLAS members coming from several universities. Many of the contributions of other members were critical to performing my analysis, while others influenced my approach. I would particularly like to express my appreciation for Eugene Pasyuk who runs our weekly meetings and always seems to be in good spirits.

Finally, I could not possibly end without thanking my family for their tireless support. My parents have always been there to lend an ear during any difficulties I had and always showed their support. My siblings Kevin, Molly, and Sara have also frequently helped lift my spirits when I had difficulty finding an end in sight and always cheered me on. To all the people who have helped me in any way, those I have mentioned and all those I have failed to explicitly mention, I offer you my heartfelt gratitude.

Chapter 1

Introduction

Ever since electron scattering experiments at SLAC in the late 1960's showed a significant number of large angle deflections confirming point like charge distributions within the proton, the scientific community has known that nucleons (protons and neutrons) are not fundamental particles.[1] Rather, they are comprised of quarks, the building block of all strongly interacting subatomic particles (hadrons). Quantum Chromodynamics (QCD) is the theory of the strong force, which governs quark interactions. QCD is a nonlinear theory which does not admit analytical solutions, but perturbative calculations are feasible in the high energy regime where quarks become "asymptotically free".

Unfortunately, the energies found inside nucleons and common hadrons fall outside this perturbative domain. Therefore, approximate models must be used to describe the nucleon spectrum. These models typically predict many more excited states of nucleons than have been experimentally detected. The undetected states are referred to as the missing baryon resonances and the search for them serves as the primary motivation for this work.

Resonances can be difficult to distinguish solely from cross section data, because the resonances are short-lived (10^{-23} s) and thus have large overlapping widths. Knowledge of the spin orientation of the incoming beam, target nucleons, and recoiling baryons can provide the necessary additional information to determine which resonances couple strongly

to a given reaction channel. Polarization of the target and photon beam allow us to explore these additional layers to the physical description of a reaction channel. Recoil polarization is not induced, but may be indirectly measured. The FROST (FROzen Spin Target) experiment uses a frozen spin butanol target together with linearly and circularly polarized photon beams to obtain the full gamut of spin polarization observables.

The specific focus of this analysis is the reaction channel $\gamma p \to K^+ \Lambda$. This channel is of particular interest as an example of strangeness production (the Λ carrying a strange quark and the K^+ an antistrange quark, conserving total strangeness). While the bulk of baryon resonance data has come from analysis of πN decay channels in pion production experiments, recent quark model calculations predict some resonances will couple strongly to photoproduction channels with decay particles carrying nonzero strangeness.[2] Further, this particular channel is of some interest, because $K^+ \Lambda$ can only couple to resonances with isospin $\frac{1}{2}$. Thus, fewer resonances are expected to be involved in the analysis of this channel, making their identification simpler. Nonetheless, cross section and recoil polarization data taken for this channel to date have shown the need for a more complete set of observables to resolve ambiguities regarding the presence of resonances. This thesis presents the set of polarization observables coming from the analysis of data on circularly polarized photons incident on a longitudinally polarized frozen spin butanol target taken during the g9a running period at Jefferson Lab (JLab).

In the remainder of this chapter, I will provide an overview of the underlying physics driving this thesis work. I will begin with QCD and quark models, move on to hadron spectroscopy, the "missing resonance" problem, polarization observables, and finally discuss the salient features of the $K^+ \Lambda$ photoproduction channel.

1.1   Quarks and QCD

In the theory defined by QCD, quarks are the pointlike, fundamental particles that, together with gluons, make up composite subatomic particles (hadrons) from the standard nuclear particles (protons and neutrons) to an array of less familiar, shorter lived particle states. Quarks are believed to exist in six flavors: up, down, strange, charm, bottom, and top. Barring some theoretical exotic forms, quarks combine in two basic ways to make two categories of hadrons: baryons and mesons. Baryons are formed from three valence quarks, while mesons consist of a quark and an antiquark.[3]

Quantum Chromodynamics is the theory of the strong nuclear force responsible for the interaction of quarks and gluons, the gluons being the mediator bosons of the strong force. The gluon plays an analogous role in QCD to that of the photon in Quantum Electrodynamics (QED), which acts as the mediator boson for the electromagnetic force. The interesting features of QCD arise, however, from what distinguishes the gluon from the photon. While photons carry no electromagnetic charge, gluons do carry color charge, the charge of QCD. Gluonic interactions, which arise in QCD as a result of this color charge, lead to nonlinear equations that cannot be solved analytically. Thus, all solutions in QCD are necessarily approximate ones.

The nature of the strong force provides the most basic method employed for calculation in high energy physics, perturbative QCD. The strong interaction grows weaker with increasing energy and quarks in the nucleon begin to behave as essentially free noninteracting particles at sufficiently high energy. This phenomenon is known as asymptotic freedom, because quarks become free at distance scales asymptotically approaching zero, which correspond with high energy scales. The impact of this asymptotic freedom for QCD calculations is that the QCD coupling constant, α_s, becomes sufficiently small at high energies to apply the same perturbative techniques used in QED.

At intermediate energies on the order of a few GeV, this approximation is no longer

valid, because the value of the coupling constant approaches unity. The result is that complicated higher order reactions make significant contributions to the overall sum and cannot be treated as vanishing terms. This describes the nonperturbative regime of QCD, which applies to both the interaction of quarks inside a nucleon and the excited baryon spectrum.

1.2 Baryon Spectroscopy

The baryon spectrum contains a multitude of excited states, or resonances, with closely-spaced and overlapping energies and are identified by their quantum numbers in addition to their mass. The notation for identifying states is given in the form $L_{2I2J}(M)$, where L is the orbital angular momentum for the resonance's πN decay (reported in the standard *s, p, d, f* notation), I is the isospin of the state, J is its spin, and M is its mass. The quantum numbers for these states are shared by different bands of energy levels with increasing masses for progressive bands. Baryon spectroscopy involves the observation and identification of these states in order to map out the entire spectrum.

Baryon spectroscopy shares more than a name with the original process, atomic spectroscopy. The fields are not merely analogous; the procedures are also roughly the same and they share the bond of describing the interaction of radiation and matter. While atomic spectroscopy is only concerned with electromagnetic interactions, baryon spectroscopy is complicated by the involvement of the strong force and, in some cases, the weak interaction. A discussion of the basics of atomic spectroscopy will be worthwhile to shed light on the particular issues that differentiate and complicate baryon spectroscopy.[4]

Atomic spectroscopy is the process of detecting and mapping out the spectra of photons emitted from atoms. The first step is to bring the electrons in atoms to excited states. The electrons will naturally return to their stable configuration and emit photons in the process. Using a diffraction grating in conjunction with some form of photon detector, one

can observe the emitted radiation mapped out by wavelength or, effectively, by the energy difference between the excited states and stable atomic states. Atomic spectral lines are quite narrow, but they are not infinitely sharp. Their natural width is proportional to their lifetime by the uncertainty relation

$$\Delta E = \Gamma \approx \frac{\hbar}{\tau} \, , \tag{1.1}$$

where τ is the mean lifetime of the excited state and ΔE is the width of the spectral line. This is not a significant complication though as the lifetime of excited atomic states is typically on the order of 10^{-8} s, giving an energy uncertainty of $\Delta E \approx 10^{-7}$ eV.[5] Compared to the separation between lines, this width is usually negligible.

Baryon spectroscopy is carried out in a similar fashion. Nucleons are excited by means of a beam of particles that has been accelerated to achieve the requisite excitation energy. The resonant states will then decay into quasi-stable baryons and mesons, which can all, in principle, be detected. These decay products will carry the energy of the resonant state just as the photons detected in atomic spectroscopy carry the energy of the atomic transitions. Clearly these procedures are more difficult to achieve in baryon spectroscopy, but they are simple extensions of the atomic spectroscopy method. The real complication in baryon spectroscopy arises from the width of the nucleon resonances. These excited states have lifetimes on the order of 10^{-23} s, resulting in energy widths on the order of ≈ 100 MeV. Thus, many of the resonances have large regions of overlap. Figure 1.1 shows the cross sections for πp along with all the resonances with the highest PDG (Particle Data Group) rating. Obviously, identification of the states by energy alone is impossible. Fortunately, the quantum numbers of the state determine the angular distribution of its decay products. The method used to extract resonances by quantum numbers is called partial wave analysis (PWA), but to perform a full PWA on a reaction channel, more than simple cross section data are required.
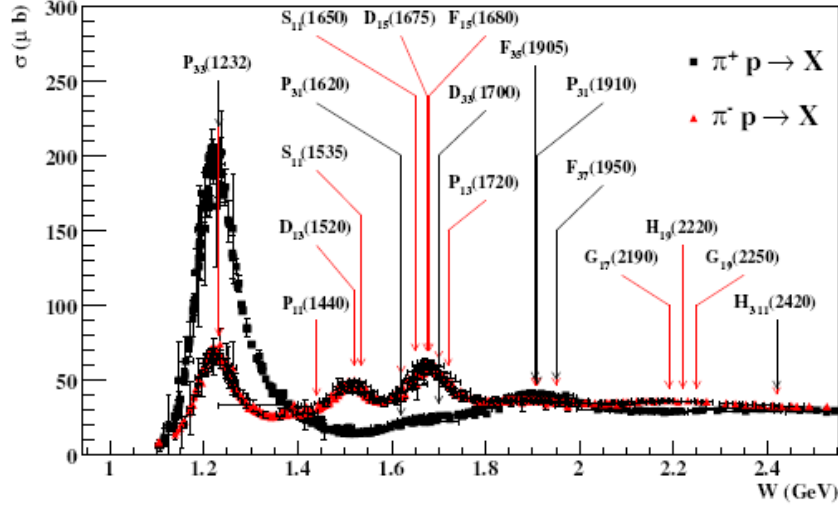
Figure 1.1: Total cross section (σ) for πp scattering experiments plotted in center of mass energy (W). All resonances with a four star PDG rating are marked at their respective masses. Many structures in the cross section are clearly shared by multiple resonances. Image Source: [21]

1.3 The Missing Resonance Problem

As discussed in Section 1.1 perturbative QCD calculations cannot be made for the baryon spectrum. Instead, some other method of approximation must be used to enumerate and predict the properties of all baryon resonances in the nonperturbative domain. A typical approach is the Constituent Quark Model (CQM), which treats baryons as a composition of the three valence quarks.[6, 7] Resonances are then described as arising from radial excitations or the angular momentum of these quarks. The inclusion of up, down, and strange quarks for SU(3) symmetry together with quark spin and orbital angular momentum leads to a veritable zoo of theoretical nucleon resonances calculated from the SU(6)×O(3) symmetry of the Constituent Quark Model. Table 1.1 provides the spectrum of N^* states calculated by Capstick and Roberts [2] along with the Particle Data Group (PDG) [8] rating for each observed state. A four star rating is given to states for which existence has been established and properties have been well explored, while the existence of resonances with

Model state	Nπ state	$A_{\frac{1}{2}}$	$A_{\frac{3}{2}}$	$A_{K\Lambda}$	$A_{K\Sigma}$
$N^-_{\frac{1}{2}}(1945)[S_{11}]_3$	$N(2090)^*$	12		2.3±2.7	$2.1^{+1.3}_{-1.4}$
$N^-_{\frac{3}{2}}(1960)[D_{13}]_3$	$N(2080)^{**}(?)$	36	-43	$-5.6^{+1.7}_{-1.3}$	-0.7±0.3
$N^-_{\frac{3}{2}}(2055)[D_{13}]_4$	$N(2080)^{**}(?)$	16	0	$-2.7^{+0.9}_{-0.8}$	$1.8^{+0.7}_{-0.8}$
$N^-_{\frac{5}{2}}(2080)[D_{15}]_2$		-3	-14	$-2.9^{+0.8}_{-0.4}$	$-2.4^{+0.9}_{-0.5}$
$N^-_{\frac{7}{2}}(2090)[G_{17}]_1$	$N(2190)^{****}$	-34	-28	$-1.3^{+0.4}_{-0.6}$	-0.2±0.1
$N^-_{\frac{5}{2}}(2095)[D_{15}]_3$	$N(2200)^{**}$	-2	-6	$-1.7^{+0.5}_{-0.4}$	$2.5^{+0.6}_{-0.9}$
$N^+_{\frac{9}{2}}(2345)[H_{19}]_1$	$N(2250)^{****}$	-29	13	-0.4±-0.1	1.1±0.3
$\Delta^-_{\frac{1}{2}}(2035)[S_{31}]_2$	$\Delta(1900)^{***}$	20			-1.9±0.3
$\Delta^-_{\frac{3}{2}}(2080)[D_{33}]_2$	$\Delta(1940)^*$	-20	-6		1.1±0.7
$\Delta^-_{\frac{1}{2}}(2140)[S_{31}]_3$	$\Delta(2150)^*$	4			-4.1±2.4
$\Delta^-_{\frac{5}{2}}(2155)[D_{35}]_1$	$\Delta(1930)^{***}$	11	19		2.1±0.4
$\Delta^-_{\frac{7}{2}}(2230)[G_{37}]_1$	$\Delta(2200)^*$	14	-4		$0.4^{+0.3}_{-0.2}$
$\Delta^-_{\frac{5}{2}}(2265)[D_{35}]_3$	$\Delta(2350)^*$				2.5±0.1
$\Delta^-_{\frac{9}{2}}(2295)[H_{39}]_1$	$\Delta(2400)^{**}$	-14	-17		$1.4^{+1.0}_{-0.8}$
$\Delta^+_{\frac{7}{2}}(2370)[F_{37}]_2$	$\Delta(2390)^*$	-33	-42		$1.9^{+0.4}_{-0.5}$
$\Delta^+_{\frac{9}{2}}(2420)[H_{3,9}]_1$	$\Delta(2300)^{**}$				0.2±0.1
$\Delta^+_{\frac{11}{2}}(2450)[H_{3,11}]_1$	$\Delta(2420)^{****}$	-13	-16		0.5±0.3
$\Delta^+_{\frac{7}{2}}(2460)[F_{37}]_3$	$\Delta(2390)^*$	24	30		0.5±0.1

Table 1.1: Model states. The amplitudes for γp helicity ($\frac{1}{2}$ and $\frac{3}{2}$) coupling, $K\Lambda$ coupling,and $K\Sigma$ coupling are given in $10^{-3}GeV^{-\frac{1}{2}}$ Source: [2]

a one star rating is supported by weak experimental evidence. Plainly, there are many predicted states that have not been observed. Indeed, there are many more than the number of verified resonances. This embarrassment for models using the constituent quark approach is referred to as the Missing Resonance Problem.

There are, broadly, two logical solutions to the Missing Resonance Problem, each with its own salient explanation. Either (1) not all the predicted resonances actually exist, or (2) all the predicted resonances do exist, but some of them have eluded detection. The first solution indicates a fundamental flaw in the CQM approach that causes an overabun-

dance of predicted baryon states, while the second solution indicates an inadequacy in the experimental search to date.

A reasonable explanation for the failure of CQM to accurately predict resonant states is that it models the interaction of the valence quarks incorrectly. Diquark models restrict the motion of two quarks by assuming that they form a tightly bound system.[9] If the two bound quarks have antisymmetric colors and spins, an attractive force will be generated between them, resulting in the diquark configuration.[10] Since the CQM allows all three valence quarks to move independently, the diquark model, by treating the diquark as essentially one body, greatly reduces the degrees of freedom for the system. The result is that fewer resonant states are predicted. It should be noted that even though there are fewer missing resonances in the diquark model, there remain predicted resonances that have not been observed.

On the other hand, if the predicted resonances all exist, then it is likely that the missing resonances do not couple or couple only weakly to those reaction channels which have seen the greater part of research concentration. Specifically, pion production channels with πN final states represented the bulk of N^* data until quite recently. A full investigation of photoproduction channels is necessary to fairly test the CQM. In particular, some missing resonances are predicted to couple strongly to hyperon final state channels of photoproduction reactions in the quark model calculations of Capstick and Roberts. Their model predicts that a number of negative-parity resonant states from the $N = 3$ band will appear clearly in the $K^+\Lambda$ channel, the channel of interest for this analysis. Figure 1.2 shows their predictions for the coupling of nucleon resonances up to 2200 MeV to $K^+\Lambda$. Those resonances with strong predicted amplitudes for both γN and $K^+\Lambda$ should make a significant contribution to the reaction channel. The $D_{13}(1960)$ resonance is of special interest as there exists some experimental evidence for its presence in this channel, but not yet sufficient proof. Capstick and Roberts predict that a full PWA of the $K^+\Lambda$ channel will reveal

N to Nγ, Nπ, and ΛK model amplitudes
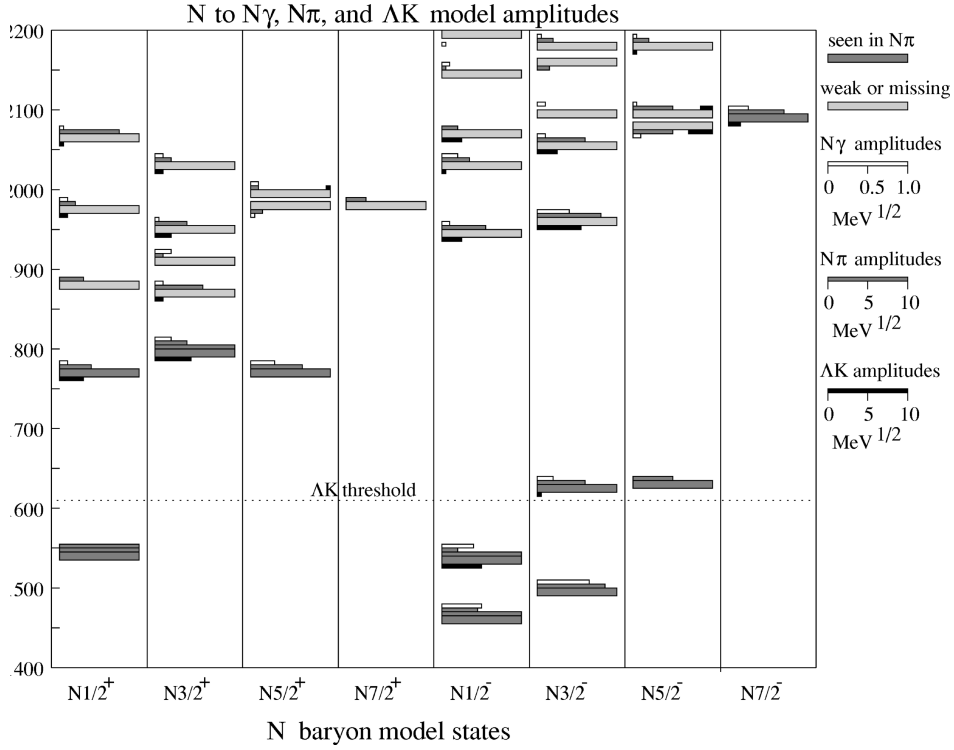
Figure 1.2: Predicted Nγ, Nπ, and ΛK amplitudes for resonances up to 2200 MeV. Image Source: [2]

this resonance plainly in its partial wave.[2]

These explanations each orient toward a different solution to the Missing Resonance Problem, but they are not entirely mutually exclusive. If the diquark model is correct, then there are certainly missing states predicted in CQM that do not exist, but there may also be missing states that couple to insufficiently explored reaction channels. In either case, the complete analysis of photoproduction channels should help sort out this issue.

1.4 Polarization Observables

In order to perform a full model independent analysis of the $\gamma p \to K^+ \Lambda$ reaction channel, it is necessary to calculate the complex amplitudes that describe the reaction channel. These

amplitudes come from the differential cross section, which is given by the expression

$$\frac{d\sigma}{d\Omega_{cm}} = \frac{(E_p + M_p)(E_\Lambda + M_\Lambda)}{128\pi^2 s}\frac{|q|}{|k|}Tr(\mathscr{F}\mathscr{F}^\dagger) , \tag{1.2}$$

where k is the momentum of the incoming photon q is the momentum of the kaon in the center of mass frame, s is the Mandelstam variable $s = (p_p + p_\gamma)^2$(or, equivalently, the square of the center of mass energy W), E_p, M_p, E_Λ, and M_Λ are the energy and mass of the proton and Λ hyperon, respectively, and $\mathscr{F}$ is given by

$$\mathscr{F} = \sigma \cdot f_1 + if_2\frac{(\sigma \cdot q)(\sigma \cdot k \times \varepsilon)}{|q||k|} + f_3\frac{(\sigma \cdot k)(q \cdot \varepsilon)}{|q||k|} + f_4\frac{(\sigma \cdot q)(q \cdot \varepsilon)}{q^2} , \tag{1.3}$$

where ε is the polarization vector of the photon and the f_i are the four complex CGLN (Chew, Goldberger, Low, and Nambu) amplitudes.[11]

These amplitudes may be expressed in the CGLN form or another basis depending on which is best suited to the application. While the CGLN amplitudes are the appropriate form for use in multipole analysis, the transversity amplitudes make a better choice when dealing with polarization observables. In terms of the CGLN amplitudes these are

$$b_1 = -\frac{i}{\sqrt{2}}(f_1 - f_2 e^{-i\theta})e^{i\theta/2} , \tag{1.4}$$

$$b_2 = \frac{i}{\sqrt{2}}(f_1 - f_2 e^{i\theta})e^{-i\theta/2} , \tag{1.5}$$

$$b_3 = -b_1 - \frac{sin\theta}{\sqrt{2}}(f_3 + f_4 e^{-i\theta})e^{i\theta/2} , \tag{1.6}$$

$$b_4 = -b_2 - \frac{sin\theta}{\sqrt{2}}(f_3 + f_4 e^{i\theta})e^{-i\theta/2} , \tag{1.7}$$

where θ is the angle between the incoming photon and the outgoing kaon in the center of

Photon	Target				Recoil			Target + Recoil			
	$-$	$-$	$-$	$-$	x'	y'	z'	x'	x'	z'	z'
	$-$	x	y	z	$-$	$-$	$-$	x	z	x	z
unpolarized	σ_0	0	T	0	0	P	0	$T_{x'}$	$-L_{x'}$	$T_{z'}$	$L_{z'}$
linearly polar.	$-\Sigma$	H	$(-P)$	$-G$	$O_{x'}$	$(-T)$	$O_{z'}$	$(-L_{z'})$	$(T_{x'})$	$(-L_{x'})$	$(-T_{x'})$
circularly polar.	0	F	0	$-E$	$-C_{x'}$	0	$-C_{z'}$	0	0	0	0

Table 1.2: Polarization Observables for pseudoscalar meson photoproduction. Source: [12]

mass frame.

Complex numbers clearly cannot represent physical observables though. In order to calculate these amplitudes, we must find real physical quantities in terms of which we can express them. By means of bilinear products, we can extract 16 real numbers from four complex amplitudes. In the appropriate combinations, these give us the 16 polarization observables that fully describe a hyperon photoproduction channel. Indeed, it is not even necessary to have all 16 observables to fully describe the channel as they are not all linearly independent. A full description of the reaction channel could be obtained with the unpolarized cross section, three single polarization observables, and four double polarization observables (with some restrictions on which observables are taken). Nevertheless, uncertainties in the extracted observables make a measurement of the full set desirable for the purposes of performing consistency checks and applying constraints to more precisely determine the reaction amplitudes. A more thorough discussion of the amplitudes and the observables can be found in the work of Adelseck and Saghai as well as those of Chiang, Tabakin, Fasano and their collaborators.[13, 14, 15, 16]

The polarization observables are tied to the polarization states of the incident photons, the target protons, and the recoiling hyperons. Table 1.2 shows how to obtain the 16 observables in terms of these polarization states. Each polarization observable has the base form of an asymmetry in the reaction channel's yield for two polarization states (or groupings of states in the case of double polarization observables).[11] These asymmetries take

the following form:

$$A = \frac{N_+ - N_-}{N_+ + N_-} \, , \tag{1.8}$$

where N_+ is the reaction yield for one polarization direction and N_- the yield for the opposite direction. In the case of double polarization observables, we are interested in the polarization state of two of the reaction particles. In this case, polarizations are grouped together for the asymmetry in this fashion:

$$A = \frac{(N_{++} + N_{--}) - (N_{+-} + N_{-+})}{N_{++} + N_{--} + N_{+-} + N_{-+}} \, , \tag{1.9}$$

where N_{++} represents the yield for a pairing of states taken to be the positive polarization direction for its respective particle and the minus sign indices represent the opposite direction. For pseudoscalar meson production, a change in the convention for what is taken to be the positive direction of one particle will only change the sign of the asymmetry, while a change for both will leave the asymmetry unchanged. It is useful for these asymmetries to group together like and opposite signs under one heading, so that $N_+ = N_{++} + N_{--}$ and $N_- = N_{+-} + N_{-+}$.

Each polarization observable carries with it a series of multiplicative factors that adjust this base asymmetry. In reality, the asymmetry in the yields is what we are interested in, but none of the aggregate bodies involved are 100 % polarized. Thus, there are correction factors for the degrees of polarization in the photon beam and target, and the degree to which the decay products can give us information about the hyperon polarization. In the limit where each event represents a photon of known polarization in the desired direction incident on a proton with known spin along the desired axis, producing a hyperon of likewise known spin, the polarization observables will equal the measured asymmetry. I will now briefly describe each polarization observable that I will be extracting for this analysis.

1.4.1 Polarization Observable E

This analysis presents the first measurement of E for the $\gamma p \rightarrow K^+\Lambda$ reaction. E is the observable measured for circularly polarized photons incident on a longitudinally polarized target. It has the following form

$$E = -\frac{D}{P_c P_t} \frac{N_+ - N_-}{N_+ + N_-} \,,$$ (1.10)

where D is the dilution factor, which accounts for events coming from unpolarized bound nucleons, P_t is the target polarization, and P_c is the circular polarization of the photon beam. The circular polarization can in turn be found from the electron beam's longitudinal polarization P_{el} by the following relation

$$P_c = P_{el} \frac{4x - x^2}{4 - 4x + 3x^2} \,,$$ (1.11)

where x is the ratio of the photon energy to the original electron energy.[17] The N_+ and N_- in equation (1.10) refer to parallel and anti-parallel configurations of the photon helicity and the target polarization, following my convention for double polarization observables.

1.4.2 Polarization Transfer Observables $L_{x'}$ and $L_{z'}$

The observables $L_{x'}$ and $L_{z'}$ concern the longitudinal polarization of the target and the polarization of the recoil hyperon along the direction of the x' and z' axes respectively. These axes are primed, because they are not the axes of the lab frame, but rather those of the hyperon's rest frame, where the positive z' axis is in the direction of hyperon motion (or traditionally in the opposite center of mass frame direction matching that of the pseudoscalar meson). The rest frame axes are rotated in the production plane, so that $y' = y$ and x' is the axis lying in the production plane which is perpendicular to the z' axis. Figure 1.3 shows the $\gamma p \rightarrow K^+\Lambda$ in the production plane with primed and unprimed coordinate systems dis-

played.

The hyperon polarization is determined by the distribution of its decay products. The parity-violating weak decay of the Λ into a proton and negatively charged pion is preferentially oriented in the direction of its polarization. The strength of this preference is given by the self-analyzing factor for the decay, α_Λ. Yet, it would be rare indeed to observe a decay particle moving directly along one of these axes. The orientation of the detected decay particle in the Λ rest frame introduces a secondary correction factor for the degree of polarization in the form of a projection onto the axis of interest.

These observables are given by the formula:

$$A(cos\vartheta_{pY}^{x',z'}) = C_{x',z'}\alpha_\Lambda DP_c \, cos\vartheta_{pY}^{x',z'} \, , \tag{1.12}$$

Here the asymmetry is taken as a function of the decay distribution. This naturally introduces a negative sign into the asymmetry for decay particles on the negative side of the primed axis. Thus, if we integrate over $cos(\vartheta_{pY})$ in the forward half of the polar range, we can take a standard double polarization asymmetry with N_+ being the number of events with same sign polarizations, where we take decay products in the positive primed axes to indicate positive hyperon polarization, and N_- being the number with opposite sign polarizations. Without integration the asymmetry is calculated like a single asymmetry for the target polarization with a multiplicative factor of $cos(\vartheta_{pY})$ adjusting the sign of the asymmetry in the same manner.

1.4.3 Recoil Polarization P and Polarization Transfer $C_{x'}$ and $C_{z'}$

These three observables have been presented in previous CLAS analyses, so I will not go into much detail concerning them, but I will be presenting my own results for the purposes of consistency checks. The hyperon recoil polarization P is given by an asymmetry in decay

products above and below the production plane. The polarization transfer observables $C_{x'}$ and $C_{z'}$ are calculated in a similar fashion to $L_{x'}$ and $L_{z'}$, simply using the helicity of the beam instead of the target polarization. I will go into somewhat more exact details when I present my calculations for these quantities.

1.5 The K$^+$ meson and the Λ hyperon

The concept of strangeness was introduced with the discovery of the Λ baryon in 1947 in the course of a cosmic ray experiment.[18] The particle exhibited the "strange" behavior of decaying quite slowly. While baryons typically have lifetimes on the order of 10^{-23} s, because they decay by the strong interaction, this particle was observed to last for approximately 10^{-10} s. The explanation proposed was that the Λ carried some additive quantum number, dubbed "strangeness", which is conserved under strong and electromagnetic interactions, forcing the Λ (along with any other strange particles) to undergo a much slower weak decay. Thus was born the category of the hyperons, the class of baryons with nonzero strangeness.

The Λ decays weakly into a proton and a π^- with a branching ratio of 63.9% and has a 35.8% branching ratio into $n\pi^0$. Detection of neutral particles is more difficult, making the secondary decay path a poor choice for analysis of this reaction channel. Therefore, the full reaction channel analyzed in this work is $\gamma p \rightarrow K^+\Lambda \rightarrow K^+p\pi^-$. The reaction with coordinate axes given by the center of mass production plane and rest frame are depicted in Figure 1.3. For my analysis of this reaction, I use the natural units convention $c = \hbar = 1$, so all factors of c will be dropped from mass and momentum units.

The strangeness quantum number was later tied to a third flavor of quark, the strange quark. The strange quark is assigned a strangeness value of $S = -1$, while its counterpart, the anti-strange quark, has a value of $S = 1$. Thus, the Λ hyperon with its valence quark
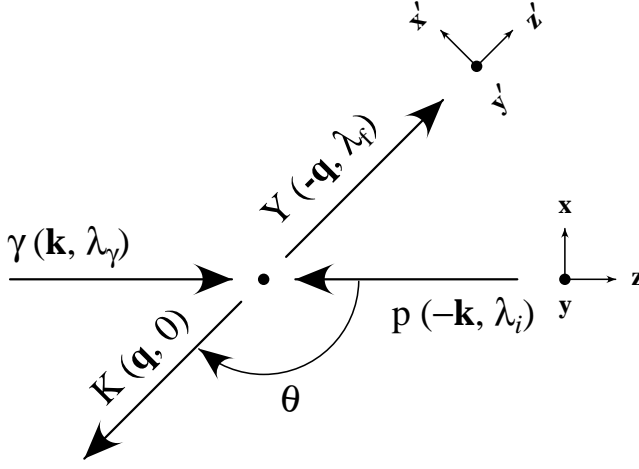
Figure 1.3: Production plane view of the $\gamma p \rightarrow K^+ \Lambda$ reaction. Production plane and primed Λ rest frame coordinate systems are shown.

composition of an up, a down, and a strange quark has $S = -1$, while the K^+ with an up quark and an anti-strange quark has $S = 1$. Therefore, the reaction $\gamma p \rightarrow K^+ \Lambda$ does not violate strangeness conservation (in contrast to the later decays of K^+ and Λ), because the total is $S = 0$ at each vertex. This process is known as associated strangeness production.

The $\gamma p \rightarrow K^+ \Lambda$ reaction can occur in several different ways as shown in the "tree level" (first order) Feynman diagrams of Figure 1.4. Each process makes a contribution to the channel, but not all processes are of interest in the search for baryon resonances. The s, t, and u channel processes are characterized by the Mandelstam variables $s = (p_p + p_\gamma)^2$, $t = (p_\gamma - p_K)^2$, and $u = (p_p - p_K)^2$ respectively, as they correspond to the momentum carried by the propagators for those processes. The first three processes shown are the non-resonant Born terms, which include s-channel proton exchange, t-channel K^+ exchange, and u-channel Λ exchange. Only in the s-channel can nucleon resonances be found, so the strength of the resonant s-channel contribution is a determining factor in finding the coupling of any particular resonance to the $\gamma p \rightarrow K^+ \Lambda$ channel. .

The K^+ is a pseudoscalar meson, so called because it changes sign under parity operation, but otherwise behaves like a scalar. In other words, it has spin 0 and odd parity. It also
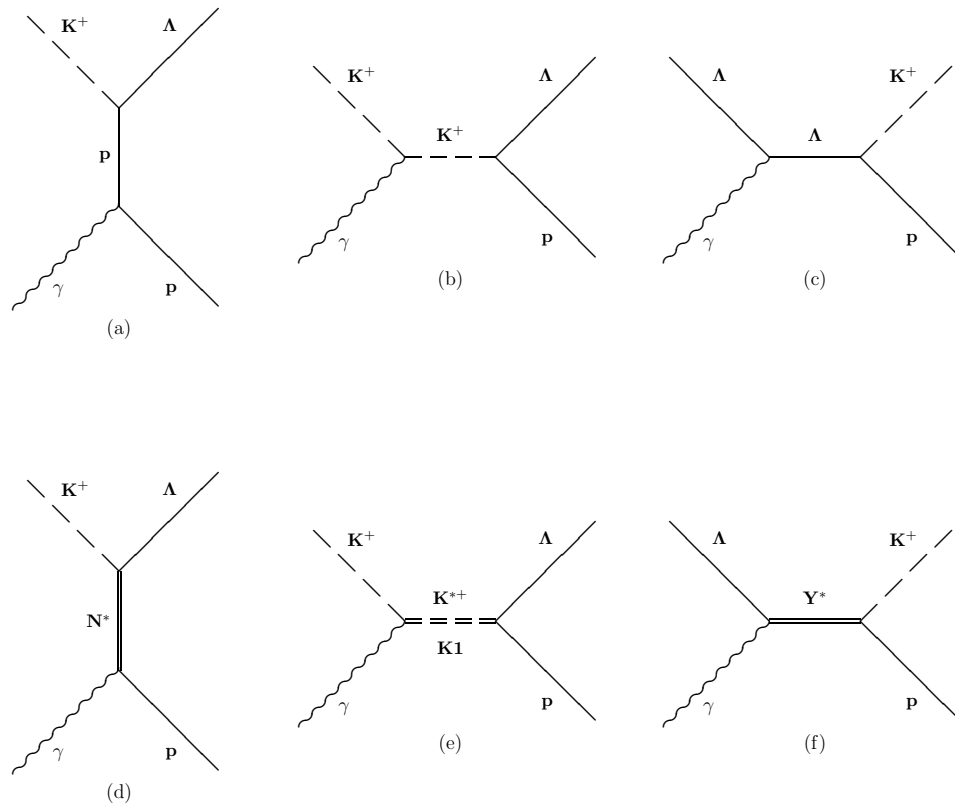
Figure 1.4: Tree level Feynman diagrams for $\gamma p \rightarrow K^+ \Lambda$. (a) - (c) are the s,t, and u channel Born terms (d)-(f)are the resonant s,t, and u channel contributions. Image Source: [11]

Particle	Mass	I	J^P	Charge	decay mode	lifetime
K^+	0.493677 GeV	$\frac{1}{2}$	0^-	$+1$	$\mu^+\nu_\mu$ (63.6%)	1.238×10^{-8} s
Λ	1.115683 GeV	0	$\frac{1}{2}^+$	0	$p\pi^-$ (63.9%)	2.631×10^{-10} s
					$n\pi^0$ (35.8%)	
Σ^0	1.192642 GeV	1	$\frac{1}{2}^+$	0	$\Lambda\gamma$ (100%)	7.4×10^{-20} s

Table 1.3: Relevant physical properties of K^+, Λ and Σ^0. I is isospin, J is spin, and P is parity. Only decay modes with significant branching ratios are listed and only the primary mode for K^+ as the particle is directly detected in g9a data. Σ^0 has multiple decay branches, but the primary path's branching ratio is high enough to be reported as 100% in PDG tables.[8]

has an isospin of $\frac{1}{2}$, arising from its up quark content. The Λ hyperon has even parity and spin $\frac{1}{2}$. Its isospin projection is zero on account of the equal number of u and d quarks in its valence composition, while its total isospin is zero because it is the isospin singlet state to the Σ hyperon isospin triplet. The Σ^0 hyperon is the isospin projection zero member of this triplet. This particle is close in mass to the Λ and decays into $\gamma\Lambda$. While I will not be analyzing this channel here, the similarity in final states and near masses of these two hyperons dictates that the $K^+\Sigma^0$ production will be a process to contend with in any analysis of $K^+\Lambda$. Therefore, I have included Σ^0 in Table 1.3, which sums up the important features of the strange particles in my analysis.

Together K^+ and Λ may only couple to resonant states with isospin $\frac{1}{2}$ and negative parity. As this limits the number of potential baryon resonances that can appear in this channel, the separation of resonant states should be easier to perform in the full analysis including all 16 polarization observables. Previous and future results will need to be compiled together with the results of this dissertation to complete the analysis of the $K^+\Lambda$ photoproduction channel. In the next section I will provide an overview of some of the previous work in this area and end by taking a look ahead.

1.6 Other Analyses of the $K^+\Lambda$ channel

Modern exploration of $K^+\Lambda$ photoproduction begins with the SAPHIR (Spectrometer Arrangement for Photon Induced Reactions) experiment performed at the Bonn Electron-Stretcher ELSA until 1998. Earlier studies of this reaction date back to the 1960s, but they are poor quality data sets compared to those following SAPHIR's introduction of large-acceptance spectrometers into the analysis. The CLAS collaboration has followed suit with several analyses of this channel using the CEBAF Large Acceptance Spectrometer (CLAS). Results include measurements for differential cross section, recoil polarization P, target polarization T, and polarization transfer $C_{x'}$, $C_{z'}$, $O_{x'}$, and $O_{z'}$. These measurements and their analyses can be found spread among the PhD theses of John McNabb, Robert Bradford, Michael McCracken, and Craig Paterson.[10, 19, 20, 21] In this section I will take a broad look at investigation of $K^+\Lambda$ photoproduction prior to SAPHIR, then I will provide a brief description of the results of the SAPHIR and CLAS analyses, and I will conclude with a look into what CLAS will bring to the effort to completely describe this interaction in the near future.

1.6.1 B.S.: Before SAPHIR

$K^+\Lambda$ photoproduction experiments performed before SAPHIR largely used smaller acceptance magnetic spectrometers that would detect only the kaon and reconstruct hyperons from missing mass. In order to find the missing mass, the photon energy was required, but photon taggers were not yet available, so less powerful techniques such as the bremsstrahlung endpoint method were employed. An alternative method, undertaken by the Aachen-Berlin-Bonn-Hamburg-Heidelberg-München (ABBHHM) collaboration, was to detect the K^+ and all charged particles of hyperon decay using a hydrogen bubble chamber.[22] This method had the advantage that the photon energy was no longer re-

quired. These experiments were performed at several facilities for a total of 144 data points on differential cross section in $cos\vartheta_{cm}^K$ and center of mass energy E_{cm}. These data points are grouped together with later, more complete measurements of the differential cross section in Figures 1.5 - 1.7. The overall coverage of these data points is poor and their error bars are large, making the data taken during this period of little use for our complete analysis of this channel.

1.6.2   M.S.: Measurements of SAPHIR

SAPHIR was the first detector to collect data on this reaction over a wide range in angle and center of mass energy. The detector made use of a photon tagging system which covered the range of 53% to 90% of the initial electron energy, which was improved before the final dataset by dropping the lower limit to 32% of the electron energy. The target was surrounded by a system of drift chambers covering the full angular range . The drift chambers, in turn, were surrounded by scintillator hodoscopes designed to measure time-of-flight. An electromagnetic shower calorimeter was used for detection of photons in the forward direction and a beam veto counter was used to prevent false triggers from photons not interacting with the target. A more complete description of the set up can be found in [23]. The SAPHIR collaboration published three sets of results for the $K^+\Lambda$ differential cross section, one each in 1994, 1998, and 2004.[24, 25, 26] The final results in 2004 were generated from data taken in the final run of SAPHIR from $1997 - 1998$. They encompass a set of 51977 $K^+\Lambda$ events spread over an energy range from threshold to $W \approx 2.4$ GeV and binned by 50 MeV sets in photon energy and 0.1 in $cos\vartheta_{cm}$. These results are plotted alongside those for earlier experiments in Figures 1.5 - 1.7. In the same publication, SAPHIR presented results for the Λ recoil polarization, coarsely binned in W because statistics were a limiting factor. The measurements were taken for 30 kinematic values, which are plotted in Figures 1.8 and 1.9. The most interesting feature of the SAPHIR data
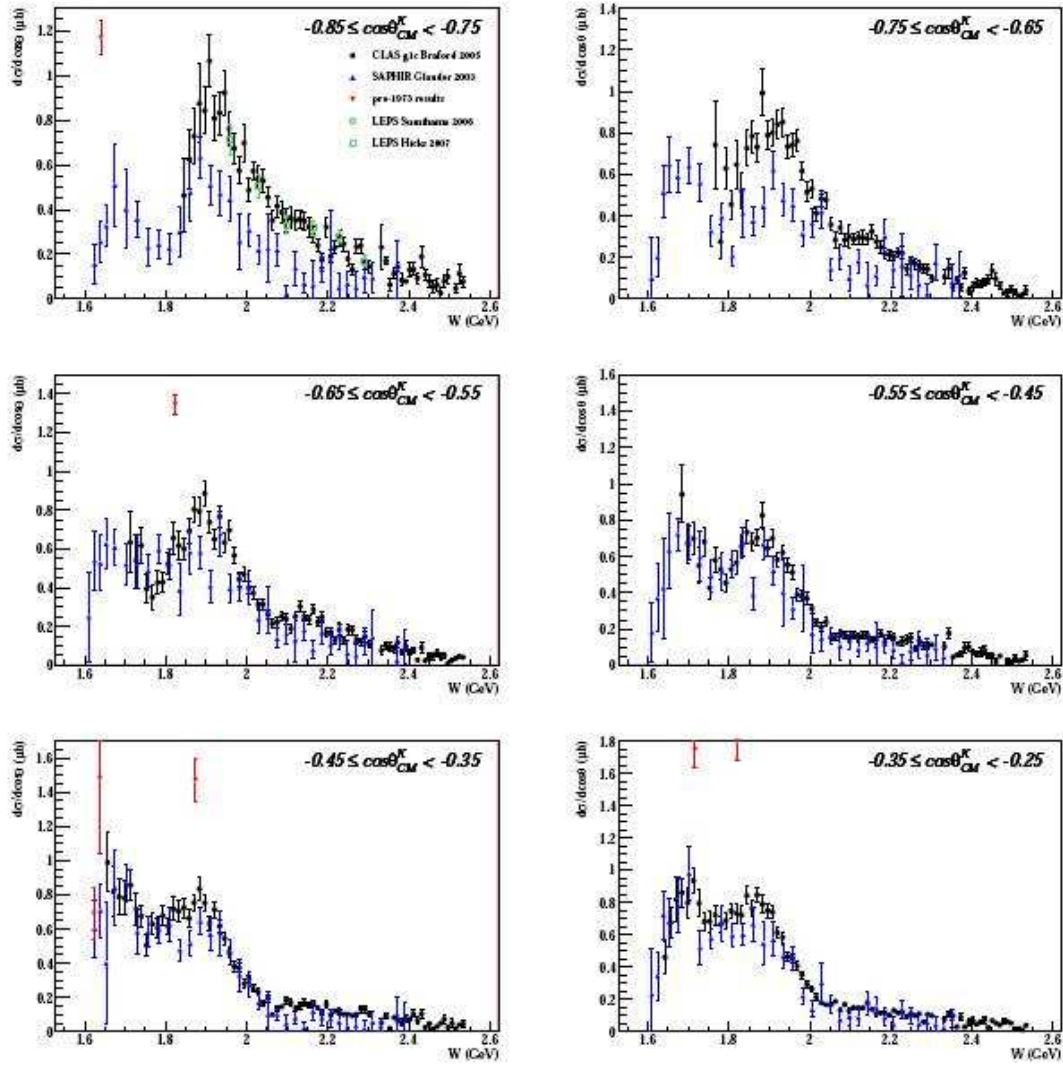
Figure 1.5: Differential cross section data from SAPHIR, CLAS, LEPS, and earlier endeavors (1). Image Source: [21]
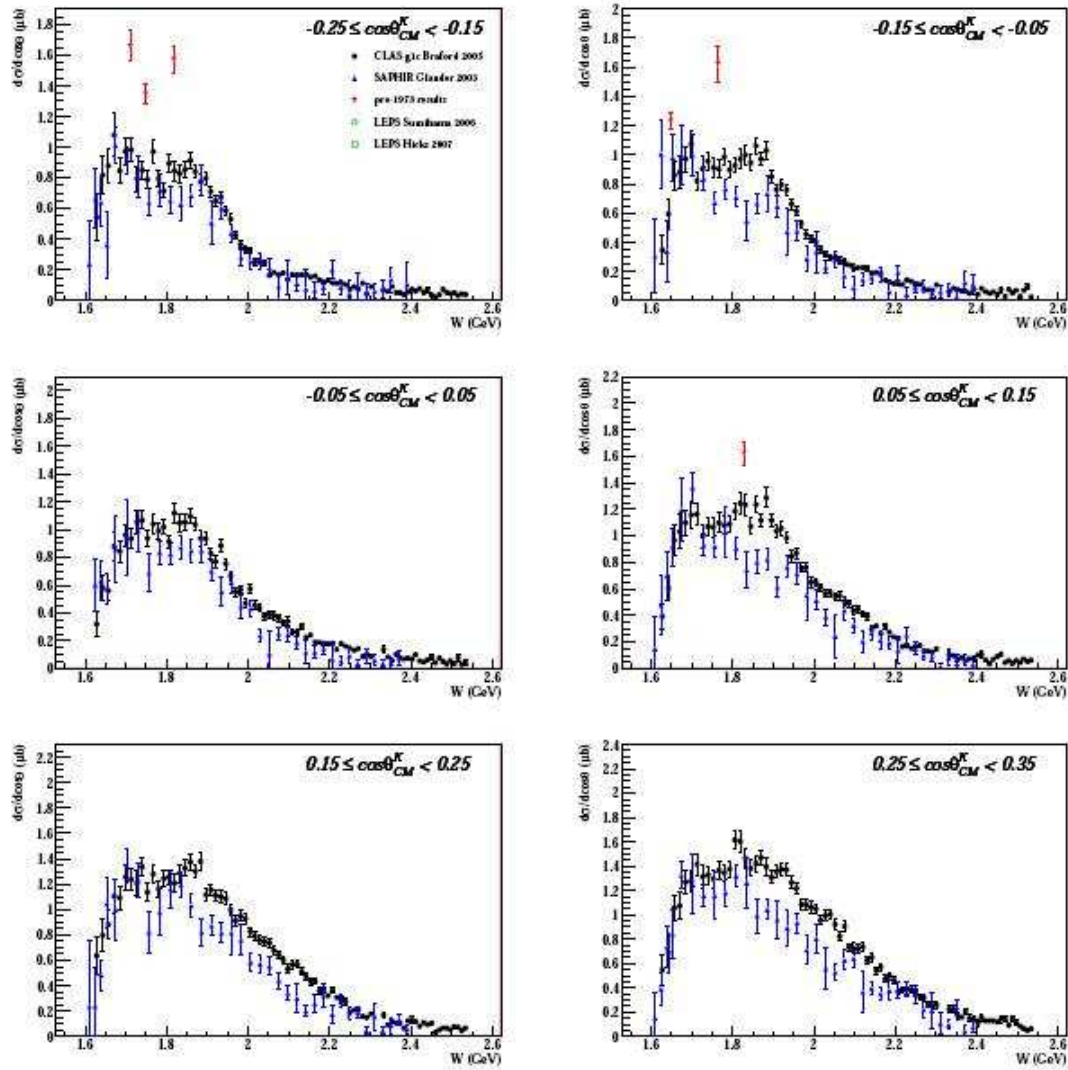
Figure 1.6: Differential cross section data from SAPHIR, CLAS, LEPS, and earlier endeavors (2). Image Source: [21]
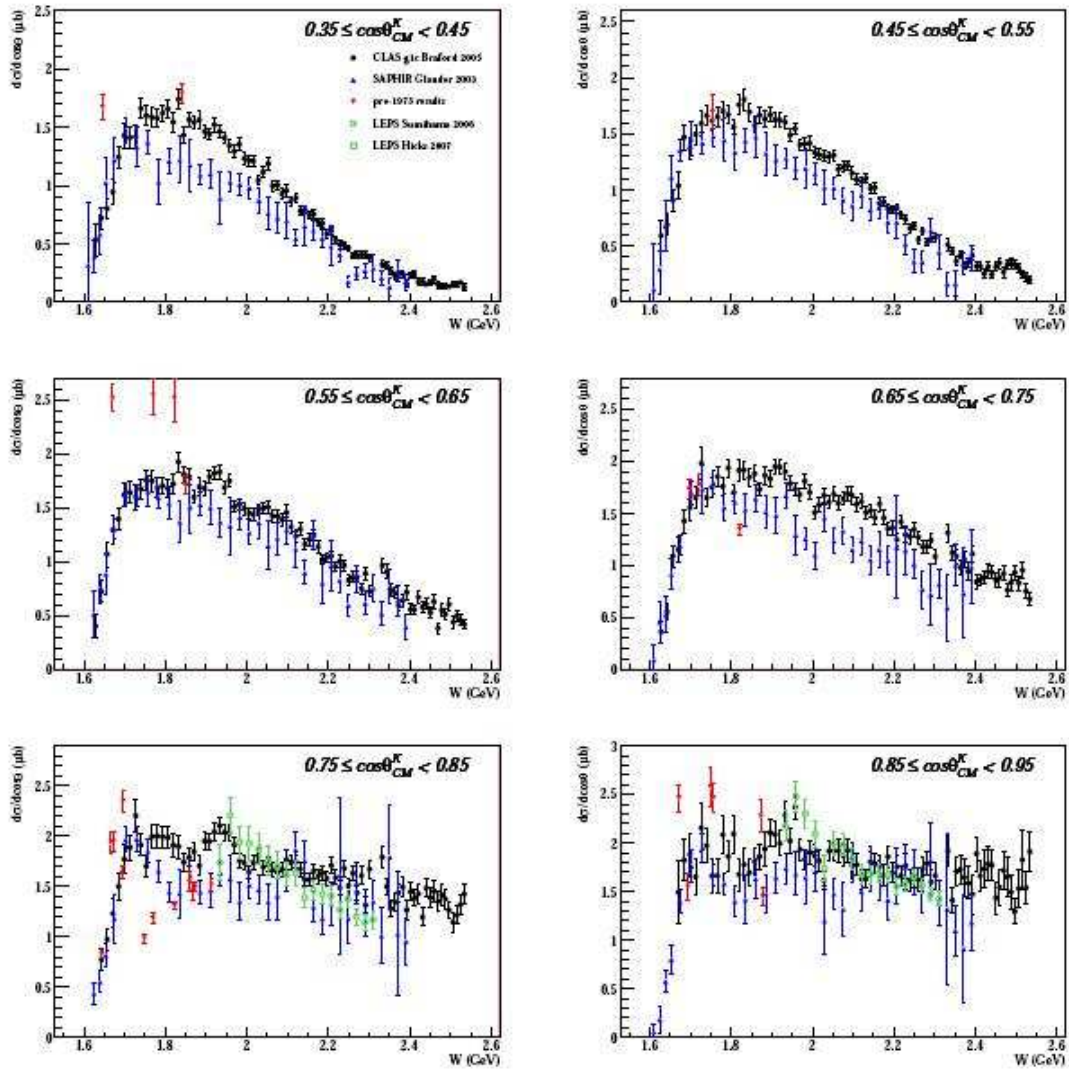
Figure 1.7: Differential cross section data from SAPHIR, CLAS, LEPS, and earlier endeavors (3). Image Source: [21]

is the structure it shows around W = 1.9 GeV, corresponding to $E_\gamma \approx 1.5$ GeV. The structure is slight and has generated controversy, but the missing resonance $D_{13}(1960)$ was posited as an explanation for the "bump" seen in the cross section. Alternative explanations have been proposed for this structure and further analysis of the channel is certainly necessary to make any definitive conclusion.

1.6.3 PhD : Plenty of hyperon Dissertations

The CLAS collaboration added its own set of high statistics to the analysis of the $K^+\Lambda$ channel. Over several experiments, beginning with the g1c run period in 1999, the CLAS was used to collect data for the collaboration's own measurements of cross section and recoil polarization as well as an array of previously unmeasured observables. The results of these measurements are presented in the PhD theses of several CLAS members. The first results for differential cross section were published by the CLAS collaboration in 2005 as an amalgam of the results of John McNabb and Robert Bradford. The high statistics set of roughly 5.6×10^5 events allowed for a fine binning of 10 MeV in photon energy from threshold up to a center of mass energy of 2.53 GeV. This extended the range of SAPHIR results by approximately 100 MeV and the finer binning produced plots more sensitive to energy dependent structures like the nucleon resonances. Indeed, the CLAS results show a more significant bump than do the SAPHIR cross section data as can be seen in Figures 1.5 - 1.7. Nonetheless, the two datasets show good agreement except in the extreme forward and backward directions where CLAS shows a large enhancement relative to SAPHIR. The LEPS experiment at Spring-8 in Japan performed these cross section measurement at extreme angles in the ranges $-1.0 < \cos\theta_{CM}^K < -0.8$ and $0.7 < \cos\theta_{CM}^K < 1.0$ where CLAS has poor acceptance.[27, 28] The results seem to confirm the measurements of CLAS for values below $W \approx 2.1$ GeV, but at higher energies there is better agreement with SAPHIR data.
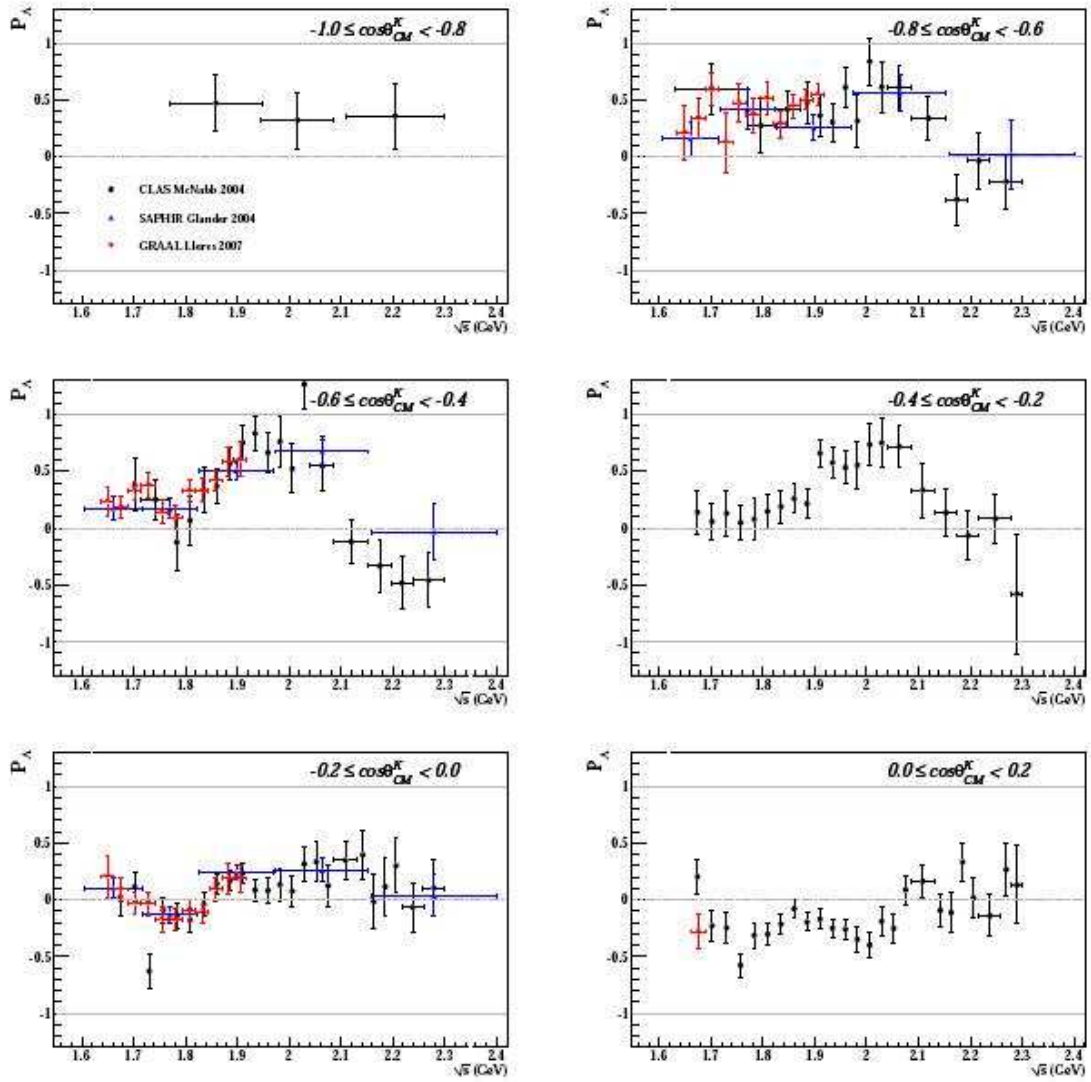
Figure 1.8: Recoil polarization data from SAPHIR, GRAAL, and CLAS g1c (1). Image Source: [21]
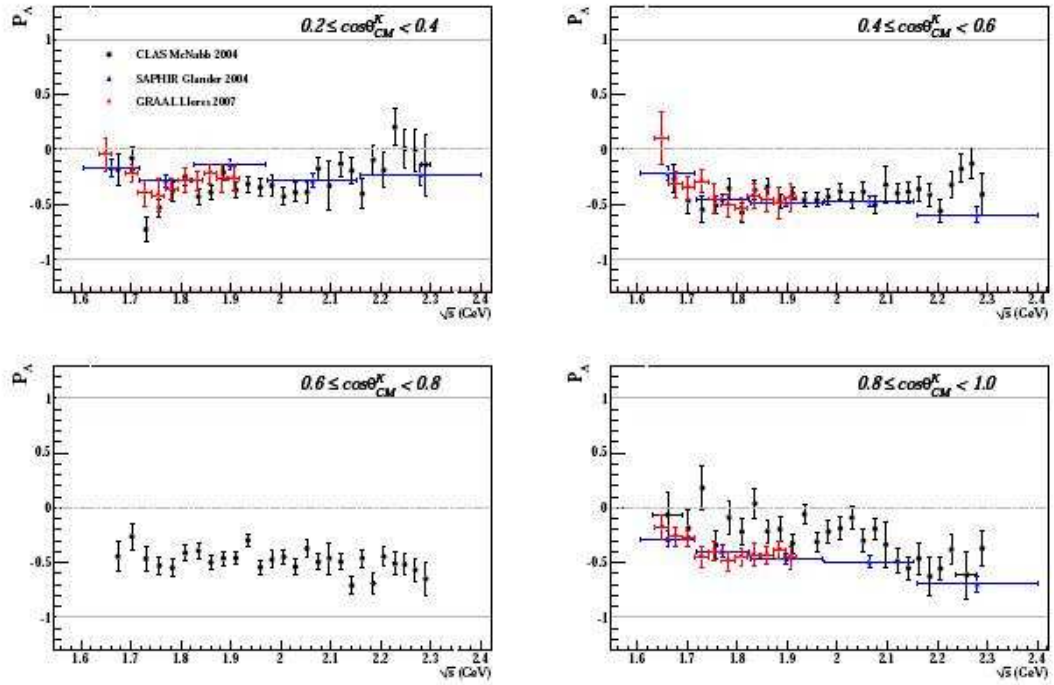
Figure 1.9: Recoil polarization data from SAPHIR, GRAAL, and CLAS g1c (2). Image Source: [21]

CLAS recoil polarization results from g1c were also presented in 2004. The 3×10^5 events used in the range of energy from threshold to $W \approx 2.3$ GeV allowed for binning of 50 MeV in photon energy and 0.2 in $cos\vartheta_{cm}$ in most regions, while areas of low statistics required wider energy bins. The results are mostly consistent with SAPHIR, although the binning in SAPHIR is too broad to make a solid determination of agreement. In particular, there is significant discrepancy in the very forward regions, but the binning of the SAPHIR data makes it impossible to determine the cause from these two sets alone. Fortunately, the GRenoble Anneau Accelerateur Laser (GRAAL) in France provided a third dataset for comparison in 2007.[29] The results, which were binned similarly to the CLAS results in energy and taken at six fixed lab frame angles are more consistent with SAPHIR at very forward angles as can be seen in Figure 1.9. Later in the same year, Michael McCracken produced new recoil polarization results using the g11 dataset.[21] His dissertation presents values at 1708 kinematic points with a binning of 10 MeV in center of mass energy. The

results showed good agreement with previous experiments and presented the most precise measurement of recoil polarization to date. While I have not plotted these data points here, a selection of point will later be plotted against my results for g9a as a consistency check.

Several other polarization observables have been measured using CLAS data. The polarization transfer observables $C_{x'}$ and $C_{z'}$ were measured by Bradford using g1c data.[20] He found the presence of possible resonant structure in the backwards angles, while $C_{x'}$ tended to 0 and $C_{z'}$ approached 1 at forward angles. The high value of $C_{z'}$ is partially explained in terms of hadronization of a photon into a ϕ meson, which is comprised of a strange and an anti-strange quark. Since the K^+ has zero spin, all spin from the photon is transferred to Λ by means of the strange quark. Craig Paterson extracted target, recoil, and beam asymmetries T, P, Σ, and beam-recoil polarization transfer $O_{x'}$, and $O_{z'}$ from the linearly polarized photon data of g8b. The measurements for P and Σ were in good agreement with previous results (GRAAL and LEPS for the beam asymmetry). For the target asymmetry, T, he found large negative asymmetries in the forward angular region. The necessity for $D_{13}(1960)$ inclusion to explain these results was model dependent. His results for $O_{x'}$ and $O_{z'}$ showed a reversal of the situation for $C_{x'}$ and $C_{z'}$, with near 100% polarization transfer for $O_{x'}$. He found that model predictions including the $D_{13}(1960)$ resonance agreed well with $O_{x'}$, while those without the $D_{13}(1960)$ better described the behavior of $O_{z'}$.[10]

1.6.4   Promise Of Single + Double Observable Compilation

The full set of polarization observables have yet to be compiled, but analysis of CLAS data leading to the complete measurement of all single and double photoproduction polarization observables is underway. This dissertation will present measurements of E, $L_{x'}$, and $L_{z'}$, coming from the portion of the g9a dataset using circularly polarized photons. A concurrent analysis of the linearly polarized photon portion of the dataset will provide a first

measurement of double polarization observable *G*. The recently finished g9b run period used a transversely polarized target. Calibration of the dataset is still ongoing, but soon analysis will begin to extract double polarization observables *H*, *F*, $T_{x'}$, and $T_{z'}$. These will round out the set, paving the way for a full PWA of the reaction channel.

1.7 Summary

The highly energy-dependent coupling factor of the strong force makes perturbative QCD calculations impossible for the nucleon resonance region. Instead, the number and properties of excited baryon states are predicted using constituent quark models, but the number and width of predicted resonances presents an obstacle to their detection. Only the sensitivity in energy and angular distribution of a broad range of observables, which, together, fully describe a reaction channel, can adequately address these complications. The advent of large-acceptance spectrometers has revitalized interest in photoproduction reactions. Theoretical predictions of strong resonance coupling to strange decay channels of photoproduction reactions has particularly bolstered interest for the search for missing resonances in hyperon channels such as $\gamma p \rightarrow K^+\Lambda$. Many polarization observables have already been measured for this channel, with some degree of success in pointing to the presence of missing resonances, but no certain conclusions have been drawn yet. The construction of FROST, a frozen spin target, has allowed us to take data from which we can extract the first double polarization observables requiring target polarization. This analysis will present measurements of three new polarization observables to be added to those already determined, bringing the world data one step closer to a full model independent analysis of the $\gamma p \rightarrow K^+\Lambda$ reaction channel.

Chapter 2

CEBAF, CLAS, and FROST: Advanced Acronym Theory with Applications

The data analyzed for this dissertation were taken during the g9a run period at the Thomas Jefferson National Accelerator Facility (also known as Jefferson Lab or JLab). During this period, data taken from FROST (FROzen Spin Target) were collected to be used for multiple experiments in hadron spectroscopy requiring a polarized target and polarized photon beam and motivated by the search for nucleon resonances. The analysis presented here is a part of experiment E02-112, "Search for Missing Nucleon Resonances in the Photoproduction of Hyperons using a Polarized Photon Beam and a Polarized Target." The running conditions for this period called for a longitudinally polarized target and an incident photon beam, which would be switched between circular and linear polarizations over the course of g9a. The photon beam was created using the CEBAF (Continuous Electron Beam Accelerator Facility) electron accelerator in conjunction with the Hall B photon tagging system. The electron beam was used at five different energies for g9a production data: 1.645, 2.478, 2.751, 3.539, and 4.599 GeV. This analysis only includes the 1.6 and 2.5 GeV datasets, for which a circularly polarized photon beam was used. The target used

was FROST, a frozen spin polarized target that allowed us to take full advantage of our detector, the CEBAF Large Acceptance Spectrometer (CLAS). CLAS provides near 4π acceptance for multi-particle final states and together with FROST has given us a dataset for polarization observables covering an unprecedented range. In this chapter I will cover the experimental setup for g9a from the CEBAF accelerator to the detection of final particle states in CLAS.

2.1   CEBAF

The Continuous Electron Beam Accelerator Facility (CEBAF) delivers continuous wave electron beams to Jefferson Lab's three experimental halls. Completed in 1996, CEBAF was the first continuous-wave electron accelerator in the multi-GeV energy region. Early facilities using electromagnetic probes produced the acceleration gradient using room-temperature (copper) radio frequency (RF) cavities, which required cooling time after beam spills on account of the heat buildup due to resistivity. These low duty factor machines simply could not produce high enough average current to measure the small electromagnetic (EM) cross sections with acceptable statistics. CEBAF's major technological achievement was to use superconducting RF cavities to accelerate the electron beam. Thus, with 100% duty factor, CEBAF produces a high-luminosity beam to counteract the effect of comparatively low interaction rates. This is desirable because, low interaction rates not withstanding, electromagnetic probes do offer some advantages over hadronic probes. In the first place, the interaction is well understood in QED, which can help circumvent thorny analysis issues. In addition, an EM beam can probe the whole volume of a nucleon.

The search for missing resonances provides further motivation for the use of EM probes as coupling to photoproduction channels is expected where πN production has failed to produce results. The continuous-wave beam of CEBAF can generate a high statistics dataset

even when running at low currents, as is necessary for coincidence experiments like g9a. Electron beam production begins at the injector, which is comprised of a photo-emission gun, an RF accelerator cavity, and an optical chopper. The gun contains three diode lasers illuminating a GaAs photocathode. These lasers are pulsed at 499 MHz, 120 degrees out of phase, to allow for each experimental hall to receive beam with its own current and polarization specifications.[30] The pulsing of the laser results in beam "buckets" spaced at intervals of 2.004 ns for each hall.

Circular polarization of photons in the hall begins at the injector with circular polarization of the laser light using two Pockel cells acting as a half-wave plate and a quarter-wave plate.[31] The polarized light produces longitudinally polarized electrons by emission from the photocathode. A change in the voltage of the quarter wave plate Pockel cells will result in an electron helicity flip. This longitudinal polarization will later be transferred to radiated photons in the form of circular polarization. After electrons are extracted from the photocathode, two superconducting RF cavities are used to accelerate them to 45 MeV, at which point they are separated into bunches by an optical chopper before passing into CEBAF's recirculating linear accelerators (LINACs).[32] The main body of CEBAF is a racetrack accelerator, composed of two parallel LINACs connected by nine recirculation arcs. Each LINAC consists of 168 niobium RF cavities immersed in liquid helium to keep them cooled to a temperature of 2K, at which point they are superconducting. The accelerating gradient for the electron beam is provided by an electromagnetic standing wave generated in each cryomodule by its own Klystron. These waves have a frequency of 1497 MHz, keeping them in phase with the beam bunches so that each bunch experiences a continuous positive electric force as it passes through an RF cavity.

When operating at full capacity, each LINAC provides a maximum 600 MeV of acceleration. The recirculation arcs allow the beam to make five passes through each LINAC for a maximum electron beam energy of about 6 GeV. A series of dipole magnets within
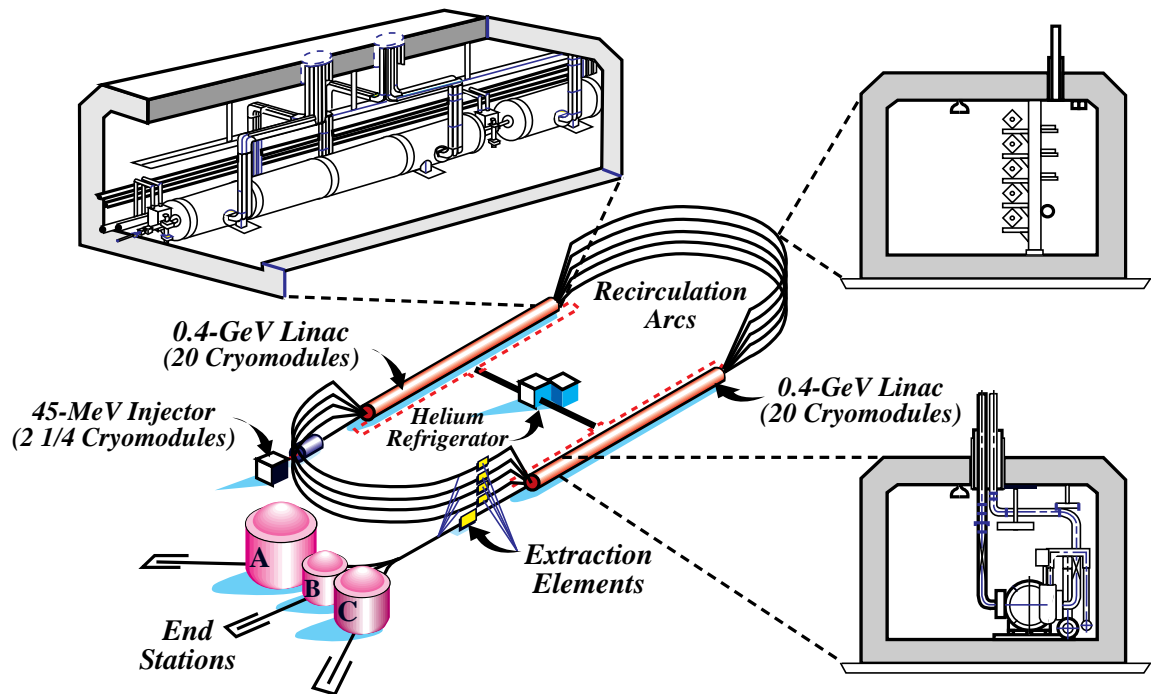
Figure 2.1: Schematic views of the CEBAF Accelerator

the recirculation arcs produce the field which bends the electron beam from one LINAC to the next. As the beam makes its individual passes through the accelerator, it is divided into sub-beams by energy so that electrons of different energies can pass through dipole magnets of different field strengths. In this manner, the radius of curvature is kept constant as the beam energy increases. The sub-beams are then recombined before they enter the next LINAC. Once a beam bucket has reached an experimental hall's requested energy, it can be extracted using RF separator cavities that take advantage of the 120 degree phase separation to direct specific beam buckets to their appropriate halls. The requested energy may be the endpoint energy for any number of passes up to five, with some restrictions. While all three halls can run with beam at maximum energy, no two halls can extract beam on the same pass for lower energies.
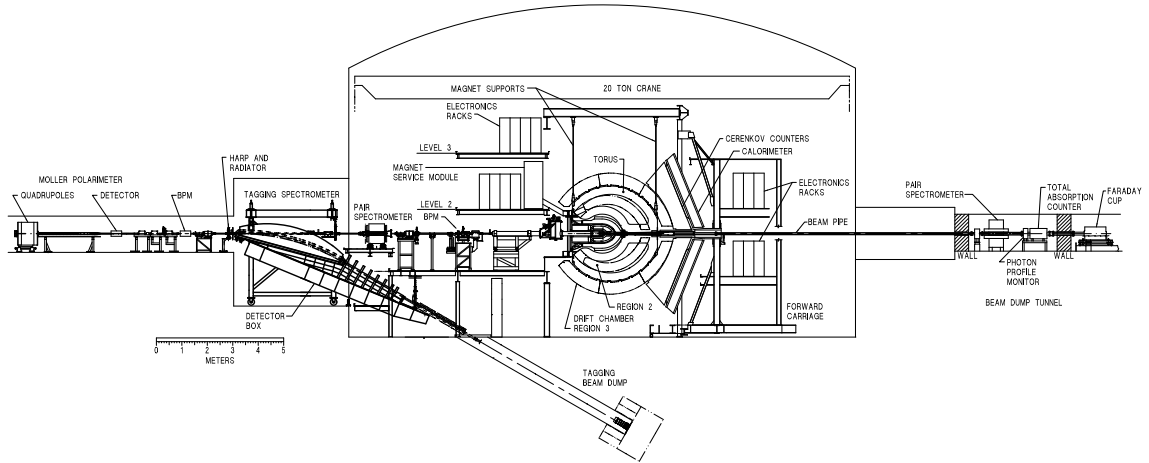
Figure 2.2: Schematic diagram of Hall B

2.2   Hall B and the CLAS detector

Hall B is the smallest and best of JLab's three experimental halls. The highlight of Hall
B is the CEBAF Large Acceptance Spectrometer (CLAS), which allows for the analysis
of exclusive reactions through detection of multi-particle final states. In addition, Hall B
houses the photon tagger, a magnetic spectrometer that measures the energy of electrons
after emission of a bremsstrahlung photon. This instrument, together with CLAS, makes
real photon coincidence experiments possible in Hall B. A schematic of the Hall B exper-
imental apparatus is shown in Figure 2.2. In this section I will give an overview of the
devices in Hall B starting from the beam's entry point at the photon tagger and moving on
to the core of the experiment at the CLAS detector where particle events are produced and
detected. I will end with some brief discussion of beamline devices.

2.2.1   The Photon Tagger

As the electron beam enters Hall B it first encounters the photon tagging system. The tag-
ging system consists of a selection of radiators, the tagger magnetic spectrometer, and a
series of collimators. This system is responsible for the production of the photon beam and

Figure 2.3: Schematic view of the Hall-B tagger. Image Source: [33]

measurement of the photon energy for photon runs. It also provides the timing information necessary in order to make coincidences with particle events detected in CLAS. For electron runs, the tagging system is not used. A schematic of the tagging system is shown in Figure 2.3.

During the circularly polarized photon runs of the g9a run period, the electron beam was incident on a gold foil radiator of 10^{-4} radiation lengths (a thin diamond radiator was used for the linearly polarized photon runs, which are not included in this analysis). Gold is an excellent choice for production of photons via bremsstrahlung radiation, because the high atomic number reduces background from electron-electron scattering. The energy transferred to the nucleus in bremsstrahlung is negligible. Thus, we can determine photon energy by the simple relation:

$$E_\gamma = E_0 - E_e \ , \tag{2.1}$$

where E_γ is the photon energy, E_0 is the initial electron energy delivered to the hall, and E_e is the final electron energy after emission of the bremsstrahlung photon. The photons will have circular polarization proportional to the polarization of the electron beam as described in the first chapter. The bremsstrahlung photons are not mono-energetic, so determination

of this final electron energy is necessary for each photon in order to calculate its energy. This is where the tagging magnetic spectrometer comes in.

The tagger magnet is a dipole producing a maximum field of 1.75 T. Electrons passing through the radiator are bent by the field toward the tagger hodoscope leaving a pure photon beam to continue to the target in CLAS. Those electrons which did not interact in the radiator and carry all of their initial energy are bent past the tagger hodoscope into a beam dump, while electrons producing photons in the range of 20% - 95% of the initial beam energy are directed into the two hodoscope planes. The two planes of the tagger hodoscope are referred to as the E-plane and the T-plane to designate their respective purposes.

The E-plane is composed of 384 scintillator paddles with dimensions of 20 cm in length, 4 mm thick, and widths varying from 6 to 18 mm so as to subtend approximately equal momentum intervals. Each scintillator has its own photomultiplier tube and multi-hit TDC. These paddles, or E-counters, are arranged in an overlapping formation to give 767 energy bins, each of width 10^{-3} of E_0.

The T-plane, by contrast, has fewer scintillators, providing poorer resolution in energy, but better timing resolution. There are 61 T-counters overlapped slightly at the edges for 121 bins. There are two photomultiplier tubes and two pipeline TDCs (one to each PMT) associated with each T-counter. The T-counter widths were chosen to give approximately equal counting rates in each of two regions: 75-95% of E_0(T1-19) and 25-75% of E_0(T20-61). The narrower counter widths in the 75-95% region allow higher counting rates near the bremsstrahlung endpoint when lower photon energies are not of interest. The T-counter paddles are 2 cm thick and yield a timing resolution of 110 ps. This is sufficient to identify the correct beam bucket so that the RF time for this bucket may be correlated with a particle event to calculate the event's vertex time.

The final portion of the photon tagging system is the series of collimators. There are two collimators placed between the tagger and the target. As the photon beam passes through

these collimators the beam halo is removed. Sweeping magnets between the collimators remove charged particles created by photons interacting with the first collimator. A more complete description of the photon tagger can be found in Ref. [33].

2.2.2 The CLAS Detector

The CLAS detector is the chief instrument of our physics analysis.[34] It houses the target in which our desired reactions take place and detects the final products of these reactions, collecting the crucial information on each particle essential to selecting and sorting the appropriate events. This selection and sorting is the crux of our analysis. We select $K^+\Lambda$ events produced from photon interactions with polarized protons and sort them according to angle and energy for each polarization state. While other instruments are involved in some of these data, all of it relies on CLAS. CLAS is composed of six superconducting magnetic coils arranged in a toroidal configuration, which split the detector into six sectors. The various detector subsystems are thus arranged in a layered fashion within these six sectors. Working in tandem, these subsystems provide information on detected particles' momentum, charge, velocity, and mass as well as information on the polar and azimuthal distributions coming from the position of particle hits. The complete detector has a near 4π solid angle acceptance, reduced somewhat in the azimuth by the presence of the magnetic coils. In the center of CLAS lies the target cell, which for g9a housed the frozen spin butanol target, FROST. Downstream from this target were a carbon and a polyethylene target to be used for determining the background from bound-nucleon reactions. The target cell is surrounded by a start counter designed to determine the time of each hadronic reaction for photon runs. From there particles move to the three drift chamber regions, which track charged particles and give their momentum information. Finally, they reach an outer scintillator shell used to determine the particle's time of flight. This information is critical to identify the particle type.
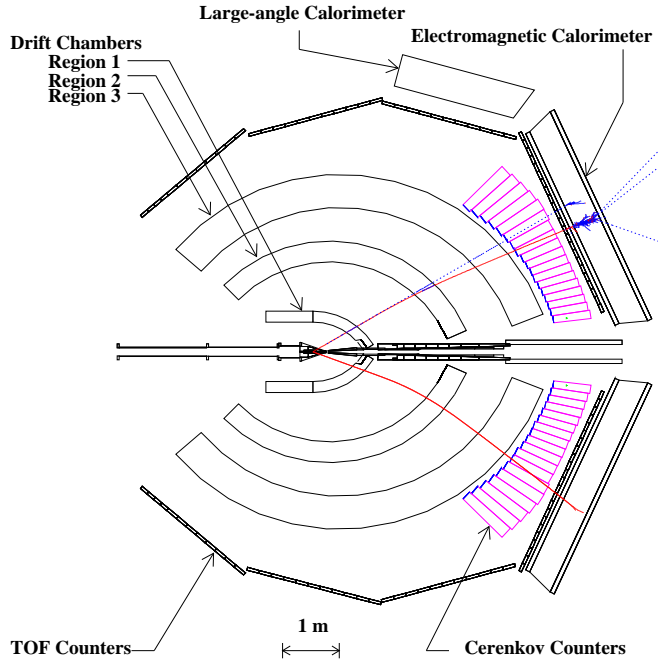
Figure 2.4: The CLAS detector

The CLAS detector also includes Cerenkov counters and forward electromagnetic calorimeters. Both of these are shown along with the rest of the CLAS detector systems in Figure 2.4, but as these systems are used primarily for electron runs, they have not been used in this analysis and will not be discussed further in this dissertation. This section will focus on the CLAS torus, the start counter, drift chambers, and time-of-flight system. The FROST target is the key feature distinguishing the g9a run period from previous CLAS run periods and will be discussed in some detail in section 2.3.

2.2.2.1   Start Counter

The Start Counter's function is to serve as part of the coincidence determination for real photon runs, a function which it shares with the time of flight system. The Start Counter surrounds the target and is the first instrument to detect charged particles traveling out from
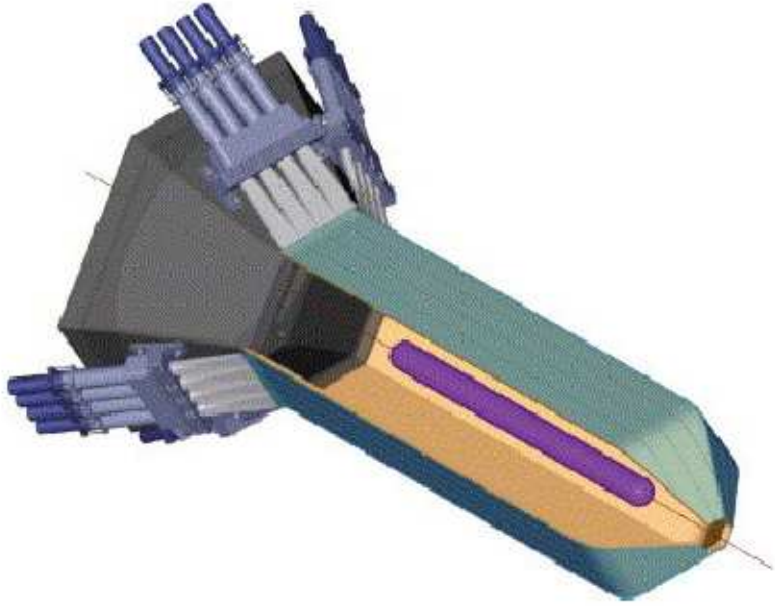
Figure 2.5: Schematic of the CLAS Start Counter

the target region. The start time at this point is later used in the calculation of the particle flight time. After the tagger T-counters are used to assign a photon to the appropriate RF beam bucket, the RF time is propagated forward to the center of CLAS to calculate the vertex time for an event. The Start Counter time (ST) should fall into a ± 1 ns interval around this propagated time at a 99% confidence level. Thus, a cut on the vertex time helps ensure an accurate coincidence measurement. The Start Counter consists of 24 scintillator paddles, each coupled to an acrylic light guide, divided equally among the sectors of CLAS as can be seen in Figure 2.5. This number of paddles allows the Start Counter to cover the full acceptance range of CLAS, from $7^o < \vartheta < 145^o$ and $-29^o < \varphi < 29^o$ for each sector. Each scintillator has a 502 mm long straight section, located between two bends, and a tapered "nose" end. They are 29 mm wide and 2.15 mm thick. This means that particles will not have much material to pass through, minimizing the effect of multiple scattering.[35]

2.2.2.2 Superconducting Torus Magnet

The CLAS torus is composed of a set of six kidney-shaped superconducting coils separated at 60 angles in the azimuth. This toroidal arrangement was set by the requirement that CLAS should have a field free region around its center where the target is held. The positioning of the coils in turn designates the geometry for CLAS, specifically its division into six sectors, while the space occupied by the coils reduces the acceptance of CLAS to about 75% of the 4π solid angle. In total, the magnet is approximately 5 m in diameter and 5 m in length. A photograph of the torus magnet is given in Figure 2.6. The purpose of the torus magnet is to obtain momentum information on charged particles through observation of their curvature in a known field. Since the system is free of any iron, the magnetic field can be calculated directly from the current in the coils. The coils all have four layers of 54 turns of aluminum-stabilized NbTi/Cu conductor. They are cooled to a superconducting temperature of 4.5 K by forcing super-critical helium through cooling tubes at the edge of the windings. The magnet has a peak current of 3861 A for a maximum field strength of 3.5 T. The field is primarily in the azimuthal direction with significant deviations only at areas close to the coils. This means that, when the current is run through the coils in the typical direction, positively charged particles will curve away from the beamline, while negatively charged particles will curve back toward it. The result is that low-momentum particles with negative charge will fail to make complete tracks. In g9a this issue was addressed by running the torus at 1920 A for a maximum field of about 1.8 T. Although the reduced field also reduces the momentum resolution, it increases the acceptance of negatively charged particles.[36]

2.2.2.3 Drift Chambers

The drift chambers provide the tracking information for charged particles before, during, and after their motion through the magnetic field of the torus. With this purpose in mind, 18

Figure 2.6: Photo of the CLAS Torus coils prior to installation. Image Source: [63]

separate drift chambers were constructed so as to have three radial regions each occupied by six chambers matching the sectors of CLAS. Each region is in turn divided into two superlayers comprised of six layers of hexagonal drift cells. The first superlayer is oriented axial to the field direction, while the other is tilted at a 6° stereo angle with respect to the first in order to obtain azimuthal information.[37]

A drift cell is made up of one 20 μm diameter gold-plated tungsten sense wire in the center of a hexagonal arrangement of six 140 μm gold-plated aluminum alloy field wires. The field wires are kept at a negative high voltage, while the sense wires are kept at a positive potential. The drift chambers are filled with a gas mixture of 90% argon and 10% CO_2. The gas will ionize as a charged particle moves through it. Electrons freed in the process will further ionize the gas as they are pulled toward the sense wires, ultimately registering as an electric pulse in the wire. Figure 2.7 shows an example of a hit pattern in drift chamber superlayers created by this ionization process.

The Region 1 chambers are located within the torus in an area of weak field. The
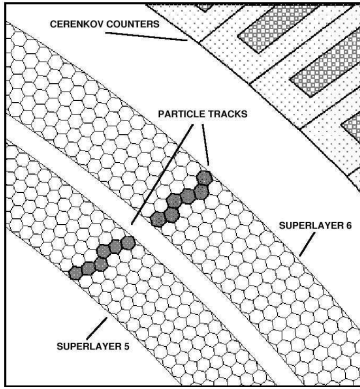
Figure 2.7: Particle track going through Superlayers 5 and 6 of the CLAS Drift Chambers. Image Source: [10]

purpose of this region is to provide information on the initial trajectory of particles before they are curved by the torus field. Region 2 lies between the torus coils, where the magnetic field is strongest. Thus, the drift chambers in this region are well suited for determination of particle momentum using the curvature of tracks within. Region 3 is situated outside the magnet coils in another region of weak field, so that tracks in the chamber will give the final trajectory of charged particles before they reach the time-of-flight system. The complete drift chamber system provides coverage of 8° to 142° in the polar angle and 80% of the azimuthal angle.

2.2.2.4 Time-of-Flight

The time-of-flight (TOF) system is a shell of scintillators about 4m from the target on the outer edge of CLAS designed to give precise timing information for charged particles as they exit the detector. This high resolution timing (between 80 and 160 ps) is used to calculate the particle velocity and is a crucial part of the particle identification process. In particular, the TOF is intended to distinguish p and K tracks for momenta up to 2.0 GeV/c.[38]

The TOF shell consists of 57 scintillator bars per sector, with widths of either 15 cm in the forward region where most particle tracks are found or 22 cm at large angles (greater

Beam
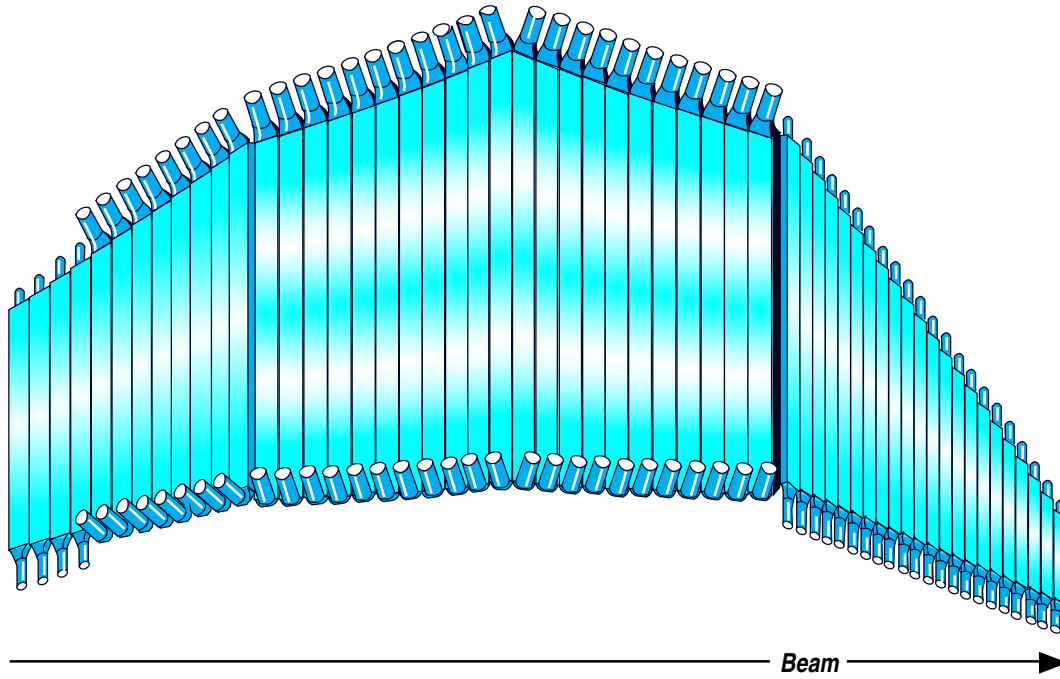
Figure 2.8: View of Time-of-Flight scintillator paddles for a single sector in CLAS

than 70°) and lengths varying from 32 cm to 445 cm as designated by the shape of the sector. The bars are all 5.08 cm thick for 100% detection of minimum-ionizing tracks. The high timing resolution of the bars comes from the scintillator material of Bicron BC-408, which offers fast response time and low light attenuation. Each bar is equipped with two PMTs mounted onto the magnet cryostats and connected to the paddles by lightguides made of lucite. The time in each PMT provides information on the azimuthal hit position, which allows for accurate calculation of the hit time by correcting for the travel time of light through the scintillators. Figure 2.8 shows the distribution of scintillator paddles for one sector of CLAS. The complete TOF system covers the polar range of $8^o < \vartheta < 142^o$ and the azimuthal range of CLAS.

2.2.3 Beamline Devices

A number of devices both upstream and downstream of CLAS were included in the operation of g9a. The upstream devices were used to monitor beam quality and included beam position monitors, harps, and a pair spectrometer. The Møller polarimeter which measures the longitudinal polarization of the electron beam is also located upstream. Downstream of CLAS a total absorption shower counter (TASC) is used to measure photon flux. This section gives a brief overview of these devices.

2.2.3.1 Beam Position Monitors

The function of the Beam Position Monitors (BPM) is to help maintain acceptable beam position during data acquisition. They operate on the principle of induced currents. The electron beam will induce a current in wires near the beamline that is proportional to the distance of the beam from the wires. The BPMs measure this current to calculate the x and y positions of the beam to a precision of better than 0.1 mm.[39]

The Hall B Shift takers, who take turns running the experiment according to the given run plan, are aided by the 1 Hz report time on the BPMs and an alarm that triggers after an extended period of beam outside set parameters. In conjunction with the MCC (Machine Control Center), they can then work to make sure the beam returns to optimal running conditions.

2.2.3.2 Møller Polarimeter

The Møller Polarimeter was an important device for this experiment. As the photon beam polarization could not be measured directly, it was crucial that the electron beam polarization should be measured periodically between production runs. The measured polarization could later be used to calculate photon polarization using equation (1.11).

The device consists of a 25 μm thick permendur foil, two quadrupole magnets, and

scintillators equipped with PMTs, forming a magnetic spectrometer for scattered electron detection. The foil target is polarized along the direction of the beam to $P_T \sim 0.075$ and oriented vertically with its plane at $\pm 20\,\mathrm{deg}$ with respect to the beam direction. This target polarization together with the helicity asymmetry of detected electrons is used to calculate the electron beam polarization according to the formula

$$P_{el} = \frac{A}{A_z P_T} \; ,$$

(2.2)

where A is a simple asymmetry in the yield by helicity following the rubric of equation (1.8), P_T is the target polarization just given, and $A_z = 0.7826 \pm 0.0079$ is the analyzing power of the target.[20]

Use of the Møller Polarimeter would interfere with data acquisition so it was limited to special Møller runs taken at intervals between production runs, typically after a change in run conditions. A frequent update of this information would consume valuable data acquisition time, so Møller measurements are fairly scarce in the g9a dataset. Thus, the technique is only reliable under the assumption that the measured polarization changes slowly, or not at all.

2.2.3.3 Total Absorption Shower Counter (TASC)

The TASC located downstream of CLAS is a nearly 100% efficient photon detector used during normalization runs for the purpose of measuring the tagging ratio of the hodoscope T-counters. The TASC consists of four lead-glass blocks of ~ 17 radiation lengths coupled to a PMT. A low intensity beam is required to prevent the TASC from overloading, so special normalization runs are taken using a 100 pA beam and a thinner radiator than that used during production runs. The ratio of "good" electrons (those with hits in the left and right TDC matching in time and a corresponding hit in an E-counter) to photons detected in the TASC gives the tagging ratio, which can later be used to calculate the photon flux

during data collection.[40]

2.3 FROST: FROzen Spin Target

The FROST target is the critical element that makes this analysis achievable. Without the inclusion of a nuclear spin polarized target, no single or double-polarization observable requiring information on the target's polarization state could be extracted. Yet, the typical field strengths and the size of magnets necessary to maintain polarization in a dynamically polarized target would reduce acceptance dramatically. Such experimental conditions are unacceptable when the variation in angular distribution of an observable is so crucial to gleaning some meaningful information from it. This dilemma could only be solved with a target that had its polarization frozen in place. By keeping a polarized target at an extremely low temperature (below 50 mK) only a small holding field would be required to maintain polarization for a relatively long time. In this section, I will describe the apparatus of the FROST target (illustrated in Figure 2.9), how it was polarized, cooled, and maintained throughout the course of the g9a run period. I will end by discussing the construction of the FROST target and the purpose of the ancillary targets of g9a in light of this construction.

2.3.1 Dynamic Nuclear Polarization

Dynamic Nuclear Polarization (DNP) is the process by which protons in FROST are initially polarized. Although it is possible to polarize nuclei directly through use of a magnet, the nuclei take much longer to polarize in this manner and it requires a very strong field. The DNP technique uses a polarizing magnet to polarize the electrons in the target material and then transfers the electron polarization to the nuclei by saturating the target with microwaves near the Electron Spin Resonance (ESR) frequency of paramagnetic radicals dissolved in the butanol.[41] The nuclear spins can be polarized either parallel or anti-parallel
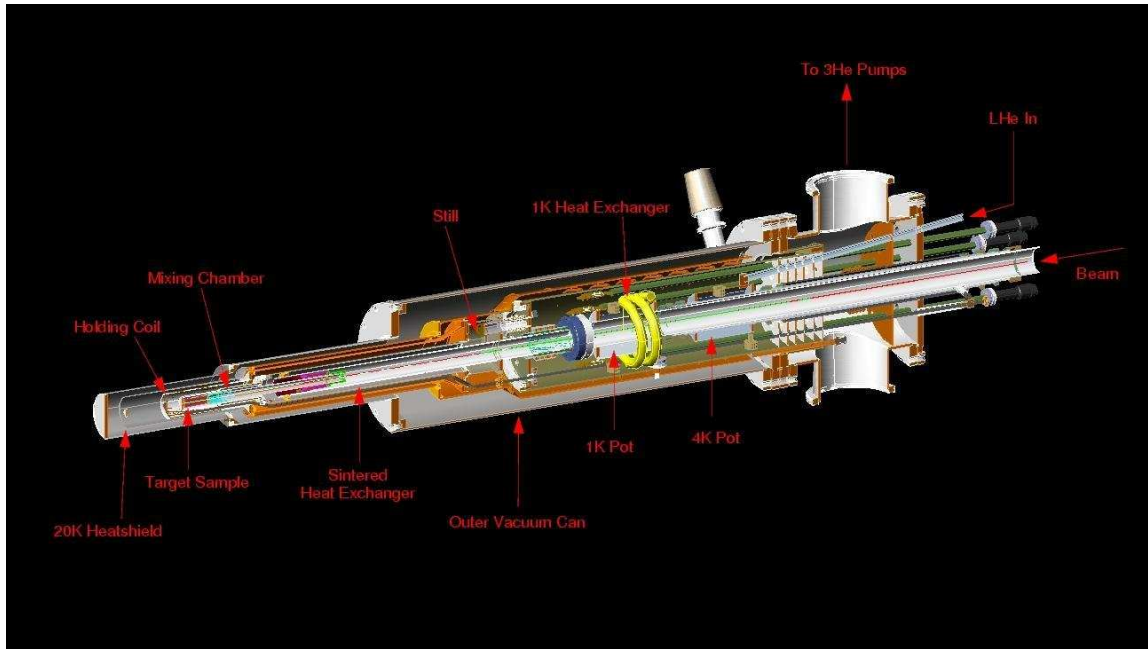
Figure 2.9: The FROST target apparatus. Image Source:[41]

to the direction of the field by adjusting the microwave frequency to be either slightly above or below the ESR frequency.

Prior to the construction of FROST, Hall B used targets with protons and deuterons continuously polarized by DNP throughout the data taking process. The problem was that this polarization method made it impossible to make full use of the CLAS detector. The large polarizing magnet significantly reduced the effective acceptance of the detector and the strong 5 Tesla field results in large deflection for low momentum particles, further reducing useful data. This large polarizing magnet is only used to set in the initial polarization of FROST while no beam is being delivered to the hall. During the actual running of the experiment, FROST's polarization is maintained only by a small holding field of 0.56 T and the refrigeration which "freezes" the spins in place for a long relaxation time. This field and the magnet that generates it are sufficiently small so as to have a negligible effect on the CLAS acceptance.

The process of polarizing FROST begins with insertion of the target cryostat into the
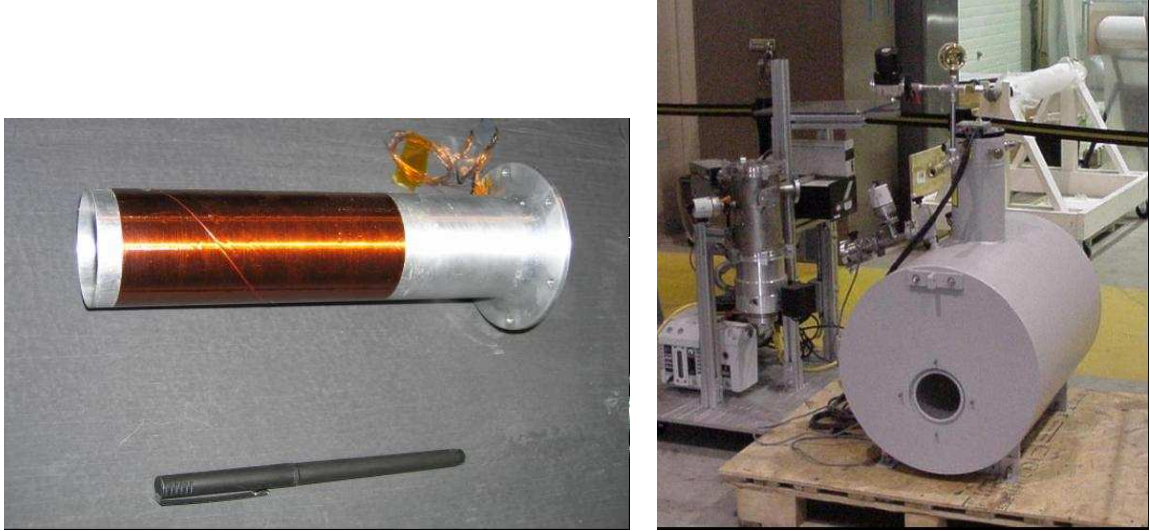
Figure 2.10: The FROST holding magnet and polarizing magnet. Image Source:[41]

horizontal bore of the polarizing magnet and energizing the microwave generator. The target is then polarized via DNP at a temperature of about 0.3 K over a period of a few hours. When the polarization is complete, the microwave generator is turned off and the dilution refrigeration takes roughly 30 – 45 minutes to cool the target below 50 mK. Once the target reaches this "Frozen Spin Mode," the polarizing magnet is ramped down and the superconducting solenoid holding magnet is energized. The polarizing magnet and holding magnet can be seen in Figure 2.10. Finally, the target cryostat is removed from the polarizing magnet and inserted into the center of CLAS, where it is ready to receive polarized photons.

The beam has a warming effect on the target which raises its temperature by approximately 2 mK while running. Under these conditions the polarization decreased by 1 – 1.5% each day. Practically, this meant that the target had to be repolarized at intervals, generally once each week, during the course of the g9a run period. On the analysis end, it means that the target polarization had some small variations over the dataset which should be accounted for when calculating polarization observables.
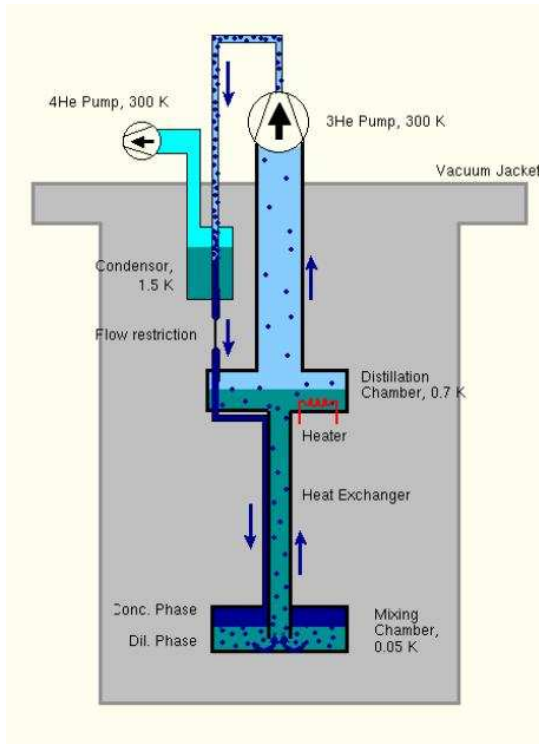
Figure 2.11: Dilution refrigeration cooling process. Image Source:[41]

2.3.2 Dilution Refrigeration

The cooling of the target is done by means of $^3He/^4He$ dilution refrigeration.[41] At temperatures below 0.8 K a mixture of ^3He and ^4He will separate into two phases: a ^3He "concentrated" phase and a ^4He rich "dilute" phase. The specific heat of the dilute phase is higher than that of the concentrated phase, which means ^3He will absorb energy in moving from the concentrated to the dilute phase. FROST takes advantage of this by distilling ^3He from the dilute phase on the bottom of a mixing chamber containing both phases. In order to maintain equilibrium, ^3He in the concentrated phase will replace the missing ^3He in the dilute phase, absorbing heat in the process. The ^3He is then cycled back into the mixing chamber after being condensed in a liquid helium bath at about 1.5 K. This cycle is depicted in Figure 2.11.

The cooling power of this process is highly dependent on the heat exchange between the
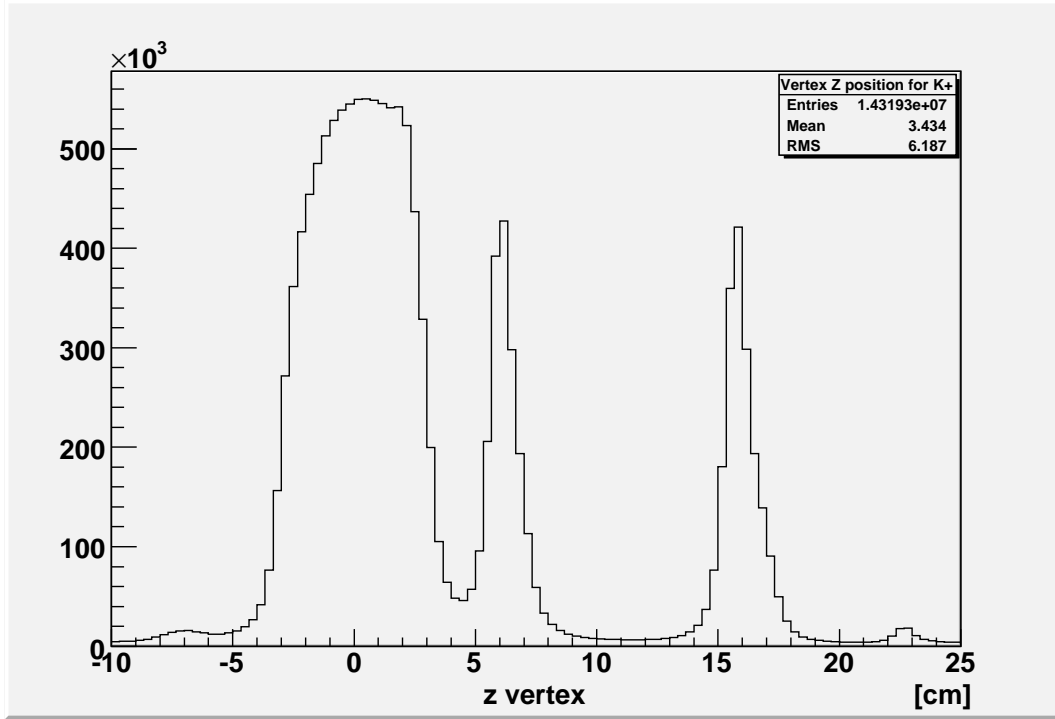
Figure 2.12: Vertex position of K^+ shows peaks for each of the three targets (butanol, carbon, polyethylene) at positions z = -2.5 to 2.5 cm, z = 6.1 cm, and z = 16 cm, respectively.

concentrated and dilute fluid streams. In order to optimize the heat exchange, the surface area between the fluids is maximized using a sintered silver powder. The end result was a target with a base temperature of 28 mK in Hall B with no beam.

2.3.3   FROST and Friends

FROST is a frozen spin target consisting of 5g of butanol (C_4H_9OH) in 1.5 mm beads immersed in liquid helium with a packing factor of 0.62. This material is held in a target cell of dimensions 15 mm by 50 mm. During the g9a run period, this target cell was placed at the center of CLAS between -2.5 cm to +2.5 cm on the z-axis as defined by the origin at the center of CLAS and the direction of the beam.

Although FROST is a frozen spin target, not all of the nuclei in butanol are polarized. Only the covalently bonded protons are polarized during the DNP process, but hadronic

events may be produced from a photon interaction with any nucleon in butanol. In order to extract a true polarization observable, it is necessary to correct for the background coming from unpolarized bound-nucleon reactions. With this purpose in mind, FROST was accompanied throughout g9a by two other targets downstream, a carbon and a polyethylene target. These targets were not intended for the collection of events for analysis. Rather, they exist solely to normalize the background from bound-nucleon reactions in butanol so that it can be accounted for appropriately. The vertex distribution of K^+ is shown in Figure 2.12 to indicate the position of the three targets. The use of the ancillary targets to address background will be discussed further in the next chapter.

2.4   Summary

In this chapter I have described the process of running an experiment to measure polarization observables. I have discussed the production of the incident particle beam, the target in which the physics reactions of interest occur, and the detection of multi-particle final states for the collection of data on and ultimate analysis of these photoproduction events. At the completion of g9a a total of 10.1 billion events had been collected, 3.4 billion of which belong to the circularly polarized photon beam dataset. The $\gamma p \rightarrow K^+\Lambda$ channel represents a small subset of these events. In the following chapter, I will detail the process of event selection to the point where we are left with only those events used in the extraction of polarization observables.

Chapter 3

Event Calibration and Selection

The complete set of g9a data is a vast (several terabyte) collection of information for every triggered event during the run period. In order to analyze all this information, the raw data had first to be "cooked," a process that involves the calibration of data from the various detector systems including the tagger, start counter, TOF, and the drift chambers. Once the calibration and cooking process were complete, the analysis of data could begin. Nonetheless, this usable data was not purely composed of data of interest for my analysis. On the contrary, the $\gamma p \rightarrow K^+ \Lambda$ reaction made up a small portion of a set dominated by more probable reaction channels, which are being analyzed elsewhere. Therefore, it was necessary to determine precisely which events could and should be used in my polarization observable analysis.

In this chapter, I delineate the decision making process that went into the final determination of these events. I will describe my contribution to the calibration process, the construction of the filtered dataset used in my analysis, the particle identification process, corrections made for lost particle energy, and the series of cuts made to remove unwanted events until I arrive at the yield for $\gamma p \rightarrow K^+ \Lambda$ events used in the extraction of polarization observables.

(a) Before calibration (b) Calibrated
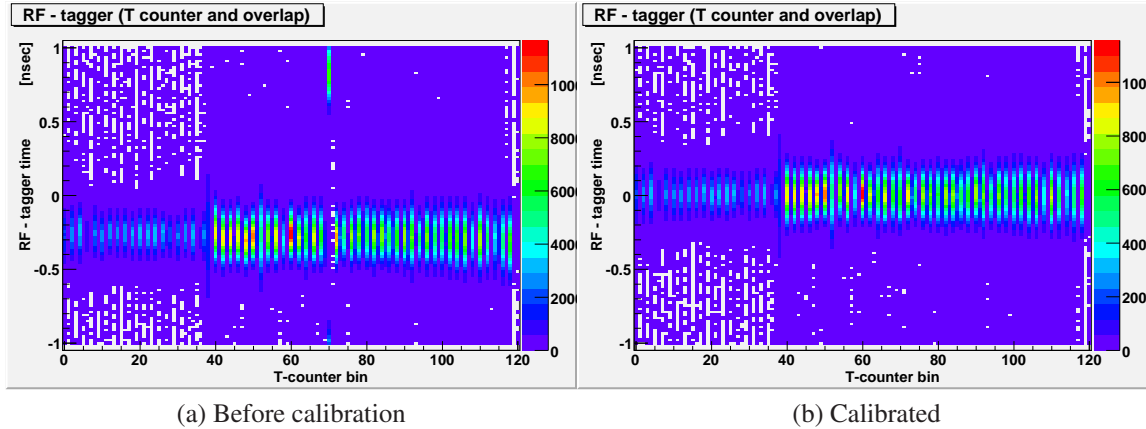
Figure 3.1: RF-Tagger time plotted before and after calibration.

3.1   Tagger Calibration

The primary purpose of tagger calibration is to assign tagger hits to the appropriate accelerator RF bucket, which provides the most precise timing information in the experimental apparatus. This task is accomplished by adjusting a set of constants which will ultimately be used to replace the tagger time with the RF time on an event by event basis. Most significantly, the set of "Ci" constants are used to account for the phase difference in the tagger and RF time. Before the phase difference correction, the correct peak position must be found by balancing the left and right TDCs for each T-counter and TDC slopes must be correctly calibrated to avoid a dependence on hit position in the T-counter. There are 122 constants for the slopes and peak positions (one for each TDC). For the phase correction, there are 121 Ci constants - one for each of the 61 T-counters and 60 for the overlap T-bins associated with hits in adjacent T-counters. When the Ci calibration is good, each T-bin will show a good alignment between the tagger time and the RF time. The peak of the phase shift should be at zero, while the timing resolution of the T-counters will be reflected in the variance of the distribution. Figure 3.1 shows the Tagger time - RF time plots before and after Ci calibration for an example g9a run.

This calibration eliminates the timing phase shift, but the timing may still be off by a

multiple of 2.004 ns if the time offsets for a counter move it to the wrong beam bucket. The CLAS start counter is used as a reference detector to determine if any counters have been assigned to the incorrect RF bucket. After a pass of "cooking" (the process of converting raw signals into tracking and kinematic information) data, the ST - Tag histograms, which use the start counter and tagger time, are examined to find any misaligned counters. The timing for these counters had to be corrected to align the tagger time with the correct RF time. A more complete description of the tagger calibration process can be found in the CLAS-Notes on the subject.[42, 43]

3.2   Event Filter

The total g9a dataset for circularly polarized photons consisted of 3.4 billion particle events, only a small subset of which could even be candidates for our $K^+\Lambda$ yield. My analysis code would require a great amount of time to run over such a large dataset and this issue would be made worse if it were necessary to maintain a connection to JLab while running the code. Therefore, a set of much smaller "skimmed" data files of potentially interesting K^+ events was created to make local storage at Catholic University feasible and reduce the running time of the analysis code.

The data for each event are stored in banks of information on each particle or for specific detector systems. The physics data for particles are stored in three different banks (EVNT, PART, GPID), each of which operate on a different particle identification scheme. The filtering code uses its own identification scheme (based on the EVNT scheme), but it must work with the physics data for each particle stored in one of these banks.

The filtering code begins with the removal of certain particles from consideration before the identification process begins. Any particle that does not correspond to a DC (drift chamber) track is removed, as our identification method depends on momentum informa-

tion from the DC. Further, any particle with $\beta < 0.2$ is skipped over as are particles with momenta $p < 0.1$ GeV or $p > 2.2$ GeV. While the filter does not automatically remove events containing such particles, they are not considered to be useful kaon, proton, or pion candidates, so they are not classified by particle type.

The K^+ were identified by charge and by the correlation of their beta and their momentum (as given in the EVNT data bank), according to the relation

$$\beta = \frac{pc}{E} = \frac{p}{\sqrt{p^2 + m^2 c^2}} \, .\tag{3.1}$$

The beta assigned to a particle is based on timing information of limited precision. This leads to detection of particles with $\beta > 1$ and requires that for each particle type we take a mass range that is significantly wider than the experimentally determined uncertainty in the particle's mass. For the purposes of the event filter, since it was prudent to err on the side of caution early in the analysis, a fairly wide mass range was accepted for K^+. All positively charged particles with beta as a function of momentum in the range $\beta_{min} < \beta < \beta_{max}$, where $\beta_{min} = p/\sqrt{p^2 + (0.65\text{GeV})^2} - 0.05$ and $\beta_{max} = p/\sqrt{p^2 + (0.35\text{GeV})^2} + 0.05$, were identified as K^+. The additional constant of 0.05 is an offset designed to adjust for the narrowing range in the high momentum region where differences in mass are less significant. K^+ identification also has a minimum momentum requirement of 0.2 GeV.

The code is also used to identify protons and negatively charged pions. While the major requirement of the filter is that an event has one K^+, it also cuts out events with excessive protons and π^-. Any event with greater than two of either particle type is cut from our dataset. A particle is identified as a proton or π^- in the same manner as for K^+, with different beta cuts and a minimum momentum of 0.25 GeV for protons. No minimum momentum is set for pions. The beta ranges are as follows:

$$\beta_{max}^{(p)} = p/\sqrt{p^2 + (0.7\text{GeV})^2} - 0.05,$$
$$\beta_{min}^{(p)} = p/\sqrt{p^2 + (1.05\text{GeV})^2} + 0.05,$$

$$\beta_{max}^{(\pi)} = p/\sqrt{p^2 + (0.25\text{GeV})^2} - 0.05 \text{ and}$$

$$\beta_{min}^{(\pi)} = p/\sqrt{p^2 + (0.05\text{GeV})^2} + 0.05.$$

There were undoubtedly many events without true kaons allowed through this filter. However, the inclusion of misidentified particles was unimportant in this preliminary stage. Rather it was essential that no K^+ event was removed (save perhaps a few with pathologically poor information), while making sure the size of the data to be analyzed would still be substantially reduced. This was accomplished, as the total number of events in our skimmed dataset was approximately 93 million or less than 3% of the original dataset.

3.3 General Cuts

Even before tracks are identified as specific particles, a few general cuts are made in my analysis code to remove from consideration particles that, independent of their classification, do not meet necessary criteria for inclusion in an event. It was first required that for any particle track there should be only one photon identified as the coincident photon for that track. All particles, regardless of their type, should fall within a reasonable coincidence window of their respective beam photons. Therefore, any particle that falls outside the range of $\pm 1ns$ of the photon time associated with it is removed from the analysis. Additionally, during the course of the g9a analysis, Hideko Iwamoto discovered that the count rate for certain scintillator paddles in the TOF system was too high.[44] Particles that ended their journey through CLAS at these paddles were also removed from the analysis.

In each case, the full event is not automatically removed from consideration, because my code continues to loop over each particle in the event, applying the same criteria to each one and those that meet the necessary conditions move on to the particle identification process. In principle, an event could still contain a K^+ and a proton in addition to the particle which is not considered. The removed particles may not even belong to the same

reaction process, because they could be produced from a different photon in the same beam bucket or a different beam bucket within the same trigger coincidence window, so it is entirely possible to identify a true $K^+\Lambda$ from missing mass without any reliance on them. The purpose of these cuts is simply to avoid using these problem particles directly in the analysis should they be identified as either a K^+ or a proton.

3.4   Particle Identification

Once the truncated dataset was constructed and in place, the analysis proper was begun in earnest. The first step was to identify all particles of interest within each event. Initially, this was done in the same manner as the filter for the skim files by cutting on beta and momentum information taken from the EVNT bank, similarly to the skimming process, only with tighter cuts for each particle type. Later, the EVNT bank proved to be a problem for the analysis when it was discovered that the φ distribution of protons and K^+ from the same events was inconsistent with $K^+\Lambda$ events.

Ultimately, the GPID bank was chosen to provide the crucial physics data on each particle and the GPID particle identification scheme was employed to assign particle types. GPID identifies charged particles by making attempts for each of the following particle types: pion, kaon, proton, deuteron, and triton. Charge is used to distinguish the first three types from their antiparticles, while a check is simply made to ensure deuterons and tritons are positively charged. If the particle is negatively charged, no attempt is made to classify it as a deuteron or triton or any analogue thereof. For each attempt, a comparison is made between an expected beta for the particle type (given by equation (3.1)) and the beta obtained by using the time-of-flight measurement from the Start Counter to the TOF scintillators and the momentum reconstructed in the DC. Since pions are the first particle attempted they essentially are the default particle classification. Only if the difference between the

expected beta and the measured beta is greater than 1 (requires serious error in timing) is a particle rejected as a pion candidate. As successive particle classification attempts are made, the condition for reclassification of the particle becomes that the difference between the measured beta and the idealized beta for the particle type in question is less than that of the previous particle classification. Ultimately, the particle will be identified as the type for which the expected beta is closest to the measured beta.

After this initial particle identification, the GPID identification scheme makes an additional check for particles identified as K^+ or K^-. The best photon for particle coincidence is determined by taking the time it takes a photon to reach the z-coordinate vertex position of the particle and choosing the photon with the closest time to the start counter time. A beta is then formed using the TOF and the time the photon reaches the particle vertex. This is compared to some predetermined offsets to decide whether the prospective kaon is actually a pion or proton. This additional step in the particle identification is intended to separate out misidentified particles at high momentum.

At the end of a loop over all particles in an event, a decision is made based on the particle content of the event to proceed with analysis on the basis of missing mass. At first only events with a proton and a K^+ identified were kept. Later, the scope of allowed events was broadened to include events where only the K^+ is identified. However, the use of these events is limited to certain regions on account of the strong background present when no cut can be made for the missing π^- mass.

3.5 Energy Loss

After particle identification, the next step is to increase the accuracy of invariant and missing mass plots by correcting for the energy lost by detected particles as they move through the target material and walls, the beam pipe, start counter and the air gap between the target
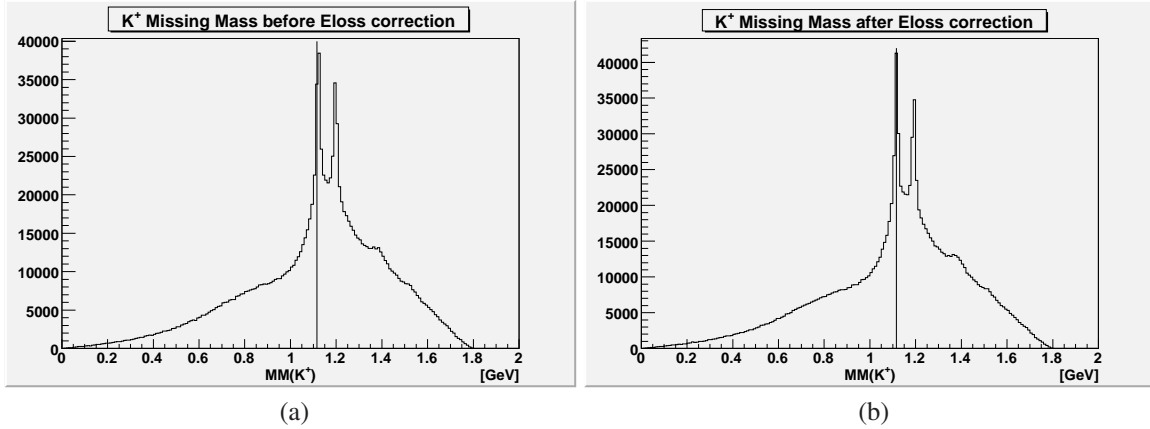
Figure 3.2: Effect of the energy loss correction on the K^+ missing mass. A stronger Λ signal in the correct mass bin (indicated by vertical line) is seen after the correction.

and the region 1 drift chambers. In order to accomplish this the ELOSS package created by Eugene Pasyuk and modified for g9a by Brian Morrison was utilized.

The energy loss corrections are applied differently in my analysis for kaons and protons, but in both cases the correction is made before any use of missing mass. Immediately upon identification of a particle as K^+ the detected momentum, particle vertex and kaon mass are used as input for the ELOSS routine and a new 4-momentum is output - one which is corrected for the kaon's loss of energy before the track providing momentum information was produced. On the other hand, the vertex stored for the proton is inaccurate because it is based on propagating the track back to the beamline. Since the proton is actually coming from a Λ decay (at least for all desired events), the real vertex must be calculated using its intersection with the Λ path, which is constructed by taking the opposite of the K^+ vector in the center of momentum frame. In practice, as a reasonable point of intersection may not exist, this means taking the point of closest approach between the proton and Λ paths as the proton vertex. Thus, the proton energy loss correction can only be made once a full pK^+ event has been identified.

The result of the ELOSS correction on the position of the Λ signal is shown in Figure 3.2. Without the energy loss correction, the Λ signal is close to the true mass, but clearly

not centered in the correct bin. After using ELOSS, the bin covering the true Λ mass is also the peak bin, meaning the energy loss correction has adjusted the missing mass for the Λ signal to the correct position to within the bin resolution of 10 MeV.

3.6   Missing Mass Technique

Once my analysis code has looped over the particle tracks in an event, identifying all K^+ and protons, I have a full reaction event to analyze. During the particle identification loop, I store 4-momentum vectors, vertex vectors (vectors holding the coordinate positions at which each particle was produced, where the center of CLAS is the origin), and the beta for each of the particles. In the next stage, I use the particle content of the event to decide on whether to proceed with analysis of said event. Then I can use my knowledge of the tagged photon energy together with my assumption of a target proton at rest to construct a center of mass frame and an associated invariant mass. The invariant mass coming from the sum of the photon and initial proton vectors is conserved. The invariant mass is obtained in the following way:

$$M(\gamma p) = M[(E_\gamma + M_p, 0, 0, E_\gamma)] = \sqrt{(E_\gamma + M_p)^2 - E_\gamma^2} \, , \qquad (3.2)$$

where the four vectors are given in (E, p_x, p_y, p_z) format and $p_x = p_y = 0$, because the beamline defines the z-axis. The last step of this process used the relation $M = \sqrt{E^2 - p^2}$, which is the general way to find the invariant mass from any momentum four-vector, whether it be for a single particle or the vector sum of multiple particle momentum vectors. The invariant mass of the difference between the initial momentum four-vector and the sum of detected final state particle four-vectors is known as the missing mass. The missing mass

for photoproduction on a stationary proton target is

$$M(X) = M[(E_\gamma + M_p, 0, 0, E_\gamma) - p_4(Y)] \,, \tag{3.3}$$

where X stands for the undetected particle and $p_4(Y)$ is the momentum four-vector of Y, where Y can be a single detected particle or a group of detected particles. If Y is a group of particles, then $p_4(Y)$ can also be used to calculate the invariant mass of those particles.

In the case of a detected K^+ from $\gamma p \to K^+ \Lambda$, the missing mass of the K^+ should be equal to the mass of the Λ or, equivalently, the invariant mass of the proton and π^- momentum vector sum. Alternatively, the invariant mass of the proton and K^+ will leave a missing mass that should be equal to the pion mass. In the first case, equation (3.3) can be used with $p_4(Y) = p_4(K^+)$, while in the latter case $p_4(Y) = p_4(K^+) + p_4(p)$.

It should be noted that even for true events of interest, there will be some spread in the missing mass beyond the known uncertainty of the particle mass. This spread is the result of the limitations of detector resolution in timing, path length, and photon energy determination. The spread caused by these uncertainties is generally expected to follow a Gaussian distribution.

In the following sections I will use the missing mass technique to identify the Λ in the missing mass spectrum of the K^+. I will do this both for events with a proton detected in addition to the K^+ and those in which only the K^+ has been identified. All events with more than 2 positive particles or more than one K^+ are removed before any kinematic analysis is performed. I will explain the multiple cuts I made to remove background events and show successive plots of the missing mass to indicate the effect of these cuts. I will end by making use of the Gaussian distribution of a particle signal to obtain my final analysis yield.

3.6.1   Cuts for pK$^+$

The first cut I make after particle identification is an additional cut on the beta vs. momentum for the kaon. This helps reduce the number of pions that are misidentified as a kaon. In Figure 3.3, I plot out the beta against the momentum of identified kaons prior to making my cut. The cut uses the momentum prior to energy loss correction so that the assumption of kaon mass in the energy loss procedure does not corrupt the results. The dashed lines in the plot show the limits of the cut, which are $\beta^{K^+}_{min} = p/\sqrt{p^2 + (0.55\text{GeV})^2} - 0.03$ and $\beta^{K^+}_{max} = p/\sqrt{p^2 + (0.44\text{GeV})^2} + 0.03$, while the solid line shows the expected kaon curve. Everything outside the regions between the red lines is cut out from my analysis. Figure 3.4 shows the effect of the beta cut on the missing mass spectrum of K^+, while Figure 3.5 shows how the distribution varies with the kaon's angular distribution in the center of mass frame. There are pronounced peaks for both the $K^+\Lambda$ and $K^+\Sigma^0$ decay channels. The cut reduces background while leaving the magnitude of the lambda peak mostly intact. Clearly the background is dominant at backwards angles in the center of mass frame at this stage. The Λ and Σ^0 peaks cannot be seen in the most backwards angular bin and scarcely become visible in the adjacent bin. Even with significant background contamination, the signals are strong in all forward angle regions.

It is also important to make sure the particle event we are analyzing originated in the target of interest (the polarized butanol target). While protons from genuine $K^+\Lambda$ events in FROST may reasonably be expected to have vertex points lying outside the target region due to the Λ hyperon's nonnegligible decay time, all kaon tracks associated with polarized proton photoproduction must have a vertex within the target region. Therefore, the next cut is made around the position of the butanol target. Figure 3.6 shows the vertex distribution of kaons on the z-axis (along the beamline) before the cut. Vertical lines indicate the region of accepted events after the cut is made, those that fall within the range -2.5 cm $< z <$ 2.5 cm.
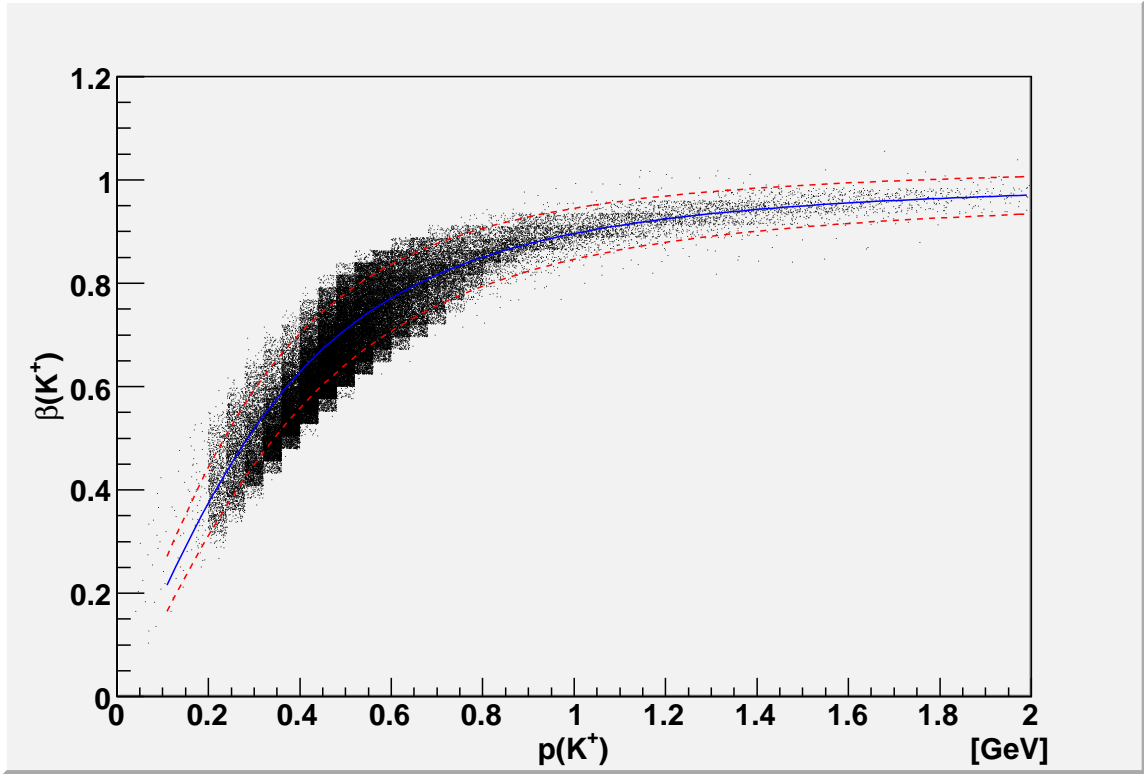
Figure 3.3: β(K⁺) vs. p(K⁺) (in GeV) plotted before energy loss correction to momentum. Only events between the dashed lines are kept after the cut on β(K⁺).

(a) Uncut Missing Mass of K^+ (in GeV)

(b) Missing Mass (in GeV) after β cut
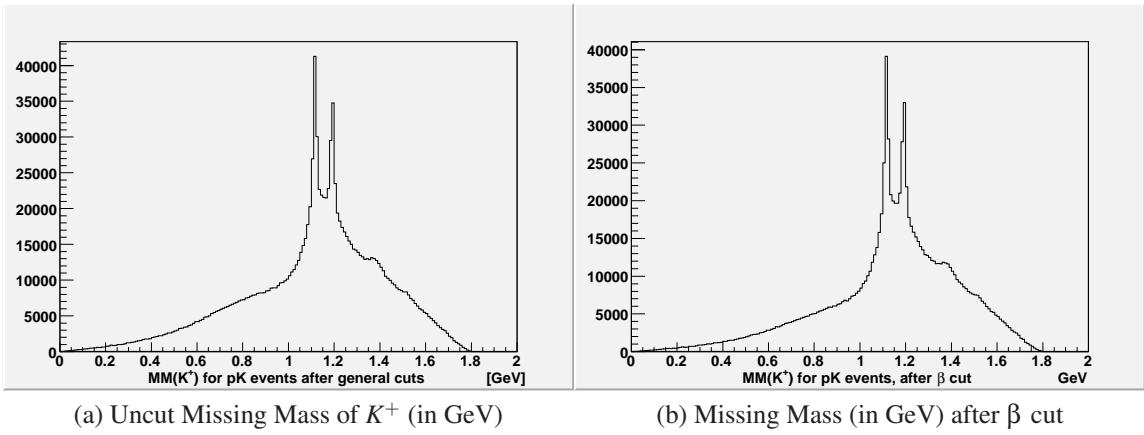
Figure 3.4: The effect of $\beta(K^+)$ cut
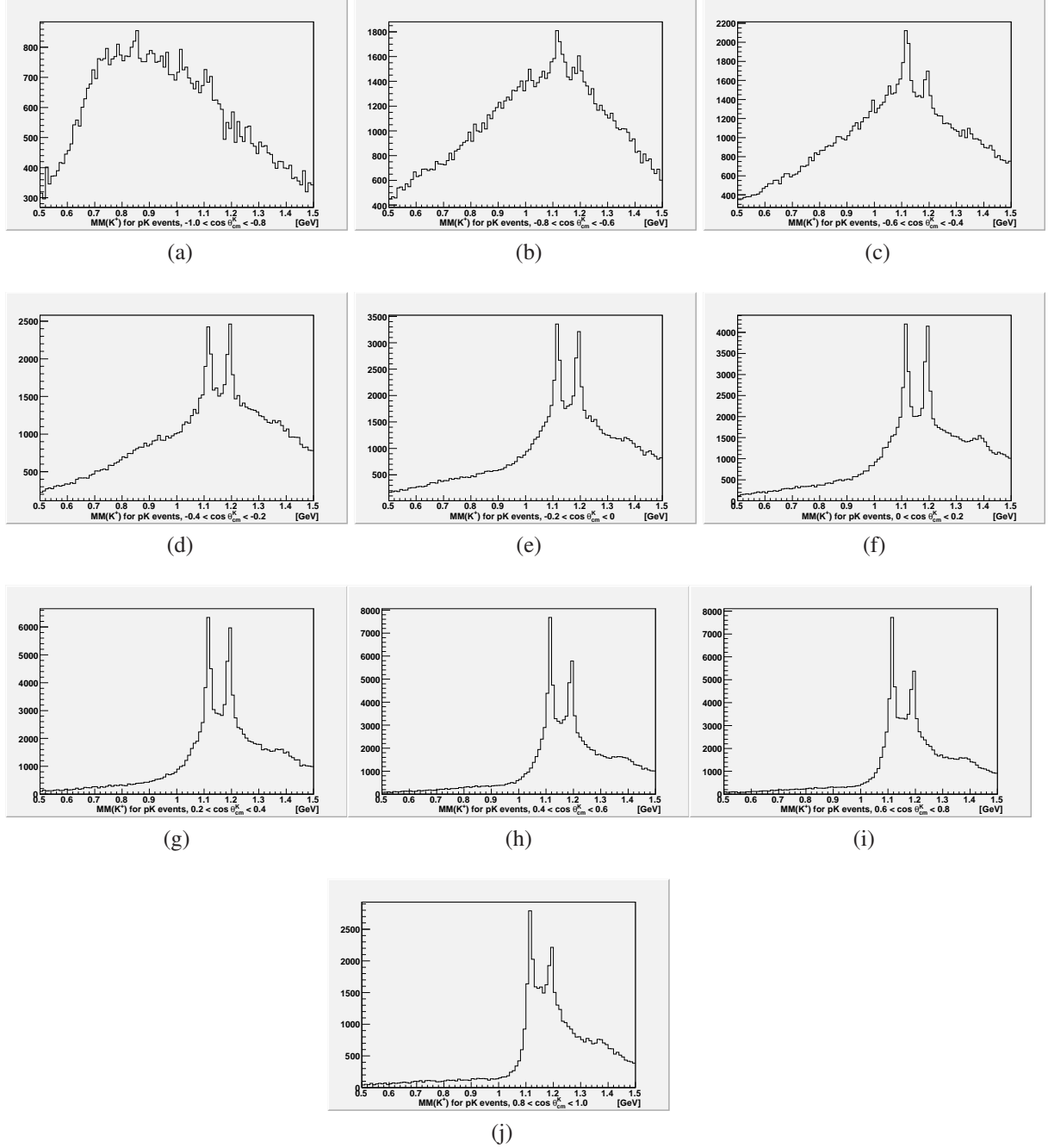
Figure 3.5: Missing Mass plots for the 10 angular regions after β cut on pK events.
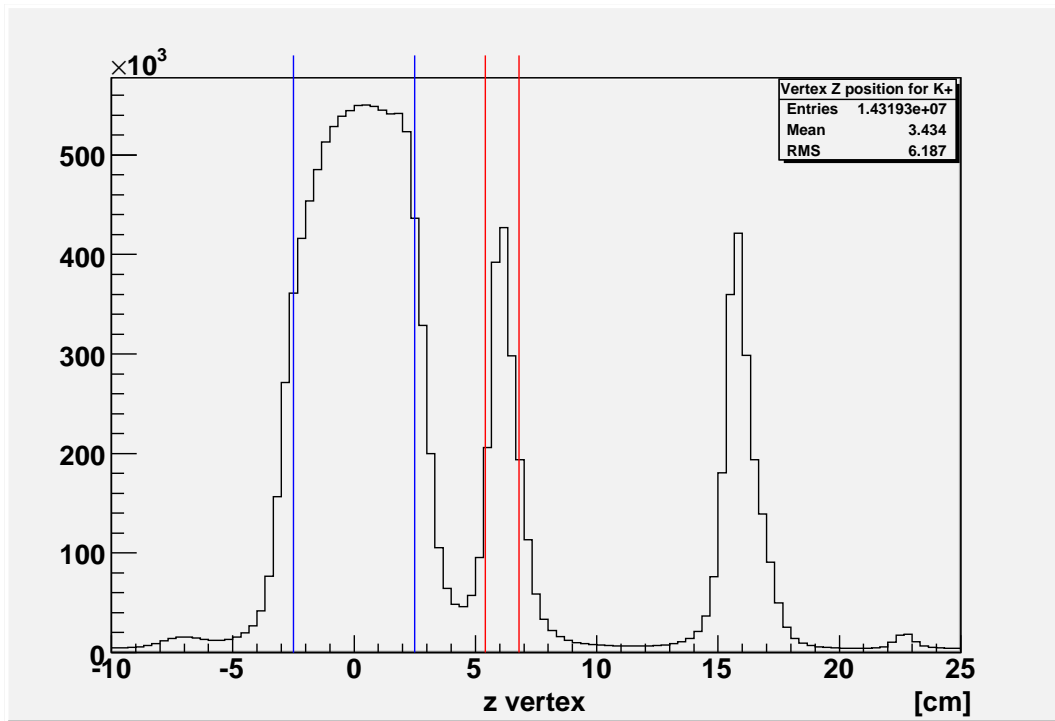
Figure 3.6: Vertex position along beamline (z-axis) for identified K$^+$. Cuts are shown for butanol (left) and carbon (center). The third peak is from the polyethylene target, which is not used in this analysis.

Kaons that fall within the range 5.4 cm $< z <$ 6.8 cm come from the downstream carbon target. These are removed from the set of events used in the extraction of polarization observables, but are not tossed out of the analysis altogether. Particle events originating in the carbon target are used to understand background from bound-nucleon reactions in the butanol target. The events of interest come from the quasi-free polarized protons in butanol. The carbon serves as a comparison target with only bound nucleons, so scaling carbon events in the unphysical region to butanol events in the same region allows us to have a good estimate of the background in the Λ signal region. This region is called unphysical, because it indicates that the assumed target energy used in the calculation of the missing mass must be incorrect. The target energy can be significantly off from the proton rest mass because of the Fermi motion of bound nucleons. If we take the ratio of bound-nucleon reactions in butanol to carbon to be fairly consistent over the whole analyzed range, than applying the scaling factor from the unphysical region to the carbon events in the Λ signal region will give a good estimate of the background from bound-nucleon reactions among the reconstructed Λ particles. This topic will be revisited after I come to the results of the final cuts on the missing mass spectrum.

The effect of the target vertex cut on the missing mass can be seen in Figures 3.7 and 3.8. It should perhaps come as little surprise that each region looks fairly similar after the cut. After all, this cut only served to separate the butanol events from those associated with the other two targets. Thus, the total distribution shows almost proportional fall off in background and signal strength. Nonetheless, some improvement is evident. While the backwards direction still has significant background contamination, the Λ and Σ^0 peaks dominate the forward angle bins and are clearly visible in all but the $-1.0 < \cos\theta_{CM} < -0.8$ angular bin. The overall reduction in the Λ peak is of no concern as the removed bound-nucleon reactions of the ancillary targets are not those of interest for this analysis.

After the butanol vertex cut one more cut remains to be performed. By plotting the
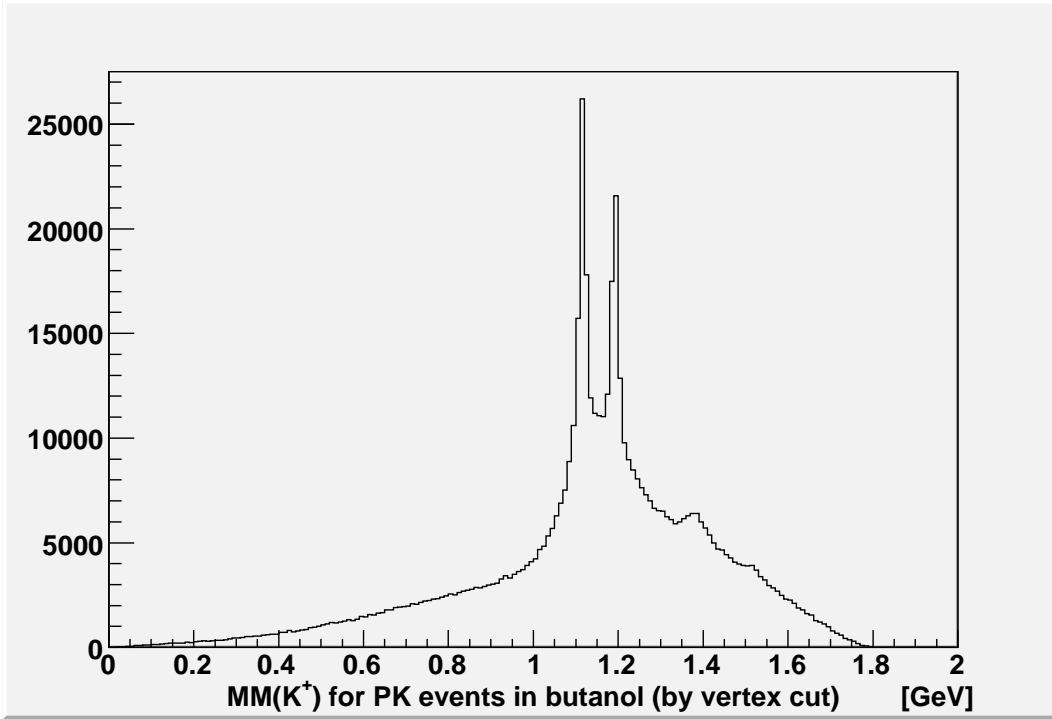
Figure 3.7: Missing Mass distribution over all angular regions after the vertex cut around butanol target

missing mass off the proton and kaon system we can identify a missing π^- as the final product of the reaction channel. Figure 3.9 shows the missing mass, in which a visible pion peak exists, as well as a secondary peak due to background from $K^+\Sigma^0$ events. A fairly wide cut of ± 50 MeV will cut out most of the Σ^0 signal and other background, while leaving a strong Λ signal. These results of the final cut on pK^+ detected events are given in Figure 3.10 and in Figure 3.11 for the angular dependence. After the cut around the pion mass a Λ signal and a Σ^0 signal sit on top of negligible background events. Nevertheless, there is still background to contend with from real $K^+\Lambda$ events of bound nucleons. This is apparent in the similarly shaped missing mass spectrum that remains when all the same cuts (with the appropriate change in vertex cut, obviously) are applied for the carbon target as seen in Figure 3.12. This background needs to be subtracted before we can get to the work of correcting for overlap with the Σ^0 signal.

(a) (b) (c)

(d) (e) (f)

(g) (h) (i)

(j)
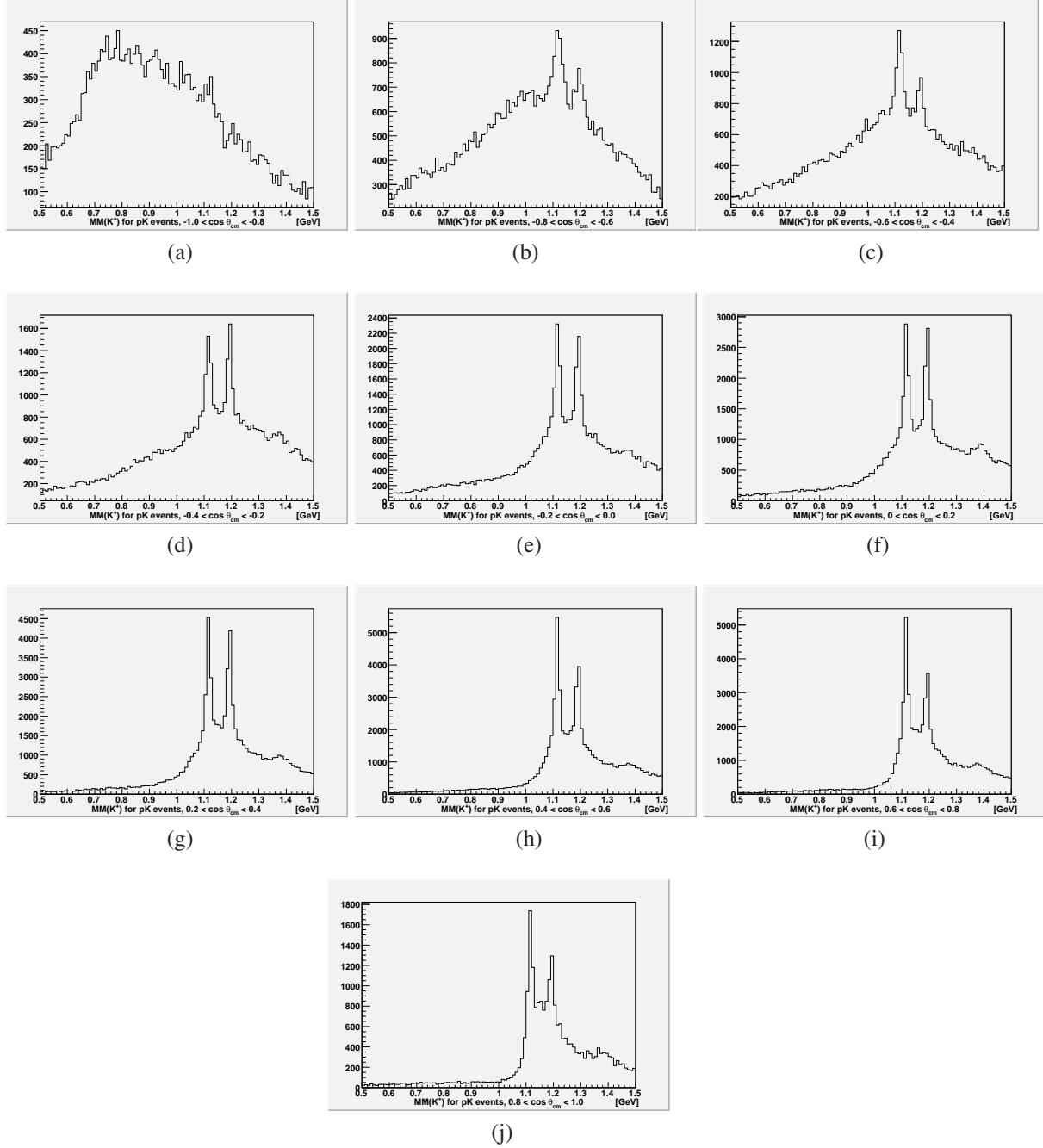
Figure 3.8: Missing Mass plots for Butanol after vertex cut
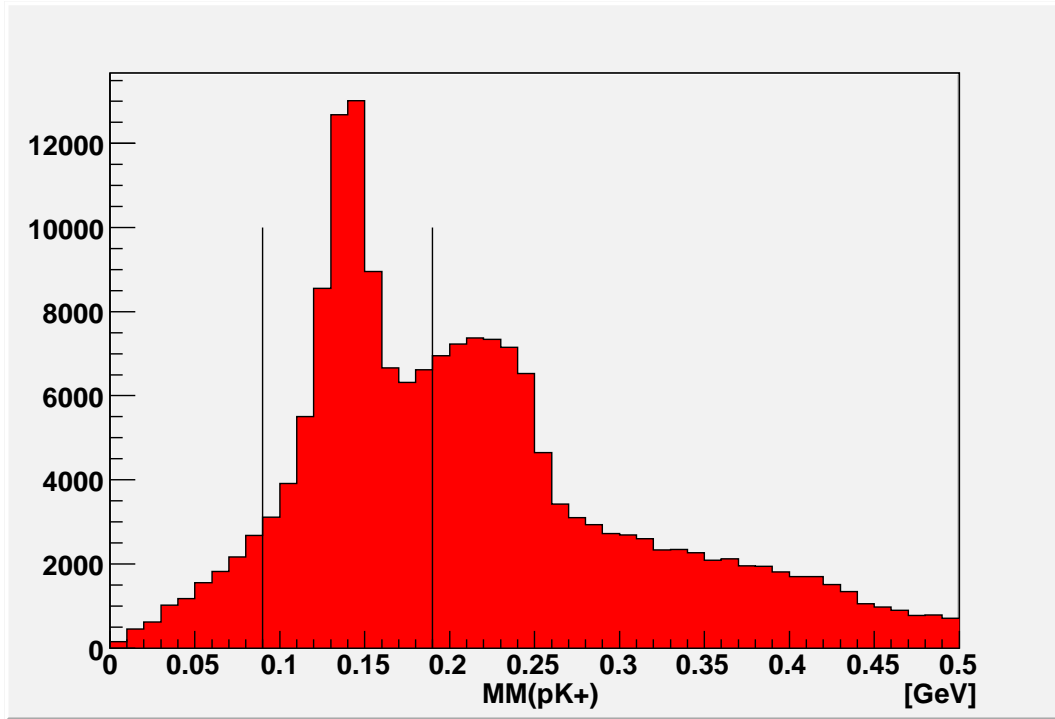
Figure 3.9: Missing Mass off pK^+ with lines indicating the cut around π^-
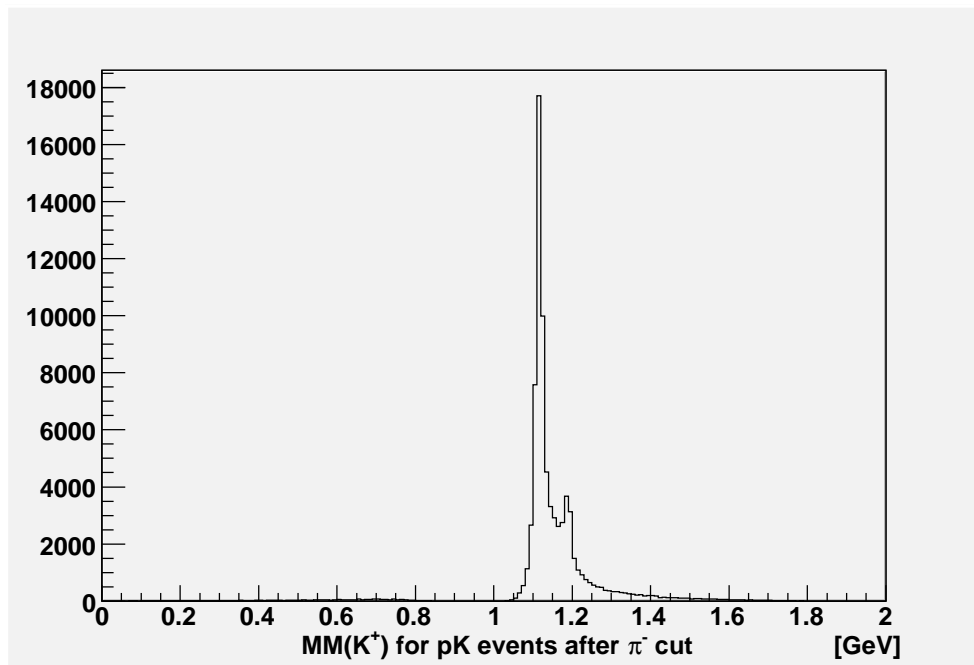
Figure 3.10: Total Missing Mass distribution over all angular regions after the cut around the π^- mass is applied to $MM(pK^+)$.

(a)

(b)

(c)

(d)

(e)

(f)

(g)

(h)

(i)

(j)
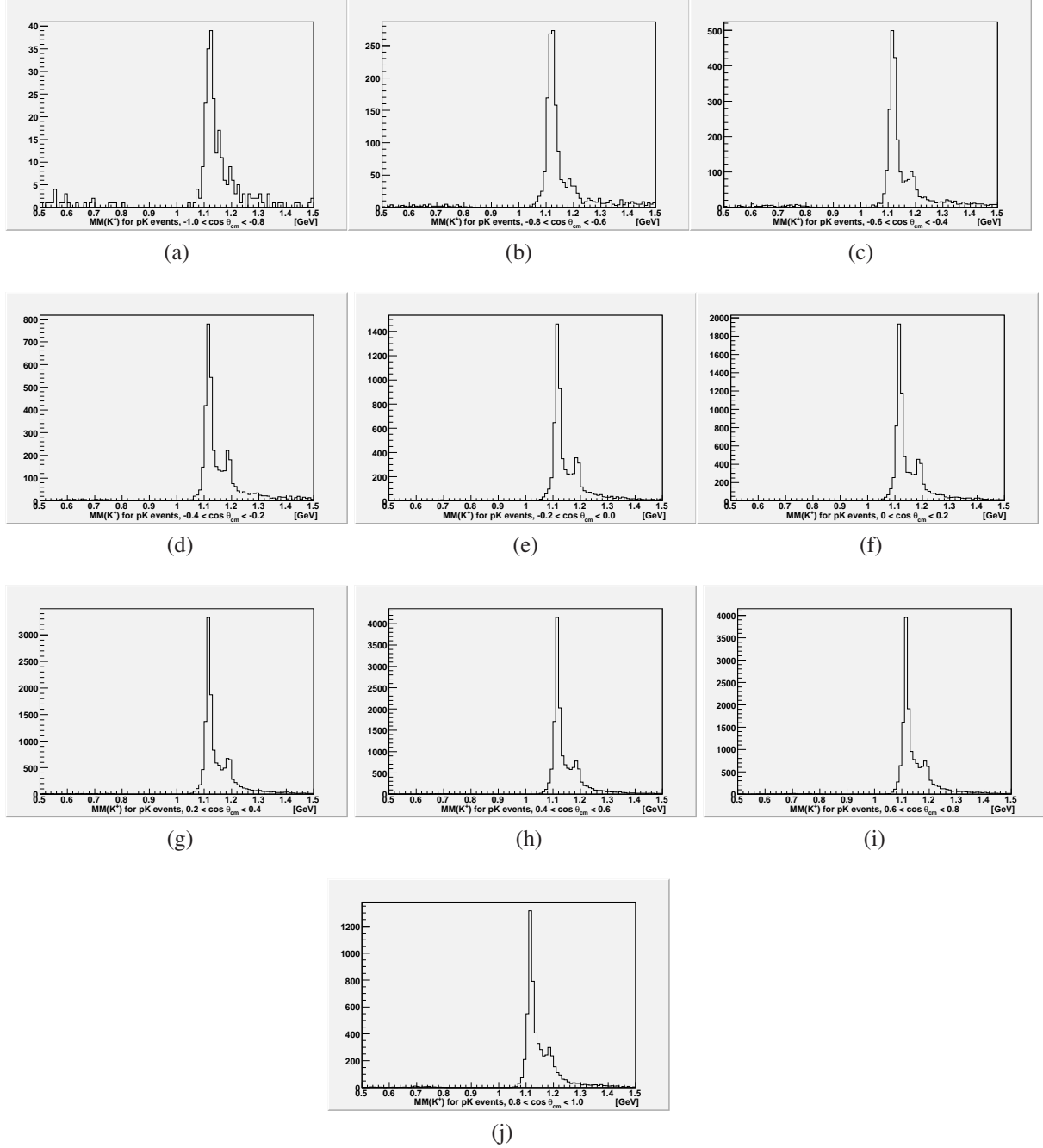
Figure 3.11: Missing Mass plots for 10 angular regions after cut on π^- mass.
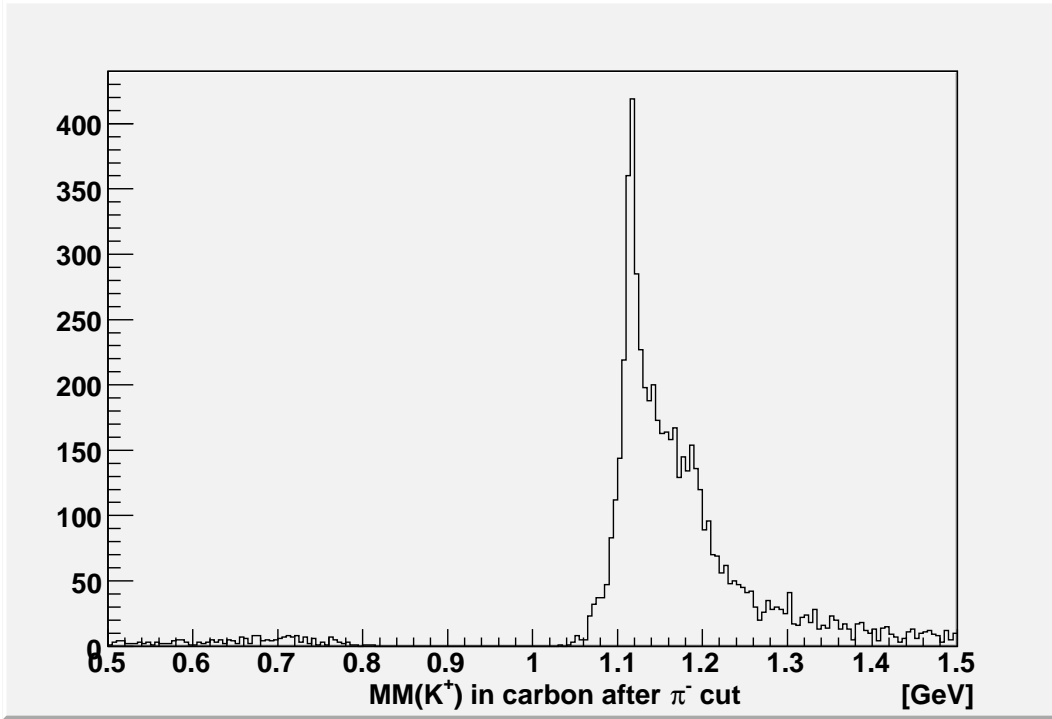
Figure 3.12: Missing Mass of K^+ for the carbon target after cutting on the π^- mass.

Since these cuts leave virtually no events in the unphysical region, they must be relaxed temporarily in order to find a scaling factor for the carbon events. The carbon and butanol distributions are both plotted without the pion cut as seen in Figure 3.14. The distribution for carbon matches the butanol fairly well, so it is not too difficult to find a scaling factor for the bound-nucleon reactions taken from carbon. There is some variation based on the missing mass point chosen for scaling, so rather than picking an arbitrary point it is convenient to plot the ratio of butanol to carbon yield over the entire missing mass distribution as in Figure 3.13. The increase of scaling in the Λ region is a comforting sight, for if the scaled carbon yield were equal to or greater than the butanol yield, we would be left to conclude that there are no polarized proton reactions or, more reasonably, that the scaling method is fundamentally flawed. A constant scaling factor must be extracted from this volatile ratio, so a constant polynomial fit is performed in the range of 0.5 to 1.0 GeV as seen in the figure. The mean value taken from this fit is used as the scaling factor.
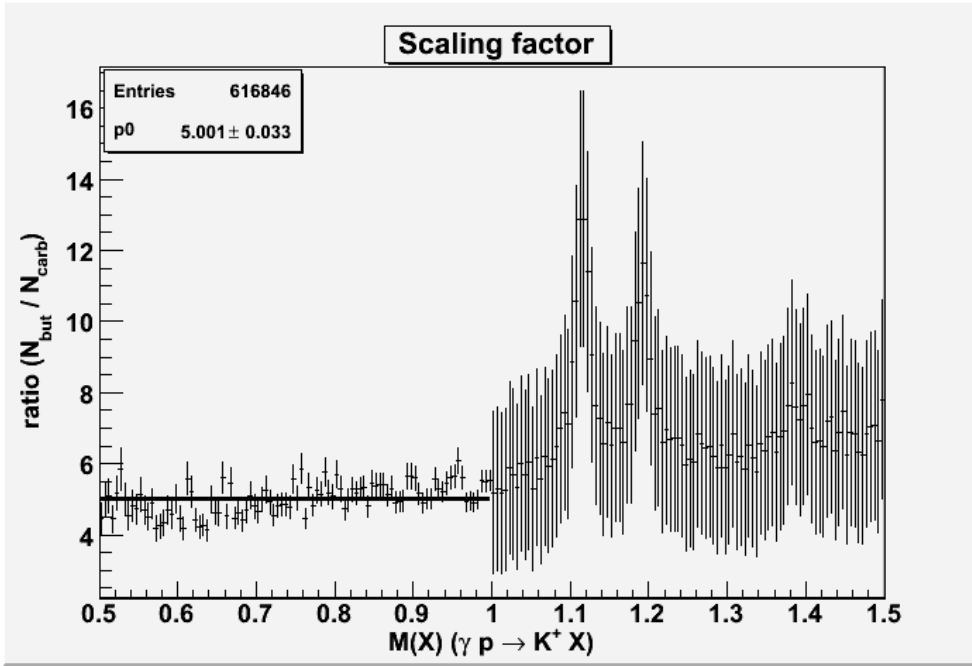
Figure 3.13: Scaling of carbon yield to butanol. The scaling factor is obtained by applying a constant fit over the yield ratio in the "unphysical" region up to 1.0 GeV

The scaling factor need not be uniform over the whole kinematic range. Indeed, there is an angular dependence to the scaling, which will be explore further in Section 3.7. For now I will apply the scaling factor that comes from analysis of the total missing mass distribution. After applying a scaling factor of 5.0 to the carbon events, this number of events is removed from the butanol missing mass plot to give the distribution shown in Figure 3.15. The cut on the pion mass is then reapplied for yield extraction, but first a fit is performed with the Σ^0 signal intact.

In order to extract the yield, it is necessary to determine the range within which we are accepting events as $K^+\Lambda$ events. This is done with full knowledge that both events of interest and events from bound-nucleon reactions will be included in the region. This background will be adjusted for by means of a dilution factor, since it cannot be directly cut from the analysis. In order to decide upon a range, I performed a double gaussian fit to model the spread of the Λ and Σ^0 peaks. The fit gives values for the mean and standard

(a) Butanol $MM(K^+)$ distribution

(b) Carbon $MM(K^+)$ distribution.
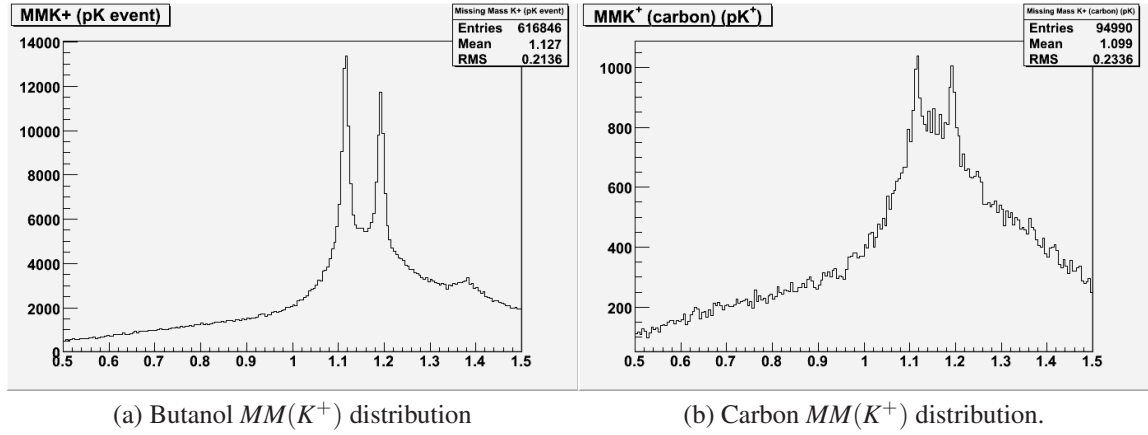
Figure 3.14: Butanol and Carbon Missing mass plots showing tails below Λ threshold. These tails can be used to scale carbon events to butanol to estimate the number of bound-nucleon reactions.
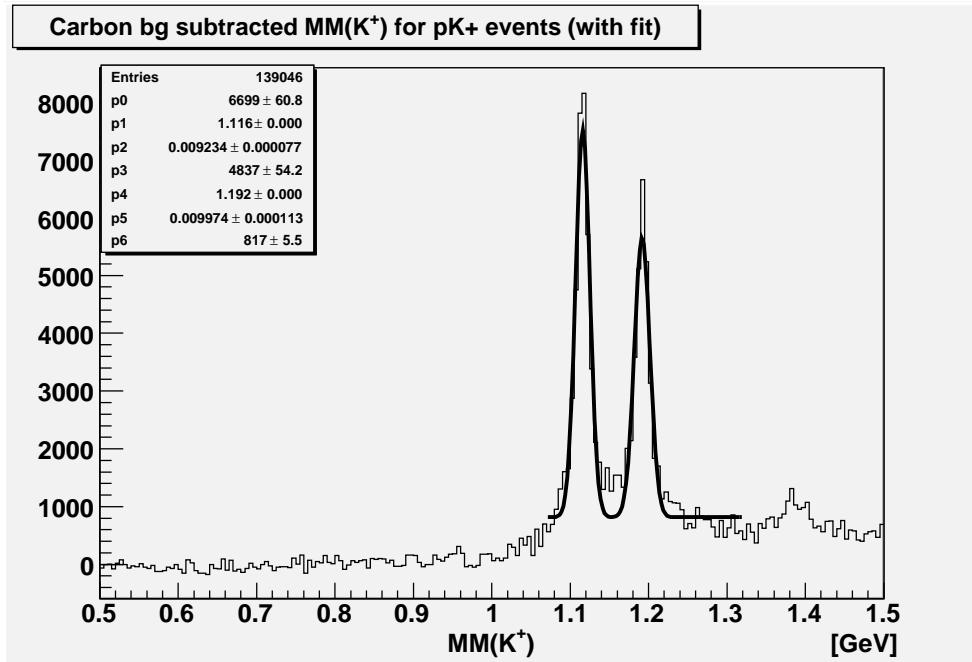
Figure 3.15: Missing Mass of K^+ for Butanol with scaled Carbon events subtracted. Λ and Σ^0 peaks are fitted with a double gaussian.

deviation of each peak. The values for the Λ signal are a mean of approximately 1116 MeV with a standard deviation of roughly 9.23 MeV, while Σ^0 has a mean of 1192 MeV with a standard deviation of 9.97 MeV. By taking a range of $\pm 3\sigma(\Lambda)$, or from 1088 MeV to 1144 MeV, I find that my yield will be free of Σ^0 interference at a level that would be significant on the scale of the precision allowed by this experiment, as the upper limit of the range lies over $4\sigma(\Sigma^0)$ away from the Σ^0 peak. The yield obtained from this range is 44,199 events with a scaled carbon yield of 12,055 events.

The signal comes out nice and clean when all the above requirements are met and the scaled carbon is used to find an effective dilution factor. The dilution factor is given by

$$D_{eff} = \frac{1}{1 - \frac{Y_{scale}}{Y_{but}}} \, , \tag{3.4}$$

where Y_{scale} is the scaled carbon yield and Y_{but} is the yield for butanol. When the yields extracted from the procedure above are entered into equation (3.4), the effective dilution factor is found to be 1.38. This is the dilution factor that must be used in the calculation of all polarization observables, with the limited exception of E. Those asymmetries involving the polarization of the recoil hyperon require the detection of a Λ decay product; for E though it is possible to use events for which only the kaon has been detected. In the next section, I will delineate the process of selecting $K^+\Lambda$ events from events with no detected proton.

3.6.2 Practical Yield for K$^+$ Analyzed Events

The set of events without a detected proton but still containing a K^+ is, at first blush, an attractive option for improving the statistics for E. The total number of events is higher than for those where a proton is also detected, and the number of true $K^+\Lambda$ events seems to be higher too, as will be seen from the missing mass plots. Nevertheless, the inability to make a cut for the missing pion mass leaves us with significant background contamina-

tion. In some regions, particularly in the negative $\cos\vartheta_{\text{CM}}$ bins, separation of signal from background would be nearly impossible. In other cases, there's a clear signal with a fairly simple subtraction process, but the effect of the background on the dilution factor is still too strong. While the additional yield would have the effect of reducing statistical uncertainty, the growth of the dilution factor will result in a proportional growth in uncertainty. For this reason, it became necessary to examine the effect of introducing these events on a bin by bin basis.

When testing each bin as a candidate for inclusion in E, the ratio of the background to the yield for events with K^+-only had to be compared to the increase in total event number for the kinematic bin. I made the comparison by stating the yield for K^+-only events in terms of the yield for pK^+ events as follows

$$Y_2 = C * Y_1 \,, \tag{3.5}$$

where Y_1 is the yield for pK^+ events and Y_2 is the yield for K^+-only events. The statistical uncertainty would then be modified by a factor of $1/\sqrt{C+1}$. The greater the relative yield in K^+-only events, the more the uncertainty would be reduced. However, the uncertainty is also modified by the dilution factor. The uncertainty once K^+-only events are included is then

$$\sigma_{\text{new}} = \frac{D_2}{D_1\sqrt{C+1}}\sigma_{\text{old}} \,, \tag{3.6}$$

where D_2 is the dilution factor for all included events and D_1 is the dilution factor obtained from pK^+ events. Clearly, D_2/D_1 has to be less than $\sqrt{C+1}$ if there is to be any benefit in including the extra events. Taking this inequality together with equation (3.4) and making the assumption that the background in pK^+ events is much less than Y_2 we arrive at the following condition for productive inclusion of K^+-only events

$$\frac{B_2}{Y_2} < \frac{C+1-\sqrt{C+1}}{C} \;,\tag{3.7}$$

where B_2 is the background in events with only the K^+ detected.

The yield for K^+-only events within the range previously chosen from my fit for pK^+ events is $Y_2 = 370904$ with a scaled carbon background of $B_2 = 304660$. Taking the yield for pK^+ events given in the previous section and applying equation (3.5), we find that $C \approx 8.4$, meaning that the ratio of background to total yield should be less than 0.67, a requirement which these events fail to meet. This condition could also be rigorously applied bin by bin to see if there is any justification for using the K^+-only statistics in the calculation of E for that bin. However, it is generally quite possible to see that the condition will not be met merely by eye. In Figure 3.16, I present some example bins to illustrate the state of K^+-only statistics. In all of the backwards bins, the background is simply too strong to even consider these events. A simple example to understand how useless these bins are is a consideration of a signal to background ratio of 1/10. This is not an atypically small ratio for this region (it is perhaps even too generous) and the requirement for inclusion is enormous. The yield for these events would have to reach 80 times that for pK^+ events before they could have a positive effect on the uncertainty in E. I dismiss all 50 backwards region bins quickly, because of their poor signal. Now let us consider the forward region. Unfortunately, while there is a greater signal to background ratio in these bins, the statistics are generally already fairly good. A bin-by-bin examination shows some possible candidates for K^+-only inclusion, but none add significantly to the statistical precision. Thus, the K^+-only events were judged to not offer a substantial enough benefit for their inclusion in this analysis.
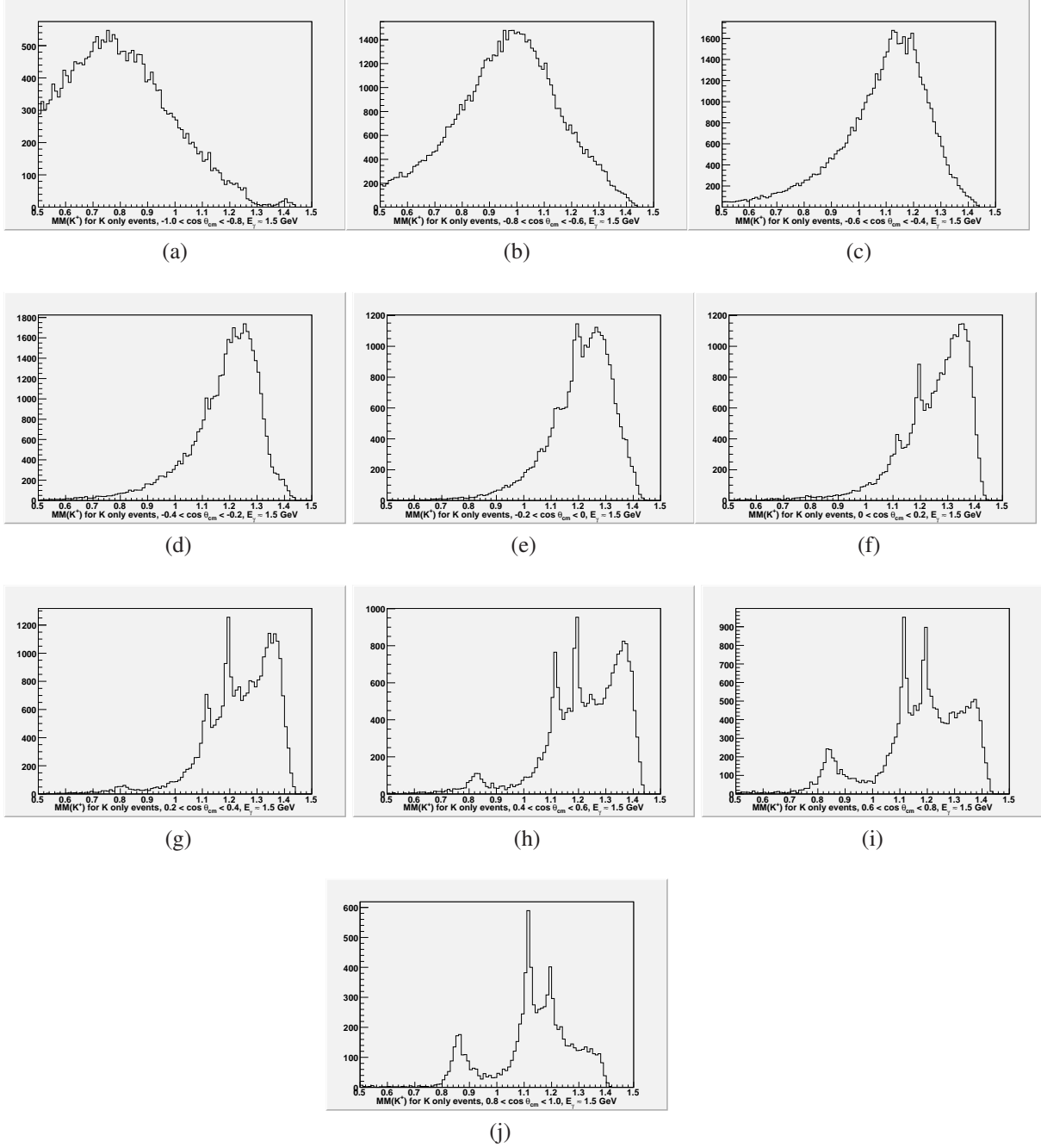
Figure 3.16: Missing Mass plots for events with no proton detected in 10 angular regions for $E_\gamma = 1.5$ GeV.

3.7 Angular Dependent Dilution

The method of obtaining the dilution factor delineated in the previous section provides a good leading order approach to handling the bound nucleon contamination of the data, but a one-size-fits-all kinematic bins approach leaves something to be desired. While the improved statistics of the full kinematic range may improve the accuracy of the fitting procedure, it fails to account for the variation in carbon yield scaling with momentum. This variation occurs partially due to the difference in energy loss of particles between the two targets.[45] Since the scaling factor measures not only the ratio of bound-nucleon reactions, but also the ratio of detection efficiency and acceptance differences, the greater loss of energy in the butanol target will affect the scaling, particularly at lower momentum.

Therefore, as the analysis proceeded it was deemed desirable to use an angular dependent dilution factor rather than a single effective dilution for the entire yield. The statistics could not allow for an independent calculation of scaling for each kinematic bin, but a different scaling for each angular bin was achievable. Figures 3.17 and 3.18 show the scaling and fit results for each angular region. The low scaling factors obtained by the fit are worthy of note, because none of them is as high as the scaling factor obtained for the entire kinematic range. This could indicate that the fit is poorer because of the lower statistics and correspondingly higher uncertainty in these plots, which makes the low uncertainty produced by the fit for the scaling factor rather confusing.

In any case, a look at the effect of the scaling is appropriate to deem whether this procedure is viable. Figure 3.19 shows the scaled carbon yield subtracted from the butanol yield for each angular bin, while Table 3.1 compiles the scaling factors and dilution factors by angular bin. An alternative method for calculating the dilution factor places it in the denominator of the complete polarization observable. When this method is used, the propagation of error from the scaling factor to the dilution factor is simpler. Therefore, I have created an entry for $\frac{1}{D_{eff}}$ in the table with the appropriate propagated errors. Direct

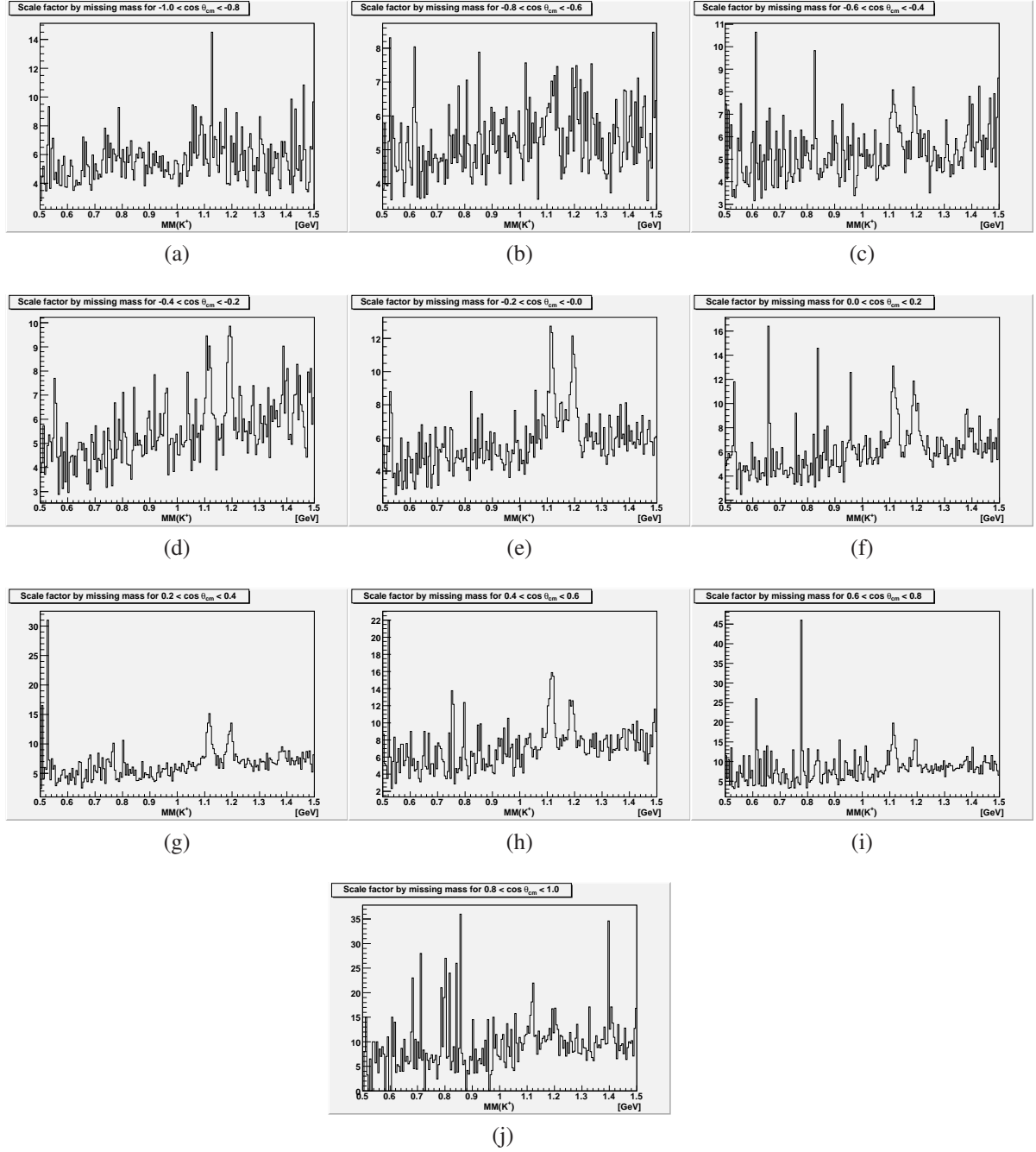Figure 3.17: Distribution of the ratio of butanol to carbon yield by missing mass for each angular region.
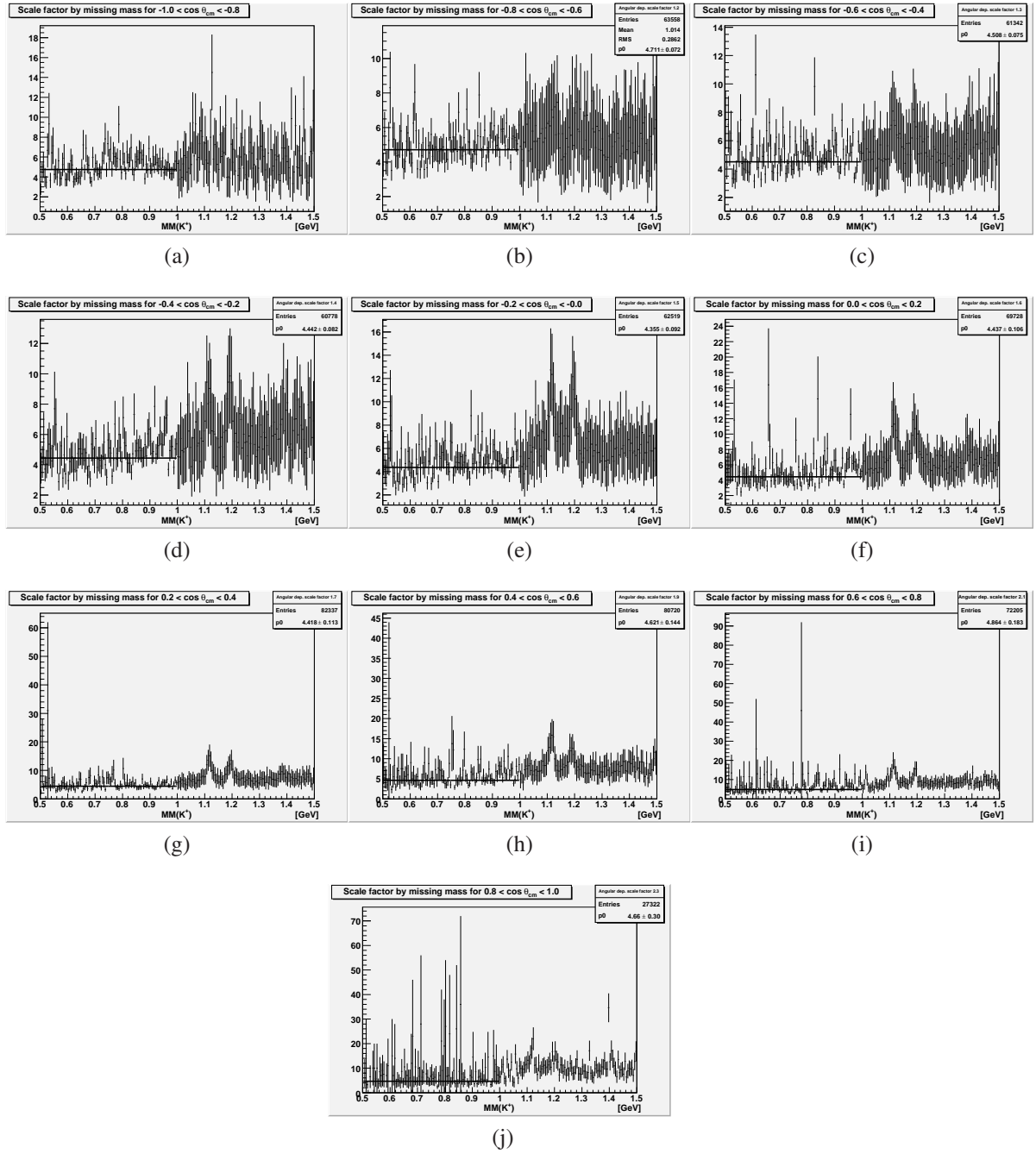
Figure 3.18: Fit of the scaling distribution for each angular bin to find the appropriate scaling factor. Horizontal bars indicate only the bin size in GeV, while vertical bars represent statistical uncertainty in the scaling.
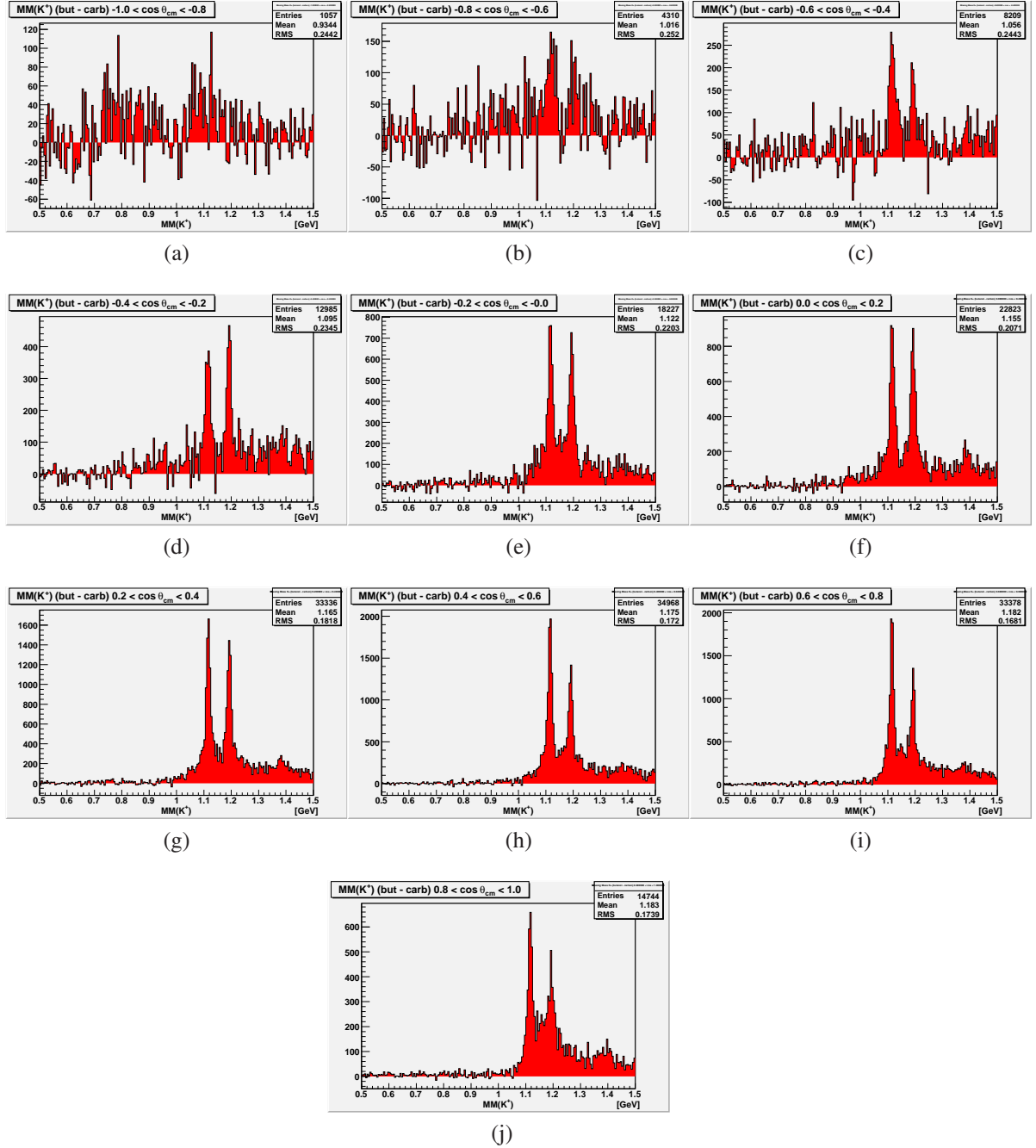
Figure 3.19: Missing Mass distribution with scaled carbon yield subtracted for each angular region.

$\cos\theta_{CM}^K$	Y_{but}	Y_{carb}	Scaling Factor	D_{eff}	$\frac{1}{D_{eff}}$
-0.9	138	6	$4.74\pm.09$	$1.26\pm.01$	$0.794\pm.004$
-0.7	977	46	$4.71\pm.07$	$1.28\pm.01$	$0.781\pm.003$
-0.5	1558	90	$4.51\pm.08$	$1.35\pm.01$	$0.741\pm.005$
-0.3	2188	142	$4.44\pm.08$	$1.40\pm.01$	$0.714\pm.005$
-0.1	3716	220	$4.35\pm.09$	$1.35\pm.01$	$0.741\pm.005$
0.1	4833	283	$4.44\pm.11$	$1.35\pm.01$	$0.741\pm.006$
0.3	8165	447	$4.42\pm.11$	$1.32\pm.01$	$0.758\pm.006$
0.5	9725	493	$4.62\pm.14$	$1.31\pm.01$	$0.763\pm.007$
0.7	9461	496	$4.86\pm.18$	$1.34\pm.02$	$0.746\pm.009$
0.9	3438	188	$4.66\pm.30$	$1.34\pm.03$	$0.746\pm.016$

Table 3.1: Scaling and Dilution by angular region. The 138 events in the most backward angular bin are removed from polarization observable analysis, because of poor statistics accompanied by poor scaling.

calculations from the extremes of the scaling factor errors yields asymmetrical error in this entry, but when using error propagation a result is obtained that falls between the upper and lower errors. In either case, the error is consistent within the precision reported for D_{eff} and it is too low to have a significant impact on the results.

The scaling apparently works fairly well in most cases, although the backwards angular bins show more variation in the tails. The most backward angular region is clearly unviable. The statistics had already made this bin of questionable value, but this plot shows that a decent scaling is impossible for this bin. While the pion mass cut leaves a clear signal in the Λ region, it is not possible to give a decent estimate of how much of this is coming from bound-nucleon reactions. Therefore, the most backward angular bin is removed from the analysis. The scaling method works decently for the other angular bins. Nonetheless, there is clearly background remaining after the scaled carbon subtraction. This background does not exist in the yields after the pion mass cut is performed, so I will not contend with it here. However, consistency between the yields obtained from the pion cut and the background subtraction done here would be a good test of the method. Thus, I have left this to Chapter 6, where I will consider any discrepancy as part of the systematic error.

3.8 Summary

In this chapter I determined the set of events to be used in the remainder of the analysis. The process was to identify potential events for the reaction channel by inspecting only events with an identified K^+ and putting particular focus on those events which also have an identified proton, omitting particles of dubious detection status. The protons and kaons of those events were corrected for energy loss and a series of cuts were performed until a clean Λ signal remained in the missing mass plots.

Ultimately, from a set of approximately 3.4 billion triggered events, I retrieve fewer than 45,000 viable $\gamma p \rightarrow K^+ \Lambda$ events with which to explore the physics of this reaction channel. In the following chapter, I will do just that by subdividing this yield between polarization states and among 90 kinematic bins in photon energy and $\cos \vartheta_{CM}$.

Chapter 4

Extraction of E, $L_{x'}$, and $L_{z'}$

The extraction of polarization observables follows rather simply from the determination of reaction channel yield. In every case, the yield is subdivided into yields for positive and negative polarization directions. In the case of double polarization observables the "negative" polarization yield is simply taken to be the yield for events with anti-aligned polarization directions in the quantities of interest, while the "positive" yield is for events with aligned polarization.

In my analysis, each of the polarization observables is calculated for 90 separate kinematic bins, 4 bins of 100 MeV width (centered at 1.3, 1.4, 1.5, and 1.6 GeV), 2 bins of 150 MeV width (centered at 1.175 and 1.725 GeV), and 4 bins of 200 MeV width in photon energy (centered at 1.0, 1.9, 2.1, and 2.3 GeV) each with 9 bins of 0.2 width in $\cos\vartheta_{CM}$. The energy binning was decided on the basis of available statistics. While binning of 100 MeV or less in energy would have been desirable over the the whole dataset, the error bars become too large on both extremes of the photon energy range to allow for anything but the coarsest binning. In any event, those energy regions most critical for the missing D_{13} resonance search were found to have viable statistics for the finer binning.

In order to plot the observables against the kaon angular distribution in the center of mass frame it is necessary to boost the momentum vectors of my particles into the center of

mass frame. This is done by using the β of the center of mass as observed in the lab frame, which is calculated by summing the photon and initial proton 4-momenta and dividing each Cartesian momentum component by the energy component as follows

$$\vec{\beta}_{CM} = (\frac{p_x}{E_T}, \frac{p_y}{E_T}, \frac{p_z}{E_T}) \, , \tag{4.1}$$

where $E_T = E_\gamma + E_p$ and $p_i = p_i(\gamma) + p_i(p), (i = x, y, z)$. In practice, this means that $\vec{\beta}_{CM} = \frac{E_\gamma}{E_\gamma + M_p}\hat{z}$ for this experiment. All of the detected particle momentum vectors are then Lorentz boosted in the opposite direction to transform into the appropriate vectors for the center of mass rest frame. The angle the boosted K^+ momentum makes with the positive z-axis is ϑ_{CM}. For the simplified β_{CM} given above, the K^+ boosted momentum is calculated by

$$\vec{p}(K^+_{CM}) = (\gamma_{CM}[E(K^+) - \beta_{CM}p_z(K^+)], p_x(K^+), p_y(K^+), \gamma_{CM}[p(K^+) - \beta_{CM}E(K^+)]) \, , \tag{4.2}$$

where γ_{CM} is the Lorentz factor, while the boosted momentum for the proton is likewise obtained by substituting p for K^+ in equation (4.2). The angle of K^+ in the center of mass frame is tied to that measured in the laboratory frame by the following relation

$$\tan\theta_{lab} = \frac{\sin\theta_{CM}}{\gamma_{cm}(\cos\theta_{CM} + \frac{\beta_{CM}}{\beta(K^+_{CM})})} \, , \tag{4.3}$$

where $\beta(K^+_{CM})$ is the velocity of the kaon in the center of mass frame.[46] From the total 4-momentum vector for the center of mass frame: (W,0,0,0) where $W = \sqrt{s}$ is the center of mass energy of the reaction together with the previously mentioned condition of invariant mass conservation, we find that the center of mass energy can be expressed in terms of photon energy as

$$W = \sqrt{M_p^2 + 2E_\gamma M_p} \, , \tag{4.4}$$

While I will be plotting the extracted observables in E_γ, this relation is important, because the masses of nucleon resonances are tied to the center of mass energy.

In this chapter I will plot the asymmetries for three observables that have yet to be measured for this reaction channel: E, $L_{x'}$ and $L_{z'}$. The requirement of a longitudinally polarized target to extract these observables has prevented their measurement up until this point. The FROST target and the g9a dataset taken using it have allowed these asymmetries to be calculated for the first time. The results here are expected to provide a significant contribution to the world dataset for the $\gamma p \to K^+ \Lambda$ channel and for the constraints on complex amplitudes.

4.1   Beam-Target Asymmetry E

E is the observable that arises from use of a circularly polarized photon beam and a linearly polarized target. The asymmetry for E is taken between the yields for parallel and anti-parallel polarizations of the target and beam, as given in equation (1.8):

$$A = \frac{N_+ - N_-}{N_+ + N_-} \ .$$

The previous chapter delineated how I extract the total yield for $K^+ \Lambda$ events from a much larger set of detected particle events. Now I will describe how that total yield is separated by polarization states for the beam and target.

During the g9a run period, both the direction field of the polarizing magnet and the direction of the target polarization with respect to the magnetic field were flipped at certain intervals in the experiment. As mentioned in section 2.3.1, the frequency of the microwaves used to transfer polarization to protons in the target could be made either slightly higher or slightly lower than the ESR frequency. If the frequency was chosen to be above the ESR frequency, the proton's spins would be aligned antiparallel to the direction of the magnetic

field. The polarizing field, in turn, could be generated in the positive or negative z direction, as defined by CLAS. Therefore, the product of the field sign and the frequency sign (where an anti-parallel polarization result is taken to be negative), gives the direction of the target polarization with respect to the direction of beam propagation.

In order to determine whether the alignment of photon polarization and target polarization is parallel or antiparallel, we still need to determine the helicity of the photon beam. The electron beam helicity is flipped at a rate of 30 Hz during production runs. The status of the beam helicity for an event is recorded and stored in the form of a "trigger bit." The status of one bit (1 or 0) in an integer storing a series of bit based information tells us the helicity of the electron beam. The helicity of the secondary photon beam is determined by the helicity of the electron beam with one other factor. The inclusion of a half-wave plate reverses the helicity state of the beam as given by the trigger bit. This means that it is necessary to know if the half-wave plate was inserted during a particular run to be certain of the true direction of photon polarization.

Early in the analysis of g9a data, the circularly polarized dataset was split into seven run groups to account for changing run conditions pertaining to beam and target polarization. Using the status of the half-wave plate, the direction of the polarizing magnet field and the frequency an overall sign was constructed to be applied to the asymmetry based purely on the 30 Hz helicity flip. Table 4.1 shows the range of runs in each group and the values determined for these groups.

Once the polarization directions of the photon beam and target have been determined, it's a simple matter to divide the yield into bins for calculating the asymmetry. As described in the first chapter, we take the four subdivisions of the yield arising from the four possible combinations of polarization directions and group them into parallel and antiparallel yields. In the interest of demonstrating a clear case for the effect of target polarization, I've plotted in Figure 4.1 the missing mass distribution for the difference in yield in butanol for each

Runs	$\lambda/2$ plate	Target	Sign
55521 - 55536	+1	+1	-1
55537 - 55555	-1	+1	+1
55556 - 55595	+1	-1	+1
55604 -55625	+1	-1	+1
55630 - 55678	+1	+1	-1
56164 - 56193	+1	+1	-1
56196 - 56233	+1	-1	+1

Table 4.1: Helicity bit assignment by run group. The half-wave plate status is given as -1 if it is inserted. The overall sign is a product of the target direction, half-wave plate status, and a negative sign incorporated in the definition of the helicity asymmetry E.

helicity state and for the corresponding $K^+\Lambda$ yields in carbon for each butanol helicity state. The butanol plot shows an evident preference for the 3/2 state, while no state is significantly favored in the carbon plot. Thus, the polarized butanol affects the reaction channel in manner that the unpolarized carbon does not and we can confidently state that a true double polarization observable is being measured. The parallel and antiparallel helicity yields generate the raw asymmetry for E. In order to calculate the full quantity, we need to apply the target polarization, photon circular polarization, and dilution factor. The dilution factor was obtained in Chapter 3. The polarizations will each be handled in the following sections, but first we will examine the statistical uncertainty in the asymmetry.

Even without imperfect polarization adjusting the true value of the asymmetry that should be observed in an ideal scenario, there would still be innate statistical fluctuations in the number of observed events for each yield, resulting in a statistical fluctuation in the differences and sums the yields. Therefore, there is some uncertainty in the raw asymmetry propagated from the uncertainty in N_+ and N_-. In this analysis, we are assuming each yield to be Poisson distributed so that its uncertainty is always

$$\sigma(N_{+,-}) = \sqrt{N_{+,-}} \, . \tag{4.5}$$

(a) Butanol yield difference
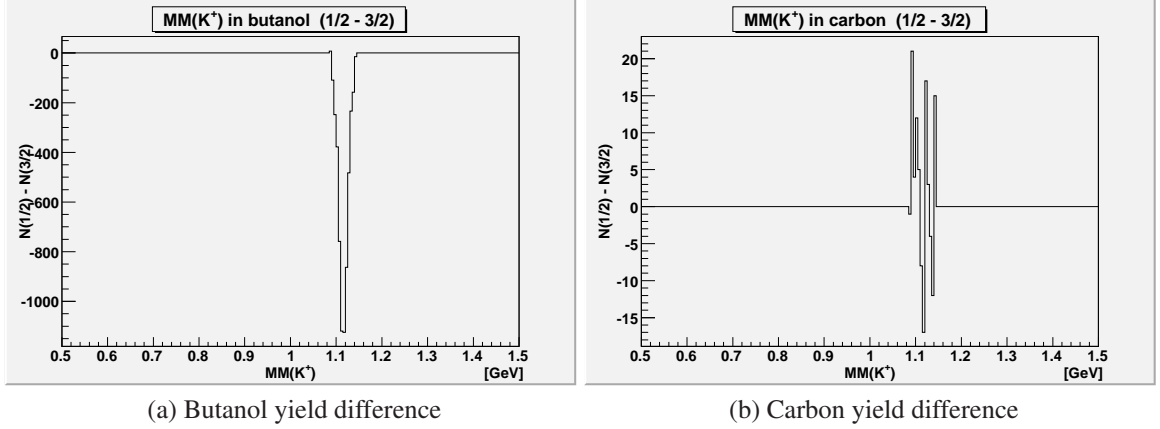
(b) Carbon yield difference

Figure 4.1: Helicity yield difference in the missing mass distribution for (a)butanol target and (b) carbon target. The helicity state for carbon is not the actual helicity state since carbon is unpolarized, but the helicity state given by the butanol polarization. A definite asymmetry favoring the 3/2 state is seen in butanol, while carbon shows small fluctuations consistent with no real asymmetry.

This is a fairly valid assumption so long as $N \gtrsim 10$, a condition that holds at least for the total N of each kinematic bin used in this analysis. The error in the asymmetry is then calculated by the standard error propagation formula

$$\sigma^2(A) = [\frac{\partial A}{\partial N_+}\sigma(N_+)]^2 + [\frac{\partial A}{\partial N_-}\sigma(N_-)]^2 , \qquad (4.6)$$

if we assume that N_+ and N_- vary independently and their fluctuations cause fluctuations in the sum $N = N_+ + N_-$.[47] Then using equation (1.8) for the asymmetry the statistical uncertainty in the asymmetry is

$$\sigma(A) = \sqrt{\frac{4N_+N_-}{(N_+ + N_-)^3}} , \qquad (4.7)$$

which varies with the magnitude of the asymmetry, but is always proportional to $1/\sqrt{N}$.

The statistical error is then quite sensitive to the number of events collected. In regions of low statistics, the error bars can be too large to obtain meaningful data on a polarization

observable even before systematics are taken into account. On the other hand, the error bars can be too small to be reasonable in certain limiting cases. In the limit of $A = \pm 1$, equation (4.7) will give zero uncertainty. In most cases, the statistics are too high to run into this problem, but in a situation where the raw asymmetry is measured to be one it makes more sense to use an error calculated from N. Plots for the raw asymmetry for E with statistical uncertainties are shown in Figure 4.2. For these plots and all polarization observable plots in this work, the vertical bars indicate uncertainty in the measurement of the observable, while the horizontal bars indicate the angular range included for that measurement. There are certainly some bins with insufficient statistics. This may not be immediately clear, but will be more apparent when the effect of correction factors on the error bars is seen. In particular, the yield for $K^+\Lambda$ is typically quite poor in the backward direction, leading to larger error bars. The job of event selection was to maximize the inclusion of true $K^+\Lambda$ events produced on free protons while minimizing inclusion of background events that would only increase the error in other ways. If this was done optimally, then there's little more to be done for these regions than to hope for a higher statistics dataset in the future.

4.1.1   Target Polarization

A frozen spin target has a long relaxation time, but FROST still has a finite, nonzero temperature and, thus, cannot maintain its polarization indefinitely. Throughout the run period, the magnitude of the target polarization steadily decreased until the target was repolarized. This means that the value of the target polarization varied between, and even within, each of the runs of g9a. Therefore, the target polarization referred to in equation (1.10) cannot be regarded as a singular observed value, but rather as an average of the target polarization measurements taken over the whole run period. The average polarization per run was calculated using NMR spectra taken by Jo McAndrew. Appendix A presents a table with her results for each run used in this analysis. The statistical errors were calculated to be
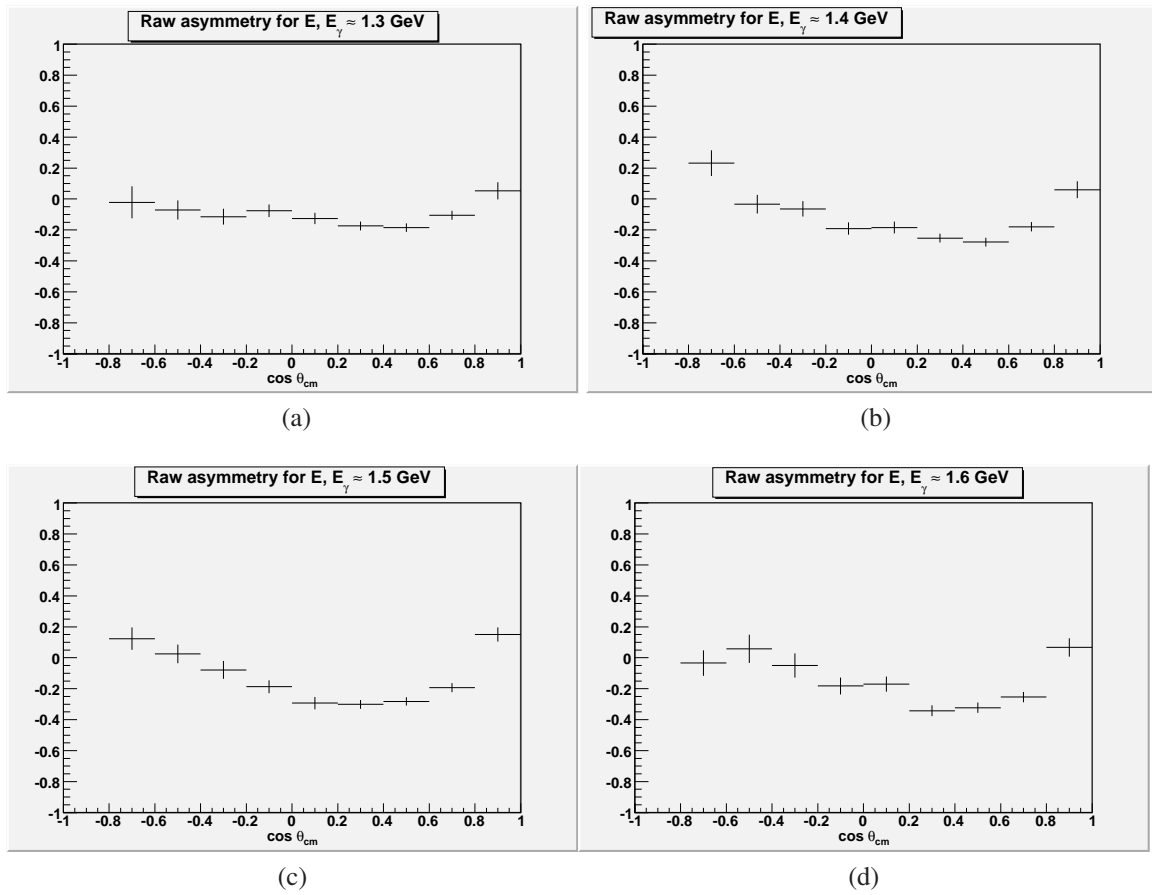
Figure 4.2: Raw asymmetry plots for E. Vertical bars indicate uncertainty, while horizontal bars indicate angular range.

$\cos\theta^K_{cm}$	-0.7	-0.5	-0.3	-0.1	0.1	0.3	0.5	0.7	0.85
E_γ=1.050 GeV	0.753	0.809	0.815	0.819	0.820	0.820	0.821	0.822	0.821
E_γ=1.175 GeV	0.828	0.815	0.814	0.820	0.821	0.819	0.821	0.822	0.820
E_γ=1.300 GeV	0.818	0.820	0.818	0.818	0.819	0.820	0.818	0.821	0.822
E_γ=1.400 GeV	0.826	0.821	0.819	0.823	0.820	0.821	0.819	0.821	0.818
E_γ=1.500 GeV	0.820	0.813	0.827	0.820	0.819	0.820	0.822	0.820	0.819
E_γ=1.600 GeV	0.821	0.811	0.802	0.799	0.818	0.810	0.808	0.814	0.808
E_γ=1.725 GeV	0.808	0.823	0.816	0.802	0.814	0.811	0.807	0.811	0.807
E_γ=1.900 GeV	0.794	0.798	0.815	0.816	0.810	0.806	0.812	0.811	0.810
E_γ=2.100 GeV	0.815	0.811	0.819	0.821	0.802	0.805	0.808	0.808	0.814
E_γ=2.275 GeV	0.816	0.777	0.816	0.817	0.807	0.819	0.810	0.814	0.816

Table 4.2: Mean Target Polarization by Kinematic Bin

nonzero, but for most runs the errors are below what could be considered significant to my results, so I only report values to three significant figures.

While runs were generally kept to a fairly standard length, there is always some variation in the amount of data in a run. Furthermore, purely statistical fluctuations resulting in some runs with higher or lower than normal yield skew the manner in which the asymmetry should be properly adjusted by target polarization. Therefore, I decided to take a weighted average of the polarization values per run. For each kinematic bin, I calculated a separate target polarization average weighted by the yield in that bin for each run. My results for each bin of E_γ are given in Table 4.2 rounded to 3 significant figures.

4.1.2 Circular Photon Polarization

The circular polarization of the photon beam is directly related to the longitudinal polarization of the accelerator electron beam by equation (1.11). The longitudinal polarization is, in turn, determined by measurements taken during special runs using the Moller polarimeter, as described in section 2.2.3.2. The requirement that data acquisition be stopped during Moller measurements meant that polarization data for the electron beam would be much more scarce than for the target. It would be impractical to stop data acquisition be-

Beam Energy	Run Number	Moller Measurement (%)
1.645 GeV	55544	85.23±1.42
		-78.52±1.35
		-79.15±1.26
		88.70±1.48
	55552	84.17±1.33
		-84.73±1.53
	55588	-86.53±1.38
		88.41±1.44
		87.75±1.48
2.478 GeV	55608	-82.53±1.40
	55627	-79.45±1.41
		80.06±1.40
	56194	-83.27±1.38
	56202	-83.25±1.32

Table 4.3: Moller Measurements for the Electron Polarization

tween each run to take a Moller measurement, so Moller runs were done infrequently at logical points when the beam was being restored after some change in run conditions. The complete list of electron polarization measurements is given in Table 4.3.

While the target polarization was constantly decreasing in magnitude, albeit at a slow rate, between each repolarization, there is no physics governing such a decay of the electron beam polarization. It is reasonable to assume that the beam polarization was fairly constant for all the runs between measurements and this assumption is necessary for this technique of circular polarization calculation to have any validity. Therefore, in order to calculate an averaged electron beam polarization, I weight each measured polarization value by the yield for all the runs after that measurement and before the next one. For the first set of runs taken before any Moller run was performed, I simply use the first Moller polarization measurement. When multiple Moller measurements have been taken in a single run, I take a simple average of their values (magnitude only).

After the average value of electron polarization is obtained for each kinematic bin, the median energy for that bin is plugged into equation (1.11) to find the value of the circular

$\cos\theta^K_{cm}$	-0.7	-0.5	-0.3	-0.1	0.1	0.3	0.5	0.7	0.85
E_γ=1.050 GeV	0.549	0.537	0.511	0.516	0.508	0.522	0.525	0.510	0.524
E_γ=1.175 GeV	0.563	0.566	0.579	0.580	0.580	0.579	0.578	0.572	0.576
E_γ=1.300 GeV	0.626	0.634	0.637	0.624	0.623	0.626	0.631	0.629	0.616
E_γ=1.400 GeV	0.648	0.672	0.674	0.673	0.667	0.674	0.671	0.668	0.653
E_γ=1.500 GeV	0.689	0.696	0.705	0.697	0.697	0.702	0.703	0.702	0.698
E_γ=1.600 GeV	0.697	0.686	0.688	0.687	0.679	0.683	0.684	0.688	0.685
E_γ=1.725 GeV	0.705	0.701	0.706	0.704	0.705	0.705	0.704	0.705	0.707
E_γ=1.900 GeV	0.754	0.756	0.755	0.749	0.754	0.752	0.751	0.751	0.751
E_γ=2.100 GeV	0.790	0.794	0.793	0.789	0.791	0.791	0.792	0.792	0.793
E_γ=2.275 GeV	0.809	0.814	0.814	0.812	0.813	0.812	0.812	0.812	0.810

Table 4.4: Mean Circular Photon Polarization by Kinematic Bin

polarization used for that bin. The lack of weighting within the energy bin and some difference between the polarization at the average energy and the average of the helicity transfer within that energy range means that this is not quite the average value of circular polarization, but the effect of this is small and will be looked at more closely in Chapter 6. My results for each E_γ bin are given in Table 4.4.

4.1.3 Full Asymmetry

Now that the polarization of the target and photon beam have been calculated for each bin, the raw asymmetry may be adjusted by these factors. The full asymmetry with statistical errors is then calculated using equation (1.10). The results are plotted in Figures 4.3-4.7. The final results for E with inclusion of systematic errors and the discussion of these results are left for the final chapter.

4.2 Target-Recoil Polarization Transfer $L_{x'}$

There are two observables for the polarization transfer from a longitudinally polarized target to the recoil Λ for the $\gamma p \to K^+\Lambda$ reaction channel. These two observables correspond
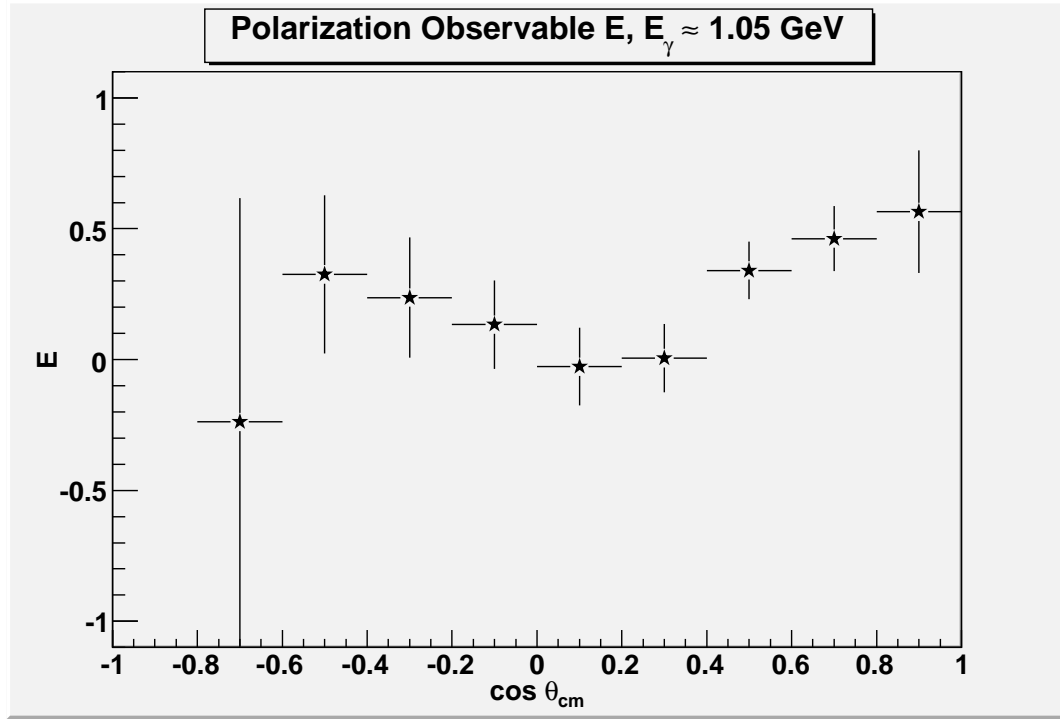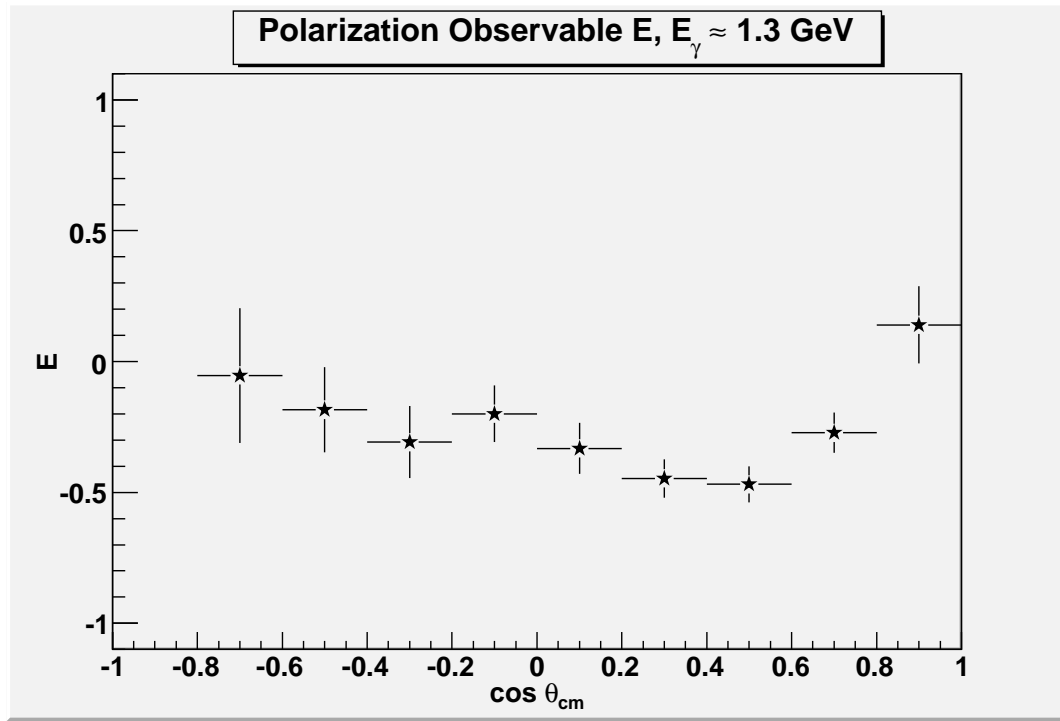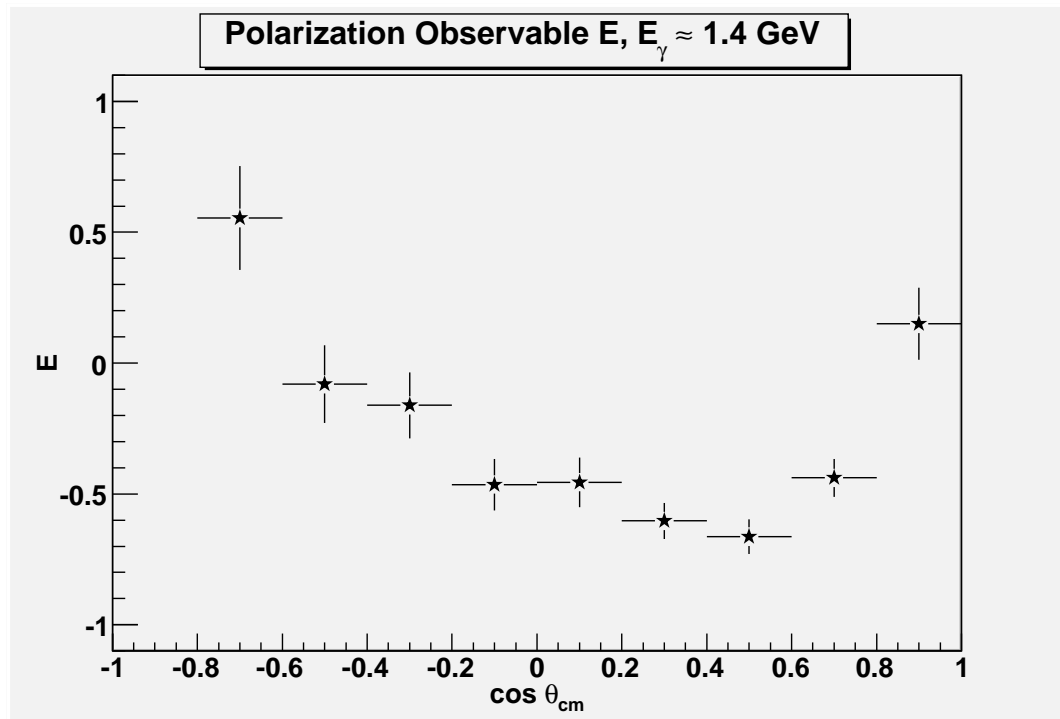
(a)
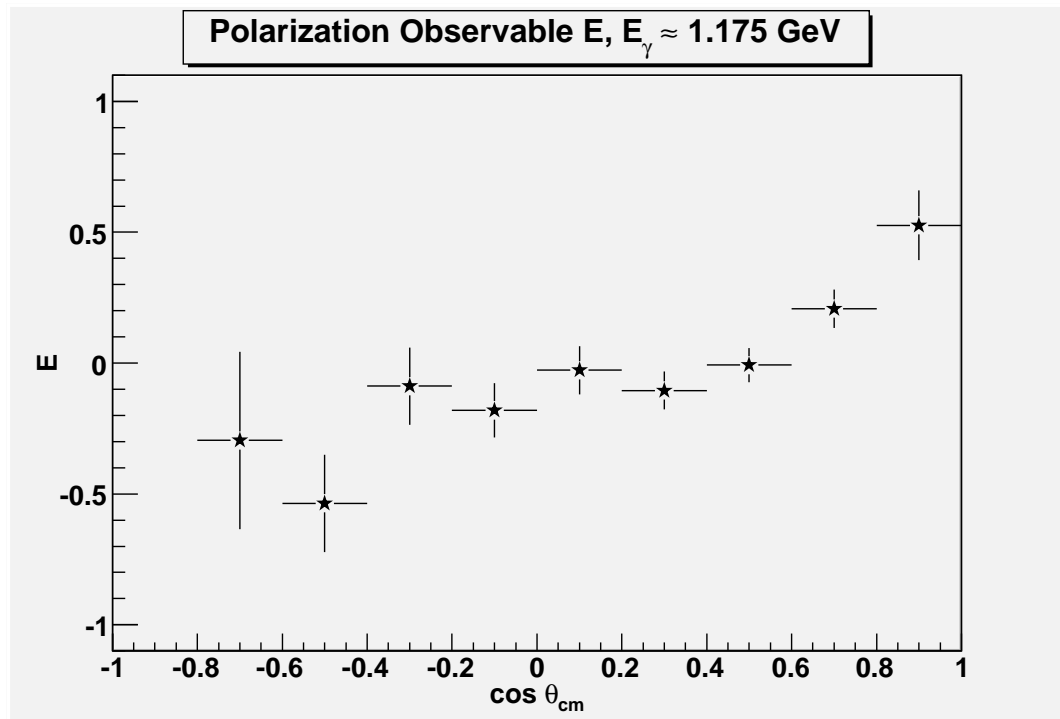
(b)

Figure 4.3: Helicity Asymmetry E for incident photon energies in the ranges (a)$0.9\,GeV < E_\gamma < 1.1\,GeV$ and (b)$1.1\,GeV < E_\gamma < 1.25\,GeV$. Threshold for $\gamma p \to K^+ \Lambda$ is 0.911 GeV. Average photon energy per bin is given to nearest 25 MeV.

(a)

(b)

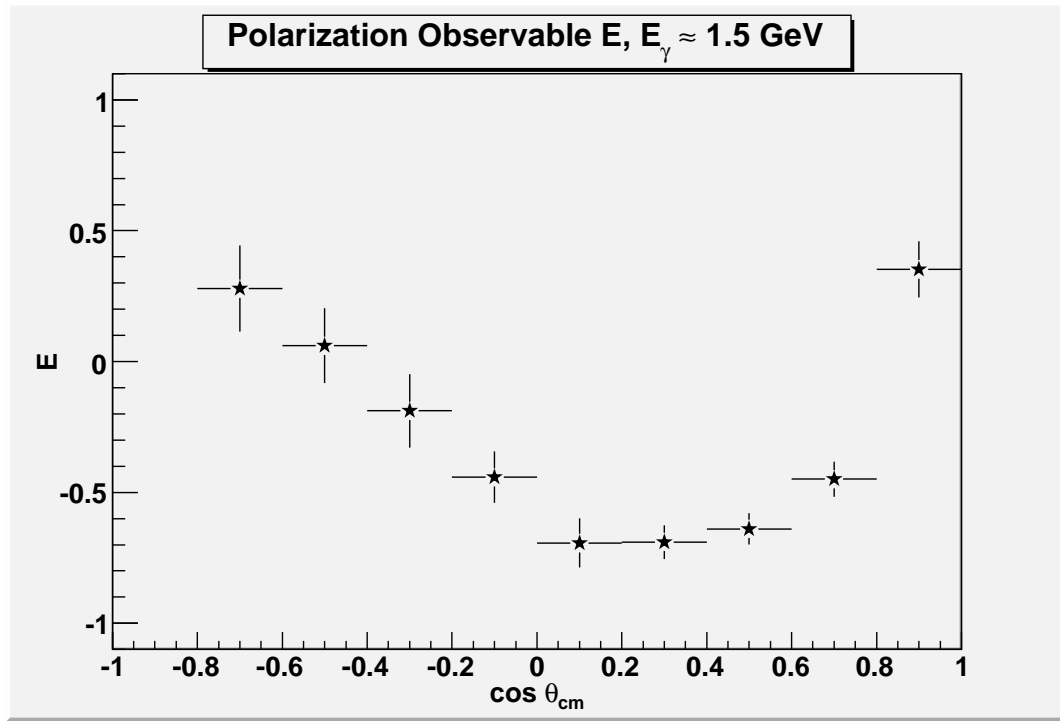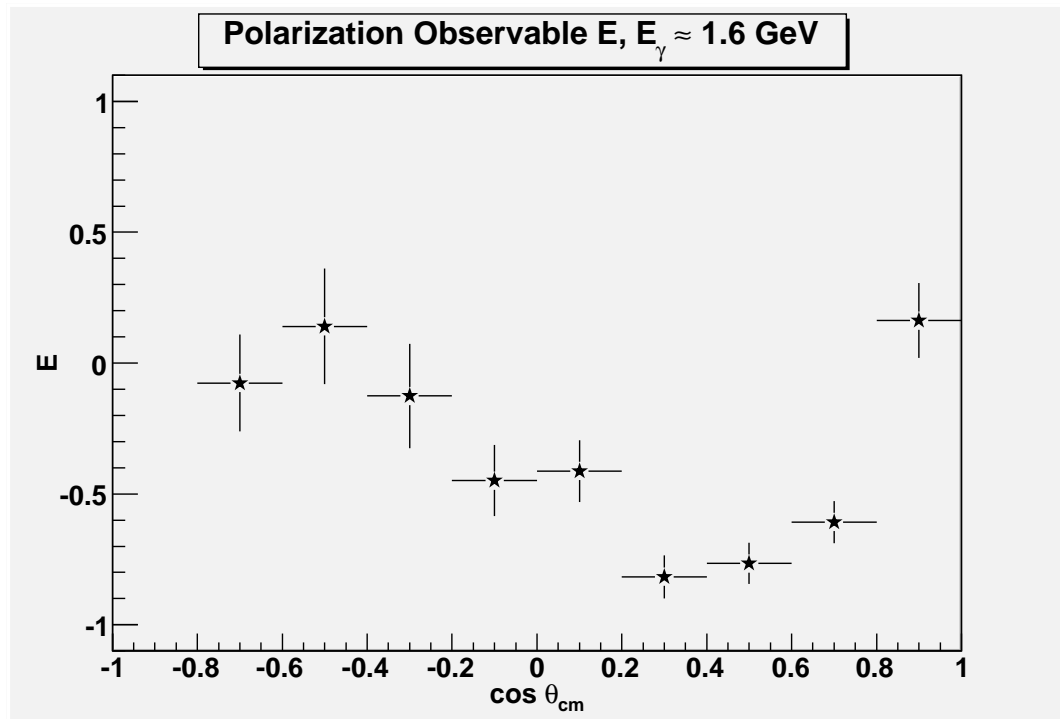Figure 4.4: Helicity Asymmetry E for incident photon energies in the ranges (a)$1.25\,GeV < E_\gamma < 1.35\,GeV$ and (b)$1.35\,GeV < E_\gamma < 1.45\,GeV$. Average photon energy per bin is given to nearest 25 MeV.
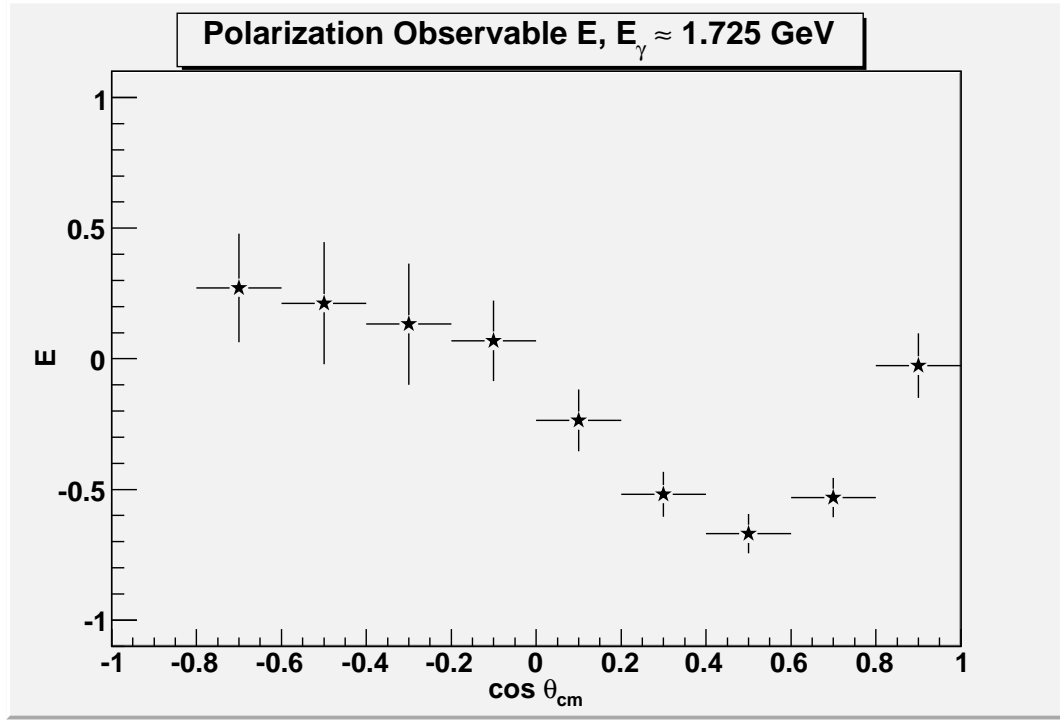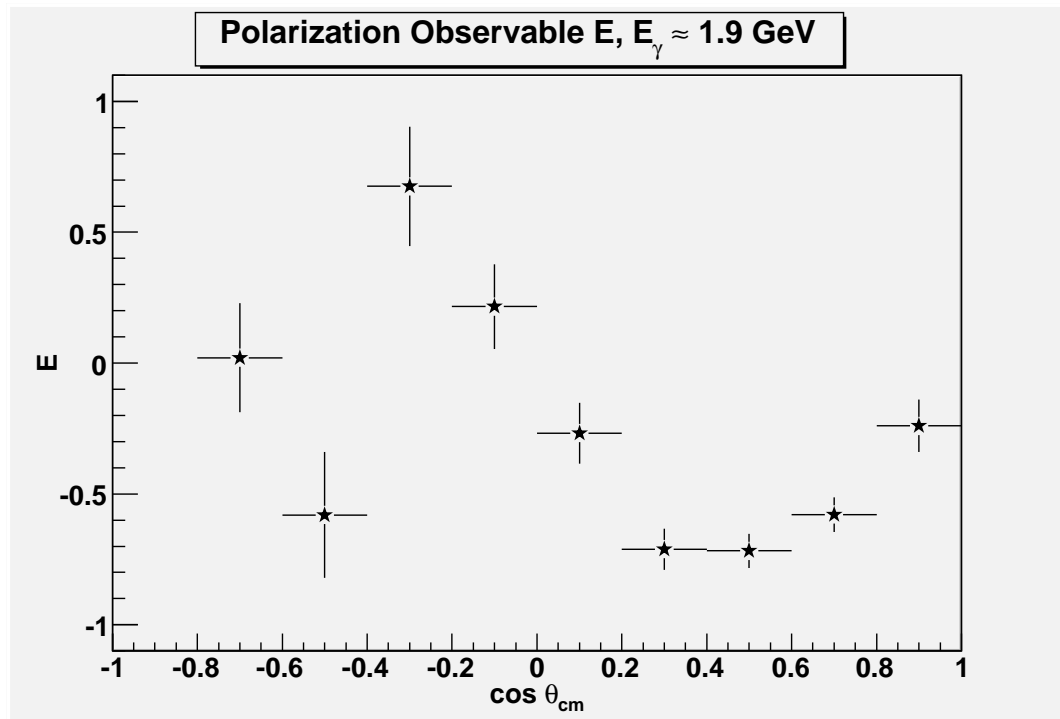
(a)

(b)

Figure 4.5: Helicity Asymmetry E for incident photon energies in the ranges (a)$1.45\,GeV < E_\gamma < 1.55\,GeV$ and (b)$1.55\,GeV < E_\gamma < 1.65\,GeV$. Average photon energy per bin is given to nearest 25 MeV.
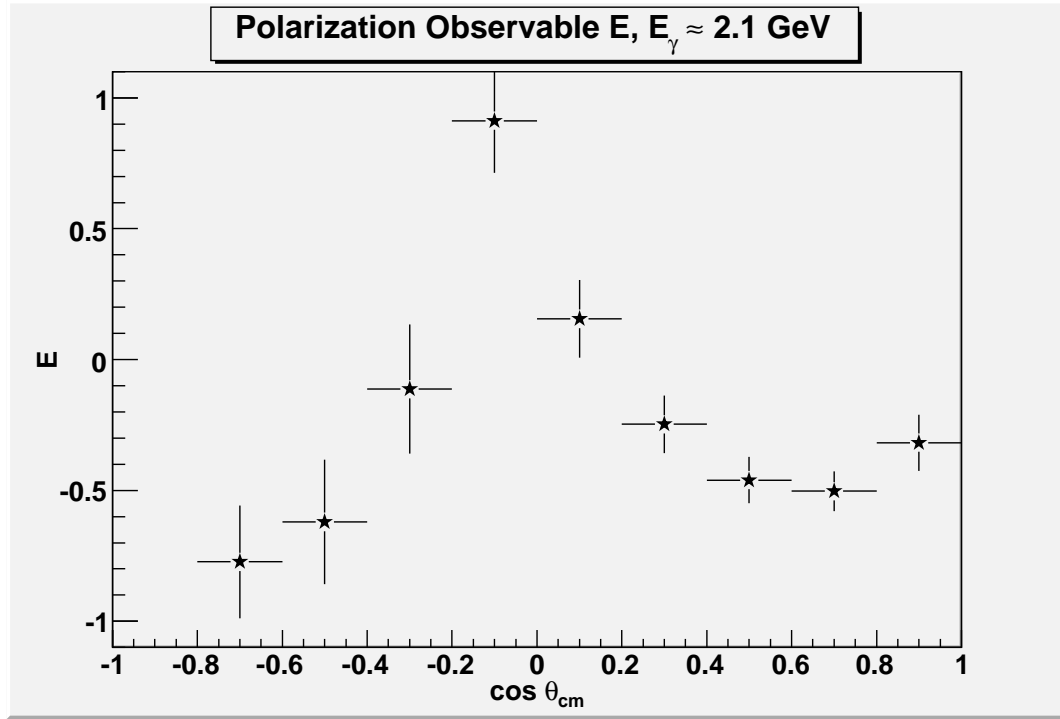
(a)
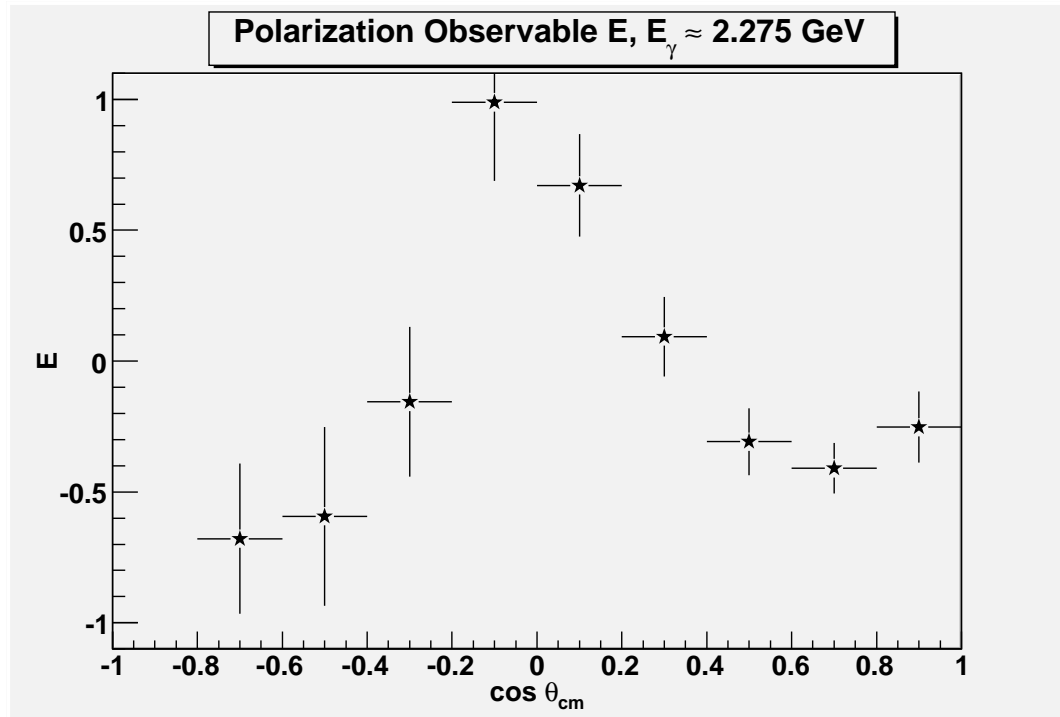

(b)

Figure 4.6: Helicity Asymmetry E for incident photon energies in the ranges (a)$1.65\,GeV < E_\gamma < 1.8\,GeV$ and (b)$1.8\,GeV < E_\gamma < 2.0\,GeV$. Average photon energy per bin is given to nearest 25 MeV.

(a)

(b)

Figure 4.7: Helicity Asymmetry E for incident photon energies in the ranges (a)$2.0\,GeV < E_\gamma < 2.2\,GeV$ and (b)$2.2\,GeV < E_\gamma < 2.4\,GeV$. Photon tagger can only detect electrons for photon energies up to 0.95 of the electron energy or 2.35 GeV for g9a. Average photon energy per bin is given to nearest 25 MeV.

to the two axes of the Λ decay plane, which is rotated with respect to the production plane. The Λ direction vector and the decay proton direction vector define a plane. The z' axis is oriented along the direction of Λ motion, with the Λ always at $z' = 0$, because the primed axes are axes for the rest frame of the hyperon. The x' axis is that axis which is perpendicular to the z' axis and which also lies in the decay plane. $L_{x'}$ is constructed from an asymmetry in the distribution of the decay proton between the positive and negative x' axis paired with the asymmetry in the longitudinal polarization of the target.

It is apparent from the definition of the x' axis that a shift into the decay plane is not even necessary to determine the asymmetry. The relative momenta of the proton and the Λ in the center of mass frame is sufficient to distinguish protons moving along the positive x' axis to those moving in the negative direction on this axis. The plane is given by z' and the proton direction, so any movement of the proton outside of the Λ direction is necessarily movement in the x' direction. The conclusion is that those protons moving more into the forward direction (higher $\cos\vartheta_{CM}$) than the Λ are in the positive x' axis, while those moving more backward are in the negative x' axis. The yields for the "same" direction of polarization and "opposite" direction are then paired up to determine the raw asymmetry.

The full asymmetry $L_{x'}$ is the raw asymmetry corrected by the dilution factor, the Λ self analyzing factor α_Λ, the target polarization, and the effect of the angular distribution of the proton in the Λ rest frame on the asymmetry. For this final purpose it would be necessary to make a transform into the hyperon rest frame, but the yield is too low to reasonably subdivide bins further into $\cos\vartheta_{pY}$ bins. Therefore, instead of explicitly addressing the sloping behavior of the asymmetry, I introduce a factor of 2 for an approximately integrated result. The target polarization and dilution factor have already been calculated and the self analyzing factor is known to be $\alpha_\Lambda = 0.642 \pm 0.013$.[8] In Figures 4.8-4.12, $L_{x'}$ is plotted for each bin with error bars calculated using equation (4.7) and modified by the

multiplicative factors.

4.3 Target-Recoil Polarization Transfer $L_{z'}$

The extraction of $L_{z'}$ does require a transformation to the Λ rest frame. The positive z' axis points in the direction of the Λ momentum, so once the momentum vectors are shifted into a frame where the Λ has zero momentum, constructing the asymmetry is a simple matter of separating protons with positive z' momentum from those with negative z' momentum. The yields for these two groups are then subdivided into those collected when the target polarization was positive and those collected when it was negative and regrouped according to the usual approach for double polarization observables.

The transformation to the decay plane is accomplished by a secondary Lorentz boost from the center of mass frame in the direction of the Λ momentum followed by two rotations to orient the z' axis with the z axis of the particle momentum vectors. The missing momentum vector from K^+ is used as the Λ momentum vector and a boost vector is constructed from this momentum in similar fashion to equation (4.1). As the momentum vector for Λ typically lies off axis, the expression for the proton momentum in the Λ rest frame is more complicated than equation (4.2), but the general transformation equation is

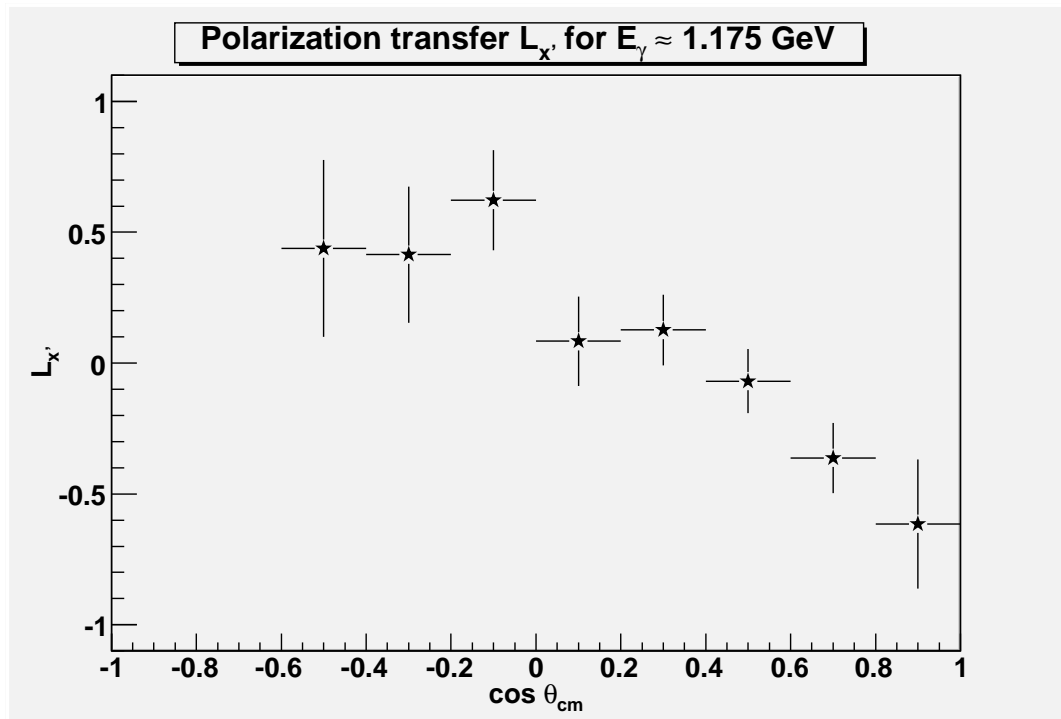$$p'_i = \frac{\gamma - 1}{\beta^2}(\beta_i)(\vec{\beta} \cdot \vec{p}) - \gamma\beta E) \, , \tag{4.8}$$

$$E' = \gamma(E - \vec{\beta} \cdot \vec{p}) \, , \tag{4.9}$$

where i = x, y, z are the space components, $\vec{p}$ is the 3-momentum vector of the particle in the center of mass frame (or original frame in general), and $\vec{\beta}$ is the boost vector constructed as previously described.

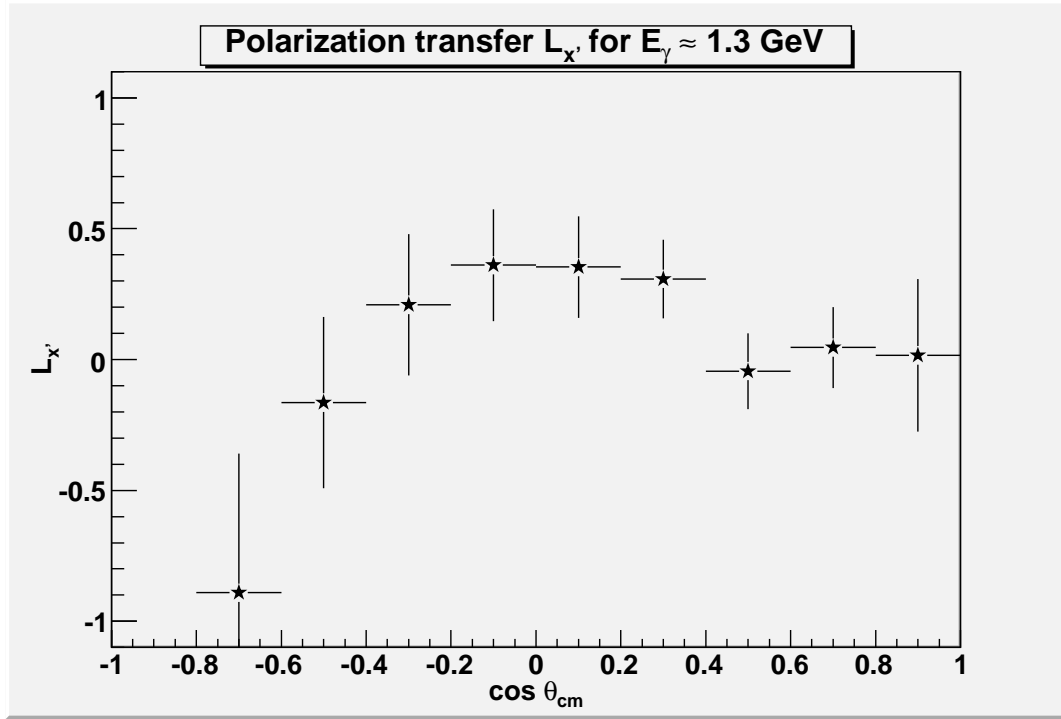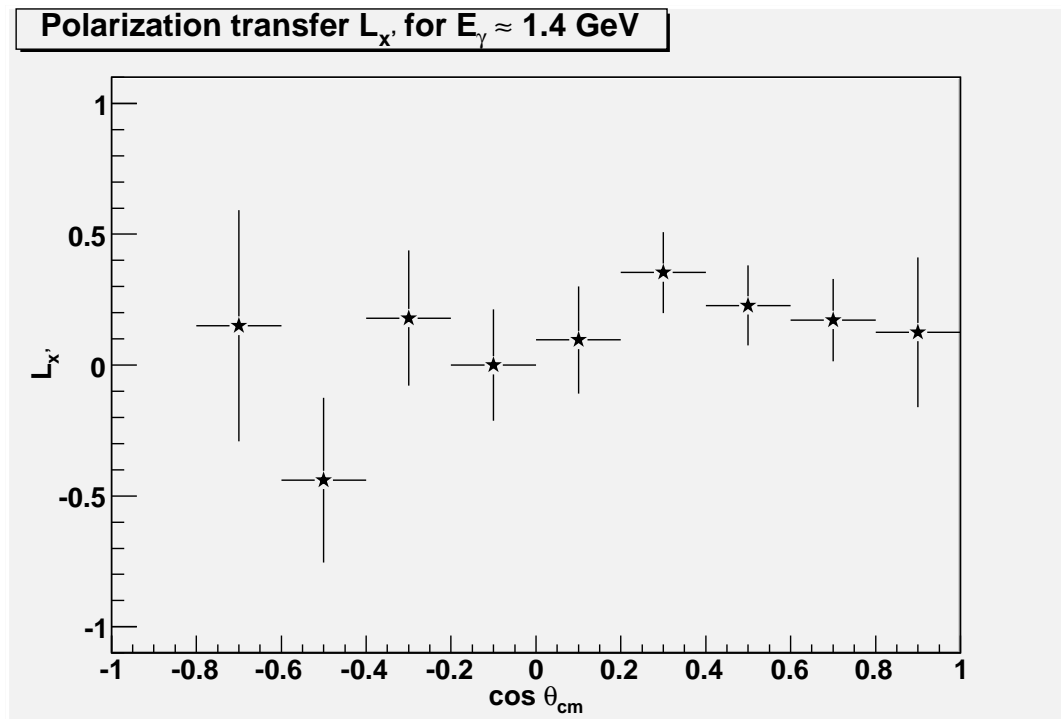After the boost operation is performed, the vectors are rotated so that the Λ direction
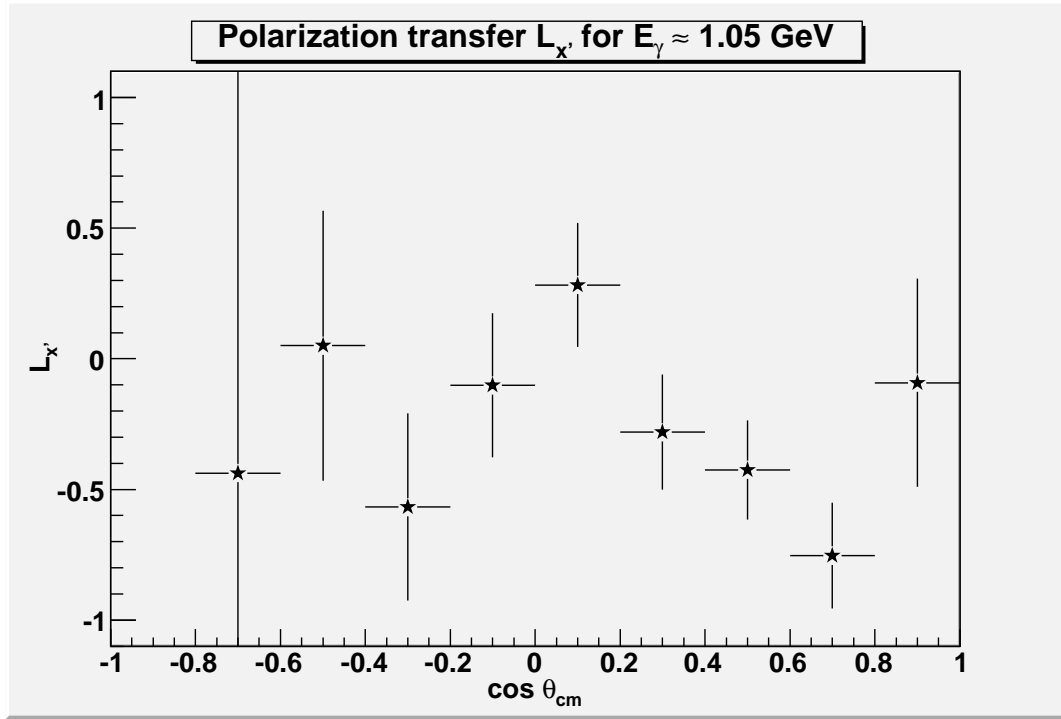
(a)

(b)

Figure 4.8: Target-Recoil Polarization Transfer $L_{x'}$ for incident photon energies in the ranges (a)$0.9\,GeV < E_\gamma < 1.1\,GeV$ and (b)$1.1\,GeV < E_\gamma < 1.25\,GeV$. Average photon energy per bin is given to nearest 25 MeV.
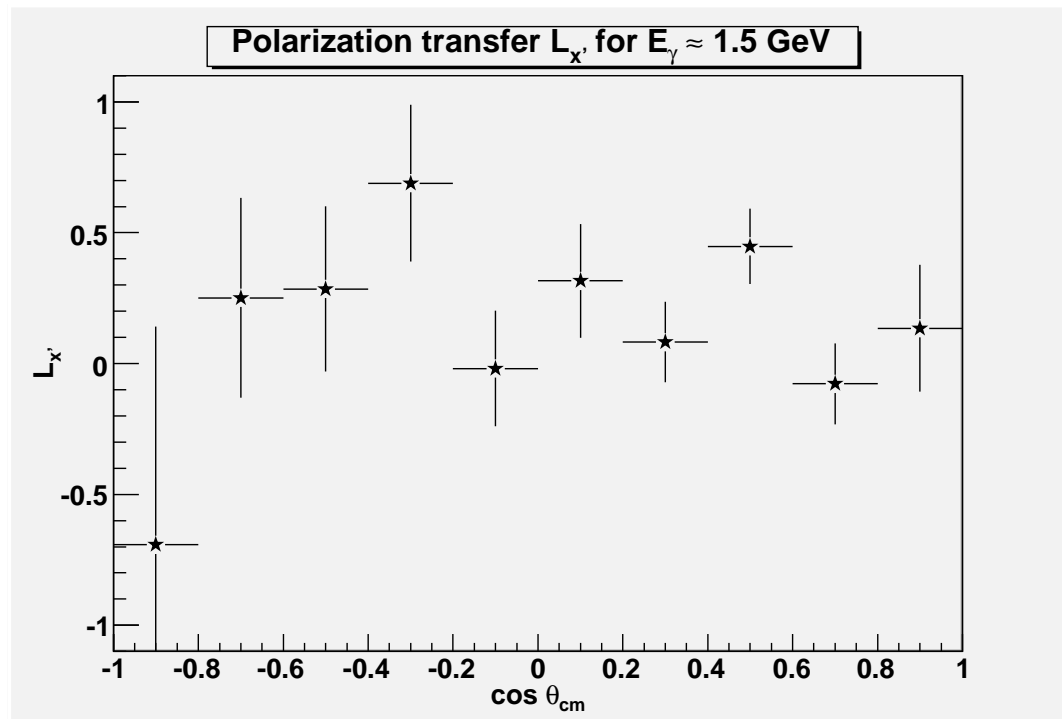
(a)

(b)

Figure 4.9: Target-Recoil Polarization Transfer $L_{x'}$ for incident photon energies in the ranges (a)$1.25\,GeV < E_\gamma < 1.35\,GeV$ and (b)$1.35\,GeV < E_\gamma < 1.45\,GeV$. Average photon energy per bin is given to nearest 25 MeV.

(a)
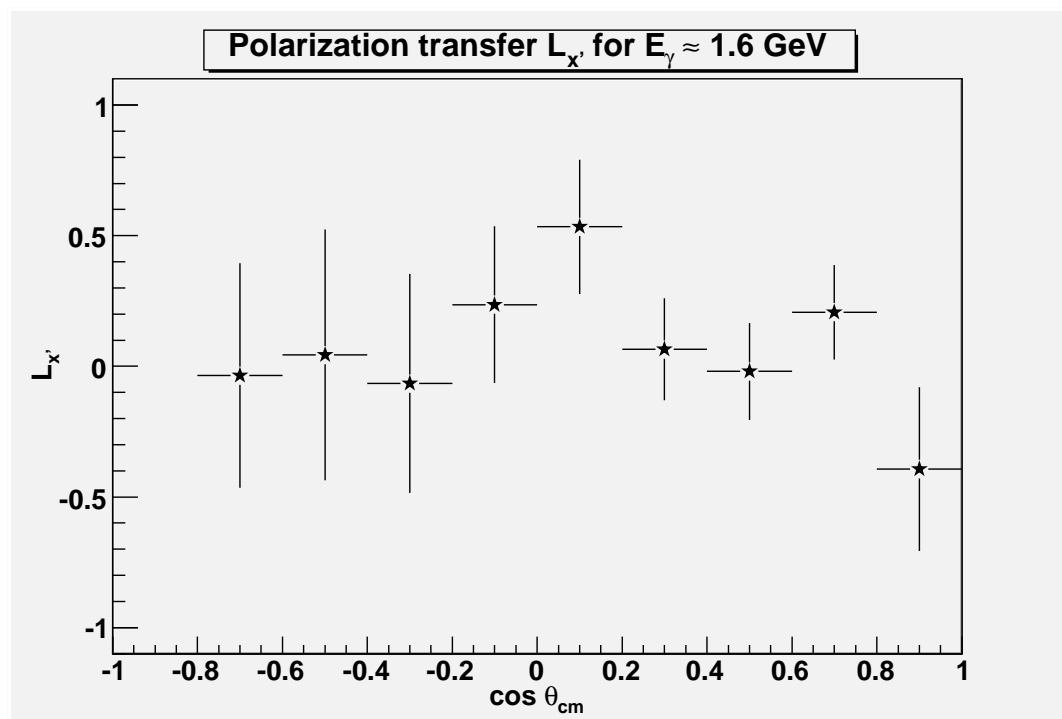

(b)

Figure 4.10: Target-Recoil Polarization Transfer $L_{x'}$ for incident photon energies in the ranges (a)$1.45\,GeV < E_\gamma < 1.55\,GeV$ and (b)$1.55\,GeV < E_\gamma < 1.65\,GeV$. Average photon energy per bin is given to nearest 25 MeV.

Figure 4.11: Target-Recoil Polarization Transfer $L_{x'}$ for incident photon energies in the ranges (a)$1.65\,GeV < E_\gamma < 1.8\,GeV$ and (b)$1.8\,GeV < E_\gamma < 2.0\,GeV$. Average photon energy per bin is given to nearest 25 MeV.
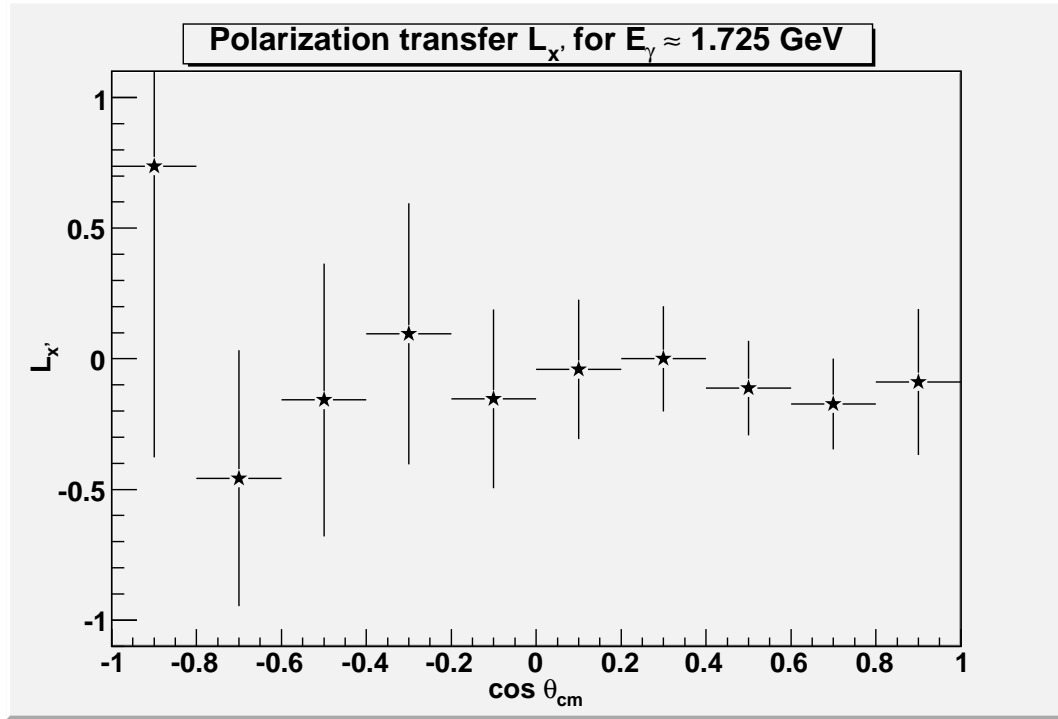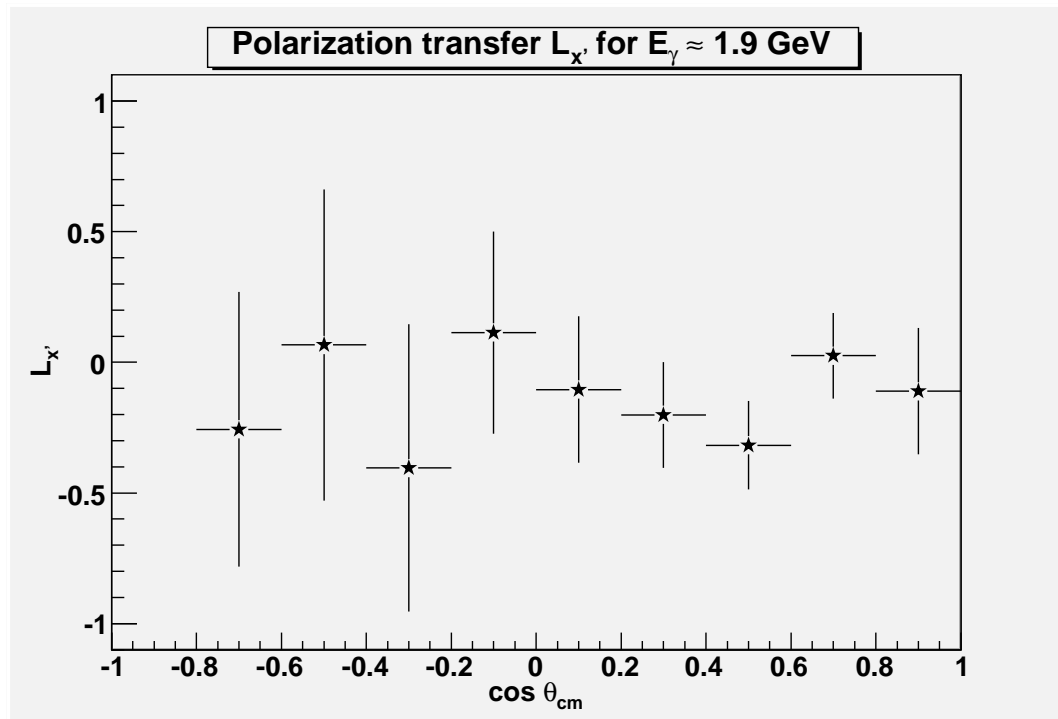
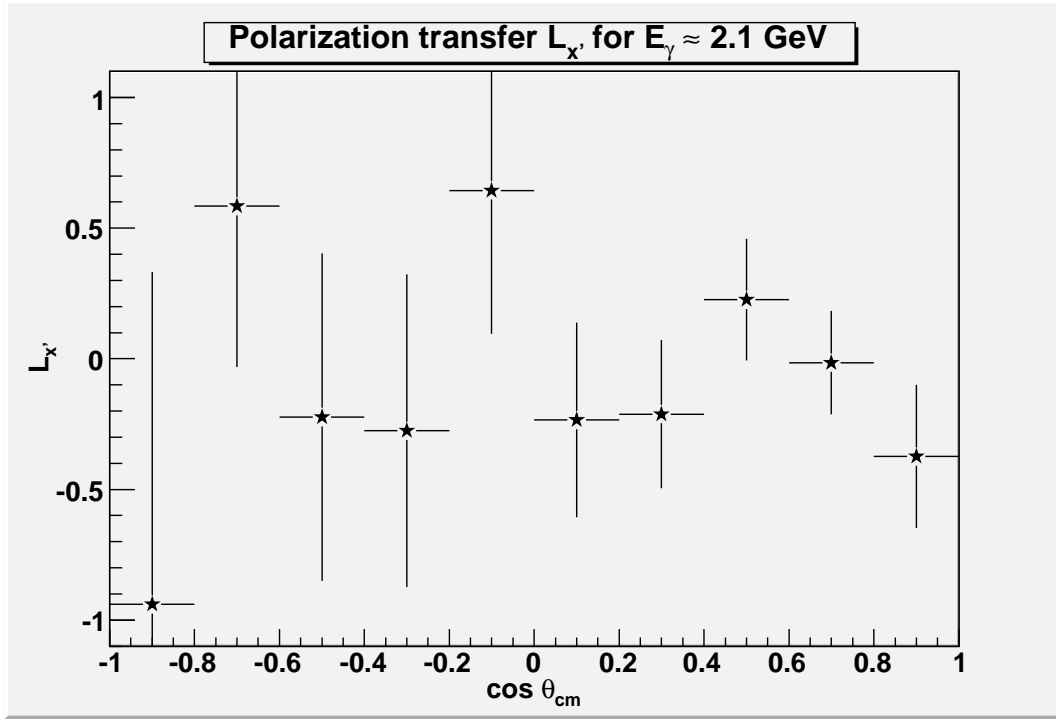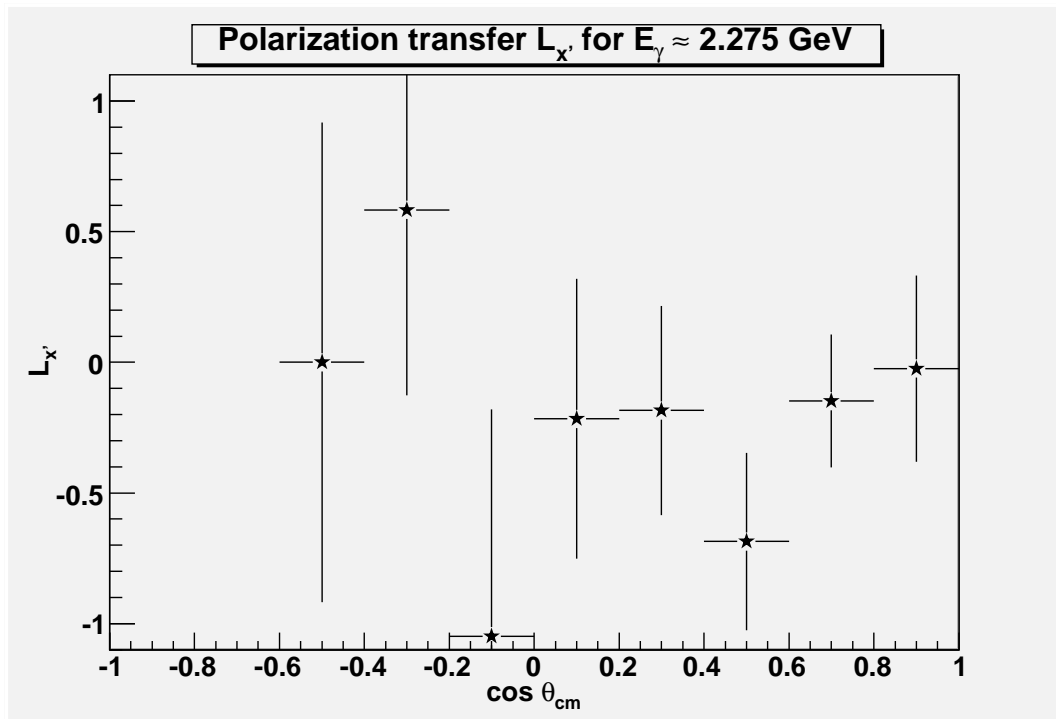(a)

(b)

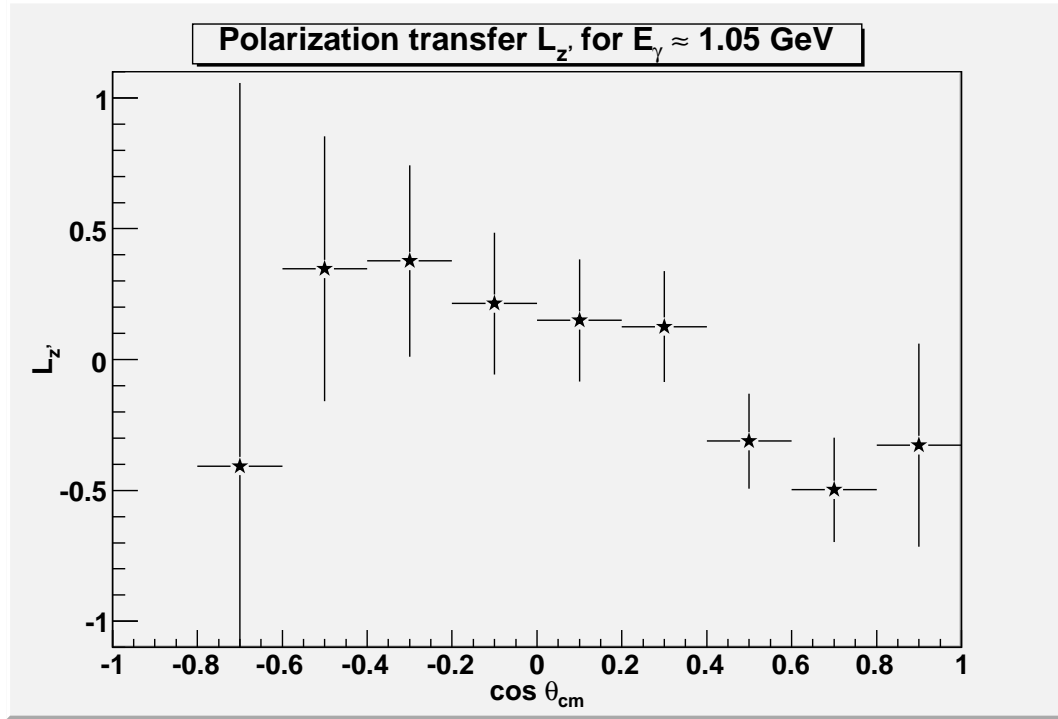Figure 4.12: Target-Recoil Polarization Transfer $L_{x'}$ for incident photon energies in the ranges (a)$2.0\,GeV < E_\gamma < 2.2\,GeV$ and (b)$2.2\,GeV < E_\gamma < 2.4\,GeV$. Average photon energy per bin is given to nearest 25 MeV.

lies in the positive z direction. First the ϕ position of Λ is used to rotate the vectors about the z-axis, which should rotate z' onto the x-z plane. Next the θ coordinate is used to make a rotation about the y-axis, which will orient the z-coordinate of the particle momentum vectors with the z'-axis. After these operations have been performed, the Λ has zero momentum in all directions and the proton distribution in the z' direction can be plotted using the z component of its momentum.

The raw asymmetry for $L_{z'}$ is modified by the same factors as $L_{x'}$ to get the full polarization observable. In Figures 4.13-4.17, I plot the full asymmetry with statistical errors for each of my 90 kinematic bins. A final result for $L_{z'}$ complete with systematic errors will be presented and discussed along with the results for $L_{x'}$ and E in the final chapter.

4.4 Summary

The first observations of $\gamma p \rightarrow K^+ \Lambda$ polarization observables involving the longitudinal polarization of the target protons have been plotted here. These measurements will no doubt be of use in carrying out a full model independent PWA of the reaction channel. In the interim, it is possible to make some inference on the presence or lack of resonances in the data by comparison with models including specific resonances and models which do not include that resonance. These comparisons will be made in Chapter 7, where I will draw my conclusions on the extracted observables.

(a)
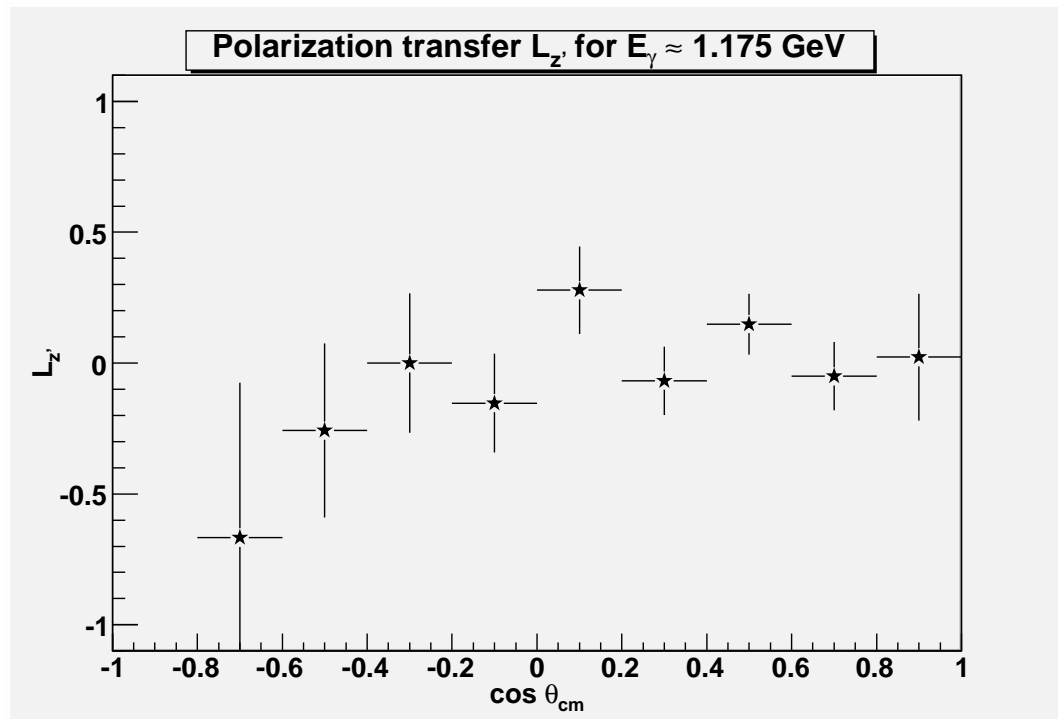
(b)

Figure 4.13: Target-Recoil Polarization Transfer $L_{z'}$ for incident photon energies in the ranges (a)$0.9\,GeV < E_\gamma < 1.1\,GeV$ and (b)$1.1\,GeV < E_\gamma < 1.25\,GeV$. Average photon energy per bin is given to nearest 25 MeV.

(a)

(b)

Figure 4.14: Target-Recoil Polarization Transfer $L_{z'}$ for incident photon energies in the ranges (a)$1.25\,GeV < E_\gamma < 1.35\,GeV$ and (b)$1.35\,GeV < E_\gamma < 1.45\,GeV$. Average photon energy per bin is given to nearest 25 MeV.

Figure 4.15: Target-Recoil Polarization Transfer $L_{z'}$ for incident photon energies in the ranges (a)$1.45\,GeV < E_\gamma < 1.55\,GeV$ and (b)$1.55\,GeV < E_\gamma < 1.65\,GeV$. Average photon energy per bin is given to nearest 25 MeV.

(a)

(b)

Figure 4.16: Target-Recoil Polarization Transfer $L_{z'}$ for incident photon energies in the ranges (a)$1.65\,GeV < E_\gamma < 1.8\,GeV$ and (b)$1.8\,GeV < E_\gamma < 2.0\,GeV$. Average photon energy per bin is given to nearest 25 MeV.
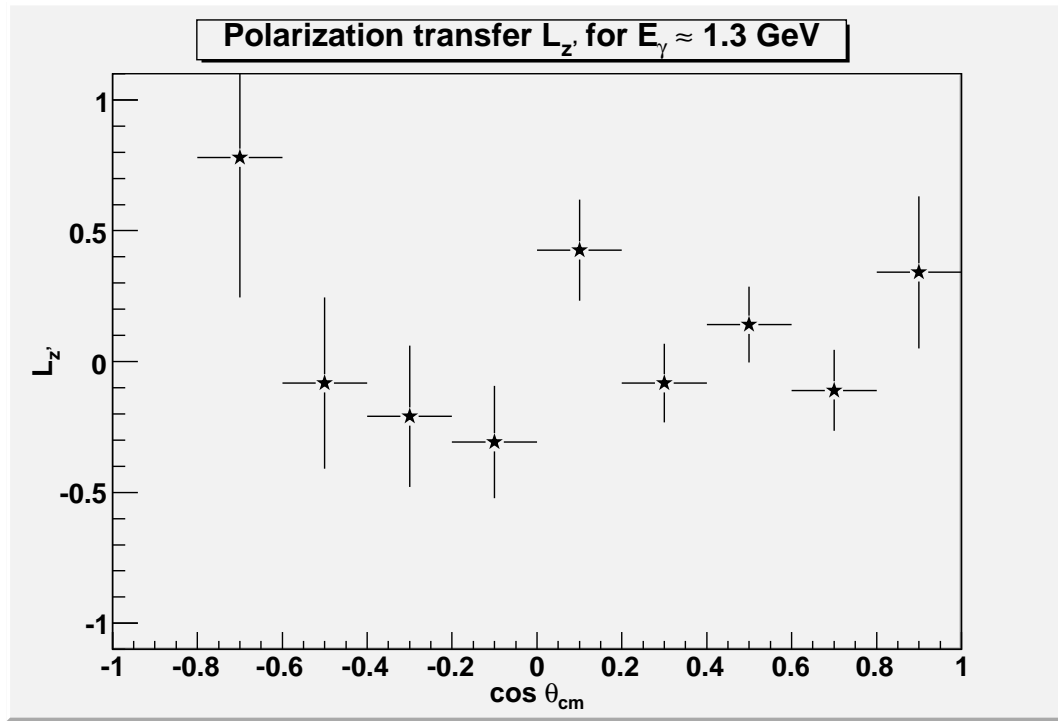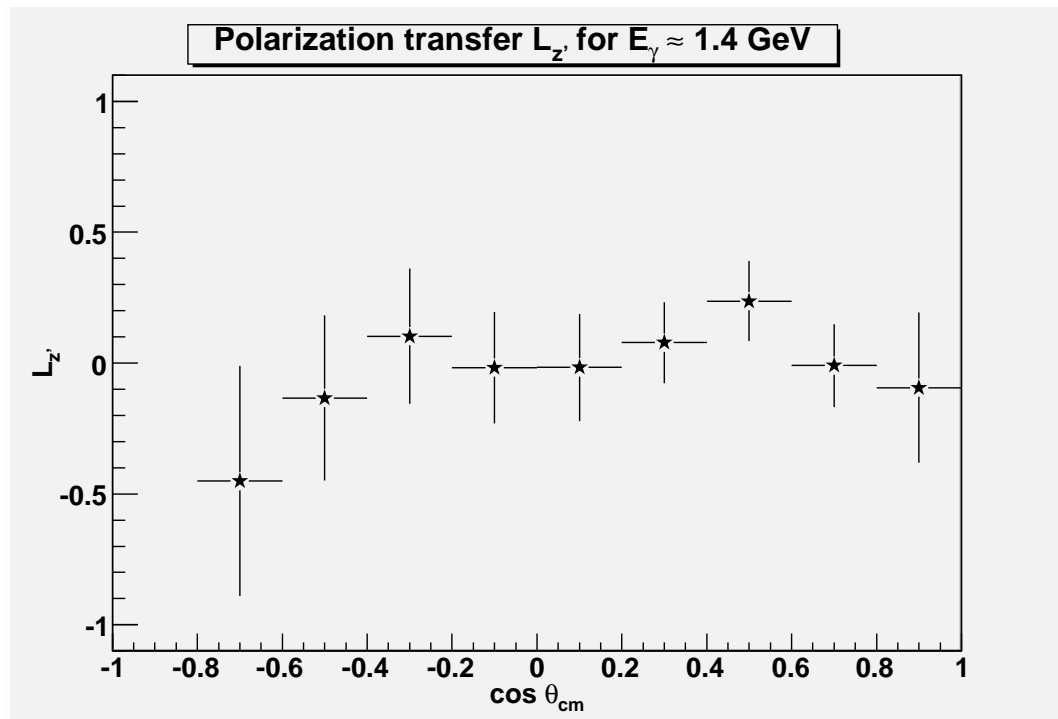
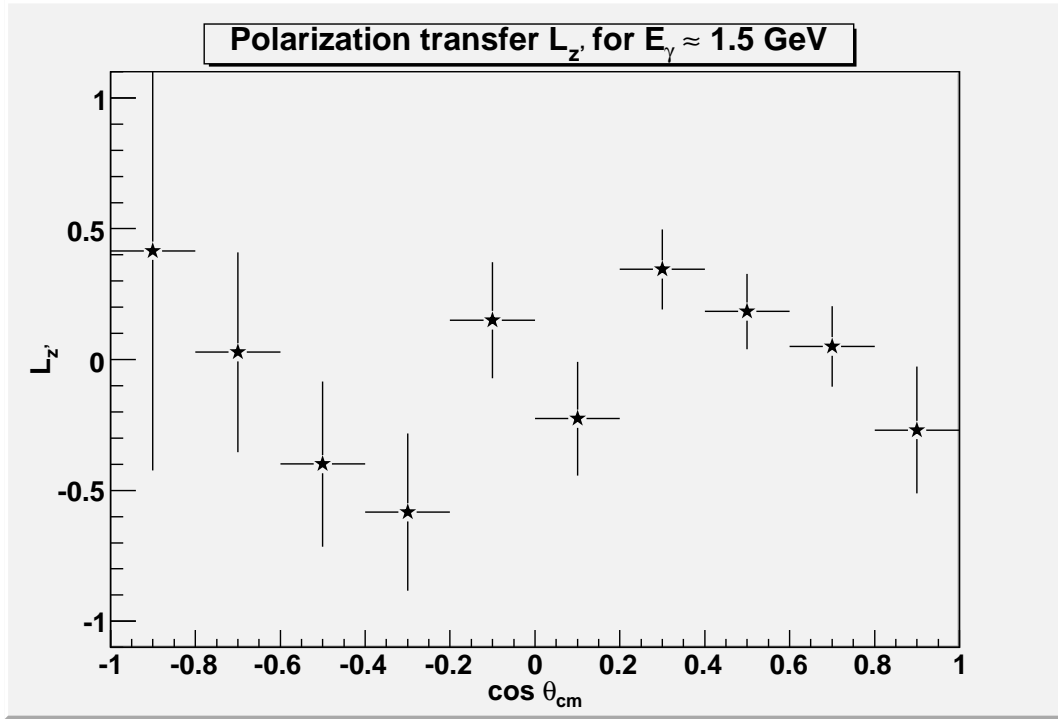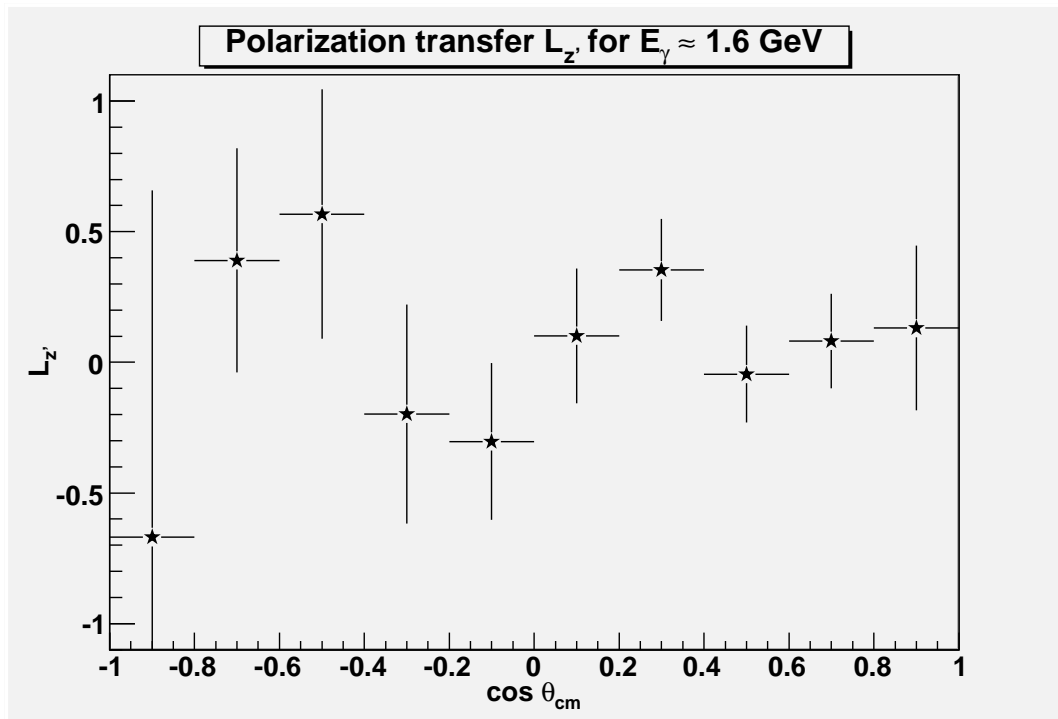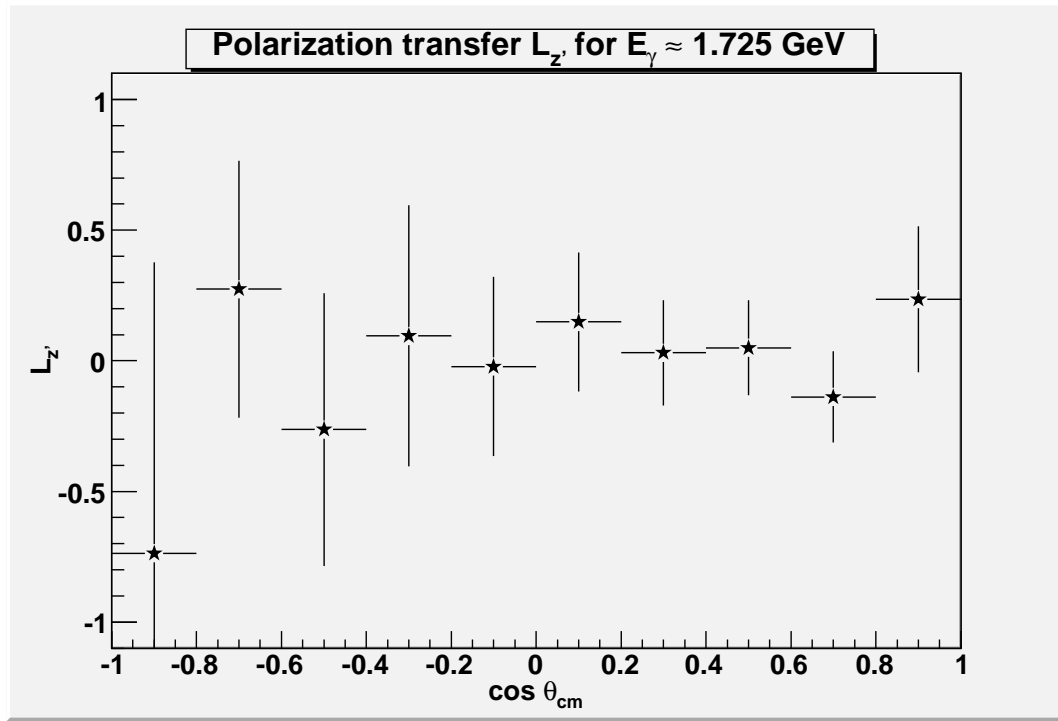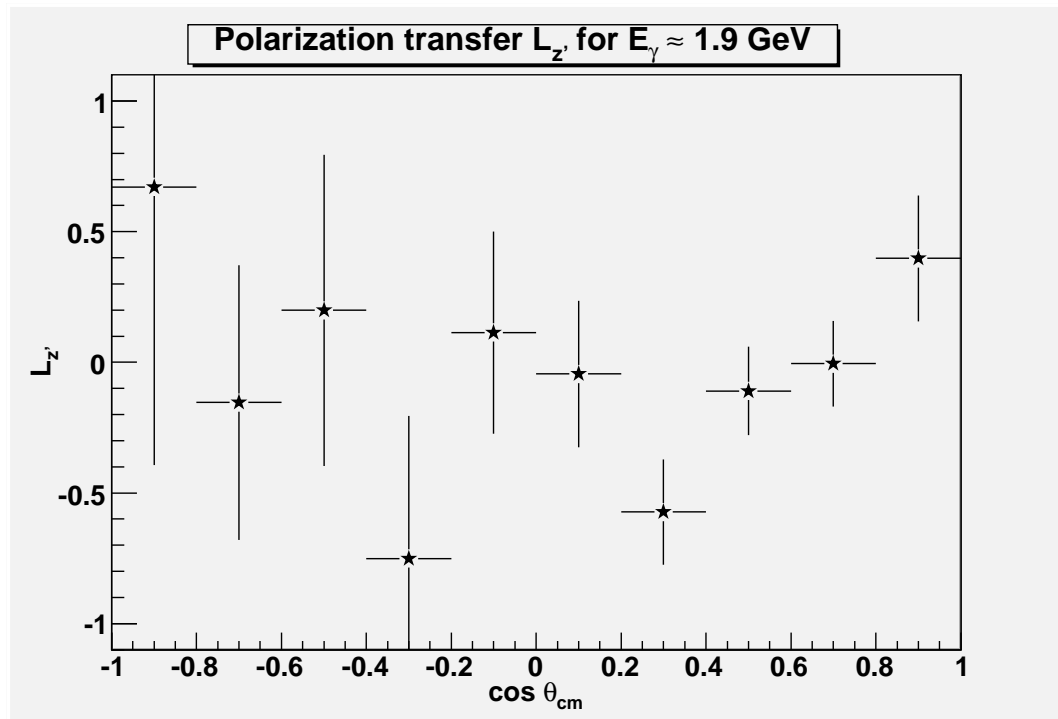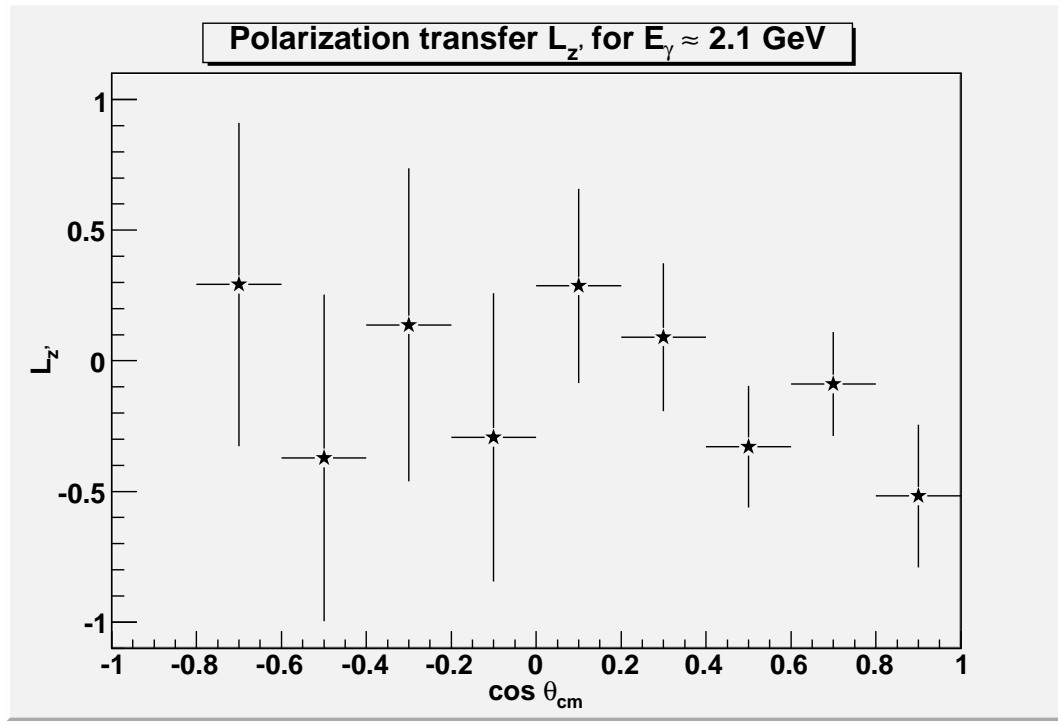(a)
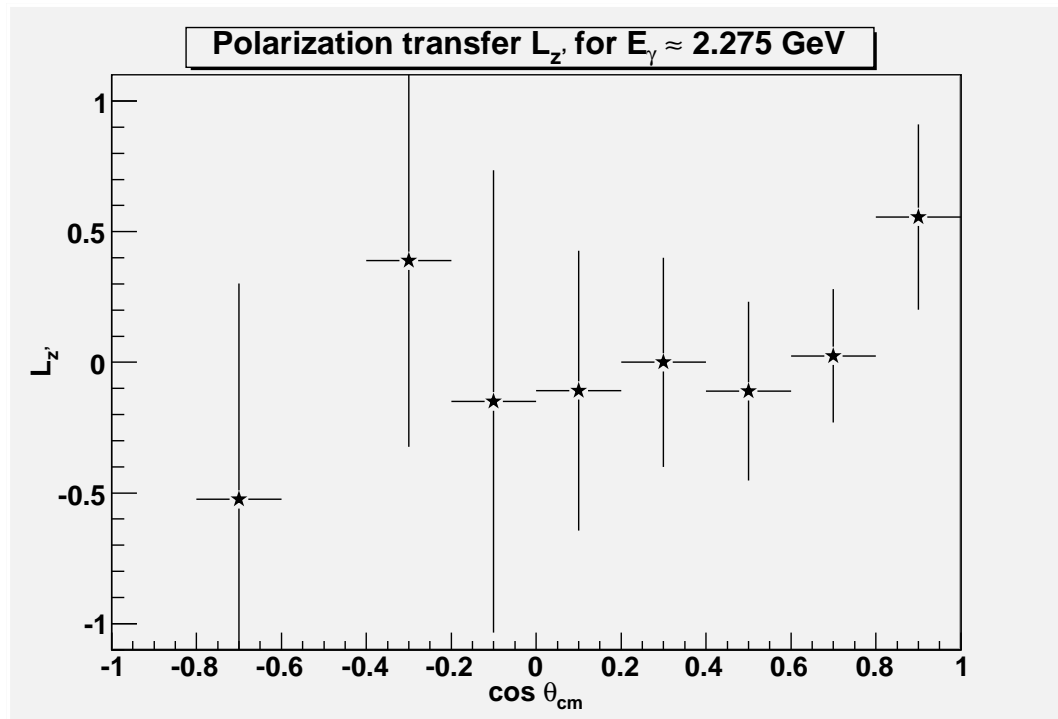
(b)

Figure 4.17: Target-Recoil Polarization Transfer $L_{z'}$ for incident photon energies in the ranges (a)$2.0\,GeV < E_\gamma < 2.2\,GeV$ and (b)$2.2\,GeV < E_\gamma < 2.4\,GeV$. Average photon energy per bin is given to nearest 25 MeV.

Chapter 5

Consistency Checks

While some of the polarization observables obtainable through the use of circularly polarized photons (those that do not require simultaneous polarization of the target) have been measured before to high precision, it behooves me to make measurements for all asymmetries possible within the constraints of the dataset. While the previous measurements of P, $C_{x'}$, and $C_{z'}$ were taken to better precision than can be accomplished with g9a data alone, the consistency between my calculations for these variables and those of previous groups can provide a good idea of the accuracy of my completely new measurements. In particular, since these observables all involve the recoil hyperon, they offer a good test of the quality of my extracted $L_{x'}$ and $L_{z'}$. Since the statistics necessitate a coarser binning in my plots for certain energy ranges than those of g11, g8b, and g1c analyses, the differences in my measurements for P, $C_{x'}$, and $C_{z'}$ may give us a decent understanding of the effect of such coarse binning on the sensitivity of this analysis to the presence of resonant structures.

5.1   Recoil Polarization

The recoil polarization is taken as an asymmetry in the distribution of the decay proton between those protons moving above the hyperon production plane and those moving below
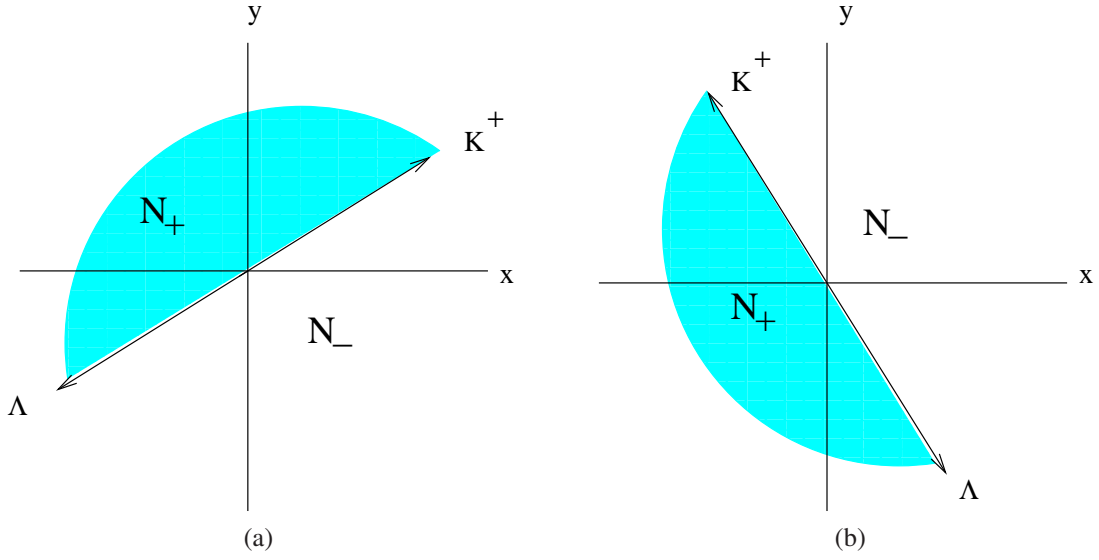
Figure 5.1: Recoil polarization yield designations by phi position of the proton. Counterclockwise rotation from K^+ to Λ vector projections in the x-y plane gives the region "above" the production plane.

it. The hyperon production plane is defined by the distribution of K^+ and Λ, such that the plane is tilted at a degree φ with respect to the x-y plane defined by CLAS. If we take the direction of K^+ as the zero angle point, than any proton detected in the range 0 to π, where π is given by the position of Λ, is allocated to the N_+ yield, while all others are allocated to the N_- yield. Figure 5.1 shows a plot of these regions depending on the relative positions of K^+ and Λ.

The recoil polarization is then modified by the self-analyzing factor of the Λ decay, α_Λ. Only pK^+ events can be used for polarization observables involving the recoil hyperon, because one of the decay products of the Λ must be detected to obtain the asymmetry. In principle, events without a detected proton, but with a π^- could be used in the same manner, but in practice the statistics offered by such events were deemed insufficient.

The inclusion of these factors gives a complete equation for extraction of recoil polarization

$$P = \frac{2D_{eff}}{\alpha_\Lambda} \frac{N_+ - N_-}{N_+ + N_-} \,, \tag{5.1}$$

The multiplicative factor of 2 is introduced to account for the integration of the asymmetry over $cos\vartheta_{pY}$. Applying this equation over my 90 kinematic bins in E_γ and $cos\vartheta_{cm}$, I obtain the results shown in Figures 5.2 - 5.6.

My results are plotted together with those for the g11 analysis.[21] The energy binning for g11 is very fine, on the order of 20 MeV in E_γ, corresponding to the selected bin size of 10 MeV in center of mass energy W, so my plots of 100 MeV bins in energy cover a range of about 5 bins for g11 data and at the extremes my bins are even larger. Nonetheless, I only plot the g11 results closest to my central point energy to determine the similarity between the asymmetry for the wide range I'm using and for a very narrow range around the energy values of interest. My binning of 0.2 in $cos\vartheta_{cm}$ is also wider than the 0.1 binning in the g11 data. In spite of the coarse binning, these plots seem to show good agreement, especially in the forward angle regions. The agreement for my 100 MeV bins is fairly good even in the backwards direction, where my $K^+\Lambda$ yield is poorer.

5.2 Polarization Transfer $C_{x'}$ and $C_{z'}$

The polarization transfer observables for the circularly polarized beam are calculated in essentially the same way as the polarization transfer for the longitudinally polarized target. The only difference is that the degree of circular polarization and the photon helicity are used instead of the target polarization magnitude and direction. Thus, the equation for calculating these is

$$C_{x'/z'} = \frac{2}{\alpha_\Lambda P_\gamma} \frac{N_+ - N_-}{N_+ + N_-} \, , \tag{5.2}$$

where N_+ and N_- are defined as for $L_{x'}$ and $L_{z'}$.

The method of extraction I used is somewhat different from the method Bradford used to obtain the g1c results for C_x and C_z. Bradford plotted the beam helicity asymmetry against the proton distribution in $cos\vartheta_{pY}$. He then took the slope for these plots and divided

(a)

(b)
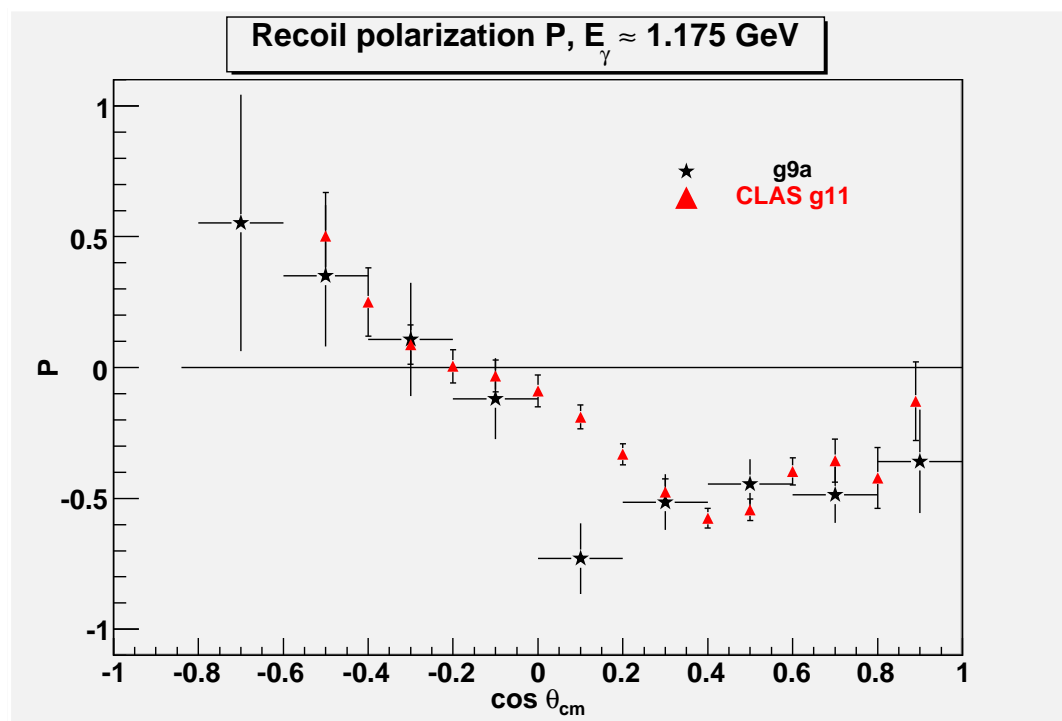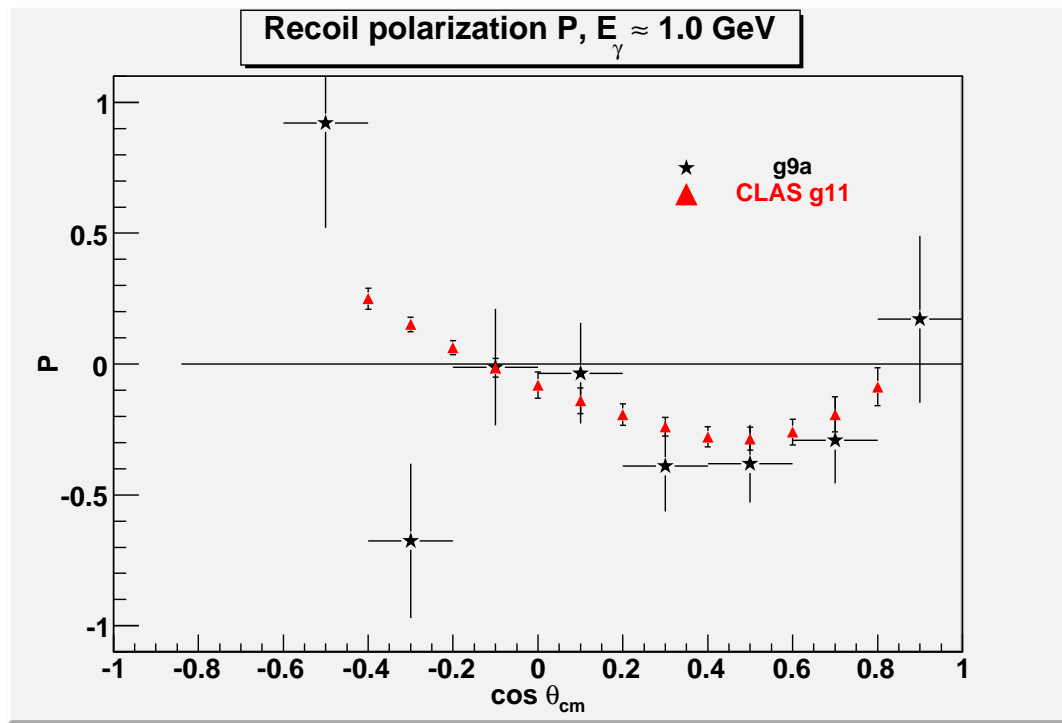
Figure 5.2: Recoil polarization for g9a plotted with the g11 analysis results (marked with triangles).
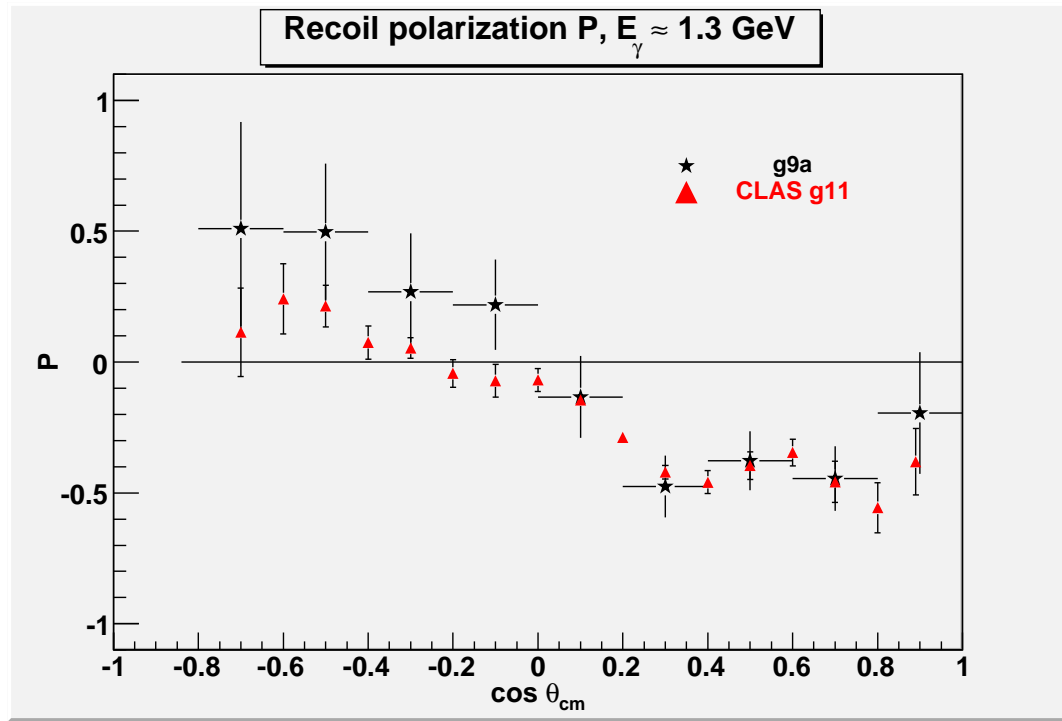
(a)
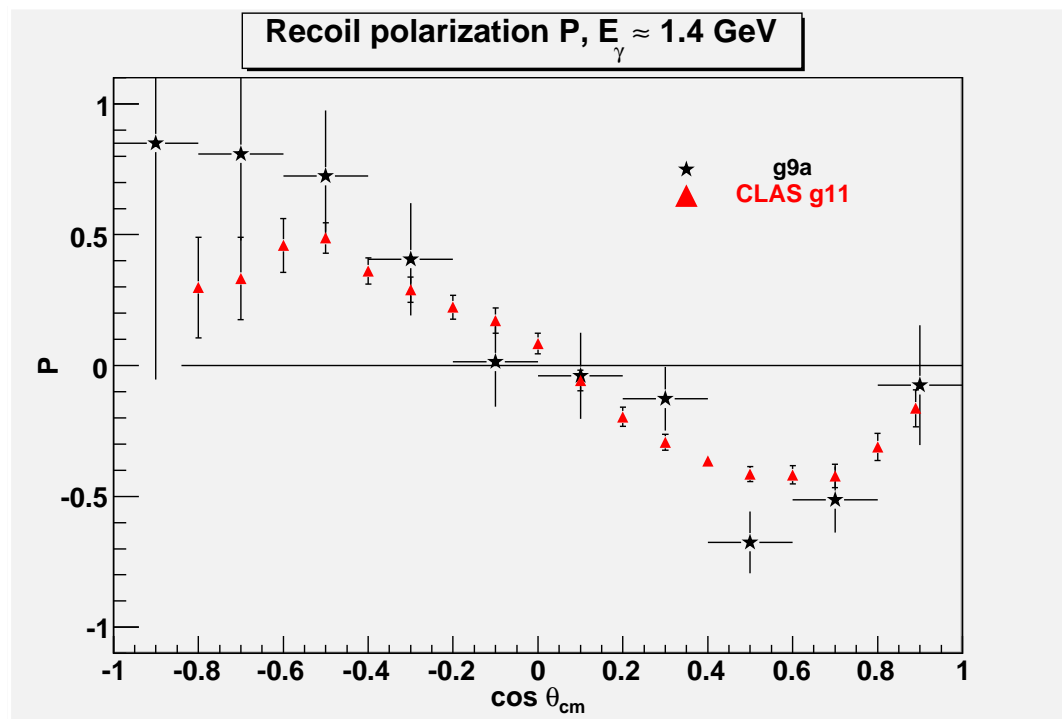
(b)

Figure 5.3: Recoil polarization for g9a plotted with the g11 analysis results (marked with triangles).
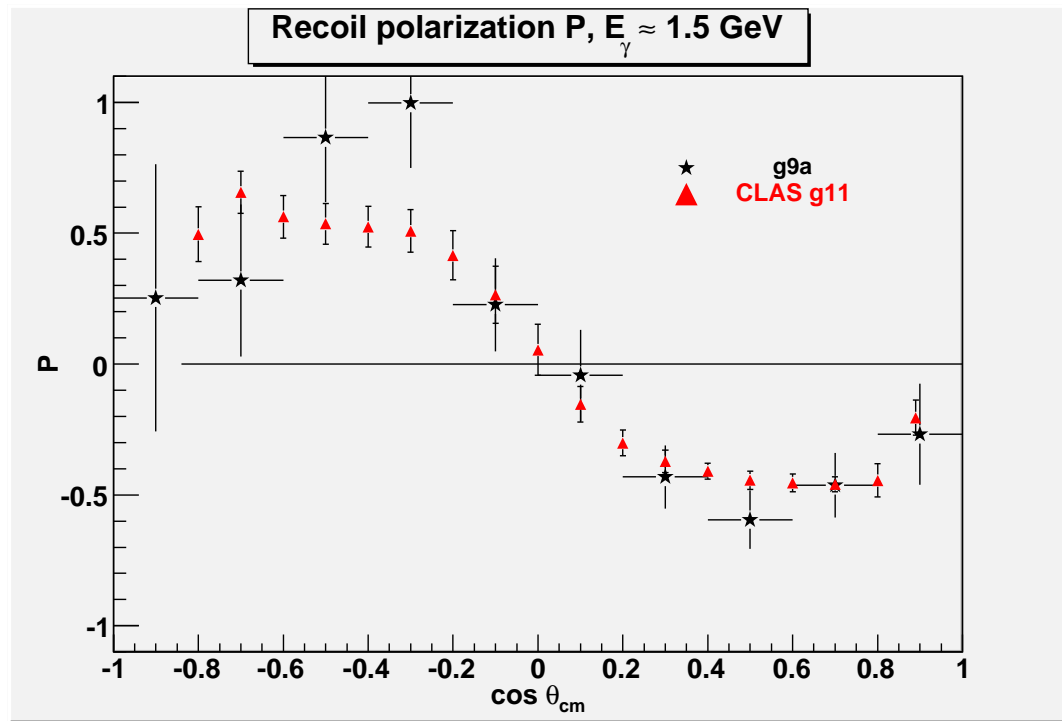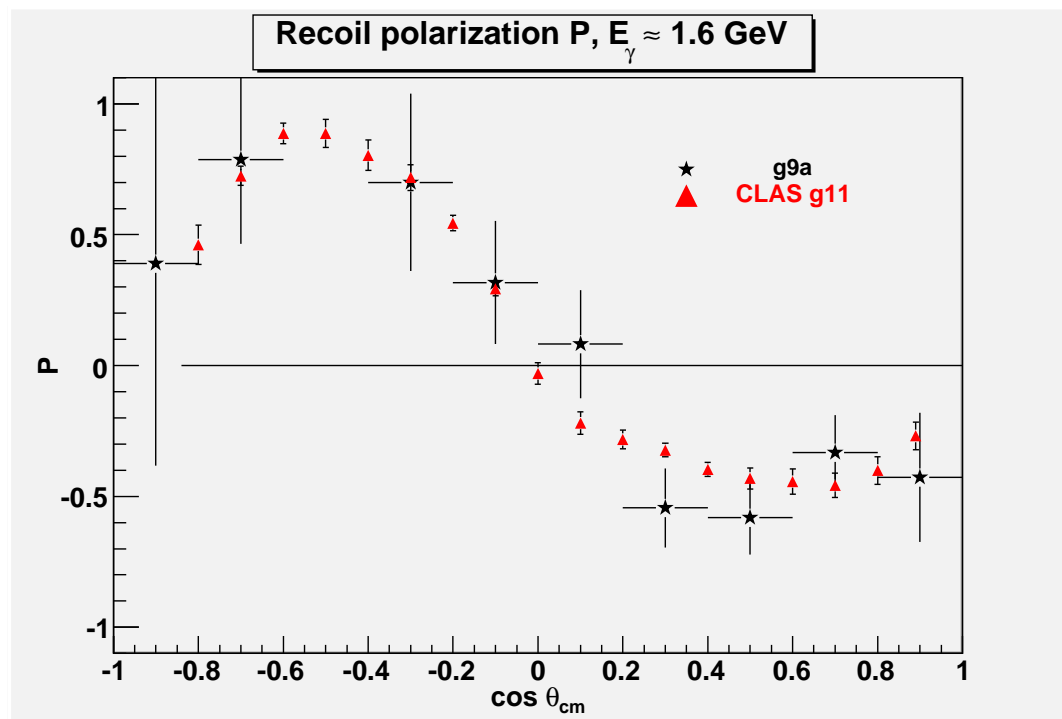
Figure 5.4: Recoil polarization for g9a plotted with the g11 analysis results (marked with triangles).
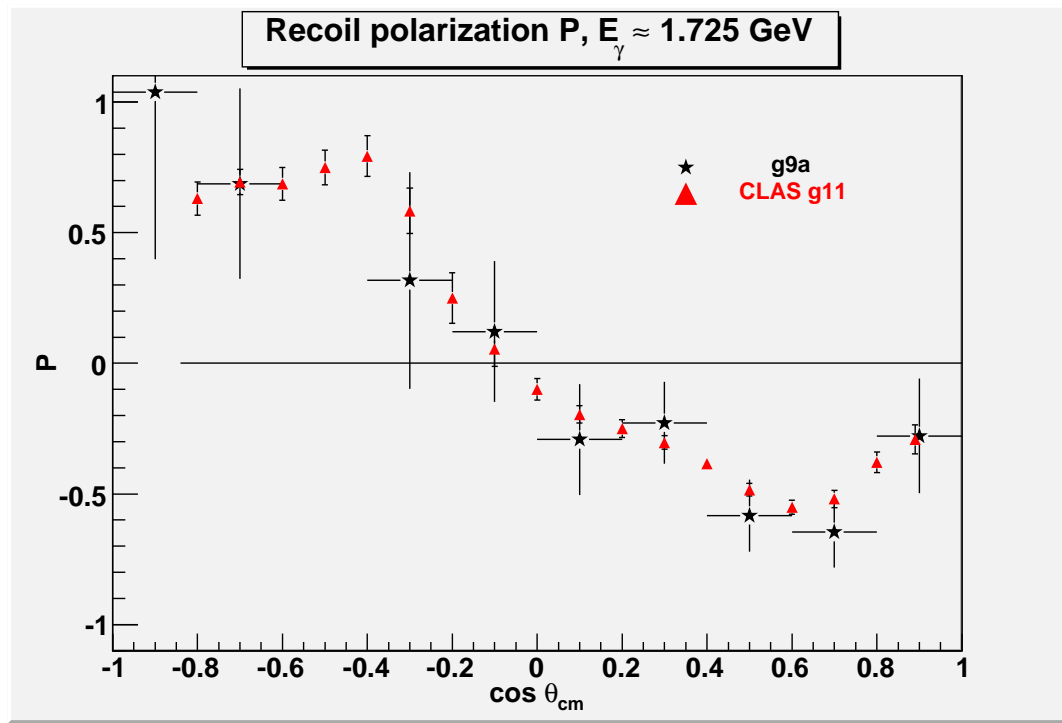
(a)
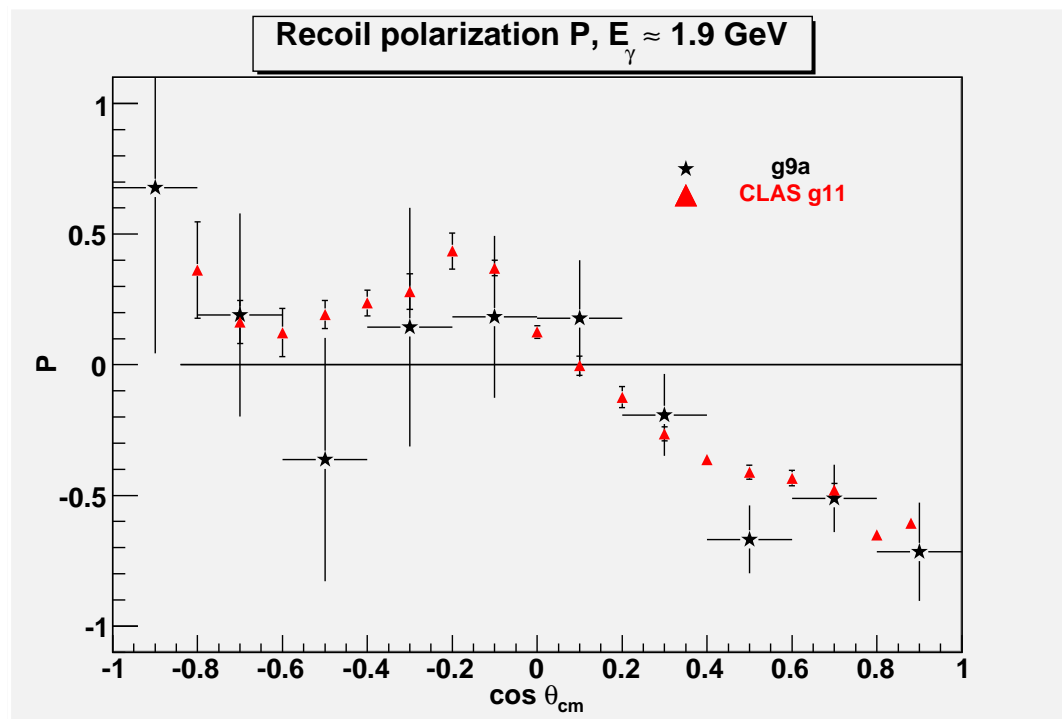
(b)

Figure 5.5: Recoil polarization for g9a plotted with the g11 analysis results (marked with triangles).
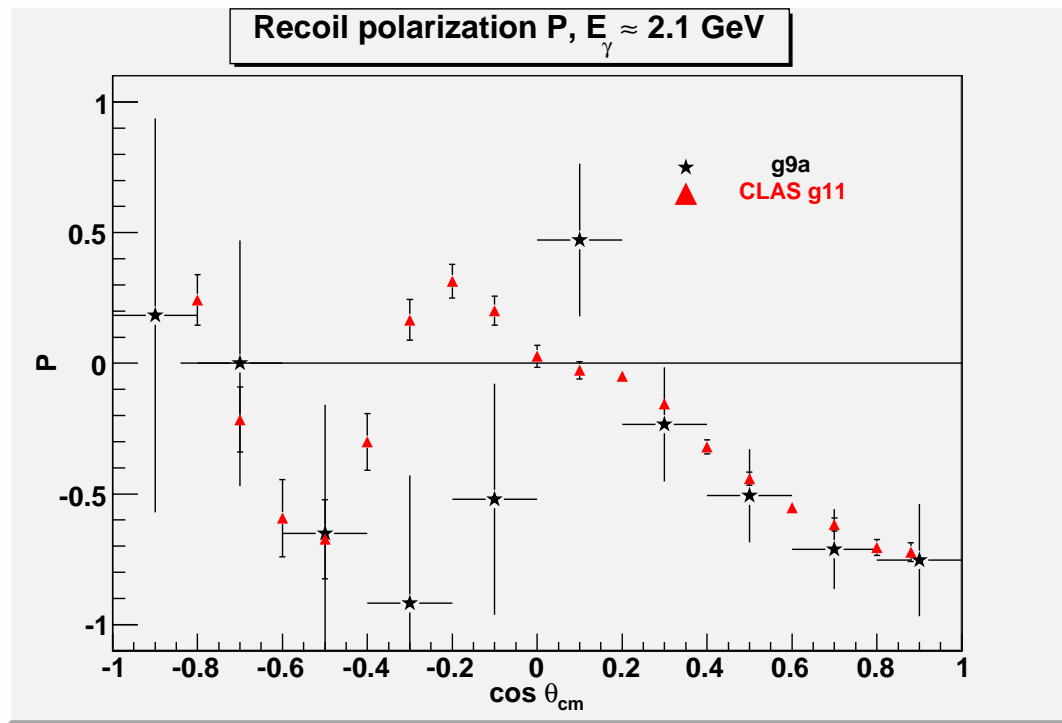
(a)
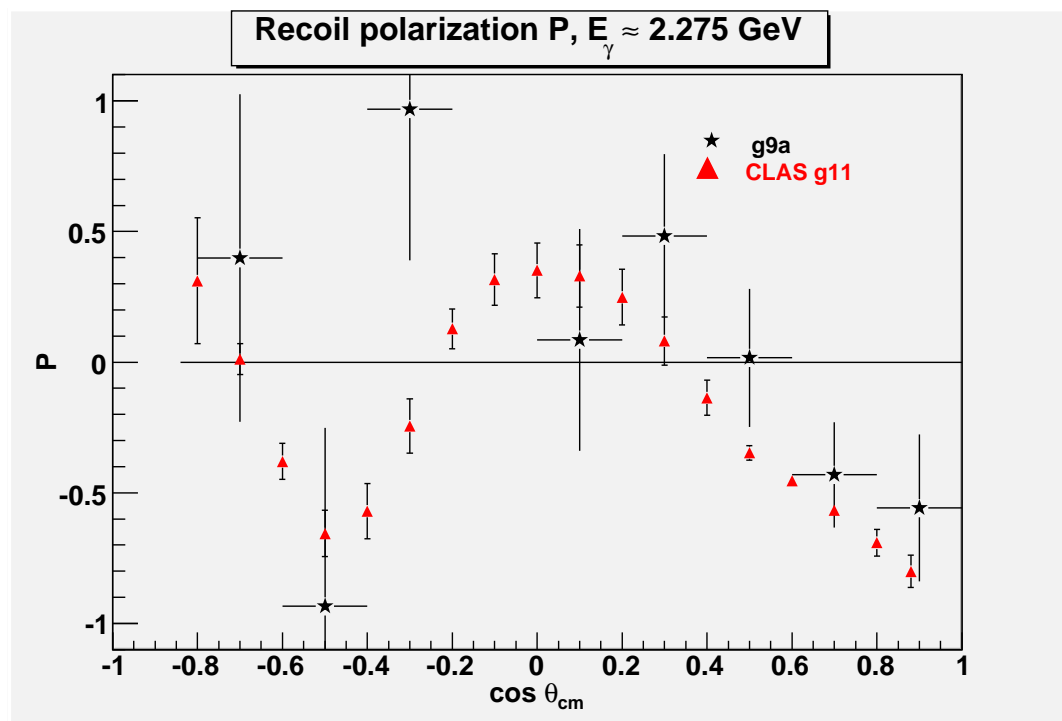
(b)

Figure 5.6: Recoil polarization for g9a plotted with the g11 analysis results (marked with triangles).
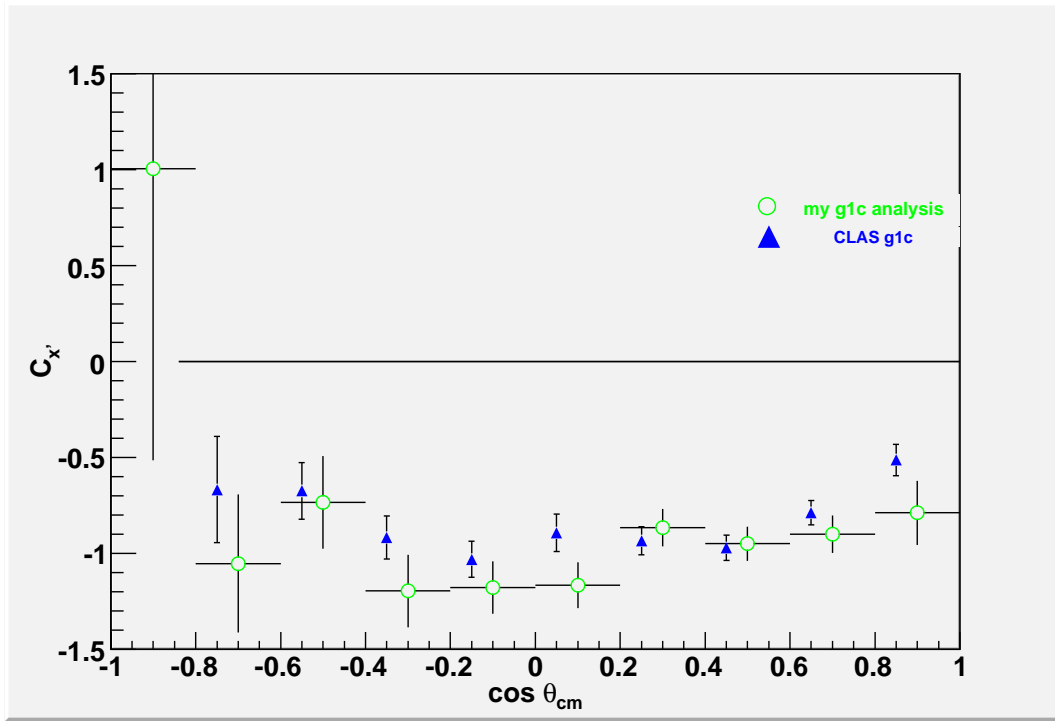
(a)
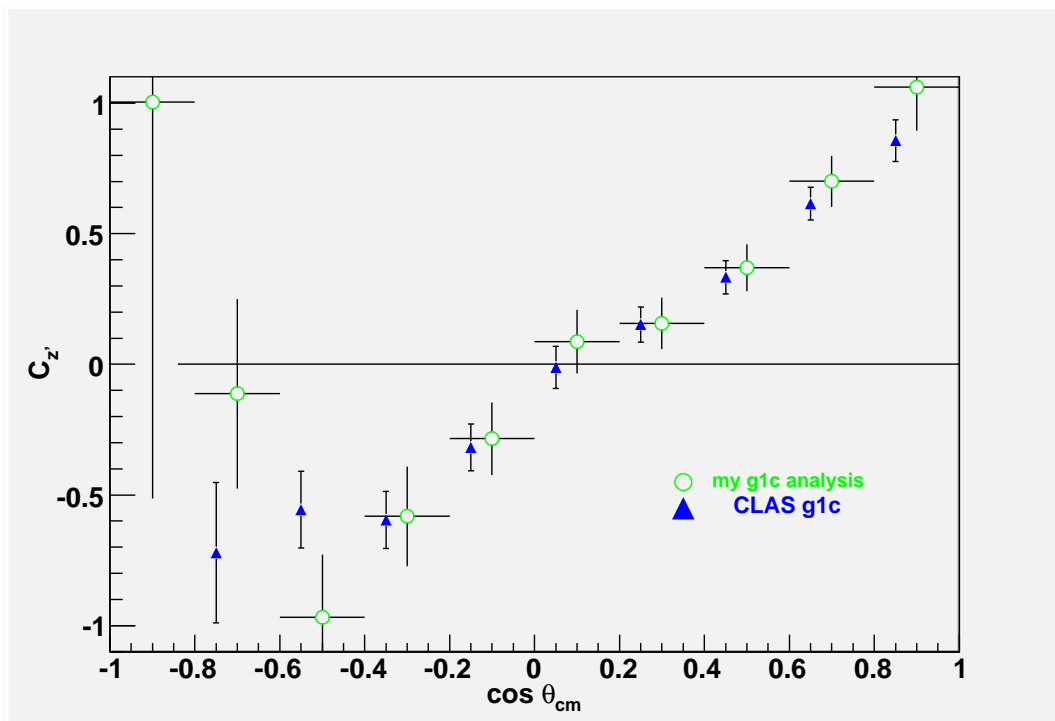
(b)

Figure 5.7: $C_{x'}$ and $C_{z'}$ for the photon energy range $1.25\,GeV < E_\gamma < 1.35\,GeV$ using my method on g1c data (marked with open circles) plotted with g1c analysis results (marked with blue triangles) converted into the primed coordinate system.
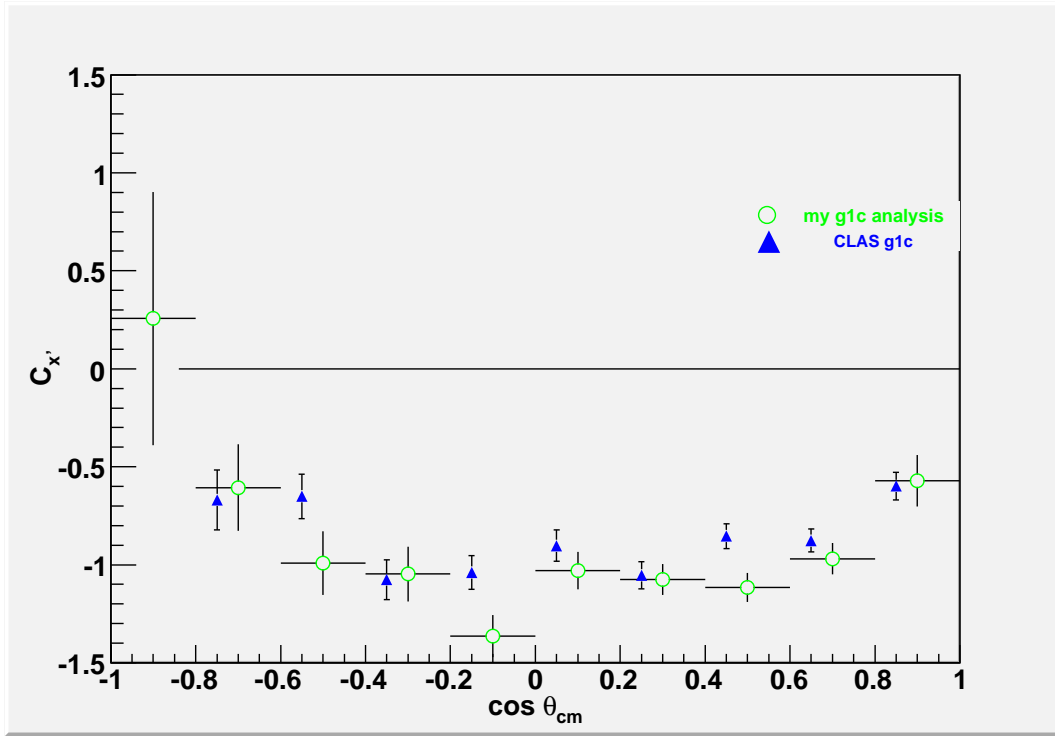
(a)
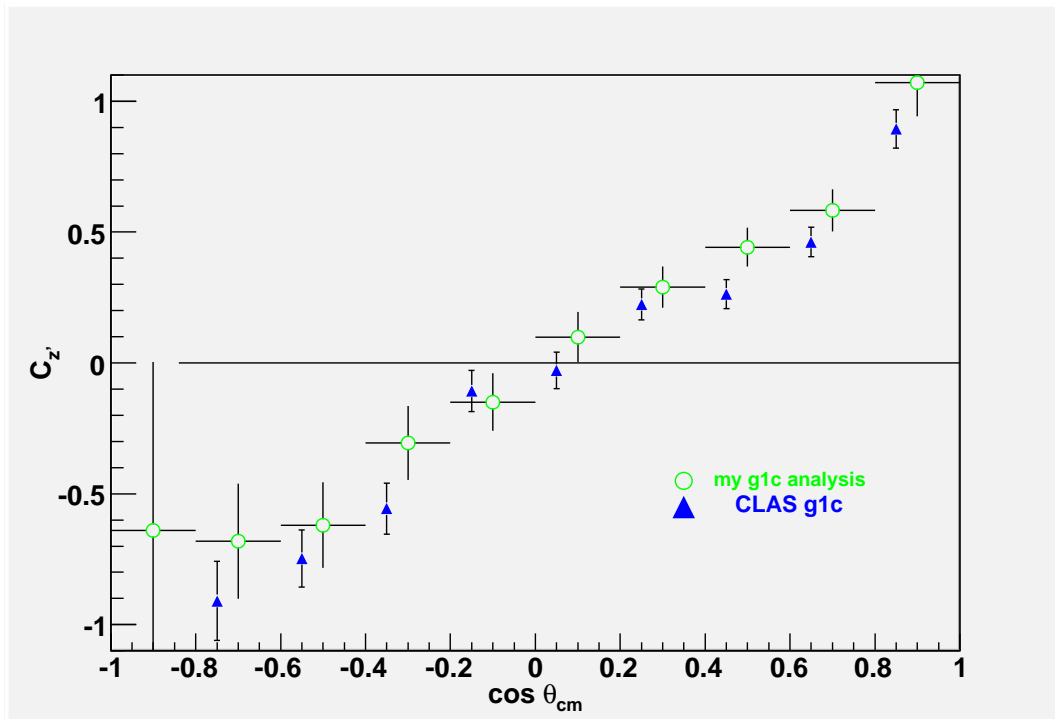
(b)

Figure 5.8: $C_{x'}$ and $C_{z'}$ for the photon energy range $1.35\,GeV < E_\gamma < 1.45\,GeV$ using my method on g1c data (marked with open circles) plotted with g1c analysis results (marked with blue triangles) converted into the primed coordinate system.
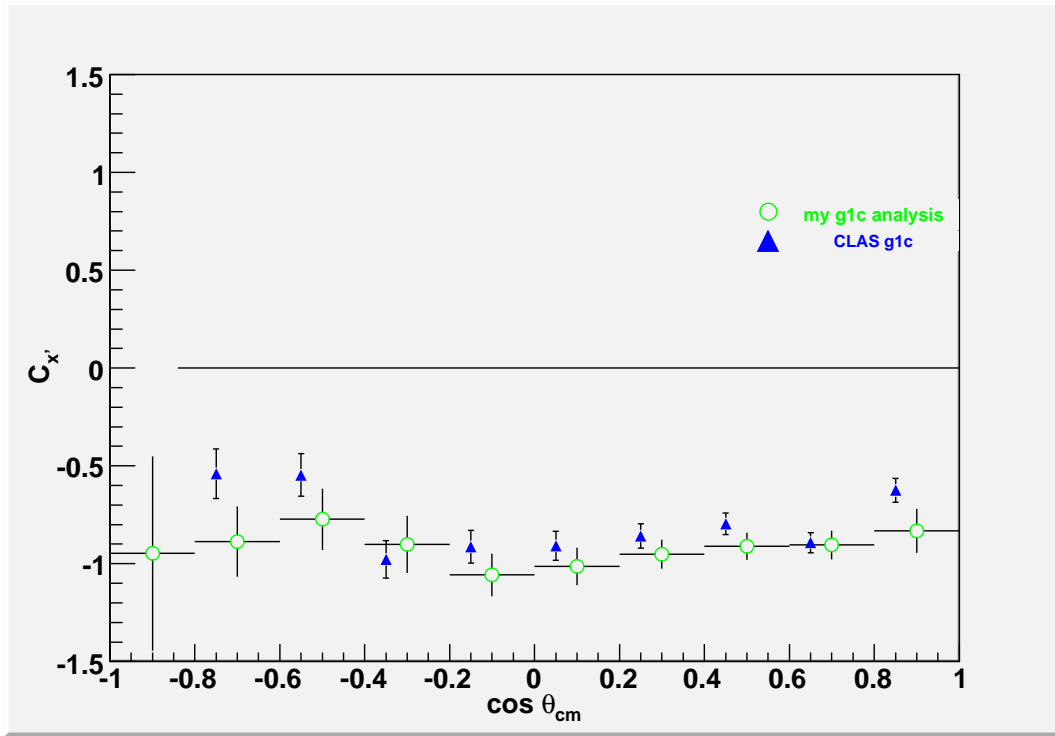
(a)
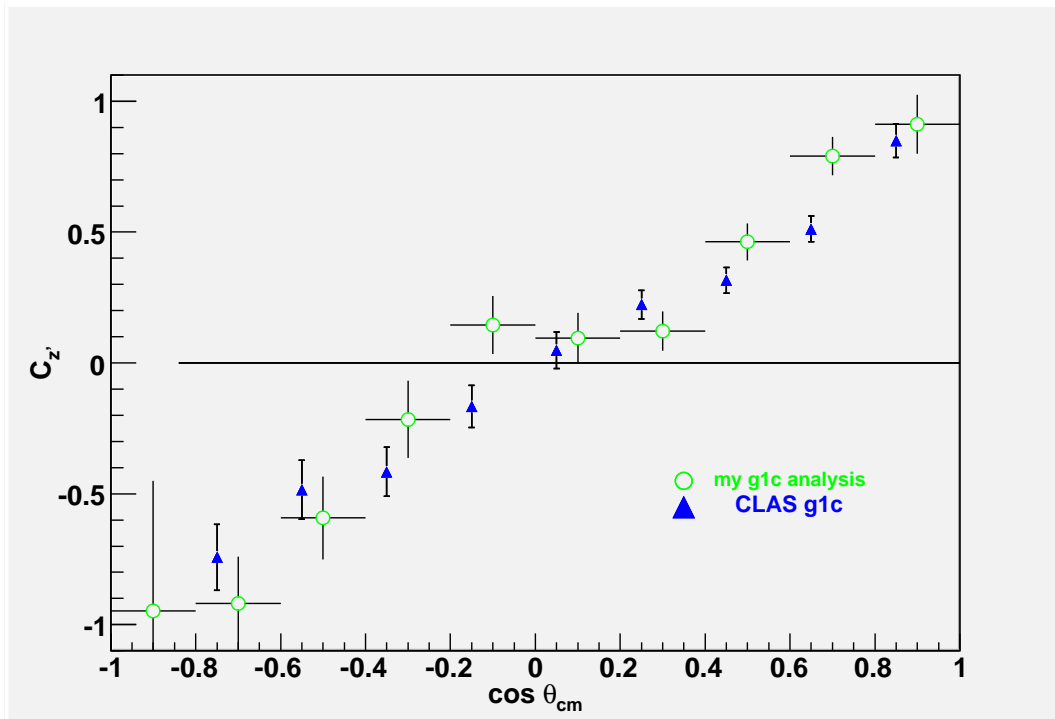
(b)

Figure 5.9: $C_{x'}$ and $C_{z'}$ for the photon energy range $1.45\,GeV < E_\gamma < 1.55\,GeV$ using my method on g1c data (marked with open circles) plotted with g1c analysis results (marked with blue triangles) converted into the primed coordinate system.
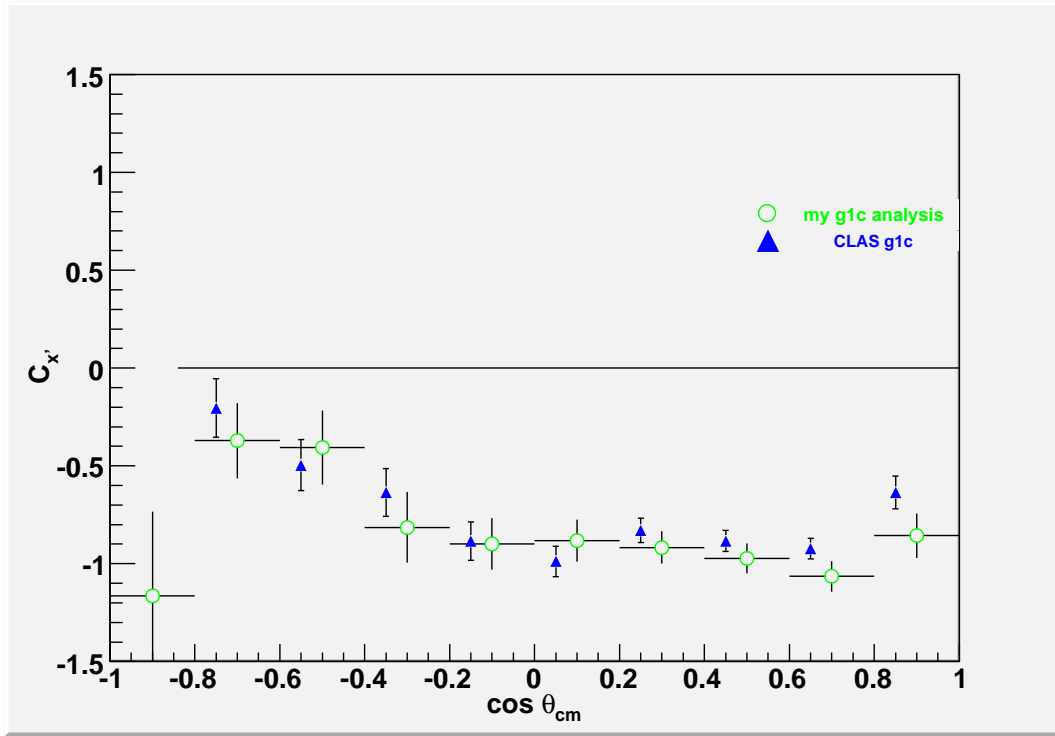
(a)
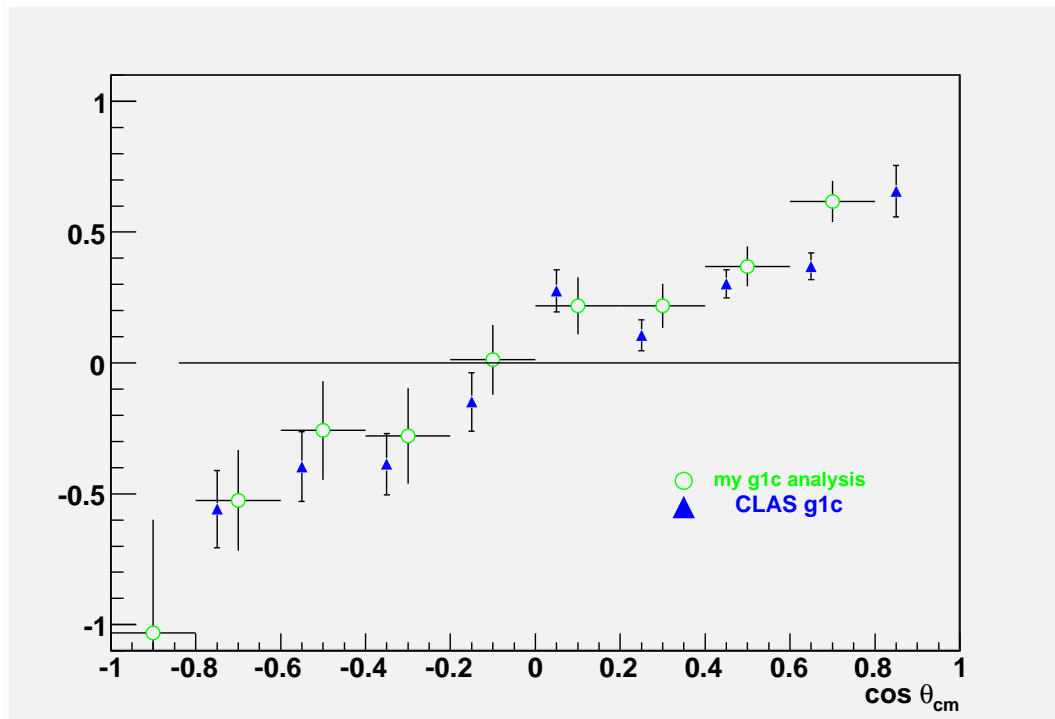
(b)

Figure 5.10: $C_{x'}$ and $C_{z'}$ for the photon energy range $1.55\,GeV < E_\gamma < 1.65\,GeV$ using my method on g1c data (marked with open circles) plotted with g1c analysis results (marked with blue triangles) converted into the primed coordinate system.
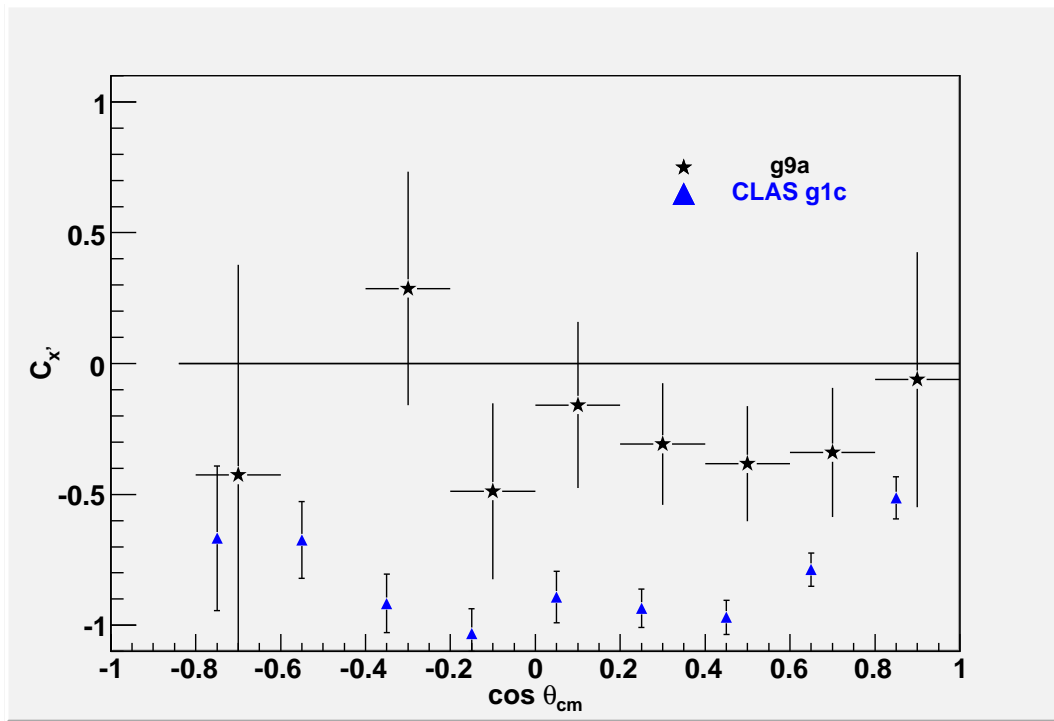
(a)
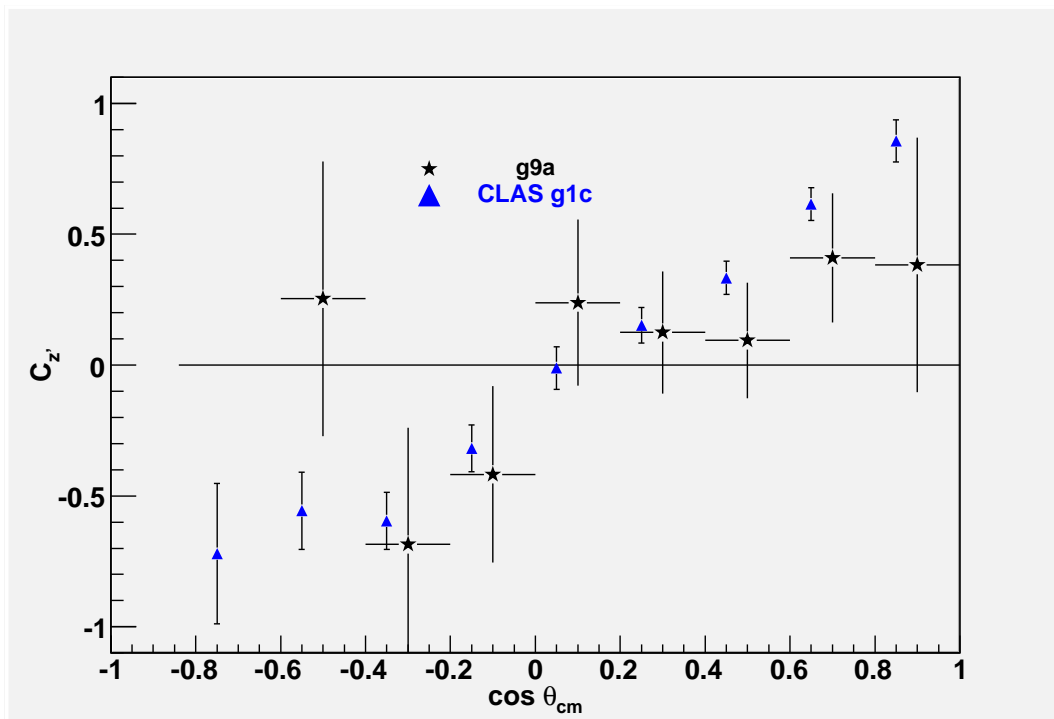
(b)

Figure 5.11: $C_{x'}$ and $C_{z'}$ for the photon energy range $1.25\,GeV < E_\gamma < 1.35\,GeV$ from FROST data (marked with stars) plotted with g1c analysis results (marked with blue triangles) converted into the primed coordinate system.
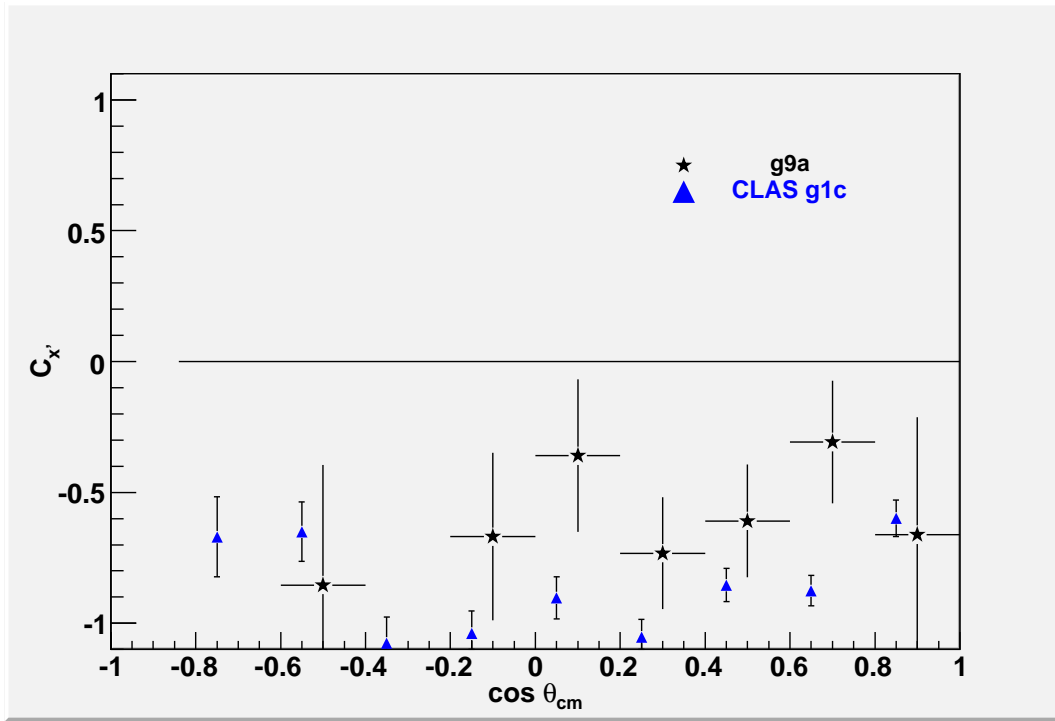
(a)
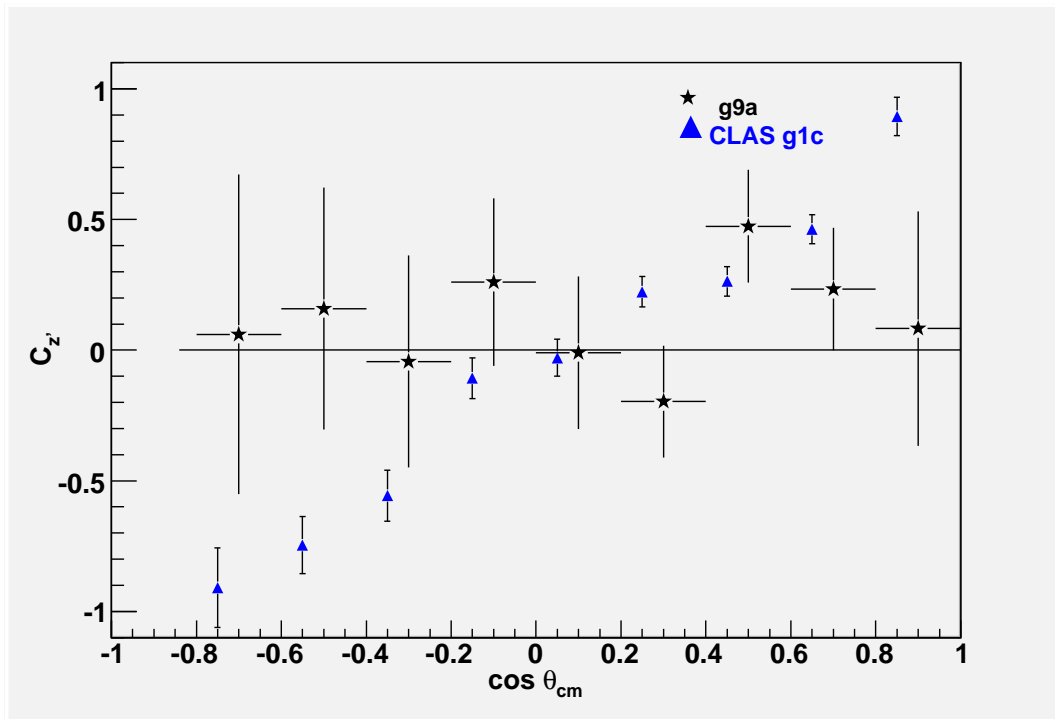
(b)

Figure 5.12: $C_{x'}$ and $C_{z'}$ for the photon energy range $1.35\,GeV < E_\gamma < 1.45\,GeV$ from FROST data (marked with stars) plotted with g1c analysis results (marked with blue triangles) converted into the primed coordinate system.
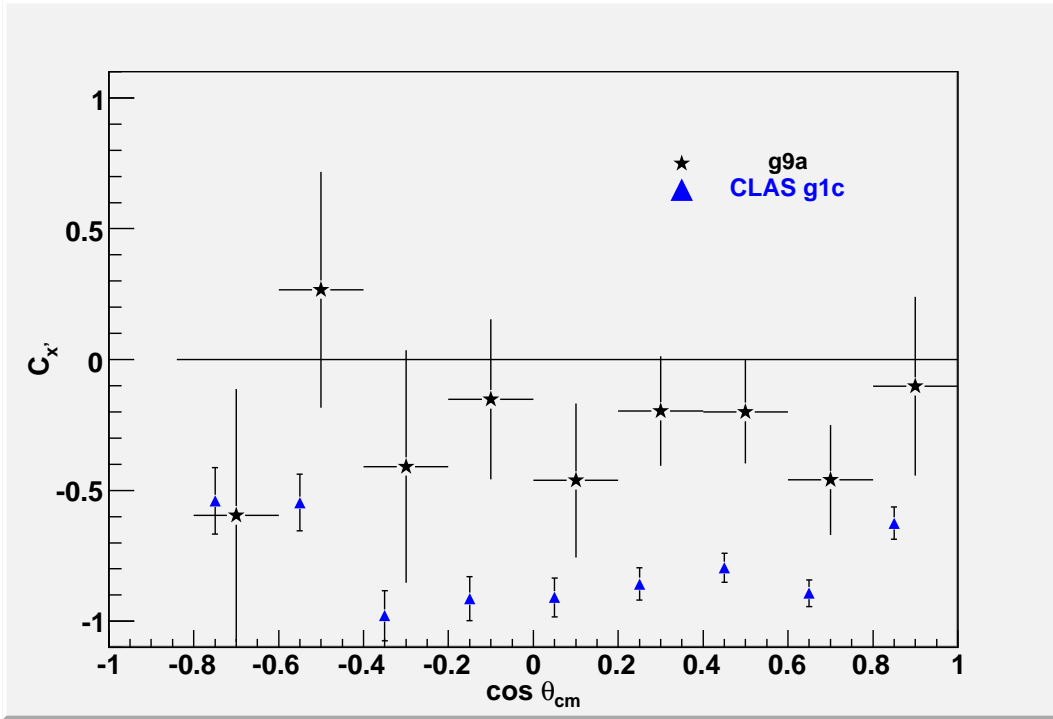
(a)
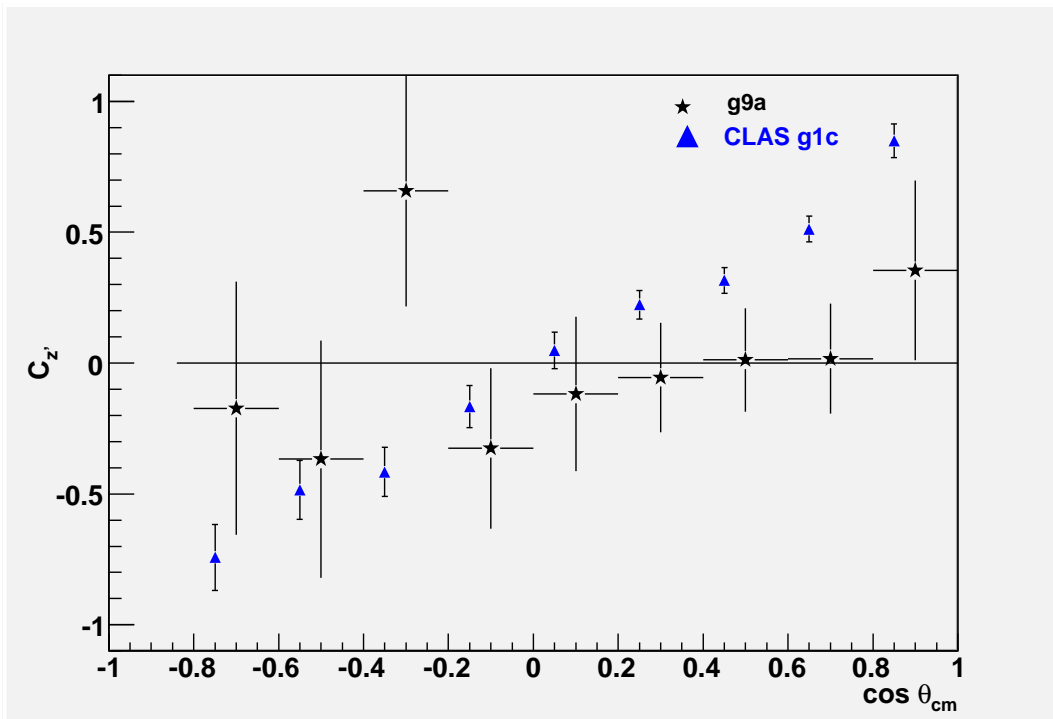
(b)

Figure 5.13: $C_{x'}$ and $C_{z'}$ for the photon energy range $1.45\,GeV < E_\gamma < 1.55\,GeV$ from FROST data (marked with stars) plotted with g1c analysis results (marked with blue triangles) converted into the primed coordinate system.
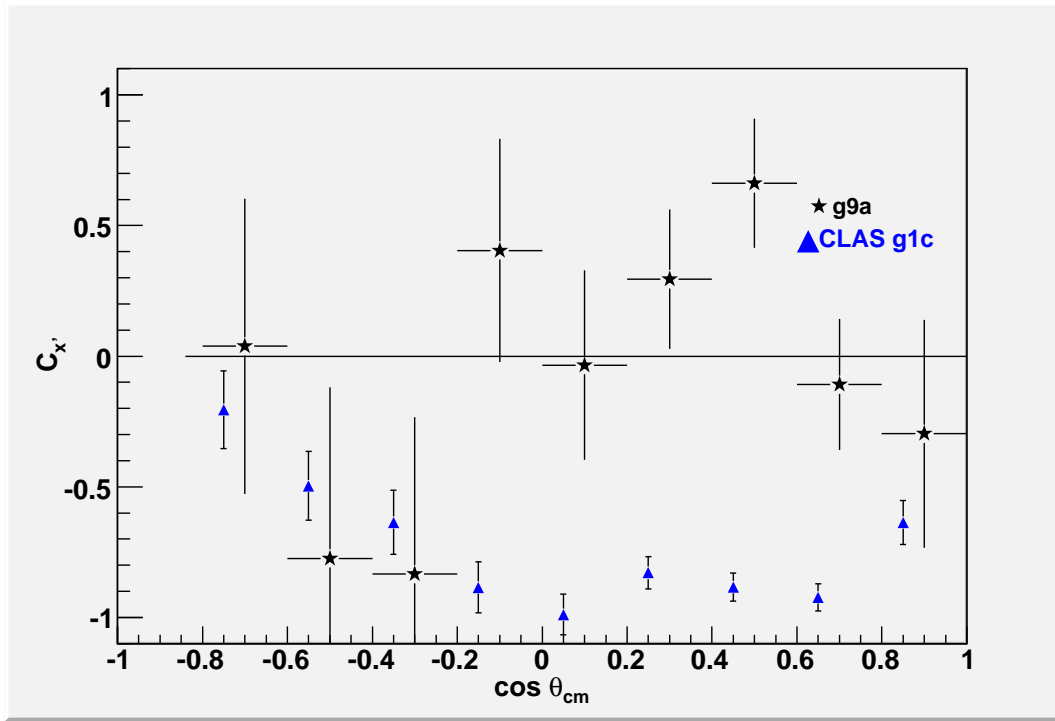
(a)
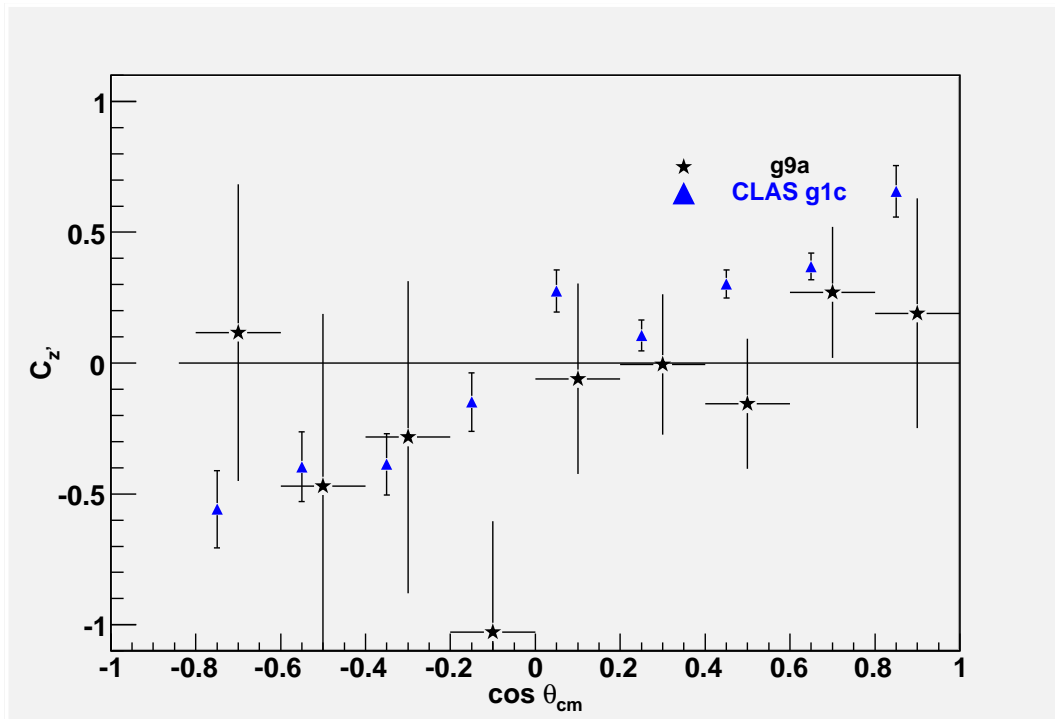
(b)

Figure 5.14: $C_{x'}$ and $C_{z'}$ for the photon energy range $1.55\,GeV < E_\gamma < 1.65\,GeV$ from FROST data (marked with stars) plotted with g1c analysis results (marked with blue triangles) converted into the primed coordinate system.

by the Λ self-analyzing factor and the circular polarization. The limitations on my statistics made it impossible to use such an approach over the whole range, so I decided simply to take the asymmetry between forward and backward distribution of the proton on the axis of interest and account for the cosine factor on average, thus the factor of 2 as seen in the recoil polarization. To determine the validity of this method, I used my method on a set of g1c data and compared my results to the g1c analyis results. At first blush, there appeared to be no correlation between my results and Bradford's, but A.M. Sandorfi et al. reported that these results were given in the unprimed CM coordinate system and could be converted to the primed asymmetries (where Sandorfi uses the convention of z' in the direction of K^+) by the relations

$$C_{x'} = C_x \cos\theta_{CM}^K - C_z \sin\theta_{CM}^K \; , \tag{5.3}$$

$$C_{z'} = C_x \sin\theta_{CM}^K + C_z \cos\theta_{CM}^K \; , \tag{5.4}$$

When I apply these relations to the g1c data for C_x and C_z, I see good agreement in both observables with my results for the g1c data using my g9a binning and methods. This rotation works in spite of an opposite convention in the definition of primed axes, which may indicate that there is a change in handedness involved in my rotations. Figures 5.7 - 5.10 show the values I obtained for $C_{x'}$ and $C_{z'}$ plotted together with the values obtained by applying equation (5.4) and the opposite sign values of equation (5.3) to Bradford's results.

While equation (5.2) is correct when there is no dilution factor, a more complicated expression incorporating the dilution is necessary for the g9a dataset. Since the target polarization is not explicitly involved in the extraction of $C_{x'}$ and $C_{z'}$, I cannot assume that the asymmetry in bound-nucleon reactions is zero. Therefore, the dilution factor is used in

a more general way

$$C_{x'/z'}(free) = D_{eff}C_{x'/z'}(but) - (D_{eff} - 1)C_{x'/z'}(carb) \; , \tag{5.5}$$

where $C_{x'/z'}(but)$ and $C_{x'/z'}(carb)$ are calculated using equation (5.2) for the events in butanol and carbon, respectively.

My g9a results for $C_{x'}$ and $C_{z'}$ are plotted together with those from the g1c analysis in Figures 5.11 - 5.14. There is little consistency between these two datasets. While the $C_{x'}$ measurements seem to follow the same shape as the g1c data they appear to be systematically too low. The $C_{z'}$ measurements may agree within statistical uncertainty, although this is a more difficult argument to make for the 1.4 GeV bin. The g9a statistics are too low to show whether there is a systematic issue with $C_{z'}$. Since these deviations are not seen in the comparable 100 MeV width bins when I analyze g1c data, the deviation comes from some particular of the FROST analysis rather than from my general extraction approach for these observables. Nonetheless, whichever factors are influencing the g9a data to show incorrect values for $C_{x'}$ and $C_{z'}$ are likely to impact the values for $L_{x'}$ and $L_{z'}$ and may even have an effect on E. Therefore, examination of the systematic causes of error in g9a could be crucial to the accuracy of the results presented in this thesis. In the following chapter I will examine some of the potential sources of error that could be responsible for the inconsistencies seen in these plots.

The 1.5 GeV energy bin which spans from 1.45 GeV to 1.55 GeV in photon energy, has some of the best statistics in my dataset and is also the most critical to this analysis, because evidence for the $D_{13}(1960)$ should come from this energy range. The data in this bin are best compared to the g1c bin at 1.53 GeV as seen in Figure 5.13. Agreement with previous results is not great for this bin, but it is better than for some others. Nonetheless, there are alternative possibilities. Since the target polarization is not specifically referenced in the calculation of these observables, inequitable production time spent on one polarization

direction may lead to the accidental measure of a triple polarization observable.

5.3 Summary

The consistency of my results for previously measured observables with those of the analyses that originally extracted those observables is rather spotty. While my recoil polarization measurements show very good agreement with the g11 results despite much coarser binning, my results for the beam-recoil transfer observables are in quite poor agreement with previous measurements. When my methods are applied to g1c data, my results are quite consistent with the g1c results, but when applied to FROST data, large discrepancies appear. The cause of these errors is yet to be fully understood, but the most likely culprits are the bound nucleons in FROST. A further exploration of the effect that bound-nucleon reactions have on the result and of other potential sources of systematic error follows in the proceeding chapter.

Chapter 6

Systematic Uncertainties

In the previous chapter I showed how consistent deviations from established results could crop up beyond the pure statistical errors arising from the yield. While the statistics for my reaction channel are low enough that there are many kinematic bins with large statistical errors, the systematics of g9a appear to be an even greater cause of inaccuracy in the measured asymmetry. In order to have trusted values for the newly measured polarization observables it is critical that the underlying causes of error are understood so that the appropriate correction factors may be applied. To this end I will explore several potential sources for error in my extracted observables throughout this chapter including beam asymmetry, errors in beam and target polarization, errors in handling background and the resulting dilution factors and errors resulting from azimuthal asymmetries in the detector efficiency, before continuing to the conclusion of my results in the final chapter.

6.1   Beam Charge Asymmetry

The beam charge asymmetry is the result of a different number of electrons being produced for each helicity setting of the beam. This effect is usually small and it is important that it be small when trying to extract polarization observables. Calculations of any observable

involving the beam would have to correct for the beam charge asymmetry if it were significant and adjustments might also have to be made for target and recoil asymmetries to avoid accidental extraction of a triple polarization observable. The error on these calculations would necessarily increase.

The beam charge asymmetry is estimated by an asymmetry in the number of particle events between the two helicity states of the beam. The skim file set used in my analysis was a poor choice for determining this asymmetry, because it was already selected for kaon events. This meant the charge asymmetry estimate might be skewed by a legitimate physics asymmetry in the reaction channel. Fortunately, the asymmetry measurement had already been made by Steffen Strauch to be on the order of 0.1% or less.[48] This is clearly has insignificant impact on my results. It simply will not affect my error bars at the level of precision that I can honestly report. Therefore, the beam charge asymmetry will not be included in any calculation of the systematic uncertainty.

6.2   Errors in the Mean Polarization

The polarizations of the target and beam were each taken as the mean for measurements made throughout the g9a run period. Yet each of these measurements had an uncertainty associated with it. This is the systematic uncertainty of the polarization measurement. While each of these individual uncertainties has already been calculated, the specific weighting I used to calculate the mean of each polarization must be incorporated into the calculation of the error in mean from these individual uncertainties, at least in principle. In reality, the variations in uncertainty beyond a certain level of precision are simply too small to matter when taken in light of the overall precision of the analysis. Since I have already rounded the target and photon polarization to three significant figures it makes little sense to consider the uncertainties beyond three significant figures either. Thus, I have reported

the uncertainties in the target polarization run table to only three decimal places, although they are carried substantially further in the source table.

At this level of precision, the uncertainty in target polarization is fairly consistent. The vast majority of runs have negligible statistical uncertainty (rounded to zero) and a systematic uncertainty of 0.001. Only ten of the 190 runs used in this analysis have a statistical uncertainty on the order of or higher than the systematic uncertainty. The bin yields for these runs were calculated separately to see if these runs could skew the mean polarization uncertainty in a meaningful way. The statistical uncertainty in target polarization on all of these runs is 0.005 or lower (mostly lower), so greater than 12.5% of the yield for a bin must come from these runs if there is to be any change in the mean error estimate. Clearly these runs contain a much lower percentage of the total events, but they may carry a heavier load for some low statistics bins. However, upon calculating the yield per bin for each of these runs and weighting it by the statistical uncertainty in polarization for that bin, it is clear that the effect of this statistical uncertainty remains negligible (less than 0.0005) over the entire kinematic range.

A more significant impact might be found in the case of the systematic polarization uncertainty where 23 runs have higher uncertainty than 0.001, five of them having over ten times the uncertainty. In this case, there is actually a nonnegligible effect on the mean error in the lower part of the energy range. The majority of kinematic bins for $E_\gamma \approx 1.5$ GeV and below have a systematic target polarization uncertainty of 0.002. The values of target polarization uncertainty per bin are given in Table 6.1. These uncertainties will have a very slight effect on the error bars of the polarization observables, but since they are on the order of the mean values reported for the target polarization, they should be considered.

It should be noted though that since the uncertainty in polarization adds a term of $(\frac{1}{P_T}O)^2\sigma^2(P_T)$ to the polarization observable variance, where O is the observable in question, the uncertainty is increased by less than $(\frac{1}{P_T}O)\sigma(P_T)$. The target polarization is

$\cos\theta_{cm}^K$	-0.7	-0.5	-0.3	-0.1	0.1	0.3	0.5	0.7	0.85
E_γ=1.050 GeV	0.001	0.002	0.002	0.002	0.002	0.002	0.002	0.002	0.002
E_γ=1.175 GeV	0.002	0.001	0.001	0.002	0.002	0.002	0.002	0.002	0.002
E_γ=1.300 GeV	0.002	0.002	0.002	0.002	0.002	0.002	0.002	0.002	0.002
E_γ=1.400 GeV	0.001	0.002	0.002	0.002	0.002	0.002	0.002	0.002	0.002
E_γ=1.500 GeV	0.002	0.001	0.002	0.002	0.002	0.002	0.002	0.002	0.002
E_γ=1.600 GeV	0.001	0.001	0.001	0.001	0.001	0.001	0.001	0.001	0.001
E_γ=1.725 GeV	0.001	0.001	0.001	0.001	0.001	0.001	0.001	0.001	0.001
E_γ=1.900 GeV	0.001	0.001	0.001	0.001	0.001	0.001	0.001	0.001	0.001
E_γ=2.100 GeV	0.001	0.001	0.001	0.001	0.001	0.001	0.001	0.001	0.001
E_γ=2.275 GeV	0.001	0.001	0.001	0.001	0.001	0.001	0.001	0.001	0.001

Table 6.1: Error in the Mean Target Polarization by Kinematic Bin

roughly 0.8 and the observables should always have a magnitude less than 1, so even for bins with 0.002 uncertainty in polarization, the effect on the observable's uncertainty will almost always be significantly less than 0.002. In reality, since the calculated statistical error bars are always of the order of 0.1 or higher, the contribution of the target polarization uncertainty to the total should be less than .00003. Such differences in uncertainty would not be discernible on a plot on the range from -1 to 1 and reflect a precision that the data gathered for this experiment cannot truly provide. Thus, the uncertainty in target polarization must also be ruled out as a leading order cause of systematic uncertainty.

The uncertainties in circular polarization are more significant as the measured uncertainties for electron beam polarization are typically on the order of 1%. The values of the electron polarization uncertainty are taking from 4.3 and a simple average is taken whenever more than one Moller measurement was taken for a run. Reporting the uncertainties to the third decimal place as with the target polarization, I find that all run groups have 0.014 uncertainty in electron polarization, save the last group, which has an uncertainty of 0.013. This difference is not very significant, nor will the contribution of the last run group be significant enough to alter the uncertainty of bins. A much greater impact falls to the distribution of yield among 1.6 and 2.5 GeV data sets, for the error propagation to

the circular polarization is dependent on it. In principle the uncertainty could be calculated event by event for each bin just as the mean circular polarization was calculated, but it is not strictly necessary, as rough approximation should be sufficient for the desired level of precision. The circular polarization per kinematic bin varies from ~ 0.5 to ~ 0.8 , or from about $0.6 * P_{el}$ to P_{el} and the circular polarization uncertainties follow the same ratio. Using the maximal contribution to the observable uncertainty of $(\frac{1}{P_C}O)\sigma(P_C)$, we find that in all cases the uncertainty contribution will not be more than 0.018. This is certainly more significant than the target polarization uncertainty and potentially a visible effect, but again it only holds if the measured observable magnitude is one and the calculated statistical uncertainty is essentially zero. When the statistical uncertainties are on the order of 0.1 and higher, as is certainly the case for my measurements, the contribution is less than 0.002. Plainly, this is yet another negligible effect, which cannot be causing large discrepancies between the calculated observables and previously known results.

6.3 Sector Distribution of Events

The helicity of the photon beam and the polarization of the target both point along the z-axis for the events used in my analysis. This means that there should be no ϕ distribution asymmetry in my reaction channel. Any difference in yield among the six sectors of CLAS points to some source of systematic error. A minor enough asymmetry can be deemed a result of statistical fluctuations that do not indicate any additional source of error, while a substantial asymmetry most likely has roots in some systemic problem.

As can be seen in Figure 6.1, the distribution of detected protons and kaons from $K^+\Lambda$ events is asymmetric. While K^+ mesons are found in higher proportions in sector 4 than in sector 1, which has roughly 70% of the kaon yield that sector 4 detects, protons for these events occur with higher frequency in sector 1. Protons for $K^+\Lambda$ events are expected to
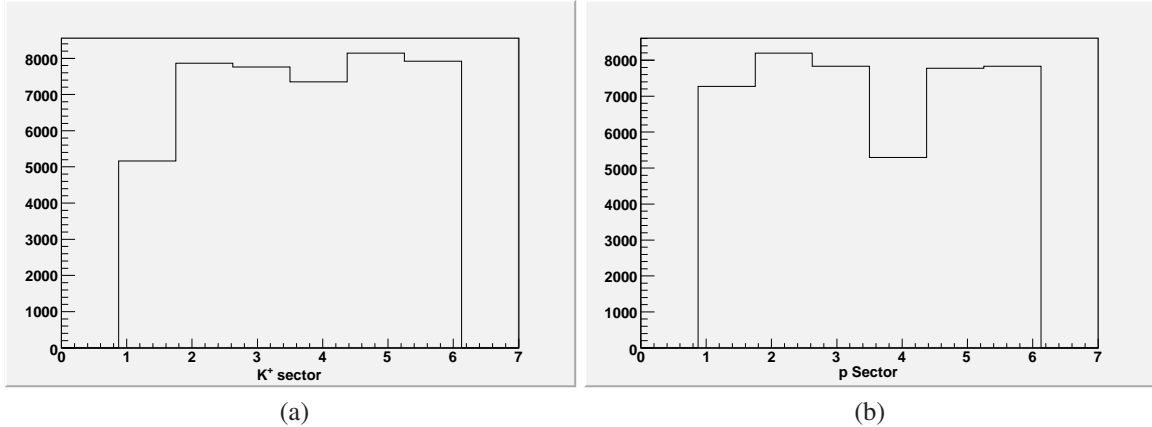
Figure 6.1: Sector distribution of the yield for (a)kaons and (b) protons

be primarily detected in opposite sectors to kaons (an expectation corroborated by Figure 6.2 because the Λ must have the opposite ϕ position to the K^+ and the proton will not usually be detected with great angular deviation from the Λ decay. Sector 4 and sector 1 are opposite sectors in CLAS, so one can argue that the asymmetry for protons follows from the asymmetry for kaons or vice versa. This is a partial explanation, but it doesn't really address the question of why a sector preferentially detects one particle type. The TOF scintillator cuts mentioned in section 3.3 provide the most likely explanation. The excess count rate for protons existed primarily in sector 1. By removing those counters, detected kaons in sector 1 were also removed. This leads to a corresponding drop in sector 4 protons as events without a detected kaon are removed from my analysis.

Another issue to be considered is a more general sector asymmetry that doesn't express itself solely between kaons and protons, but for each particle type. When sectors 1 and 4 are removed from consideration, there is only an asymmetry of $\sim 2.4\%$ between sector 3, the sector with the next lowest yield, and sector 5, the one with the highest yield. Such variation can be purely statistical but may also be explained by differences in the paddles cut from analysis. Measurements of asymmetry generally should not require acceptance corrections, especially for observables that don't involve recoil polarization. In the case
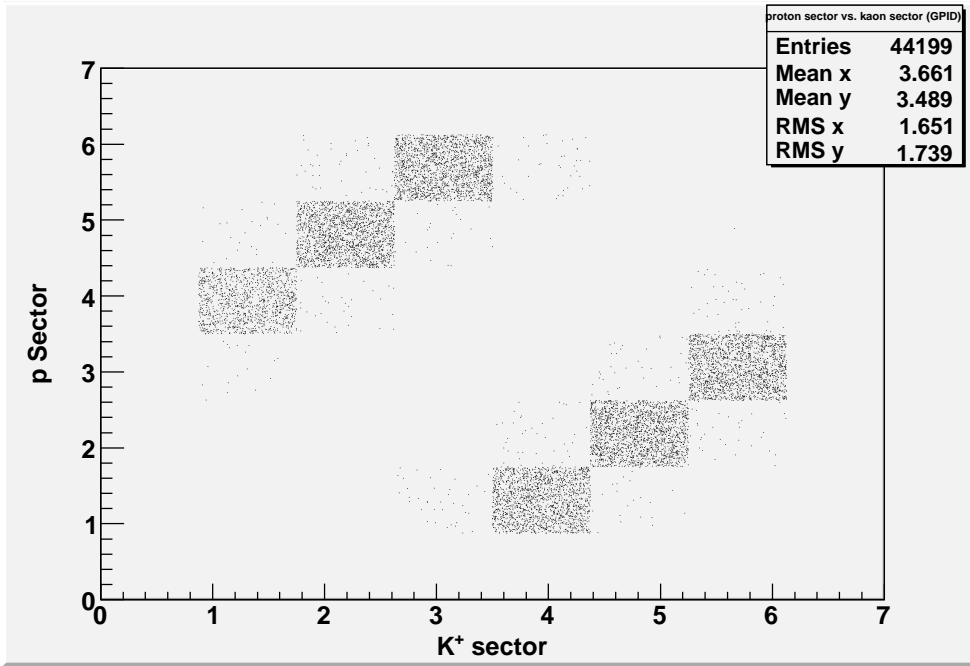
Figure 6.2: Sector distribution of protons vs distribution of kaons. Typically the particles are detected in opposite sectors as is expected.

of recoil polarization, the asymmetry is also not strictly ϕ-dependent, but as relative measurements of ϕ are used in its calculation, it is conceivable that efficiency differences could have some effect. Further, in the event that a Λ decays close to the torus coils, the protons from highly polarized lambda may be preferentially detected or removed, depending on proximity to the coils. It's difficult to argue that such effects should be unbalanced in the overall impact on the observable, but it is possible. Indeed, while such explanations for discrepancies are not very compelling, the measured observables are found to have inconsistent values when yields are subdivided among sectors. In order to determine if this problem could be placed solely at the feet of the sector 1 kaon detection efficiency, both sectors 1 and 4 were removed from the sector based polarization observable studies while sectors 2 and 3 were grouped together and compared against sectors 5 and 6. The results, a sampling of which can be seen in Figure 6.3, are fairly encouraging.

The promising feature is that agreement in E is very good for this bin. This evidence
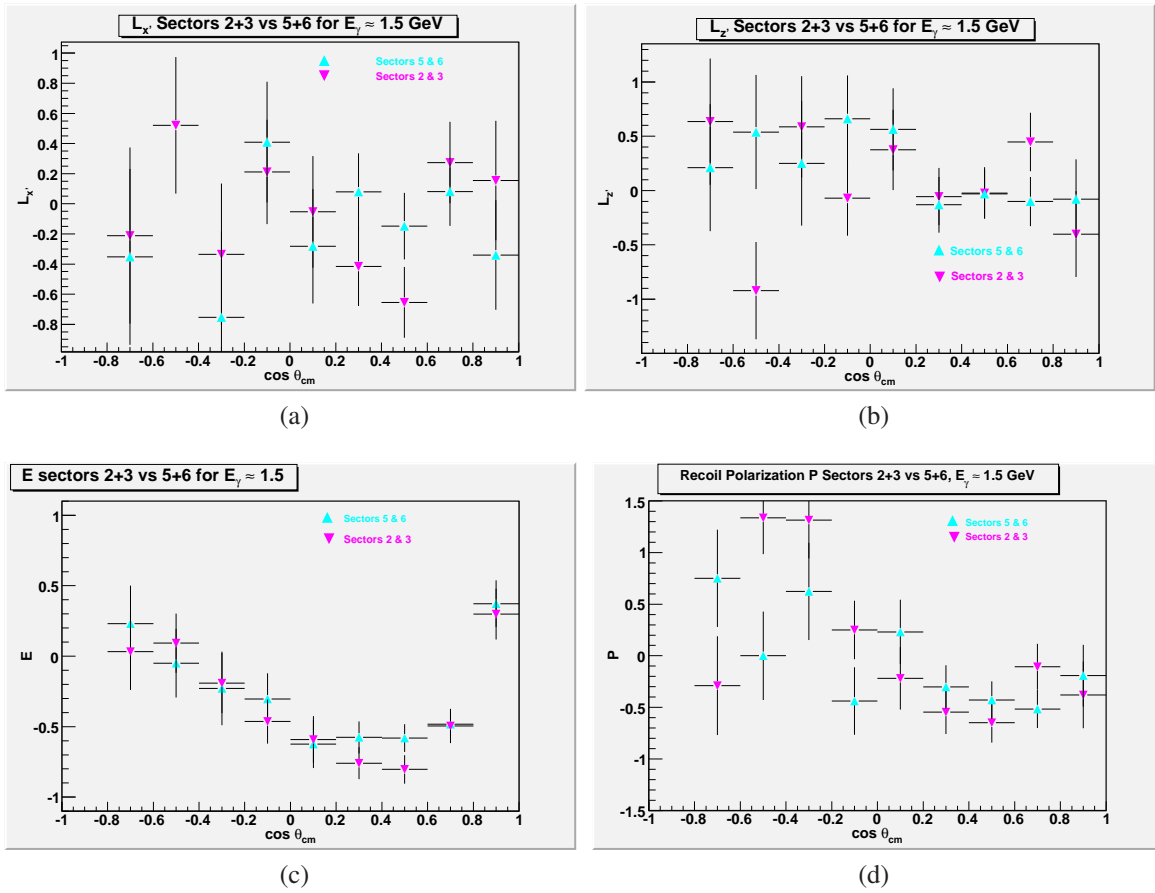
Figure 6.3: Sector asymmetry of polarization observables in the critical 1.5 GeV photon energy bin

bolsters the hypothesis that only the observables involving the recoil polarization are affected by sector asymmetry issues. Yet, even for these observables the agreement between opposite sector groups is good, with no more discrepancy than would be expected based on the statistical uncertainty. Given that the yield in sectors 1 and 4 is lower and thus these represent less than one third of gathered statistics, the effect of sector asymmetry in polarization observables appears to be unable to explain the discrepancy between g9a and g1c measurements of $C_{x'}$ and $C_{z'}$. The reason for this dramatic effect is still not fully understood, nor is there a clear path to correcting the error. The fact that there are no significant discrepancies between groupings of sectors when sectors 1 and 4 are removed may point to a need of acceptance corrections for the events in those sectors. However, it scarcely offers succor in a search to explain the differences between g9a and g1c results.

6.4   Background Subtraction Method

There is not one standard way to estimate the ratio of signal to background events in the missing mass spectrum. For this analysis, I chose to estimate the background by first scaling the events in the carbon target and subtracting the scaled events before performing a fit. Then I took all events in the 3σ range given by the fit. Alternatively, I could calculate a fit to the combined background and signal without doing any subtraction. The fit would give me the maximum of the signal events for the gaussian fit, from which I could calculate an approximate number of signal events in the 3σ range. Thus, I would have a number for signal events and the rest of the events in the region would be considered background.

Neither of these methods is perfect. The method I employ in my analysis can fail to adequately determine the size of the background from the start, while the fit method can determine the yield in the fit range incorrectly. The imperfections of each method add some measure of uncertainty to the final results. In order to make an estimate on the degree of
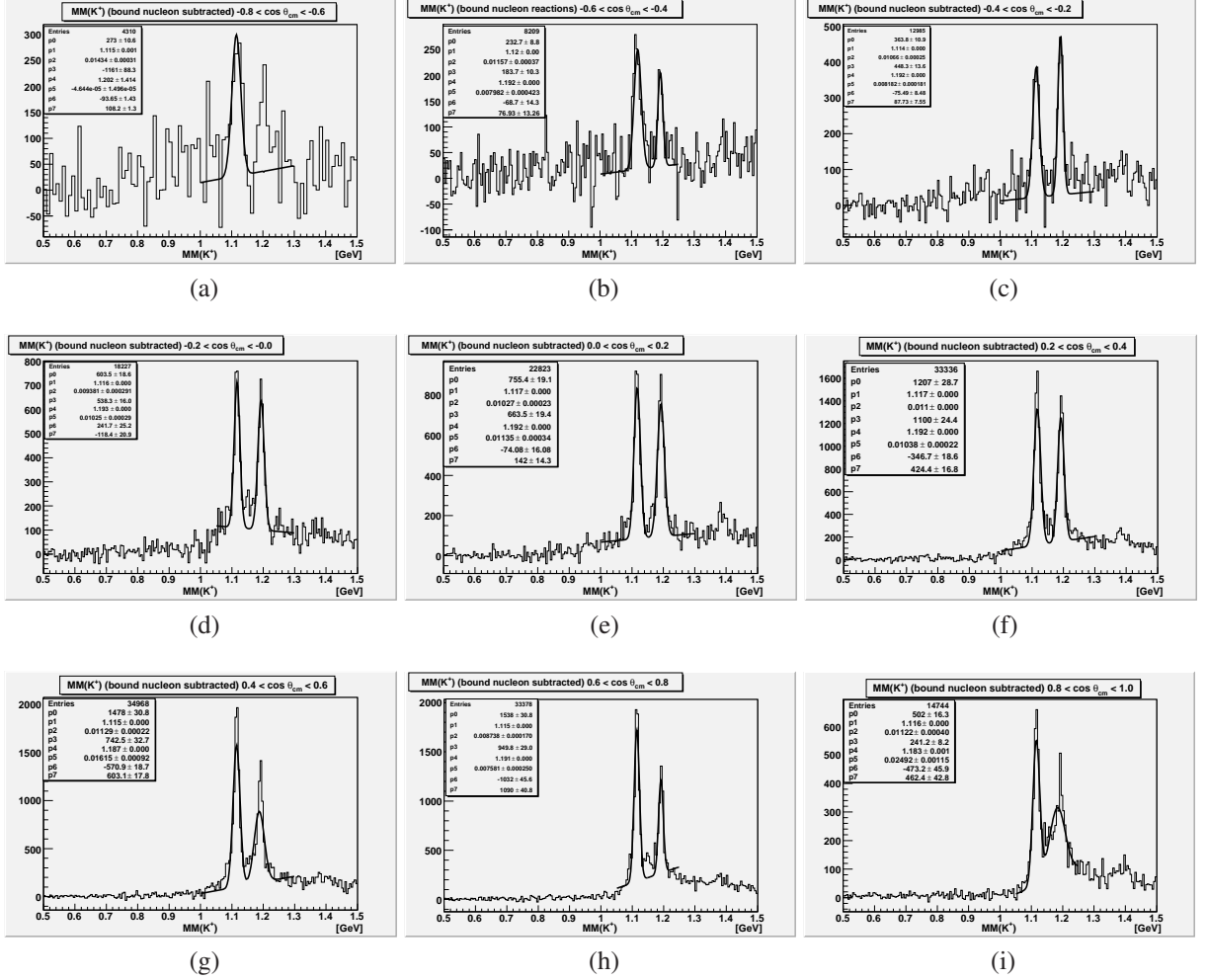
Figure 6.4: Double gaussian plus linear fit of the background after scaled carbon subtraction. Fits are very sensitive to input ranges and the same ranges will not work well for all plots.

this uncertainty, it is prudent to make a comparison of the estimated bound-nucleon yield from each method.

This study can be done by comparing the results of my pion cuts with a fit to the background remaining in the scaled carbon subtracted plots of Chapter 3. In order to determine the remaining background, I add a first order polynomial fit to the double gaussian fitting the Λ and Σ^0 peaks as seen in Figure 6.4. I take the $\pm 3\sigma$ range for Λ given by the fit and calculate the yield in the following manner

$\cos\theta^K_{CM}$	$Y_{but} - Y_{scale}$	Y_{gauss}
-0.7	763	1957 ± 76
-0.5	1154	1355 ± 52
-0.3	1562	1953 ± 59
-0.1	2754	2846 ± 90
0.1	3581	3899 ± 98
0.3	6189	6657 ± 160
0.5	7420	8373 ± 176
0.7	7057	6708 ± 135
0.9	2565	2819 ± 90

Table 6.2: Comparison of different methods of yield estimation.

$$Y_{gauss} = \sqrt{2\pi}A\sigma_{bin} , \tag{6.1}$$

where A is the maximum value of the gaussian given in the first parameter of the fit and σ_{bin} is the number of bins covered by the standard deviation parameter of the fit. The parameters of the gaussian are automatically adjusted for the linear background by the fit, so calculation of the background yield is unnecessary. The signal yield is what I will need to check the consistency of results between the two methods.

Ultimately, the yield Y_{free} should be consistent between, $Y_{free} = Y_{but} - Y_{scale}$ and $Y_{free} = Y_{gauss}$, where Y_{but} and Y_{scale} are the extracted yields from the butanol missing mass distribution after the pion cut has been applied and the scaled carbon distribution after the same cut. Y_{but} has already been given for each angular bin in Table 3.1 and Y_{scale} is easily obtainable from the same, so it only remains to apply equation (6.1) to the parameters of the fit and compare. These comparisons are show in Table 6.2 with errors computed using error propagation solely from the dominant error in the maximum.

The results clearly show a considerable amount of inconsistency. The estimates of the gaussian fit are typically too high for the yield extracted from the pion cut, but too low to indicate that bound-nucleon reactions have been removed after the pion cut. The discrepancy is too significant for additional error terms to make up the difference. The fit

is obviously poor in the backwards directions and very sensitive to the input range. These factors lead me to lean in favor of the yield after the pion cuts and attribute the discrepancy to error in the fit method, where necessary, but the fit is still a step in determining the range taken for the Λ yield after performing the pion cut, so there needs to be some reliability. Most of the difference may be explained in terms of different missing mass ranges. The gaussian for each of these fits have different variances and, therefore, different ranges. I applied cuts on the same range for each of the angular bins to extract the yield after the pion cut. This range is taken from a fit on the total missing mass distribution (applied prior to the cut). The differences that lie beyond uncertainties may be purely explained by the range differences, at least for the forward angle bins where the fit is fairly good.

6.5 Summary

In this chapter I considered several additional sources of error that could potentially lead to inaccurate results. For the most part these error sources are so minor that they don't contribute at the level of precision allowed by the experiment. A couple of the potential error sources are more ambiguous. The asymmetry in the sector distribution of events and the corresponding asymmetry in polarization asymmetries extracted from these sectors may serve as a partial explanation for the poor fit of g9a results for $C_{x'}$ and $C_{z'}$ to those previously established in g1c, but it hardly seems to be the most significant source of error. The potential for error in the background estimation should not be ignored. The discrepancies can be rationalized, but they are large enough that they could be a significant source of inaccuracy in the final results.

Chapter 7

Final Results and Discussion

The events for $\gamma p \to K^+ \Lambda$ have been selected, the polarization observables have been extracted, and a full analysis of the experimental uncertainty has been performed. Now it is time to see what, if anything, each of these measurements can tell us about the underlying physics of the reaction. The central problem motivating this thesis is the search for missing resonances, so this study will focus on seeking evidence for the presence of resonant structure in the behavior of the polarization observables as the energy and angle vary. Model calculations will be employed to aid in this endeavor, but attention will also be paid to the variation in asymmetry among adjacent bins. Ultimately, the full PWA of the reaction channel will give the definitive answer on resonance coupling to $\gamma p \to K^+ \Lambda$, but just as cross section and recoil polarization data have pointed to potential resonant activity, so to may the double polarization observables extracted for this dissertation. Therefore, in this final chapter I will examine each observable seeking for such activity and judging whether my measurements support established ideas about the channel.

7.1   Discussion of *E*

A comparison of my final results for E with model predictions has the prima facie benefit of helping to discern the presence of resonances based on whether models including the resonance in their calculations or those that do not include the resonance agree better with the data. My results do not show strong agreement with any of the model predictions. This means that a stronger argument can be made from the data for the faultiness of all models than one in favor of any particular model's core features. Nonetheless, it is useful to examine the degree to which consistency between data and models can be found and see if potential explanations for similarities and differences arise. The exact discrepancy between my data and model predictions can be seen in Figures 7.1 - 7.5, which show my data plotted alongside the KAON-MAID model of Terry Mart and Cornelius Bennhold, with and without the inclusion of the $D_{13}(1960)$ resonance.[49] This model requires the D_{13} resonance at 1895 MeV to explain the structure at 1.9 GeV in the differential cross section. Still it is important to see the effect the additional resonance has on model predictions, so the same model is also given without the $N = 3$ band D_{13} resonance. Additionally, a SAID partial wave analysis for $K^+\Lambda$ is shown for the first 8 energy bins. This PWA makes use of CLAS g1c and SAPHIR data for the differential cross section and recoil polarization.[19, 26]

Particular interest is taken in the asymmetry distribution at $E_\gamma \cong 1.5$ GeV, because this is the photon energy for which the N=3 band D_{13} state is expected to be found. For the corresponding energy bin, I have also included the model of Saghai, which includes off-shell effects rather than incorporating the $D_{13}(1960)$ resonance to explain the cross section data. The results show some qualitative agreement with the Mart model in the backward direction, while a completely different behavior from those predicted by the models is expressed in the forward region. As the forward angles tend to have less background dominance, the values that stray most from predictions actually appear to be the most trustworthy of my
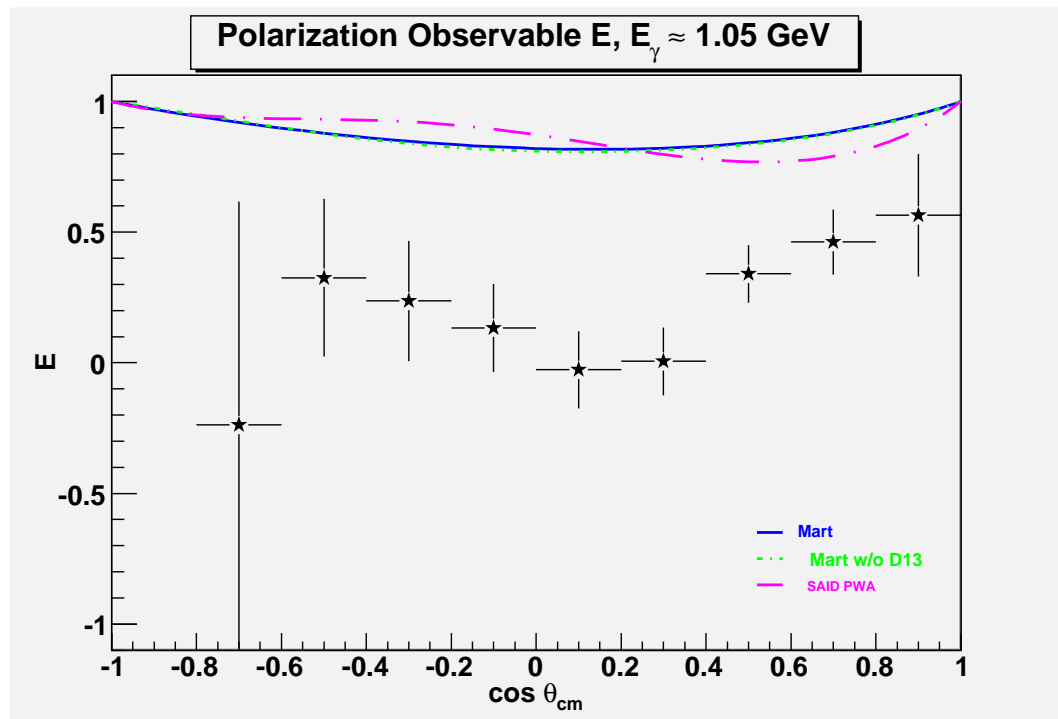
(a) 0.9 GeV $< E_\gamma <$ 1.1 GeV
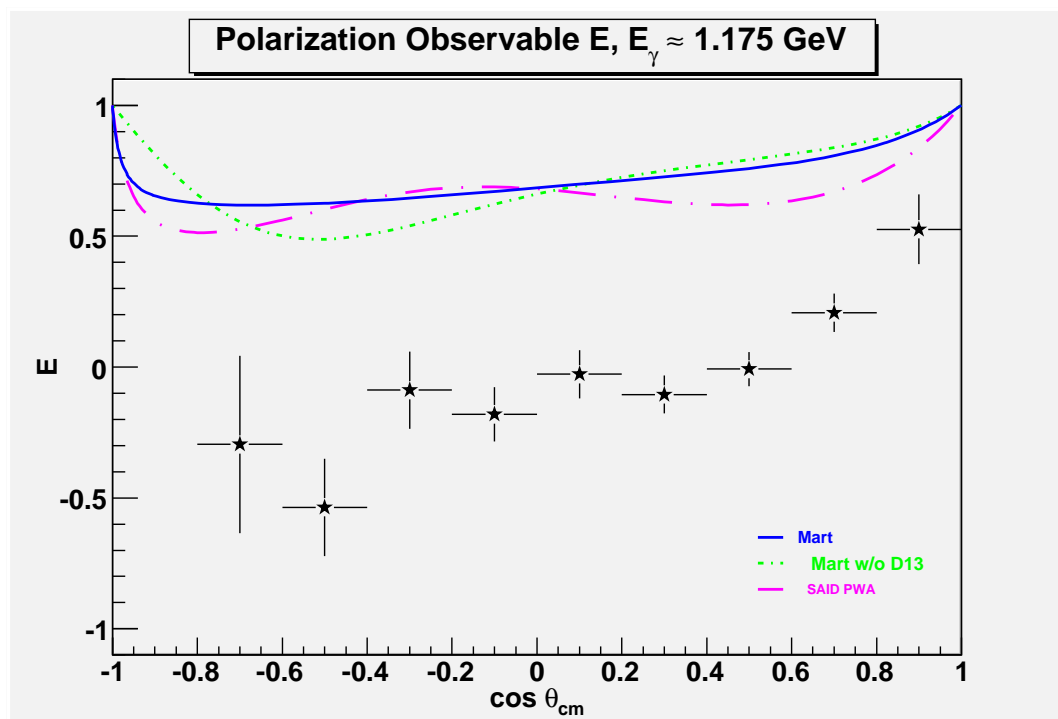
(b) 1.1 GeV $< E_\gamma <$ 1.25 GeV

Figure 7.1: Model comparison plots for E. The Mart model is represented by the solid blue line, while the model without D_{13} is represented by the dot-dash green line. The SAID PWA result is given by the long dash-dot magenta line.

(a) 1.25 GeV < E_γ < 1.35 GeV

(b) 1.35 GeV < E_γ < 1.45 GeV
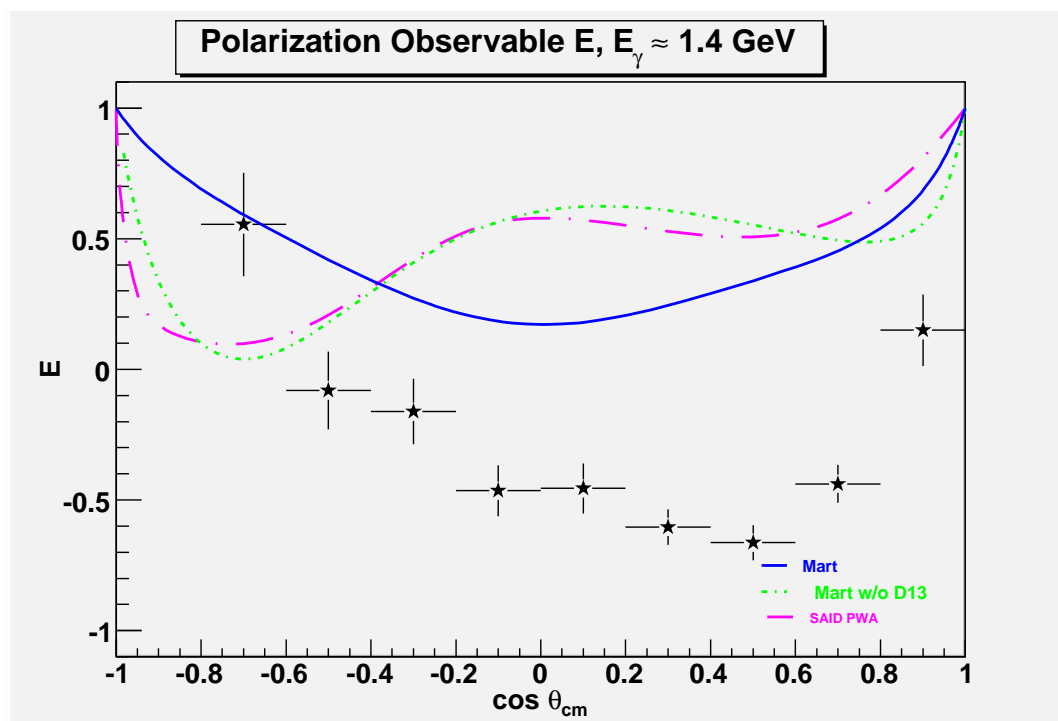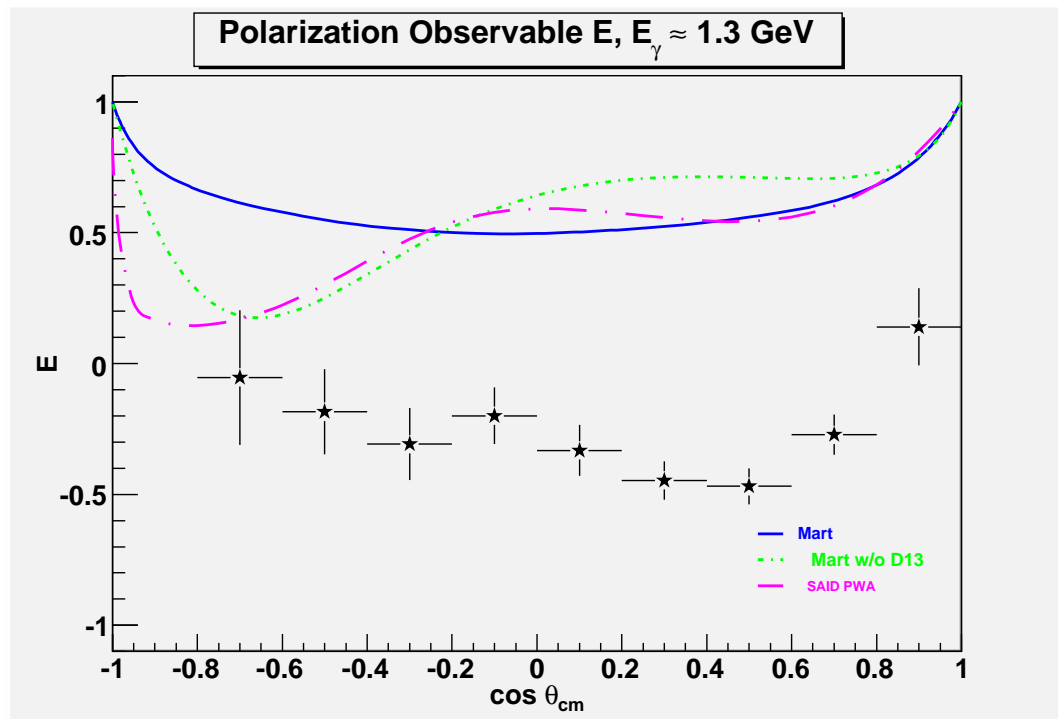
Figure 7.2: Model comparison plots for E. The Mart model is represented by the solid blue line, while the model without D_{13} is represented by the dot-dash green line. The SAID PWA result is given by the long dash-dot magenta line.
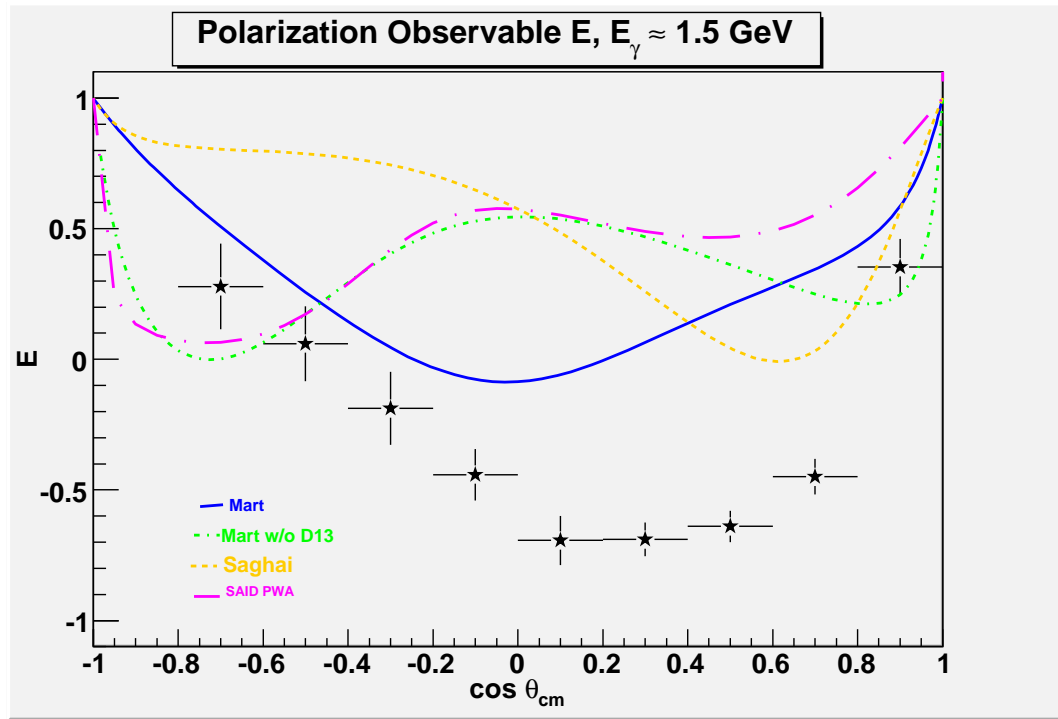
(a) 1.45 GeV < E_γ < 1.55 GeV
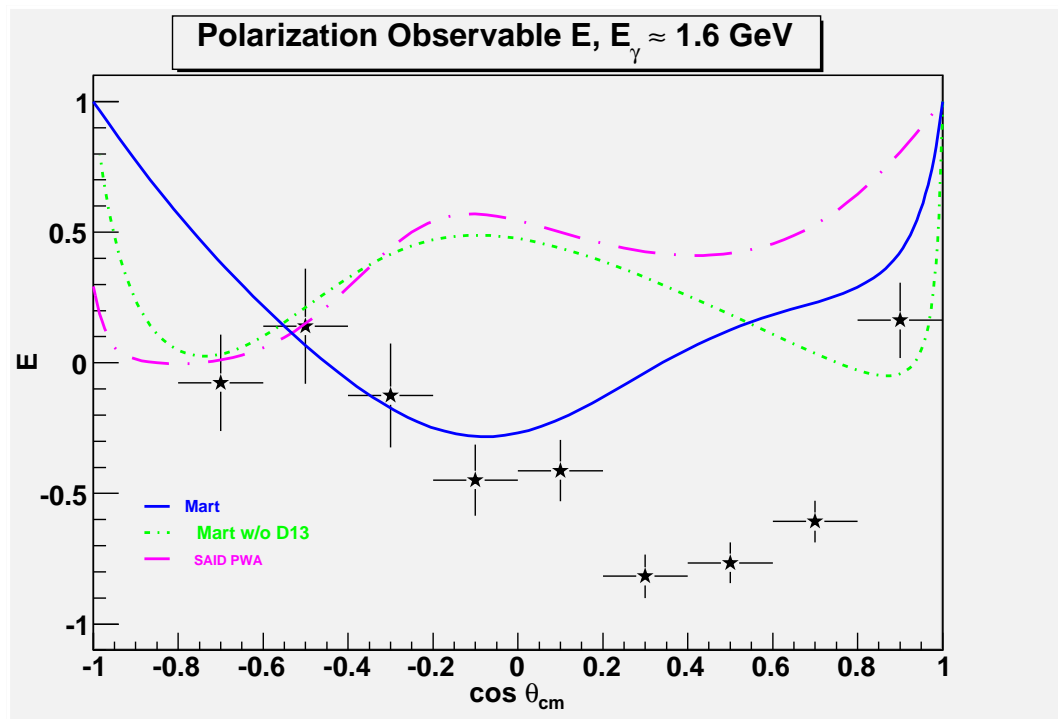
(b) 1.55 GeV < E_γ < 1.65 GeV

Figure 7.3: Model comparison plots for E. The Mart model is represented by the solid blue line,, while the model without D_{13} is represented by the dot-dash green line. The SAID PWA result is given by the long dash-dot magenta line and the Saghai model is represented by the dashed orange line.

(a) $1.65\,\text{GeV} < E_\gamma < 1.8\,\text{GeV}$

(b) $1.8\,\text{GeV} < E_\gamma < 2.0\,\text{GeV}$

Figure 7.4: Model comparison plots for E. The Mart model is represented by the solid blue line, while the model without D_{13} is represented by the dot-dash green line. The SAID PWA result is given by the long dash-dot magenta line.
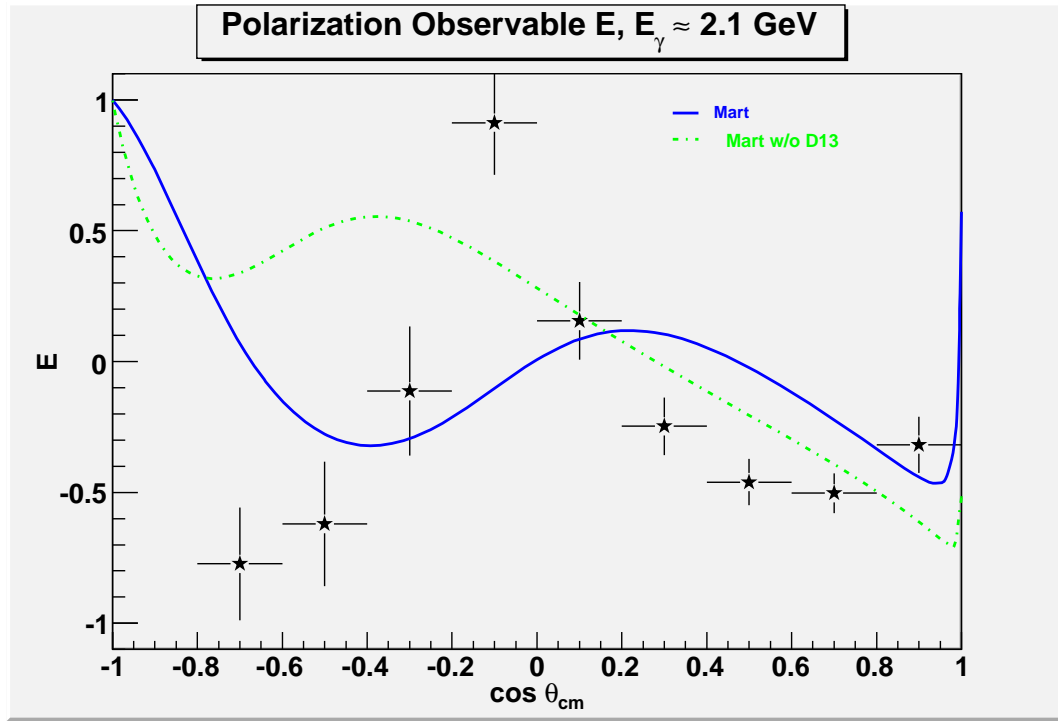
(a) 2.0 GeV $< E_\gamma <$ 2.2 GeV
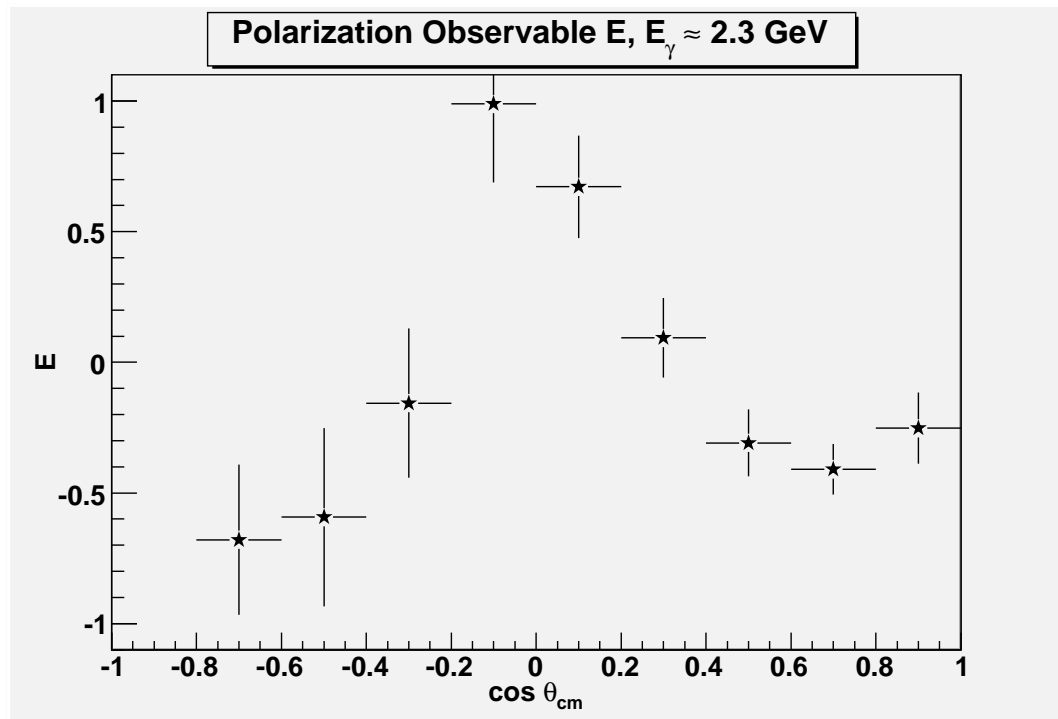
(b) 2.2 GeV $< E_\gamma <$ 2.4 GeV

Figure 7.5: Model comparison plots for E. The Mart model is represented by the solid blue line, while the model without D_{13} is represented by the dot-dash green line. The SAID PWA result is given by the long dash-dot magenta line.
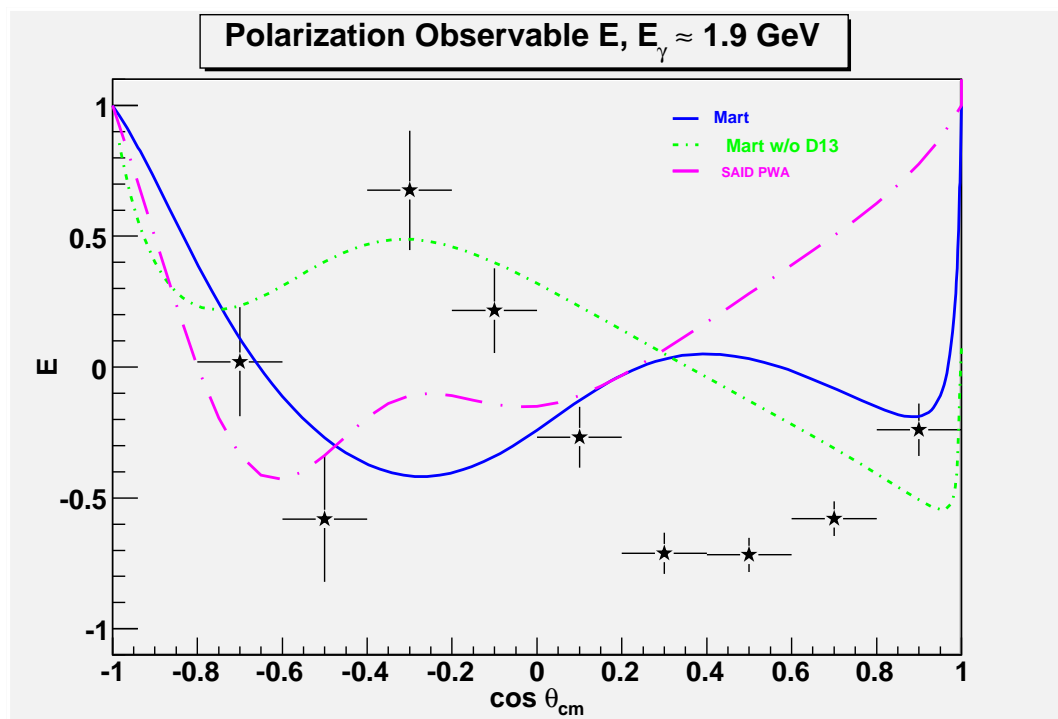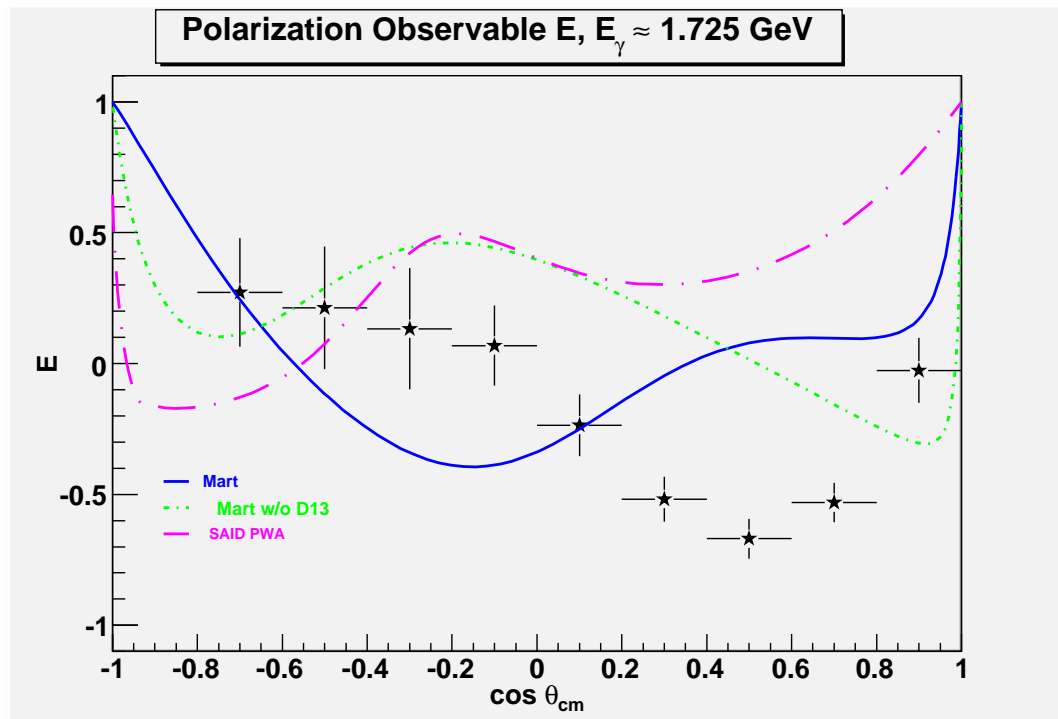
analysis. The only potential problem I can imagine is that the calculated overall dilution factor is too high for these regions. This could lead to a slight reduction in magnitude over this range, but cannot explain the discrepancy in magnitude and sign. In general though, consistency checks seemed to show that the dilution factors used were more likely too low rather than too high.

The only real comment to be made in favor of $D_{13}(1960)$ presence affecting this asymmetry is that the Saghai model, which does not include the resonance, maps out the asymmetry so poorly. Likewise, the Mart model shows even poorer agreement when the missing D_{13} is not included. However, there are a great number of possible isobar models and the failure of one such model can say little about the underlying physics. Saghai's inclusion of off-shell effects is done in a model dependent manner so the idea that these contributions can explain the behavior of the cross section around $W = 1900$ MeV remains plausible.

Of far greater significance is the manner in which the asymmetry changes with the photon energy. When one looks at the very next bin on either side of the 1.5 GeV energy range, one can see that there is little change in the behavior of E at forward angles in the center of mass frame. Indeed, the plots for 1.4, 1.5, and 1.6 GeV are very similar over the entire range. It is notable that both the SAID result and the Mart model without D_{13} show the dip in the 1.6 GeV plot at $\cos\theta_{CM}^K \approx -0.7$ in agreement with my data, but neither agree with my data at more forward angles, so that none of these models predict the oscillation in my data. The full Mart model shows better, although still poor, agreement overall. At any rate, the distribution at 1.5 GeV seems too smooth to suggest resonant contribution.

Fewer model predictions are available for the other energy ranges. Nonetheless, it is worthwhile to examine the disparity in the predicted and observed distributions where possible. The D_{13} resonance appears to be particularly broad as it affects the Mart model predictions across many bins. Therefore, while comparison of results for energy bins closer to the resonance's predicted mass are more valuable in the search for this resonance, com-

parisons over the whole energy range have some merit. Further, these comparisons serve as a test of the predictive power of the model in general. At low energies, the Mart model never seems to depart far from the constraints at $\cos\theta_{CM}^{K} = \pm 1$. The data in the 1.05 GeV bin shows some oscillation and values that are significantly lower than those predicted. The PWA also has some oscillation, but the oscillation is about the Mart model curve and so the predicted values are still too large. At 1.175 GeV, Mart models the skewness of the distribution, but the magnitude is yet far off. My plot has a significant departure from $E = 1$ with values in the negative range and close to zero. The same problem exists with the Mart model prediction for 1.3 GeV. Whereas, the distribution of my data is taking on a shape similar to the 1.5 GeV distribution, the Mart prediction continues to remain too close to 1. Removal of the D_{13} resonance improves the fit only in the very backward direction and the result for SAID is similar. My measurements show an asymmetry that is largely negative and of low magnitude. A poorly modeled dilution factor cannot explain this discrepancy as the sign would not change. Only if bound-nucleon reactions are so dominant that a random asymmetry in those reactions is stronger than a physics based asymmetry in polarized proton reactions would they result in a sign change of the measured asymmetry. The scaling procedure indicates that free proton interactions dominate, showing that the model is flawed in these energy ranges.

At 1.725 GeV the Mart model continues to give the same qualitatively adequate description of the backwards angle calculations for E that it gave for 1.5 GeV and begins to move lower in the forward region so that it actually shows some agreement there. The Mart model with D_{13} resonance gives the best fit but it is still too poor to be meaningful. Whether or not the resonance is included, the model continues to fail to predict the extreme dip in the forward direction. Above 1.725 GeV this forward dip does not disappear but begins to be reflected at backwards angles, so that the asymmetry appears to have an almost sinusoidal oscillation with a periodicity half that of $cos\theta_{CM}$. Contributions of higher partial

waves may be responsible for this behavior at 1.9 GeV and above. This also explains why the SAID PWA does a better job of showing this oscillation, but the magnitude is far off. The oscillation is seen in the Mart model as well, but the crests and troughs are positioned in poor agreement with my data. The crest is modeled better when the D_{13} resonance is turned off, but the curvature is not steep enough. The crest begins at $cos\theta_{CM} \approx -0.3$ in the 1.9 GeV bin and moves forward to $cos\theta_{CM} \approx -0.1$ for the 2.1 GeV and 2.3 GeV bins. The Mart model shows this crest in the forward direction and moves it backward with increasing energy. Moreover, the strength and sharpness of this oscillation is underestimated by the model.

Beyond 2.1 GeV, I do not have values for even the Mart model, so my commentary is limited only to the actual content of my plot for the 2.3 GeV bin without any comparisons to draw upon. The 2.3 GeV plot follows the behavior at 2.1 GeV quite well. Therefore, it is safe to say that no one resonant contribution is responsible for the oscillation. It is worth noting that the constraints on E at the limits $cos\theta_{CM} = \pm 1$, will demand a rather steep incline over the final angular bin range on both sides. Nevertheless, several model predictions show equally steep curvatures, so there's no immediate call to suggest more moderate values. The large error bars in the backwards direction cover the possibility of a more symmetric distribution of the asymmetry that will still demand a steep incline over the terminal angular bins.

7.2   Discussion of $L_{x'}$

When analyzing the distribution of $L_{x'}$, it is important to remember that, aside from the use of target polarization magnitude and direction in the place of photon circular polarization, it has been extracted in the exact same manner as $C_{x'}$. This means that axis conventions are necessarily the same for both observables. In each of the plots shown in Figures 7.6 - 7.10,

I have plotted the model calculations as given with no sign change. There is no real basis for making a claim about sign convention from $L_{x'}$ data alone, but so long as the rotation for $C_{x'}$ given by Sandorfi is correct, as it appears to be, this signs must be kept the same in spite of axis conventions.

The crucial energy bin for this analysis is the 1.5 GeV bin, due to the aim of answering the question of $D_{13}(1960)$ resonance existence. None of the plotted models agrees very well with the data. The SAID PWA is better than the model predictions with the most consistent bins (within errors) and a fairly slight alteration of the behavior in the forward direction would improve the fit. The Mart model agreement is not so much worse though and it is superior for the other two observables presented in this chapter, so the disparity here is not critical. Certainly there is no evidence for a resonance at $W = 1900$ MeV to be found in this plot alone. It should be noted that the values measured here are fairly consistent with a flat asymmetry and the SAID result may agree so well simply because the range of its oscillation is fairly small.

A look at the neighboring energy bins at 1.4 GeV shows lower asymmetry values in a flatter distribution. The elevated asymmetry in the next bin could be a sign of resonance, if it were more consistent, but in reality there is simply a lot of unphysical jumping around from bin to bin. Smaller errors might smooth out this distribution or make clear how much oscillation actually exists. Again, the PWA which stays closer to zero is more consistent with my results. At 1.6 GeV the data begins to agree a bit better with the Mart model, but not adequately so to draw conclusions. The asymmetry is still largely consistent with zero and the SAID results give the best fit. The negative asymmetry peak seen at $\cos\theta \approx -0.3$ in the previous energy bin has perhaps propagated forward to $\cos\theta \approx 0.1$ as this sort of behavior is frequently observed in distributions among neighboring energy bins. It does not appear to have any connection to resonant contributions.

The Mart model predictions for $L_{x'}$ are likewise poor for all the energy bins (more so
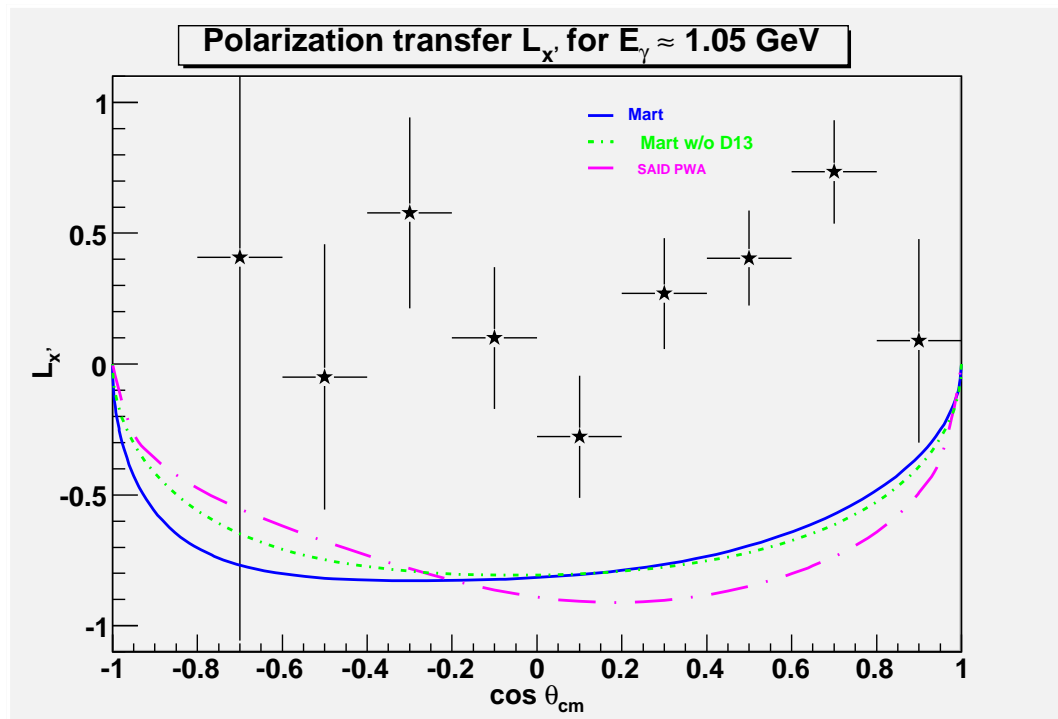
(a) 0.9 GeV < E_γ < 1.1 GeV
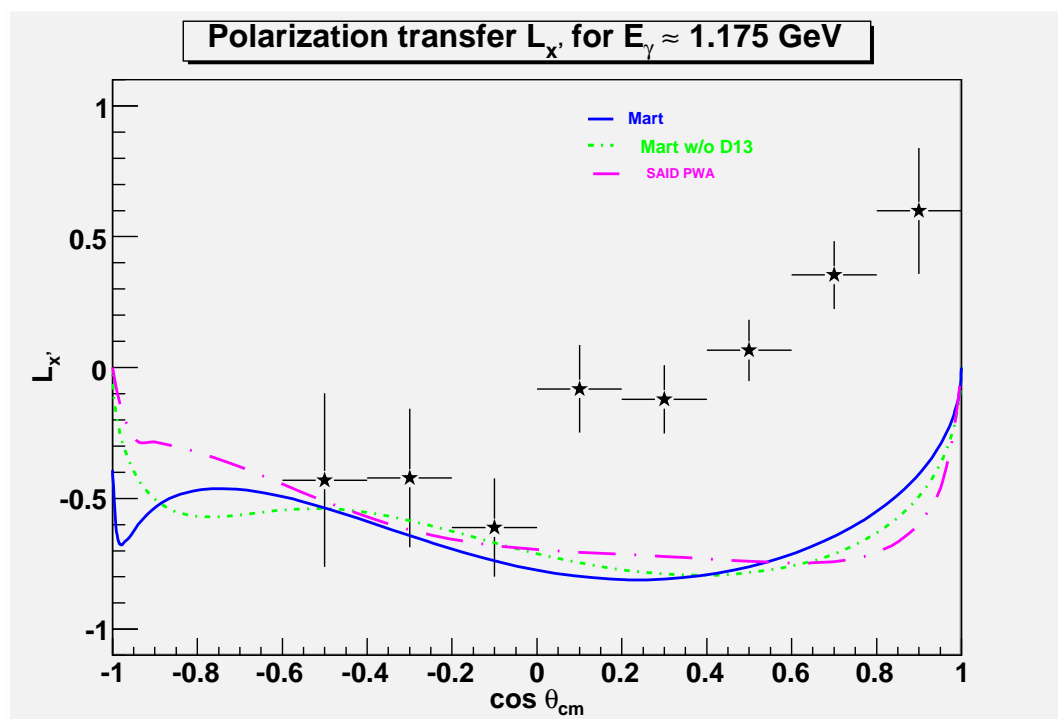
(b) 1.1 GeV < E_γ < 1.25 GeV

Figure 7.6: Model comparison plots for $L_{x'}$. The Mart model is represented by the solid blue line.

(a) 1.25 GeV $< E_\gamma <$ 1.35 GeV

(b) 1.35 GeV $< E_\gamma <$ 1.45 GeV

Figure 7.7: Model comparison plots for $L_{x'}$. The Mart model is represented by the solid blue line.

(a) 1.45 GeV < E_γ < 1.55 GeV

(b) 1.55 GeV < E_γ < 1.65 GeV

Figure 7.8: Model comparison plots for $L_{x'}$. The Mart model is represented by the solid blue line, the Saghai model is represented by the dashed orange line, and the SAID PWA are shown in the dash-dot magenta line.

(a) 1.65 GeV < E_γ < 1.8 GeV

(b) 1.8 GeV < E_γ < 2.0 GeV
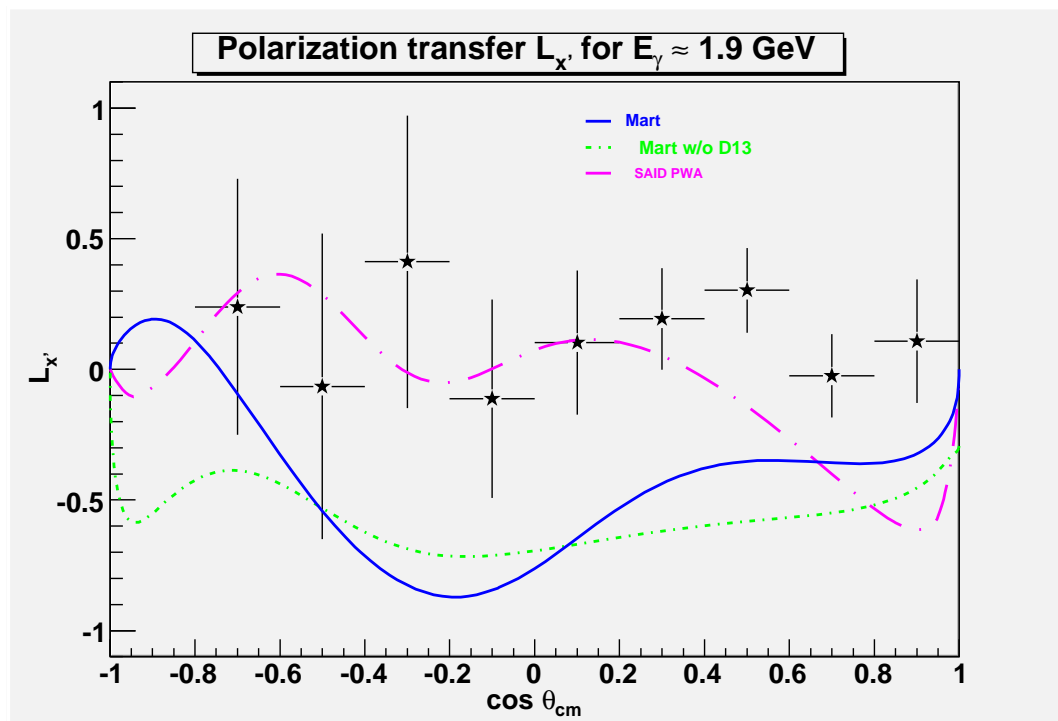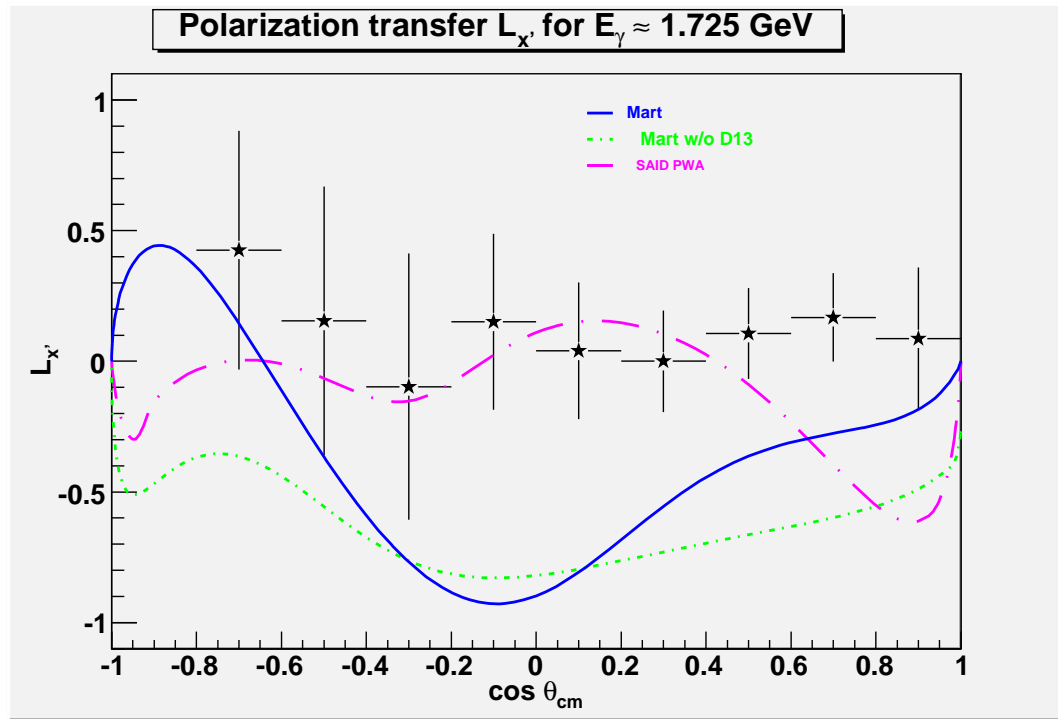
Figure 7.9: Model comparison plots for $L_{x'}$. The Mart model is represented by the solid blue line.

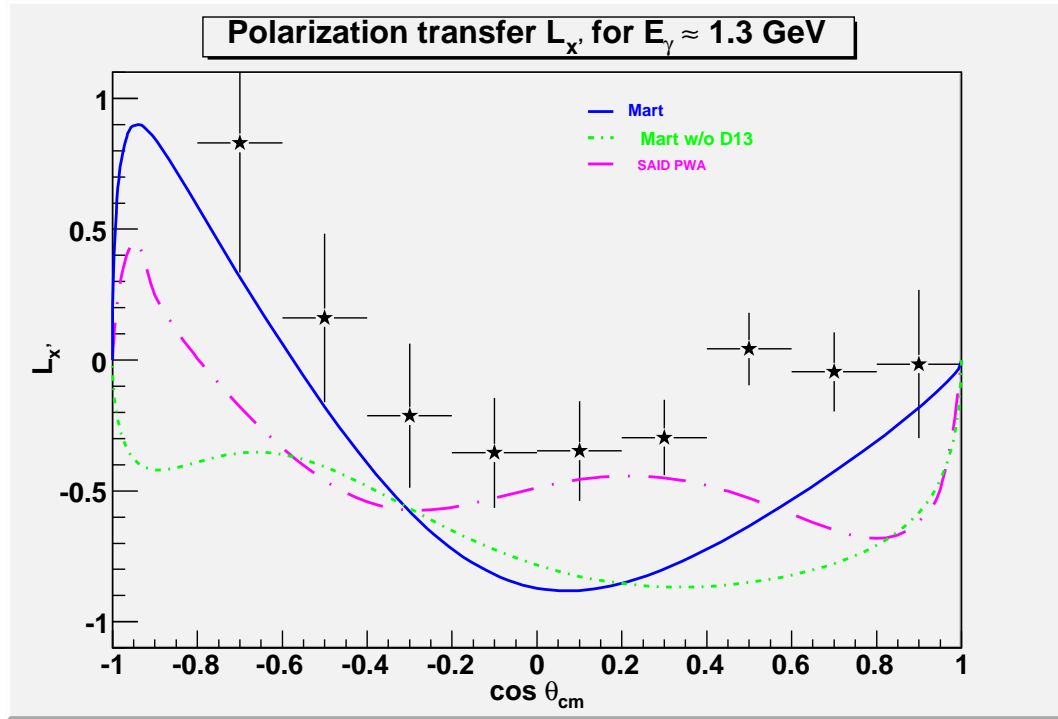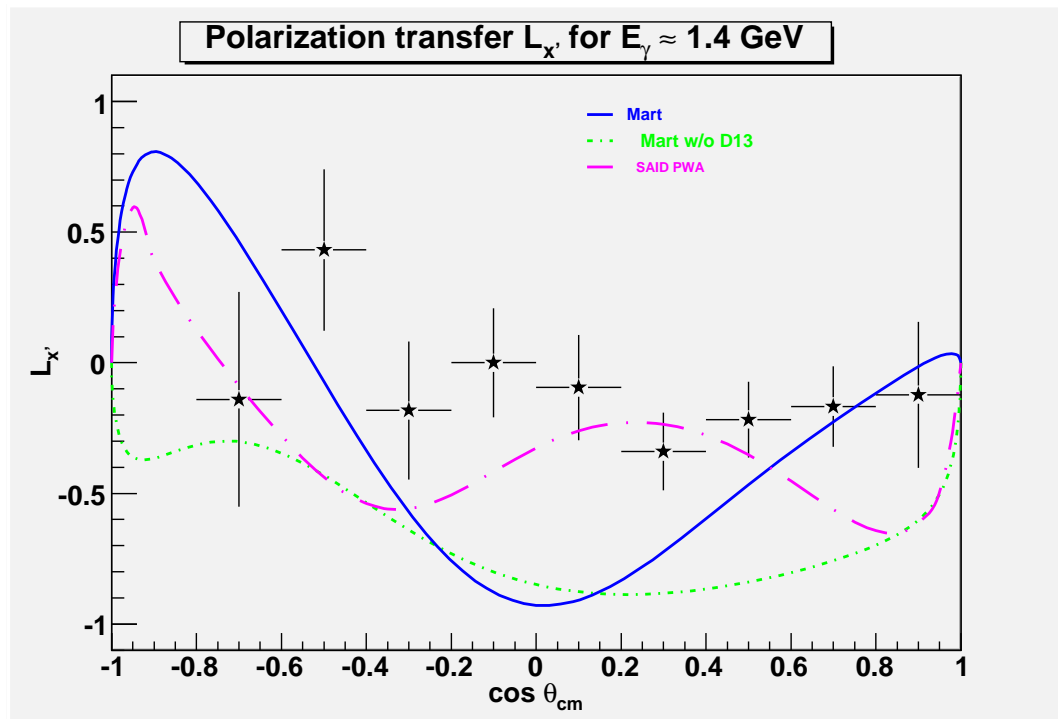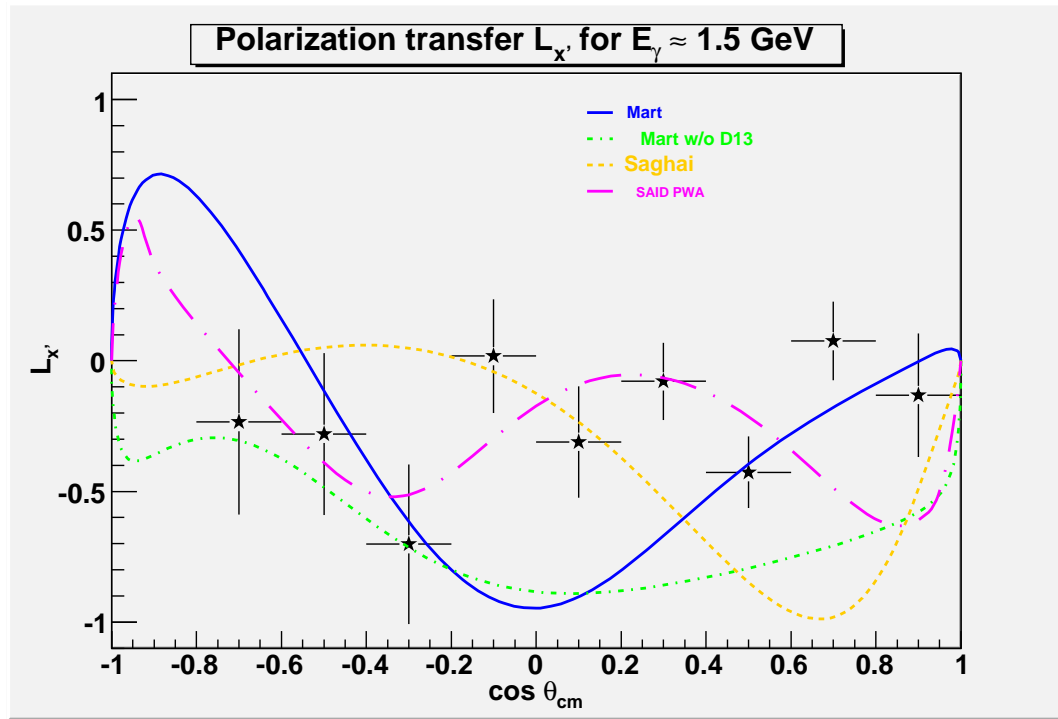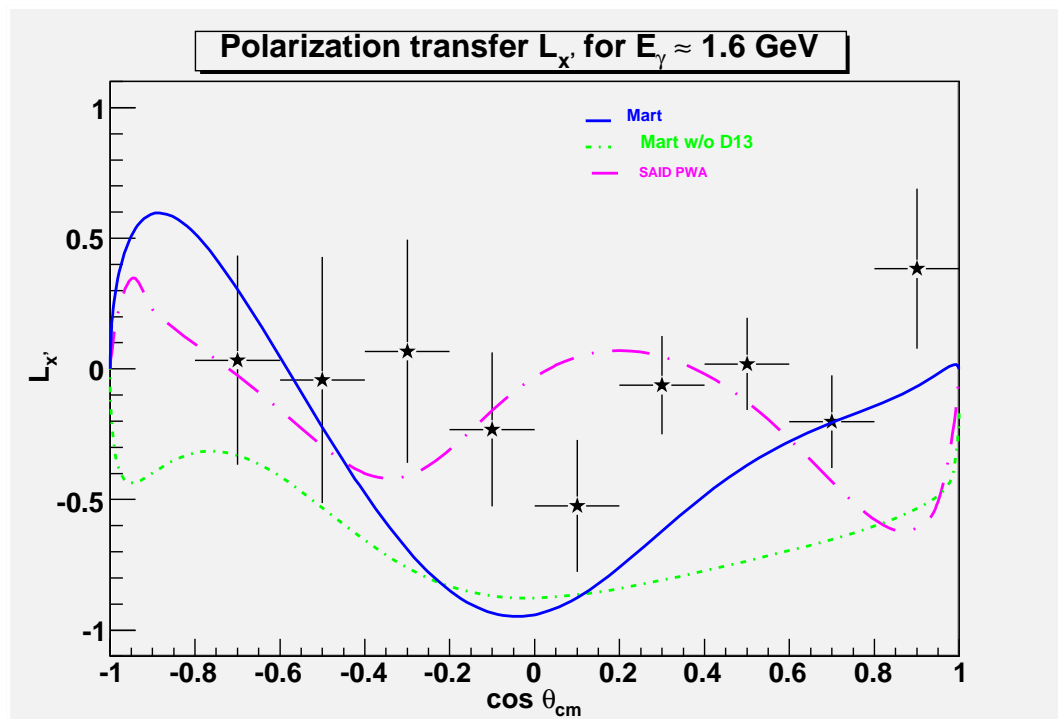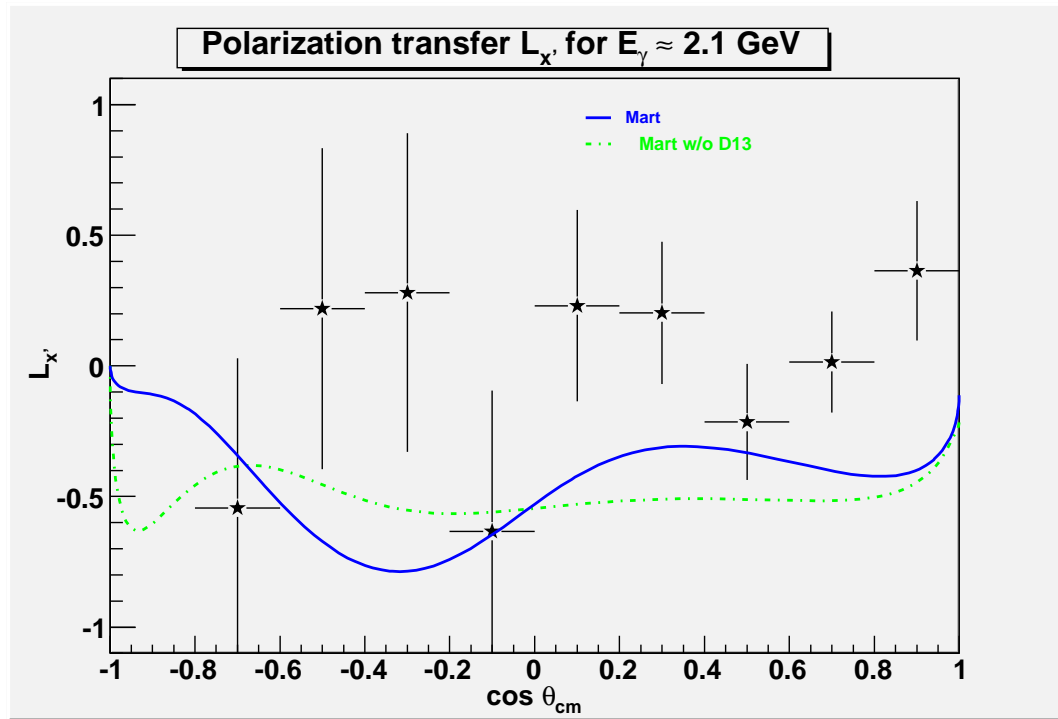(a) 2.0 GeV $< E_\gamma <$ 2.2 GeV
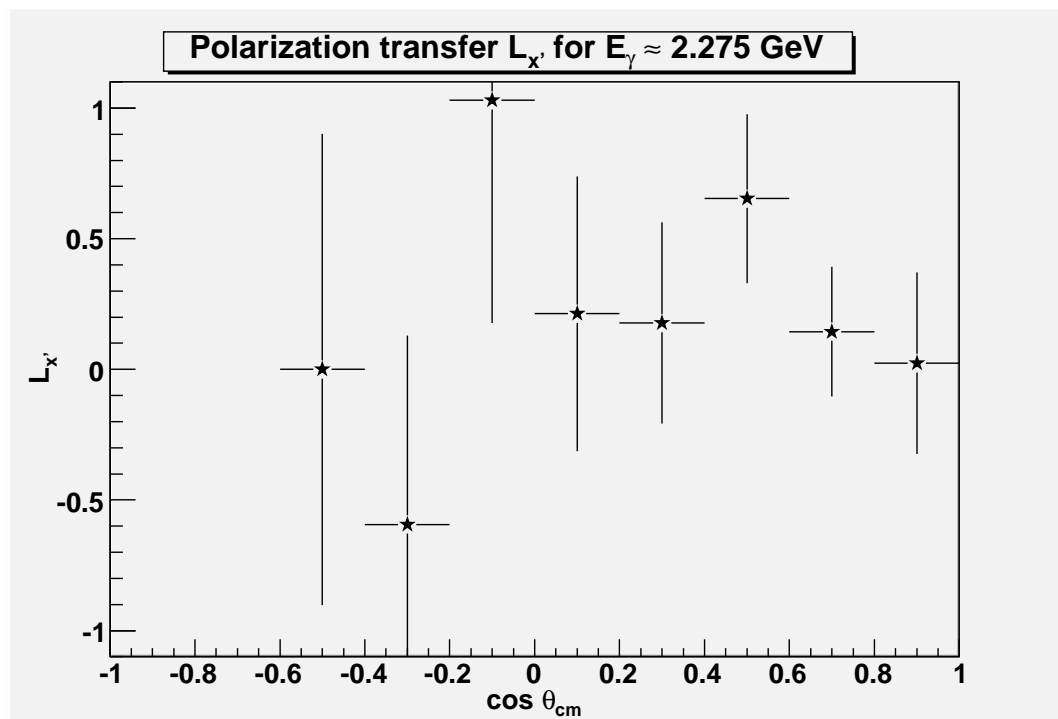
(b) 2.2 GeV $< E_\gamma <$ 2.4 GeV

Figure 7.10: Model comparison plots for $L_{x'}$. The Mart model is represented by the solid blue line.

when the missing D_{13} resonance is not take into consideration). The best agreement occurs at 1.3 GeV, but even there the magnitude places it outside of the error ranges of all but a few angular bins. Even so, the curvature of the plot does seem to match my results, even if the actual curve of measured values is disturbed in the most forward two angular bins. A slight change of a relatively ambiguous factor like the effective dilution could bring the data points to fit the model curve quite well. enough to not be inconsistent with my results if the curve was simply adjusted upward slightly. It should not be forgotten that this is just one of ten energy bins and the model predictions are even poorer for every other bin. If each plot looked like the 1.3 GeV bin, it would stand as a good confirmation that the model is generally correct and only some systemic flaw in the data is causing the inconsistency or a only slight modification to the model would be necessary for the sake of accuracy. The more erratic inconsistency of my results with the Mart model point to either a deeper flaw in the model or a more significant and complicated correction that needs to be made for the data - possibly both.

7.3   Discussion of $L_{z'}$

Model calculations for $L_{z'}$ fare much better than those for E and $L_{x'}$. Even where the distribution of my asymmetry values does not follow the shape of the model curve well, the curve most often falls within my measured errors. At 1.5 GeV, the Mart model is rarely far off from my measured values. In stark contrast, the Saghai model and SAID PWA seem to agree with my data only where they follow the Mart model closely. At all serious points of departure between the models, the Mart model retains the advantage. The level of agreement here between Mart model predictions and data would make a powerful argument for the existence and presence of the $D_{13}(1960)$ resonance in the $\gamma p \to K^+ \Lambda$ reaction channel were it not for the failures of the model to describe the behavior of the previous two observ-

ables shown in this thesis. Nonetheless, the Mart model has overall, if barely, shown the best agreement of the models shown with data at 1.5 GeV and the evidence here should not be dismissed. $L_{z'}$ should be grouped with cross section and recoil among the observables pointing to the existence of the $D_{13}(1960)$ resonance. It is also interesting to note that just as Craig Paterson saw a reversal from $C_{x'}$ and $C_{z'}$ for the polarization transfer in $O_{x'}$ and $O_{z'}$, I now see a reversal of which polarization axis offers better evidence for the presence of the $D_{13}(1960)$ resonance. For, while he saw better agreement with models that include the resonance in $O_{x'}$, but not in $O_{z'}$, I see it in $L_{z'}$ and $L_{x'}$ shows slightly better agreement with the Saghai model.

The Mart model makes very similar predictions for the neighboring energy bins at 1.4 GeV and 1.6 GeV. Therefore, it is difficult to argue for the presence of resonances on the strength of variation in energy. Nonetheless, my data do seem to show a flatter asymmetry distribution at least for 1.4 GeV. However, the error bars are mostly large enough that one cannot argue this way unambiguously. The error bars are certainly too large to resolve between the Mart model with and without the D_{13} resonance as they follow each other rather closely here. The model looks flatter, like the data, without the missing resonance, but this does not always make it more consistent with the data. Thus, a model curve which is very similar to 1.5 GeV predictions remains in agreement with most of the angular bins although the nominal values for neighboring angular bins are closer together than the model would suggest. This degree of flatness is also seen in the 1.6 GeV data, except in the backward direction. Indeed the oscillations are slight over the whole energy range and are typically consistent with zero within the uncertainty. Thus, the SAID solution, which shows a particularly strong oscillation is in poor agreement with all my $L_{z'}$ data.

For the other energy bins, I again only have Mart model predictions or no predictions. The 1.05 GeV bin is consistent with the Mart model curves only in the backward angle region. The asymmetry does not slope down in the manner predicted, but the SAID solution

remains close to measured values throughout. The 1.175 GeV plot shows some oscillation, which agree well with the Mart model except at the most forward angles. The SAID PWA does better in this region, but makes a poorer fit overall. The 1.3 GeV data really seems to show a very flat asymmetry, so the Mart model does best when the missing resonance is not included, although no model shows great agreement with the measurements at this energy.

This trend continues through to 1.9 GeV. At the 1.725 GeV bin, the Mart model follows the flat asymmetry distribution in the forward angle region. When the D_{13} resonance is excluded, the model curve slopes up giving better agreement in the most forward bins, but again the statistics are not good enough to resolve the disparity. The Mart model curve and data points both show an asymmetry hovering closer to zero than what was seen in the previous bin at 1.6 GeV. Depending on the mass of the $N = 3$ band D_{13} resonance, the signature could appear in the 1.6 GeV plot and could explain the return to a flat asymmetry distribution in the following energy bin. At 1.9 GeV the data still shows considerable agreement with model predictions, but error bars are starting to become large enough that this statement loses some impact, particularly when most agreement in the backward direction falls near the extremes of the error bars. The data show more oscillation here than the models for once. While there is still significant agreement with all predictions in the forward direction at 1.9 GeV, there is not as much in the most forward bins at 2.1 GeV. Overall though agreement is pretty good here whether or not the missing resonance is included. Yet much of this agreement is due to the significant uncertainty in all backward angle bins. The uncertainties at 2.3 GeV are too large to make any claim about the shape of the asymmetry. While it seems to follow a similar path to the 2.1 GeV measurements, the statistics are too low to be certain.

In spite of some inconsistencies, the agreement between $L_{z'}$ data and the Mart model is fairly good for the whole dataset. While no one observable can resolve the question of
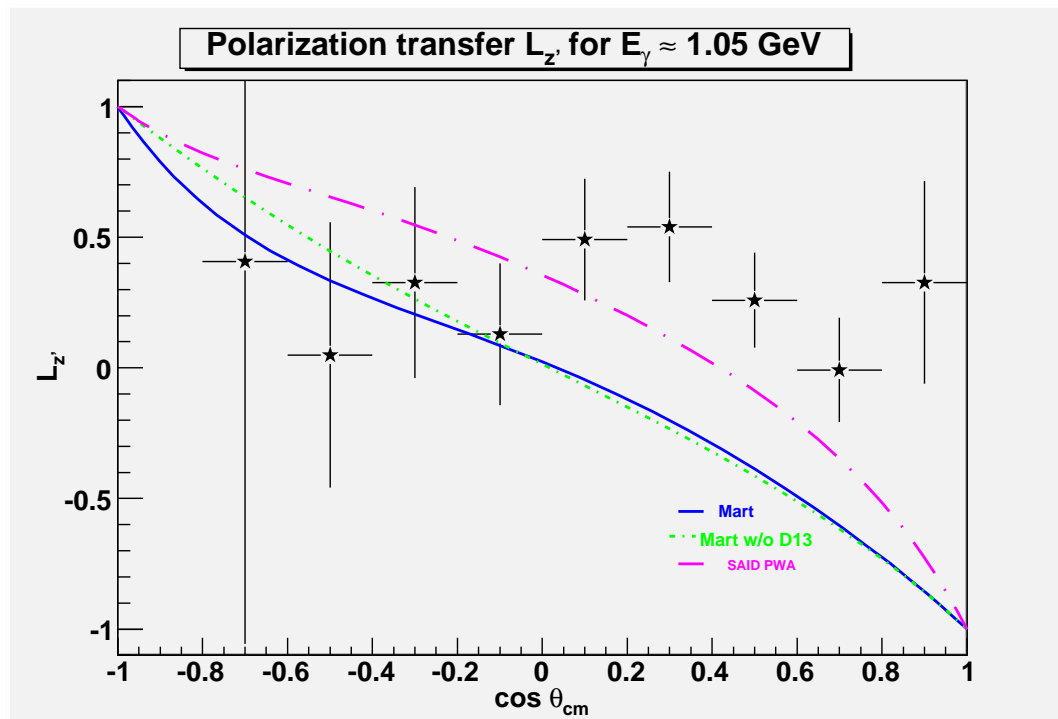
(a) 0.9 GeV < E_γ < 1.1 GeV
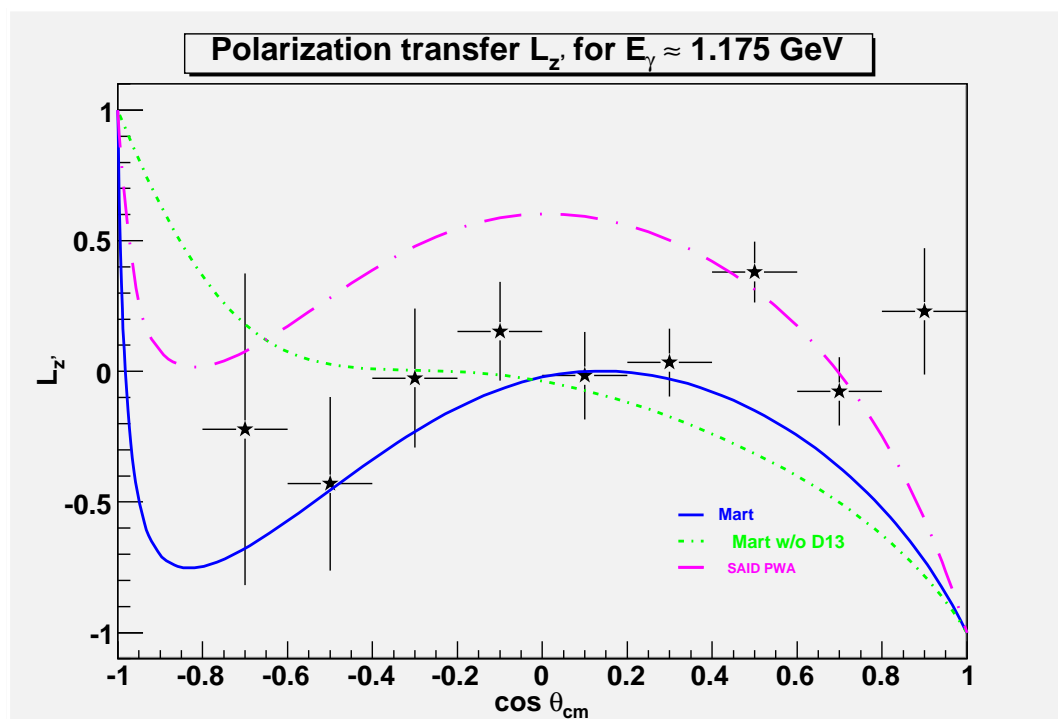
(b) 1.1 GeV < E_γ < 1.25 GeV

Figure 7.11: Model comparison plots for $L_{z'}$. The Mart model is represented by the solid blue line.
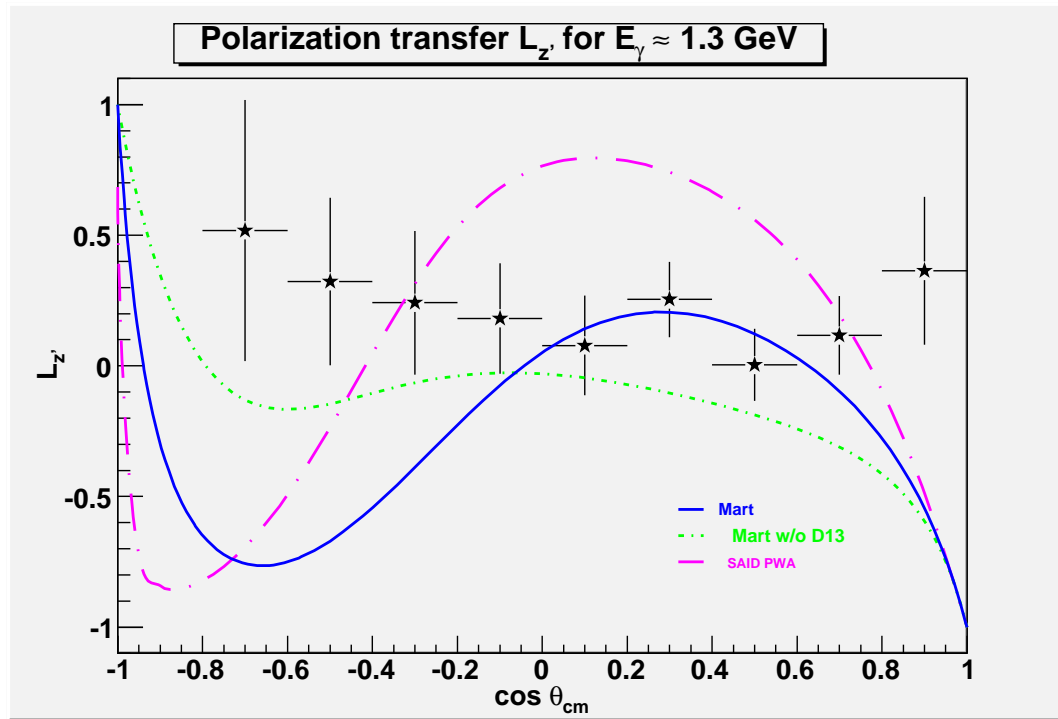
(a) 1.25 GeV $< E_\gamma <$ 1.35 GeV
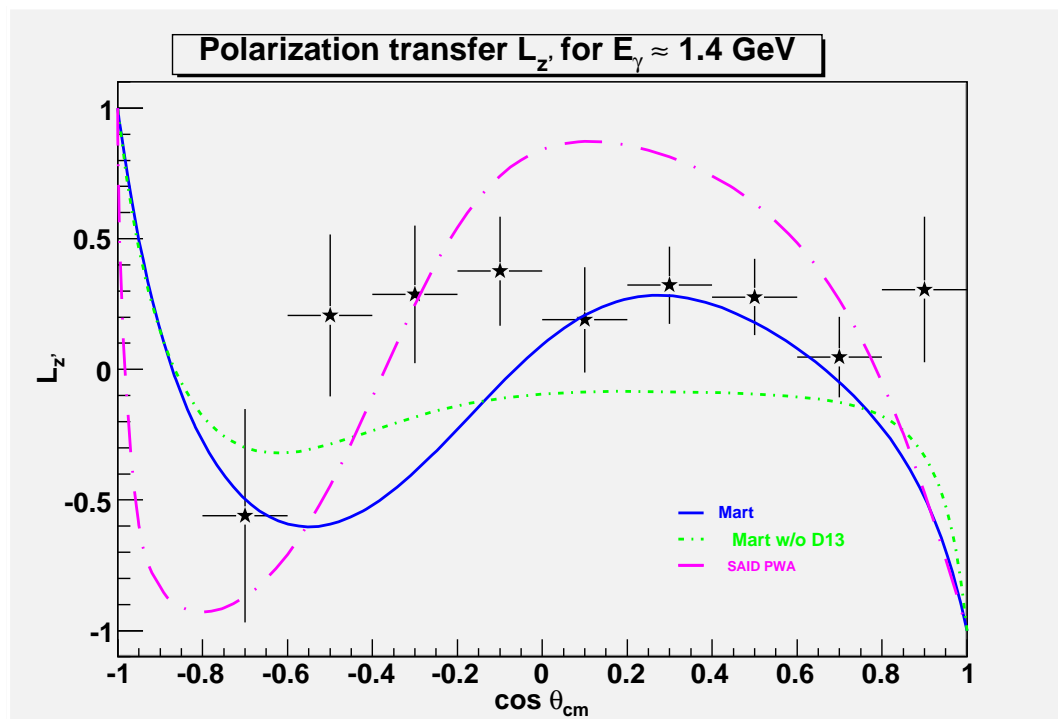
(b) 1.35 GeV $< E_\gamma <$ 1.45 GeV

Figure 7.12: Model comparison plots for $L_{z'}$. The Mart model is represented by the solid blue line.
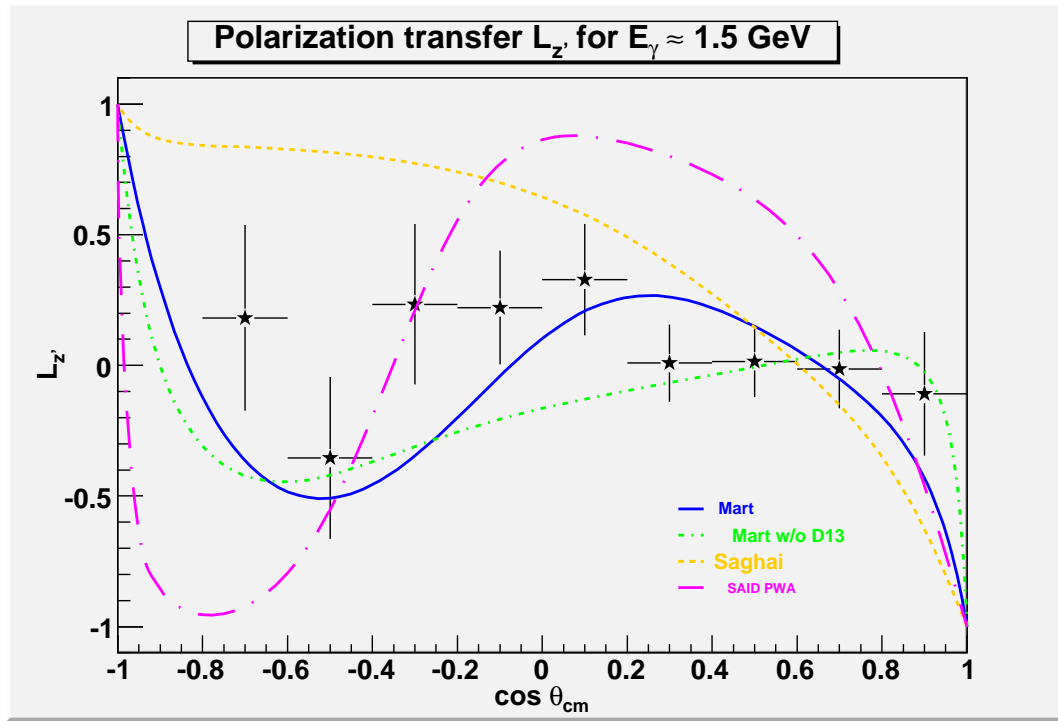
(a) 1.45 GeV < E_γ < 1.55 GeV
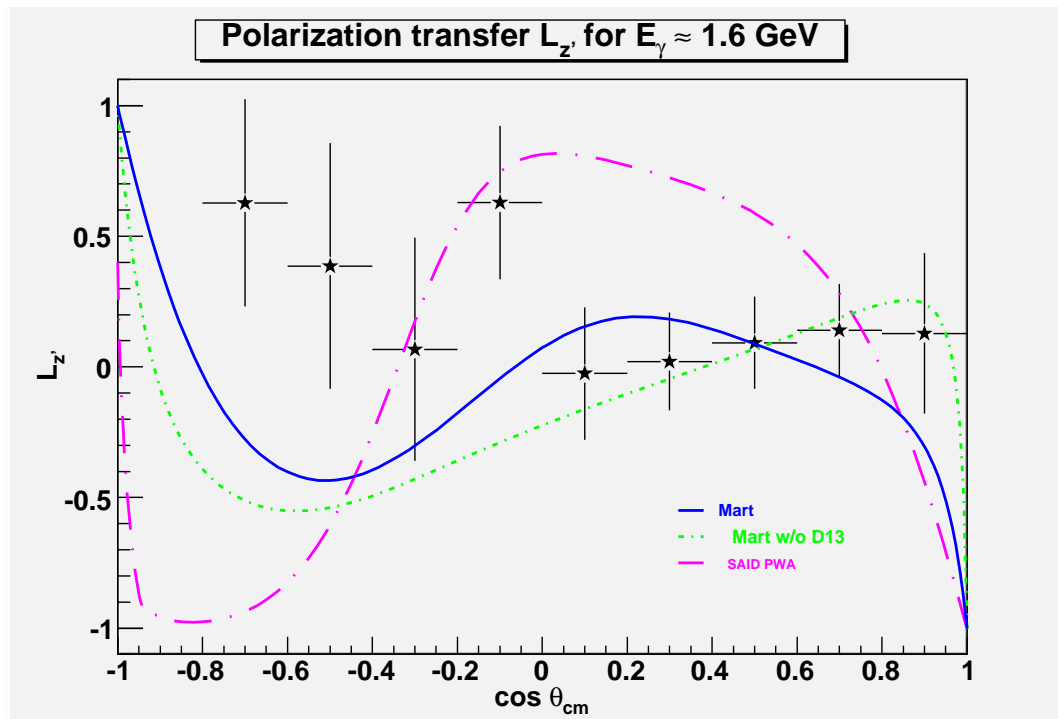
(b) 1.55 GeV < E_γ < 1.65 GeV

Figure 7.13: Model comparison plots for $L_{z'}$. The Mart model is represented by the solid blue line, the Saghai model is represented by the dashed orange line, and the SAID PWA are shown in the dash-dot magenta line.

(a) 1.65 GeV $< E_\gamma <$ 1.8 GeV

(b) 1.8 GeV $< E_\gamma <$ 2.0 GeV
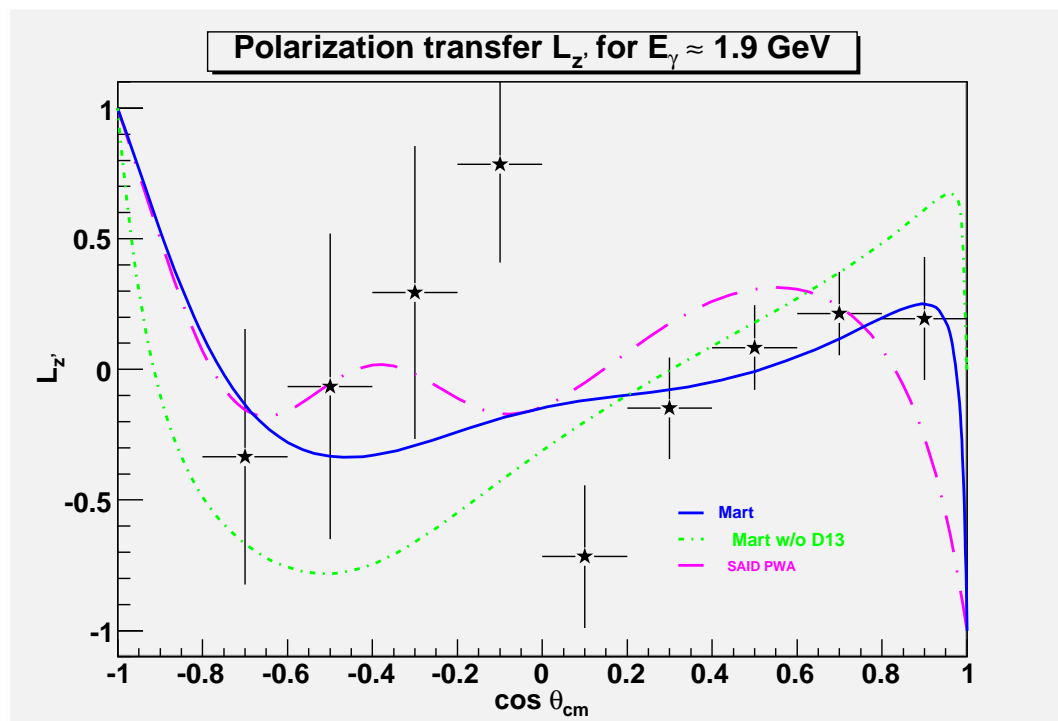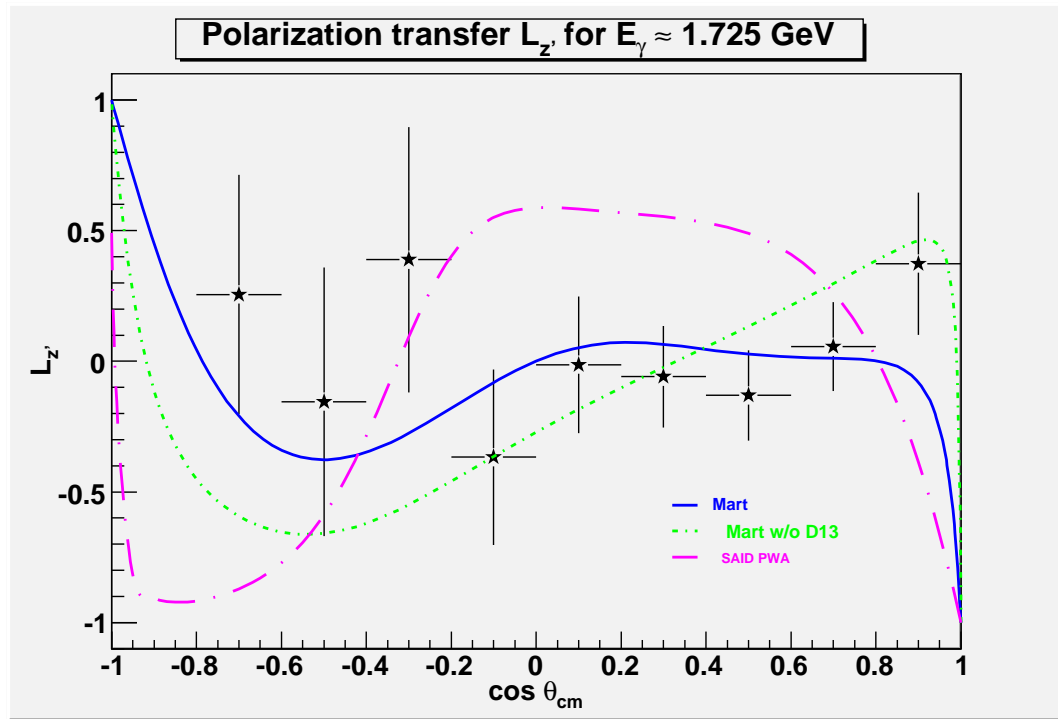
Figure 7.14: Model comparison plots for $L_{z'}$. The Mart model is represented by the solid blue line.
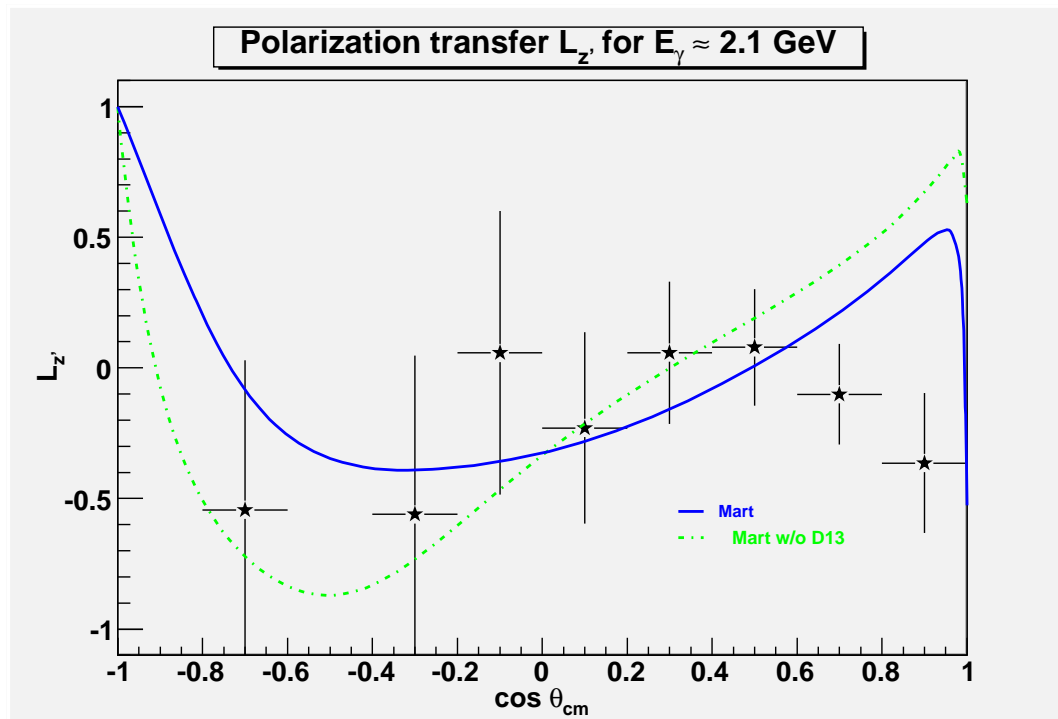
(a) 2.0 GeV < E_γ < 2.2 GeV
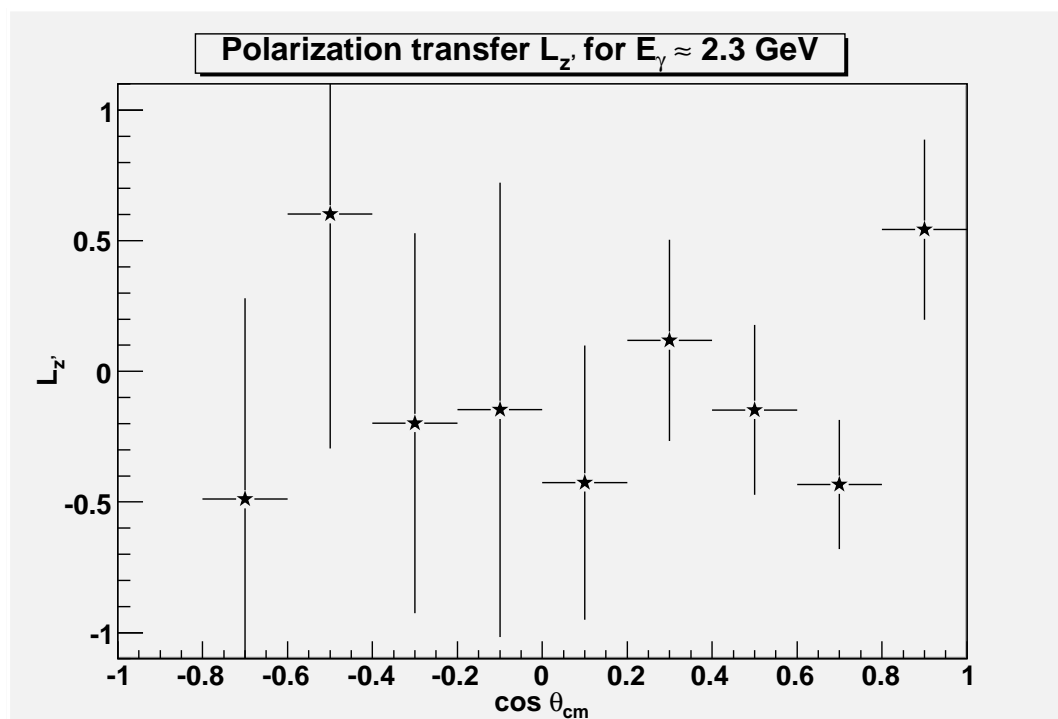
(b) 2.2 GeV < E_γ < 2.4 GeV

Figure 7.15: Model comparison plots for $L_{z'}$. The Mart model is represented by the solid blue line.

resonant contributions, or else the matter of the $D_{13}(1960)$ resonance would have already been resolved, the agreement between measured asymmetry and predicted, particularly at 1.5 GeV, adds yet more supporting evidence in favor for its existence.

7.4 Conclusion

Examination of the polarization asymmetries plotted over $cos\theta_{CM}$ and photon energy has revealed some interesting features. Relatively abrupt structures exist in some plots that may point to resonant coupling in the channel and the Mart model, which includes the $D_{13}(1960)$ resonance, generally shows better agreement with the data than the Saghai model, which does not. Nevertheless, it is important to note that no model adequately describes the asymmetry distribution seen in all these plots. The data for the observables obtained in this analysis alone are insufficient to determine which resonances are present and which are not coupling to the reaction channel. Rather, the values obtained in this thesis work for three double polarization observables across 90 kinematic bins will be more valuable as constraints for the calculation of the complex amplitudes describing the reaction. A complete coupled-channel analysis incorporating the $\gamma p \to K^+ \Lambda$ reaction channel will be performed using the complete set of polarization observables obtained from g1c, g8b, g9a, and g9b. This analysis is expected to offer the best word on the existence of the missing baryon resonances.

Bibliography

[1] M. Breidenbach, *et al.*, Phys. Rev. Lett. **23**, 935 (1969).

[2] S. Capstick, Phys. Rev. **D46**, 2864 (1992); S. Capstick and W. Roberts, Phys. Rev. **D49**, 4570 (1994);S. Capstick and W. Roberts, Phys. Rev. **D58**, 074011 (1998); Prog. Part. Nucl. Phys. **45, Suppl. 2**, 5241 (2000).

[3] M. Gell-Mann, Phys. Lett. **8**, 214 (1964).

[4] M. Williams. *Measurement of Differential Cross Sections and Spin Density Matrix Elements along with a partial wave analysis for* $\gamma p \rightarrow \rho \omega$ *using CLAS at Jefferson Lab*. Ph.D. Thesis, Carnegie Mellon University, 2007.

[5] M. Breinig. *FM Saturation Spectroscopy*, <http://electron9.phys.utk.edu/optics507/modules/m10/saturation.htm> (Accessed 27 Feb. 2011).

[6] R. Koniuk and N. Isgur, Phys. Rev. **D21**, 1868 (1980); N. Isgur and G. Karl, Phys. Lett. **72B**, 109 (1977).

[7] S. Capstick and N. Isgur, Phys. Rev. **D34**, 2809 (1986).

[8] K. Nakamura et al., Review of Particle Physics. J. Phys. **G37**, 1149 (2010).

[9] D. B. Lichtenberg, Phys. Rev. **178**, 2197 (1969); R.E. Cutkosky and R.E. Hendrick, Phys. Rev. **D16**, 2902 (1977).

[10] C.A. Paterson, *Polarization Observables in Strangeness Photoproduction with CLAS at Jefferson Lab*. Ph.D. Thesis, University of Glasgow, 2008.

[11] TJNAF proposal PR02-112 (2002): "Search for missing Nucleon Resonances in the Photoproduction of Hyperons using a Polarized Photon Beam and a Polarized Target", spokesperson F. J. Klein.

[12] G. Knöchlein, D. Drechsel, and L. Tiator, Z. Phys. **A352**, 327 (1995).

[13] R.A. Adelseck, C. Bennhold, L.E. Wright, Phys. Rev. **C32**, 1681 (1985); R.A. Adelseck and B. Saghai, Phys. Rev. **C42**, 108, 1990.

[14] C.G. Fasano, F. Tabakin, B. Saghai, Phys. Rev. **C46**, 2430 (1992).

[15] W.-T. Chiang, F. Tabakin, Phys. Rev. **C55**, 2054 (1997).

[16] W.-T. Chiang, F. Tabakin, T.-S.H. Lee, B. Saghai, Phys. Lett **B517**, 101 (2001).

[17] H. Olsen and L.C. Maximon, Phys. Rev. **114**, 887 (1959).

[18] G.D. Rochester, C.C. Butler, Nature **160**, 855 (1947).

[19] J.W.C. McNabb, *Photoproduction of Λ and Σ^0 Hyperons off Protons in the Nucleon Resonance Region using CLAS at Jefferson Lab*. Ph.D. Thesis, Carnegie Mellon University, 2002.

[20] R.K. Bradford, *Measurement of differential cross sections and C_x and C_z for $\gamma p \to K^+\Lambda$ and $\gamma p \to K^+\Sigma^0$ using CLAS at Jefferson Lab*. Ph.D. Thesis, Carnegie Mellon University, 2005.

[21] M.E. McCracken, *A Study of $K^+\Lambda$ Photoproduction in the CLAS g11a Dataset: Differential Cross Section, Recoil Polarization, and a Partial Wave Analysis*. Ph.D. Thesis, Carnegie Mellon University, 2007.

[22] R. Erbe, *et al.* (ABBHHM collaboration), Phys. Rev. **188**, 2060 (1969).

[23] W.J. Schwille, *et al.*, Nucl. Inst. Meth. **A344**, 470 (1994).

[24] M. Bockhorst, *et al.*, Z. Phys. **C63**, 37 (1994).

[25] M.Q. Tran, *et al.*, Phys. Lett. **B445**, 20 (1998).

[26] K.H. Glander, *et al.*, Eur. Phys. J. **A19,** 2 (2004).

[27] M. Sumihama, *et al.,* Phys. Rev. **C73**, 035214 (2006).

[28] K. Hicks, *et al.,* Phys. Rev. **C76**, 042201 (2007).

[29] A. Lleres, *et al.,* Eur. Phys. J. **A31**, 79 (2007).

[30] M. Crofford, *et al*., *The RF system for the CEBAF Polarized Photoinjector*. Technical report, Thomas Jefferson National Accelerator Facility, 1993.

[31] C.K. Sinclair, *Polarized electrons at Jefferson Laboratory*. Technical report, Thomas Jefferson National Accelerator Facility, 1997

[32] B.M. Dumham, *Jefferson Lab, a status report*. Thomas Jefferson National Accelerator Facility, 1997.

[33] D.I. Sober, *et al*., *The bremsstrahlung tagged photon beam in Hall B at JLab*. Nucl. Inst. Meth. **A440**, 263 (2000).

[34] B. Mecking, *et al*., *The CEBAF Large Acceptance Spectrometer (CLAS)*. Nucl. Inst. Meth. **A503/03**, 513, 2003

[35] Y.G. Sharabian, *et al*., *A new highly segmented start counter for the CLAS detector*. Nucl. Phys. **A556**, 246 (2006).

[36] Alan J. Street, *et al.*, *Final site assembly and testing of the superconducting toroidal magnet for the CEBAF Large Acceptance Spectrometer* (CLAS). IEEE Trans. Mag. **32**, No. 4, 2074 (1996).

[37] M.D. Mestayer, *et al.*, *The CLAS drift chamber system*. Nucl. Inst. Meth. **A449**, 81 (2000).

[38] .E.S. Smith, *et al.*, *The time of flight system for CLAS*. Nucl. Inst. Meth. **A432**, 265 (1999).

[39] R. Ursik et al. *1 nA beam position monitoring system*. Proceeding of the 1997 Particle Accelerator Conference, 2131 (1999) .

[40] J. Ball and E. Pasyuk. *Photon Flux Determination Through Sampling of "out-of-time" Hits with the Hall B Photon Tagger*. CLAS Note 2005-002.

[41] C. Keith. *Jefferson Lab Frozen Spin Target*, <http://www.jlab.org/~ckeith/Frozen/Frozen.html>

[42] J. Li, *The New Tagger Calibration Program*. CLAS Note 03-004, 2003.

[43] E. Anciant, *et al*. *Tagger Hit Reconstruction Software and Tagger Calibration Overview*. CLAS Note 99-004, 1999.

[44] Personal communication with Hideko Iwamoto.

[45] Personal communication with Michael Dugger.

[46] Samuel S. M. Wong. *Introductory Nuclear Physics*. Prentice-Hall Inc., 1990.

[47] Philip R. Bevington and D. Keith Robinson. *Data Reduction and Error Analysis for the Physical Sciences*. McGraw-Hill, 2003.

[48] FROST wiki. <http://clasweb.jlab.org/rungroups/g9/wiki/index.php/Beam_Polariz-ation_(Circ.)>

[49] T. Mart and C. Bennhold, Phys. Rev. **C61**, 012201 (2000).

[50] B. Saghai, *et al.*, in: Proceedings of the *Workshop on Hypernuclear Physics with Electromanetic Probes*, Hampton (VA), Dec. 1999; B. Saghai, invited talk at *International Symposium on Hadrons and Nuclei*, Seoul, Feb. 2001, nucl-th/0105001.

[51] G9a Run Table <http://www.jlab.org/~clasg9/g9a_allruns.dat>

[52] J.C. David, C. Fayard, G.H. Lamot, B. Saghai, Phys. Rev. **C53**, 2613 (1996).

[53] B. Saghai, Nucl. Phys. **A639**, 217c (1998).

[54] R.L. Anderson, *et al.*, Phys. Rev. Letters **9**, 131 (1962); C.W. Peck, Phys. Rev. **135**, 830 (1964); A.J. Sadoff, *et al.*, Bull. Am. Phys. Soc. **9**, 23 (1964); R.L. Anderson, *et al.*, Proc. Int. Symp. on electron and photon interactions, Hamburg (1965), 203; S. Mori, Ph.D. thesis, Cornell University, 1966; H. Thom, a compilation, Phys. Rev. **151** 1322 (1966); N.B. Mistry, *et al.*, Phys. Lett. B **24** 528 (1967); D.E. Groom, J.H. Marshall, Phys. Rev. **159**, 1213 (1967); A. Bleckmann, *et al.*, Z. Phys. **239**, 1 (1970); T. Fujii, *et al.*, Preprint (INS, Univ. of Tokyo, 1970); P. Feller, *et al.*, Nucl. Phys. B **39** 413 (1972); M. Grilli, *et al.*, Nuovo Cim. **38** 1467 (1965).

[55] C.L. Schat, J.L. Goity, N.N. Scoccola, hep-ph/0111082 (2001); J.L. Goity, Phys. Lett. **B414**, 140 (1997); C.E. Carlson, C.D. Carone, J.L. Goity, and R.F. Lebed, Phys. Lett. **B438**, 327 (1998), Phys. Rev **D59**, 114008 (1999).

[56] D. Decamp, *et al.*, L.A.L. 1236 (1970).

[57] G. Goeing, W. Schorch, J. Tietge, W. Weilenbock, Nucl. Phys. **B26**, 121 (1971).

[58] R. Haas, *et al.*, Nucl. Phys. **B137** 261 (1978).

[59] R.L. Anderson, *et al.*, Phys. Rev. **D14**, 679 (1976).

[60] K. Abe, *et al.*, Phys. Rev. **D32**, 2869 (1985).

[61] TJNAF experiment E89-004 (1989): "Electromagnetic Prodcution of Hyperons", spokesperson R. Schumacher.

[62] G.F. Chew, M.L. Goldberger, F.E. Low, and Y. Nambu, Phys. Rev. **106**, 1345 (1957).

[63] R.A. Williams, C-R. Ji, S.R. Cotanch, Phys. Rev. **C46**, 1617 (1992).

[64] T. Mart, C. Bennhold, C.E. Hyde-Wright, Phys. Rev. **C51**, 1074 (1995).

[65] S.S. Hsiao, D.H. Lu, S.N. Yang, Phys. Rev. **C61**, 068201 (2000).

[66] S. Janssen, J. Ryckebusch, D. Debruyne, and T. Van Cauteren, Phys. Rev. **C65**, 015201 (2001).

[67] T. Feuster and U. Mosel, Phys. Rev. **C58**, 457 (1998); Phys. Rev. **C59**, 460 (1999).

[68] T. Sato and T.-S.H. Lee, Phys. Rev **C54**, 2660 (1996).

[69] C. Bennhold, T. Mart, A. Waluyo, H. Haberzettl, G. Penner, T. Feuster, and U. Mosel, in *Proceedings of the Workshop on Electron Nucleus Scattering*, Elba, Italy, 1998, nucl-th/9901066 (1999); H. Haberzettl, C. Bennhold, T. Mart and T. Feuster, in *Proceedings of Baryons 98*, Bonn, Germany, 1998, nucl-th/9811024 (1998).

[70] D.H. Saxon, *et al.*, Nucl. Phys. **B162**, 522 (1980).

[71] K.W. Bell, *et al.*, Nucl. Phys. **B222**, 389 (1983).

[72] G. Niculescu, *et al.*, Phys. Rev. Lett. **81**, 1805 (1998).

[73] C. Bennhold, H. Haberzettl, T. Mart, invited talk at the *2nd ICTP International Conference on Perpectives in Hadronic Physics*, Trieste Italy, June 1998, nucl-th/9909022 (1999).

[74] Z. Li, B. Saghai, Nucl. Phys. **A644**, 345 (1998); Z. Li, B. Saghai, T. Ye, Q. Zhao, *work in progress*; Z Li, H. Ye, M. Lu, Phys. Rev **C56**, 1099 (1997).

[75] F.X. Lee, T. Mart, C. Bennhold, H. Haberzettl, L.E. Wright, nucl-th/9907119.

[76] .R A. Arndt, I. I. Strakovsky, and R. L. Workman, <http://gwdac.phys.gwu.edu>

[77] R. A. Arndt, C. H. Oh, I. I. Strakovsky, R. L. Workman, and F. Dohrmann, Phys. Rev. **C56**, 3005 (1997).

[78] M. Guidal, *et al.*, Nucl. Phys. **A627** 645 (1997); M. Guidal, J. M. Laget, and M. Vanderhaegen, Phys. Rev. **C61**, 025204 (2000).

[79] S.U. Chung, *et al.*, Phys. Rev. **D65**, 072001 (2002); C. Amsler, Nucl. Phys. **A663**, 93 (2000).

[80] W. Meyer, in *Proceedings of the GDH2000 Symposium* Mainz, Germany, 2000, (World Scientific, 2001) p. 157.

[81] Y. Miyachi, in *Proc. 8th Int. Workshop on Polarized Materials and Techniques*, Vancouver, Canada, 1996; SPring8 proposal 2001, "The test of the GDH sum rule at SPring8", spokesperson T. Iwata, Nagoya, Japan; T. Iwata, N. Horikawa, *private communication*.

[82] D.G. Crabb and W. Meyer, Ann. Rev. Nucl. Part. Sci. **47**, 67 (1997).

[83] H. Dutz, *et al.*, NIM **A356**, 111 (1995).

[84] TJNAF experiment E01-104 (2001): "Helicity Structure of Pion Photoproduction", update of E91-015, spokespersons D. I. Sober, M. Khandaker, D. G. Crabb.

[85] I.S. Barker, A. Donnachie, J.K. Storrow, Nucl. Phys. **B75**, 347 (1975).

[86] G. Keaton and R. Workman, Phys. Rev. **C53**, 1434 (1996).

[87] R.L. Walker, Phys. Rev. **182**, 1729 (1969)

Appendix A Target Polarization by Run

The measured target polarization values and errors are presented here for each run used in the analysis. The full table can be found at [51].

Run	P_T	Stat Err	Sys Err
55521	-0.807	0.000	0.001
55522	-0.805	0.000	0.001
55523	-0.804	0.000	0.001
55524	-0.803	0.000	0.001
55525	-0.801	0.001	0.002
55527	-0.802	0.000	0.001
55528	-0.801	0.000	0.001
55531	-0.800	0.000	0.001
55532	-0.799	0.000	0.001
55533	-0.797	0.000	0.001
55534	-0.797	0.000	0.001
55535	-0.796	0.000	0.001
55536	-0.795	0.000	0.001
55537	-0.795	0.000	0.001
55538	-0.793	0.000	0.001

55539	-0.793	0.000	0.001
55540	-0.792	0.000	0.001
55541	-0.791	0.000	0.001
55542	-0.790	0.000	0.001
55543	-0.790	0.000	0.001
55545	-0.786	0.000	0.003
55546	-0.785	0.000	0.005
55547	-0.784	0.000	0.007
55548	-0.783	0.000	0.010
55549	-0.782	0.000	0.014
55550	-0.782	0.000	0.018
55551	-0.781	0.000	0.026
55552	-0.780	0.000	0.034
55556	0.897	0.000	0.001
55557	0.894	0.000	0.001
55558	0.893	0.000	0.002
55559	0.894	0.000	0.001
55560	0.892	0.000	0.001
55561	0.890	0.000	0.001
55562	0.889	0.000	0.002
55563	0.886	0.000	0.001
55565	0.884	0.000	0.001
55566	0.882	0.000	0.001
55567	0.881	0.000	0.001
55568	0.879	0.000	0.001

55569	0.878	0.001	0.002
55570	0.875	0.001	0.002
55571	0.874	0.000	0.001
55572	0.866	0.000	0.001
55573	0.866	0.000	0.001
55574	0.866	0.000	0.001
55575	0.863	0.000	0.001
55576	0.862	0.000	0.001
55577	0.860	0.000	0.001
55578	0.859	0.000	0.001
55579	0.854	0.000	0.001
55580	0.853	0.000	0.001
55581	0.852	0.000	0.001
55582	0.848	0.000	0.001
55583	0.846	0.000	0.001
55584	0.807	0.001	0.001
55585	0.803	0.001	0.001
55586	0.801	0.001	0.001
55589	0.916	0.004	0.001
55590	0.913	0.004	0.001
55591	0.911	0.004	0.001
55592	0.909	0.003	0.001
55593	0.905	0.003	0.001
55594	0.903	0.003	0.001
55595	0.902	0.005	0.002

55604	-0.853	0.000	0.001
55605	-0.852	0.000	0.001
55606	-0.851	0.000	0.001
55610	-0.848	0.000	0.002
55611	-0.847	0.000	0.001
55612	-0.846	0.000	0.001
55613	-0.846	0.000	0.001
55614	-0.845	0.000	0.001
55615	-0.844	0.000	0.001
55616	-0.842	0.000	0.001
55617	-0.842	0.000	0.001
55618	-0.842	0.000	0.001
55619	-0.841	0.000	0.001
55620	-0.840	0.000	0.001
55621	-0.839	0.000	0.001
55622	-0.839	0.000	0.001
55623	-0.837	0.000	0.001
55624	-0.836	0.000	0.001
55625	-0.835	0.000	0.001
55630	0.876	0.000	0.001
55631	0.874	0.000	0.001
55632	0.872	0.000	0.001
55633	0.871	0.000	0.001
55634	0.869	0.000	0.001
55635	0.867	0.000	0.001

55636	0.866	0.000	0.001
55637	0.865	0.000	0.001
55638	0.864	0.000	0.001
55639	0.862	0.000	0.001
55640	0.861	0.000	0.001
55641	0.859	0.000	0.001
55642	0.857	0.000	0.001
55643	0.856	0.000	0.001
55644	0.854	0.000	0.001
55645	0.852	0.000	0.001
55646	0.850	0.000	0.001
55647	0.848	0.000	0.001
55648	0.846	0.000	0.001
55649	0.845	0.000	0.001
55650	0.843	0.000	0.001
55651	0.842	0.000	0.001
55652	0.841	0.000	0.001
55653	0.838	0.000	0.001
55654	0.833	0.000	0.002
55655	0.834	0.000	0.001
55656	0.833	0.000	0.001
55657	0.830	0.000	0.001
55658	0.829	0.000	0.001
55659	0.828	0.000	0.001
55660	0.827	0.000	0.001

55661	0.826	0.000	0.002
55662	0.826	0.000	0.001
55663	0.825	0.000	0.001
55664	0.822	0.000	0.001
55665	0.821	0.000	0.001
55666	0.819	0.000	0.001
55667	0.818	0.000	0.001
55668	0.817	0.000	0.002
55669	0.776	0.000	0.001
55670	0.775	0.000	0.001
55671	0.773	0.000	0.001
55672	0.772	0.000	0.001
55673	0.770	0.000	0.001
55674	0.769	0.000	0.001
55675	0.768	0.000	0.001
55676	0.767	0.000	0.001
56164	-0.809	0.000	0.001
56165	-0.808	0.000	0.001
56166	-0.807	0.000	0.001
56167	-0.805	0.000	0.001
56168	-0.805	0.000	0.001
56169	-0.803	0.000	0.001
56170	-0.803	0.000	0.001
56171	-0.801	0.000	0.001
56172	-0.800	0.000	0.001

56173	-0.800	0.000	0.001
56174	-0.799	0.000	0.001
56175	-0.798	0.000	0.001
56176	-0.797	0.000	0.001
56177	-0.796	0.000	0.001
56178	-0.796	0.000	0.001
56179	-0.795	0.000	0.001
56180	-0.794	0.000	0.001
56182	-0.794	0.000	0.002
56183	-0.793	0.000	0.001
56184	-0.792	0.000	0.001
56185	-0.791	0.000	0.001
56186	-0.791	0.000	0.001
56187	-0.790	0.000	0.001
56188	-0.789	0.000	0.001
56189	-0.788	0.000	0.001
56190	-0.788	0.000	0.001
56191	-0.787	0.000	0.001
56192	-0.786	0.000	0.001
56193	-0.785	0.000	0.002
56196	0.827	0.000	0.001
56197	0.824	0.000	0.001
56199	0.821	0.000	0.001
56200	0.819	0.000	0.001
56201	0.817	0.000	0.001

56202	0.815	0.000	0.001
56203	0.812	0.000	0.001
56204	0.811	0.000	0.001
56205	0.810	0.000	0.001
56206	0.809	0.000	0.001
56207	0.808	0.000	0.001
56209	0.806	0.000	0.001
56210	0.805	0.000	0.001
56211	0.804	0.000	0.001
56215	0.801	0.000	0.001
56216	0.800	0.000	0.002
56220	0.796	0.000	0.001
56221	0.795	0.000	0.001
56222	0.794	0.000	0.001
56223	0.793	0.000	0.001
56224	0.792	0.000	0.001
56225	0.787	0.000	0.001
56226	0.786	0.000	0.001
56227	0.784	0.000	0.001
56228	0.782	0.000	0.001
56229	0.782	0.000	0.001
56230	0.781	0.000	0.001
56231	0.779	0.000	0.001
56232	0.778	0.000	0.001
56233	0.776	0.000	0.001